

**Mid- to Late Holocene geomorphodynamics and  
their interactions with climate changes and  
settlement activities in the Pergamon micro-  
region (Bakırçay and Madras River catchment,  
western Türkiye)**

**A Dissertation**

Submitted in Fulfilment of the Requirements for the Degree of

Doctor rerum naturalium (Dr. rer. nat.)

to the Department of Earth Sciences  
of Freie Universität Berlin



by

XUN YANG

Berlin, Germany, 2023



## **Supervisor**

Univ.-Prof. Dr. Brigitta Schütt

Freie Universität Berlin

Department of Earth Sciences

Institute of Geographical Sciences

Malteserstraße 74-100

12249 Berlin

Germany

## **Second examiner**

Prof. Dr. Manfred Frechen

Freie Universität Berlin

Department of Earth Sciences

Institute of Geographical Sciences

Malteserstraße 74-100

12249 Berlin

Germany

and

Leibniz Institute for Applied Geophysics

Stilleweg 2

30655 Hannover

Germany

Date of defense: Sep 12, 2023



The principle of comprehensive research:

with an ancient statue,

you can not only dig up the head

and leave the rest lying there,

and the same applies to an ancient city.

--- by Alexander Conze (Pirson and Scholl, 2014)

And the same applies to scientific research.



# Acknowledgments

This doctoral study is a part of the ongoing DFG-funded project “Die Transformation der Mikroregion Pergamon zwischen Hellenismus und römischer Kaiserzeit” (TransPergMikro; The Transformation of the Pergamon micro-region between the Hellenistic Period and the Roman Imperial Age) and is funded by the China Scholarship Council.

I am deeply grateful for the support and guidance provided by my supervisor, Prof. Dr. Brigitta Schütt (Freie Universität Berlin, FU Berlin). Her invaluable comments and encouragement have significantly contributed to the progress of my research. Prof. Dr. Manfred Frechen (FU Berlin and Leibniz-Institut für Angewandte Geophysik) is acknowledged for his suggestions to improve this doctoral thesis. Meanwhile, I would like to thank Prof. Wiebke Bebermeier (FU Berlin) as the head of the doctoral committee and Junior Prof. María Piquer-Rodríguez (FU Berlin) as the committee member.

I would like to express my sincere appreciation to my colleagues and also the co-authors of my papers, Dr. Fabian Becker and Dr. Moritz Nykamp (FU Berlin), for their generous assistance during field and laboratory work. Their valuable perspectives and comments have greatly enhanced the quality of our manuscripts. I am also grateful to Dr. Daniel Knitter (OEKO-LOG field research) for assisting in the drafting process.

I am also thankful to Prof. Felix Pirson (DAI) for granting permission to conduct the fieldwork within the frame of the Pergamon Excavation. I extend my thanks to the Ministry of Culture and Tourism of the Republic of Türkiye, as well as Ayşe Tok (Directorate Museum Demre) and Yalçın Yılmaz (Directorate Museum Bergama), for their kind permission and support during the fieldwork. I would also like to acknowledge the help and collaboration of many colleagues from the DAI, Manisa Celal Bayar Üniversitesi, and the Bergama Museum, including Dr. Ulrich Mania, Paula Michalski, Nicole Neuenfeld, Dr. Güler Ateş, and Dr. Bernhard Ludwig. Their guidance and willingness to share their findings have been invaluable. Particularly, Dr. Bernhard Ludwig is appreciated for sharing the important archaeological data and discussing with me to improve the data.

Prof. Mehmet Doğan, Dr. Murat Tozan, and geography students from Ege University Izmir (Nami Yurtseven, Minel Korkmaz, Hakan Güler, Yaren Bozoğlu, and Elif Gültekin) and FU Berlin (Lena Schimmel) are acknowledged for their help during the fieldwork (drillings) and laboratory analyses. I also thank Tom Dauer (FU Berlin) for additional laboratory analyses.

Additionally, I would like to express my appreciation to Dr. Xiaoxu Shi (Alfred Wegener Institute, Bremerhaven) for sharing their climate data and Dr. Fabian Kirsten (FU Berlin)

for helpful communication. I am also thankful to Chenzhi Li (Alfred Wegener Institute, Potsdam) for clarifying the usage of LegacyClimate data.

I am grateful to the chief editors, anonymous reviewers, and English editors whose constructive comments and suggestions have significantly improved the manuscripts. The support from the Open Access Publication Fund (FU Berlin) is also acknowledged.

I also appreciate the university, the entire research team, and many colleagues for their companionship and support. The enjoyable moments we shared, such as BBQs and football games, have made my time memorable. Thank all of you – Prof. Margot Böse, Prof. Tilman Rost, Prof. Wiebke Bebermeier, Dr. Philipp Hoelzmann, Dr. Nadav Nir, Luise Haufe, Shih-Hung Liu, Robert Busch, Mawuli Asempah, Dr. Andrew K. Maronedze, Dr. Tendai Musindo, Annika Bigos, Helena Weber, Dr. Ricarda Braun, Dr. Subham Mukherjee, Dr. Jacob Hardt, Julia Pagels, Jens Jouaux, Dr. Juliet Katusiime, Dr. Vincent Haburaj, Henry Schubert, Joris Starke, Michèle Dinies, Ellen Leiper, and Christiane Reuter.

I would like to express my heartfelt appreciation to my family and friends. The unwavering love and support from my parents have been a tremendous source of encouragement. Many friends also delighted my time in Germany, including Dr. Man Fang, Dr. Thomas Bruhn, Xi Sun, Dr. Sisi Zhang, Li Dong, Minqin, Luna, Huachong, Ziyang, Xiaorong, Yunyun, Zhennan, Shilei, Xiaojiang, Guangpu, Yunfei, Shanshan, and many others. I also want to thank my old friends in China for their continuous contact and support. A special thanks to Dr. Kexin Wang, a dear friend who has always been there to provide encouragement and assistance whenever needed.

Lastly and most importantly, I would like to acknowledge and thank myself. Despite the challenging circumstances, you have persevered and achieved this milestone.

Xun Yang, Berlin, June 2023

## 致谢

每每到写毕业论文的时候，我脑海里都会浮现过去几年求学时光的漫长和短暂。也许是因为在开始前，我从未想过一离开就是四年之久。疫情带来的冲击是人与人之间的疏离和科研上的不便。幸好，一切都是最好的安排，虽然“大雨”可以延迟我们达到的时间，但是不能阻止我们前进。

首先，我要感谢国家留学基金委对我的博士项目的资助。在此期间，野外收集和分析数据受到了德国科学基金会项目的支持。我的课题隶属于是在德国考古研究院（DAI）牵头下的一个多学科项目“佩加蒙地区在希腊和罗马帝国时期的转变”。在第一次见面时，项目负责人 Felix Pirson 教授就告诉我，我是佩加蒙地区近 150 年考古历史上的第一个来自东亚的工作人员，这件事让我现在想来都很激动。

我非常感谢我的导师 Brigitta Schütt 教授给予我这个学习和研究的机会。在整个过程中，她也尽心地对我的每篇小论文进行了指导和修改。感谢 Manfred Frechen 教授对我博士论文的修改和建议。同时也感谢答辩委员会主席 Wiebke Bebermeier 教授和成员 María Piquer-Rodríguez 教授。

我的两位博后同事 Fabian Becker 和 Moritz Nykamp 是给予我最大帮助的人。他们在野外工作、实验室样品测试、和论文写作修改等各个方面都付出了大量的时间，并提出了许多宝贵的建议。如果没有他们的帮助，我相信我的博士课题很难顺利完成。

此外，项目的顺利进行也离不开其他同事的支持。考古小组的 Felix Pirson 教授、Bernhard Ludwig 博士、Ulrich Mania 博士、Güler Ateş 博士、Nicole Neuenfeld、Paula Michalski 等在考古小院里给我们提供了工作空间，带领我们在野外观察，也分享了他们的研究成果。土耳其爱琴海大学的 Mehmet Doğan 教授、Murat Tozan 博士及学生们（Hakan Güler、Nami Yurtseven、Minel Korkmaz、Yaren Bozoğlu 和 Elif Gültekin）帮助我们进行了钻孔采样和实验分析。此外，Daniel Knitter 博士、Robert Busch、Fabian Kirsten 博士、Lena Schimmel、Tom Dauer 也给予了他们的帮助。

此外，我也很感激学校和课题组，许多同事也都给予了他们的陪伴，以及生活和工作中的支持，一起 BBQ 和足球运动会的时间值得留念在生活和工作。组里的老师同事包括 Margot Böse 教授、Tilman Rost 教授、Wiebke Bebermeier 教授、Philipp Hoelzmann 博士、Nadav Nir 博士、Luise Haufe、Shih-Hung Liu、Andrew K. Maronedze 博士、

Tendai Musindo 博士、Annika Bigos、Helena Weber、Ricarda Braun 博士、Subham Mukherjee 博士、Jacob Hardt 博士、Mawuli Asempah、Julia Pagels、Jens Jouaux、Juliet Katusiime 博士、Vincent Haburaj 博士、Henry Schubert、Joris Starke、Michèle Dinies、Ellen Leiper、Christiane Reuter 等许多人。

生活中，我非常感谢我的家人和朋友们。我的父母一直默默地鼓励和支持我。在德国的日子也因为认识了新的朋友而不那么单调，感谢曼、托马斯、溪溪子、思思、applepen、敏琴、Luna、小白马、子暘、晓荣、云云、震楠、石磊、小蒋、光浦、云霏、姗姗等等，感谢你们让我蹭饭、一起组饭局和游戏局，参加 retreat，并一起讨论学术和学术外的事儿，你们都是一群最可爱的人。同时，也要感谢在国内的朋友不时打来电话关心我，特别是王阿姨，经常在我最困难的时候鼓励我，帮助我，并提出最中肯的建议。现在想来，这些都是很温暖的时光。

最后，我想郑重地感谢我自己。只有经历过的人才能体会博士期间的种种困难，感谢自己在最艰难的时候仍然没有放弃，也很高兴自己有勇气尝试了许多以前未曾做过的事情。我看到了岁月如何奔驰，熙熙攘攘，人来人往，那些起舞抑或不曾起舞的日子都是生命的一种形式，都是值得被尊重的。窗外，鸟妈妈一直站在鸟巢边陪伴着刚出生的孩子，这种自然世界的美好也让我感受到了独特的力量。

杨汛，柏林，2023 年 6 月

# Outline

<b>Acknowledgments</b> .....	<b>i</b>
致谢 .....	<b>iii</b>
<b>Outline</b> .....	<b>v</b>
<b>List of figures</b> .....	<b>xi</b>
<b>List of tables</b> .....	<b>xv</b>
<b>List of acronyms</b> .....	<b>xvii</b>
<b>Abstract</b> .....	<b>xx</b>
<b>Zusammenfassung</b> .....	<b>xxiii</b>
<b>1. General introduction</b> .....	<b>1</b>
1.1 Background .....	1
1.2 Research objectives .....	3
1.3 Dissertation outline .....	4
<b>2. State of the art</b> .....	<b>9</b>
2.1 Holocene geomorphodynamics in the Mediterranean .....	9
2.1.1 Geomorphodynamics: interpretation and consequence .....	9
2.1.2 Methods to reconstruct geomorphodynamics .....	10
2.1.3 The Mediterranean geomorphodynamics .....	12
2.1.4 Key debates: climate vs. human impacts .....	12
2.2 The Pergamon micro-region .....	17
2.2.1 Natural background .....	17
2.2.2 Archaeological research .....	18
<b>3. Material and methods</b> .....	<b>23</b>
3.1 Geomorphological mapping and analyses .....	23
3.1.1 Survey of geomorphological features .....	23

3.1.2 Extraction of basic geomorphometric parameters.....	24
3.2 Field work .....	25
3.3 Laboratory analyses of the sediments.....	27
3.3.1 Mass percentage of the coarse components.....	28
3.3.2 Electrical conductivity and pH.....	28
3.3.3 Loss on ignition .....	28
3.3.4 Magnetic susceptibility .....	29
3.3.5 Element composition based on pXRF .....	29
3.4 Statistical analyses of sediment data .....	29
3.5 Radiocarbon dating.....	30
3.6 USPED model.....	31
3.6.1 Rainfall–runoff erosivity factor (R) .....	35
3.6.2 Cover and management factor (C) .....	36
3.6.3 Topographic factor (LS).....	39
3.6.4 Soil erodibility factor (K) .....	39
3.6.5 Support practice factor (P) .....	41
3.6.6 Model validation .....	41
<b>4. The geomorphological characteristics of the Pergamon micro-region... 43</b>	
4.1 Introduction .....	44
4.2 Natural Characteristics of the Pergamon Micro-Region.....	48
4.2.1 Geographical Setting.....	48
4.2.2 Tectonic, Bedrock, and Soil.....	49
4.2.3 Climate.....	51
4.2.4 Vegetation.....	52
4.3 Materials and Methods.....	53
4.3.1 Survey of Geomorphological Features .....	53
4.3.2 Extraction of Basic Geomorphometric Parameters .....	53
4.4 Results.....	55

4.4.1 General Geomorphological Characteristics .....	55
4.4.2 Major Geomorphological Units .....	59
4.5 Discussion .....	67
4.5.1 Development of the Major Landform Units .....	67
4.5.2 Usage Suitability and Human Impact during the Late Holocene .....	72
4.6 Conclusions .....	75
<b>5. Sediment analyses from Tekkedere catchment .....</b>	<b>77</b>
5.1 Introduction .....	78
5.2 Study area .....	81
5.2.1 Natural setting.....	81
5.2.2 Settlement history .....	85
5.3 Methods.....	86
5.3.1 Fieldwork.....	86
5.3.2 Laboratory work .....	88
5.4 Sediment characteristics .....	93
5.4.1 Tekkedere valley infill: Key-profile Tek-2 .....	93
5.4.2 Tekkedere mid-fan: Key-profile Tek-5 .....	95
5.4.3 Tekkedere fan toe: Key-profile Tek-6 .....	99
5.5 Sediment facies .....	103
5.5.1 Facies A: Tekkedere valley bottom sediments .....	103
5.5.2 Facies B: Tekkedere alluvial fan sediments.....	105
5.5.3 Facies C: Bakırçay river sediments .....	105
5.6 Middle and Late Holocene geomorphodynamics.....	107
5.6.1 Phase 1 (ca. 6.2 to 5–4 cal ka BP): Aggradation of the Bakırçay floodplain	107
5.6.2 Phase 2 (between ca. 5 and 4 cal ka BP): Formation of floodplain soils.....	110
5.6.3 Phase 3 (ca. 4–3.8 cal ka BP): Transition from floodplain to fan environment/onset of human impacts.....	113

5.6.4 Phase 4 (after ca. 3.8 ka BP): Alluvial fan dynamics and changing human settlement pattern .....	114
5.7 Conclusions .....	119
<b>6. Sediment analyses from Deliktaş catchment .....</b>	<b>121</b>
6.1 Introduction .....	122
6.2 Study site .....	124
6.2.1 Natural setting .....	124
6.2.2 Settlement history .....	127
6.3 Methods .....	127
6.3.1 Field work .....	127
6.3.2 Laboratory work .....	128
6.4 Sediment facies .....	129
6.4.1 Facies B: Deliktaş alluvial fan sediments .....	130
6.4.2 Facies C: Geyikli river sediments .....	131
6.5 Sediment profiles .....	131
6.5.1 Key profile Del-3 .....	133
6.5.2 Other Deliktaş fan sediment profiles .....	136
6.6 Holocene geomorphodynamics .....	140
6.6.1 Pre- to Early Holocene (phases 1–2) .....	142
6.6.2 Middle Holocene (phase 3) .....	142
6.6.3 Mid- to Late Holocene transition (phase 4) .....	144
6.6.4 Beginning of Late Holocene (phase 5) .....	144
6.6.5 Late Holocene (phases 6–7) .....	146
6.7 Conclusions .....	147
<b>7. Linking processes with records: modeling the Mid- to Late Holocene soil erosion and deposition risk .....</b>	<b>149</b>
7.1 Introduction .....	150
7.2 Study area .....	153

7.3 Methods and materials .....	153
7.4 Results .....	154
7.4.1 Present-day situation of soil erosion and deposition .....	154
7.4.2 Soil erosion and deposition risk since 6 ka BP .....	157
7.4.3 Comparison with the updated <sup>14</sup> C meta-data analysis .....	162
7.5 Discussion .....	164
7.5.1 Geomorphodynamics during the last 6000 years.....	164
7.5.2 Factors: climate and human .....	169
7.5.3 Further research: soil erosion model improvements .....	173
7.6 Conclusions .....	175
<b>8. Overall conclusions .....</b>	<b>177</b>
<b>9. References.....</b>	<b>181</b>
<b>Supplementary materials.....</b>	<b>I</b>
To chapter 1.....	I
To chapter 2.....	III
To chapter 4 (working package 1).....	VII
To chapter 5 (working package 2).....	XVII
To chapter 6 (working package 3).....	XXIX
To chapter 7 (working package 4).....	XLII
<b>Curriculum vitae.....</b>	<b>XLVI</b>
<b>Eidesstattliche Erklärung .....</b>	<b>L</b>



## List of figures

1.1 The location of the Pergamon micro-region in different research .....	2
1.2 The general concept and structure of the dissertation .....	6
2.1 The spatial and temporal distribution of the archaeological sites .....	19
2.2 The raw count of archaeological sites .....	20
3.1 Flow chart of the USPED model .....	33
4.1 Topographical map of the Bakırçay and Madra River catchments .....	45
4.2 Geological map of the Bakırçay and Madra River catchments .....	50
4.3 Climate diagrams of Dikili and Bergama .....	51
4.4 Geomorphological map of the Bakırçay and Madra River catchments .....	57
4.5 Morphometric characters of the Bakırçay and Madra River catchments .....	58
4.6 Swath profiles of the asymmetrical geomorphological characteristics .....	59
4.7 Distribution of the morphometric and lithologic characteristics .....	62
4.8 Longitudinal profiles of channel courses and major knickpoints .....	63
5.1 Topographical map of the Tekkedere catchment .....	80
5.2 Geomorphological and geological maps of the Tekkedere area .....	82
5.3 Sedimentological analyses of profile Tek-2 .....	94
5.4 Sedimentological analyses of profile Tek-5 .....	96
5.5 Sedimentological analyses of profile Tek-6 .....	100
5.6 Longitudinal profile along with the Tekkedere alluvial fan .....	108
5.7 Calibrated <sup>14</sup> C ages from the Tekkedere area and the natural and cultural variables in the Pergamon micro-region .....	112
6.1 Topographical map of the Deliktaş catchment .....	123
6.2 Geomorphological map and field photos of the Deliktaş catchment .....	126
6.3 Sedimentological analyses of profile Del-3 .....	134

6.4 Longitudinal profile along with the Deliktaş alluvial fan .....	139
6.5 Age-depth modeling of profiles Del-2, Del-3, and Del-6 .....	143
7.1 Topographical map of the western lower Bakırçay plain .....	151
7.2 Spatial distribution of the input factors and results of the USPED model during recent times .....	155
7.3 Spatial distribution of soil erosion and deposition risk and the rainfall and cover factors at 6000, 4200, 2000, and 100 yr BP .....	158
7.4 Temporal trends of rainfall and cover factors, and soil erosion and deposition risk during the last 6000 years .....	159
7.5 Ridgeline plot of archaeological sites on geomorphic locations of soil erosion or deposition risk .....	161
7.6 Relationship between soil erosion risk and factors of rainfall and cover .....	161
7.7 Comparison of soil erosion risk with an updated <sup>14</sup> C meta-data analysis .....	163
S4.1 Generation of the geomorphological map: example at Çalibahçe basin .....	X
S4.2 Terrace examples .....	XI
S4.3 Slope with bare rock in Tekkedere valley .....	XI
S4.4 Field photos .....	XII
S4.5 The western lower Bakırçay plain .....	XIII
S4.6 Land cover map: Corine Land Cover (CLC) 2018 .....	XIV
S4.7 Geomorphometric parameter maps: aspect, TPI, and TWI .....	XV
S5.1 Location of the Tekkedere sediment profiles .....	XVII
S5.2 Sedimentological analyses of profile Tek-1 .....	XVIII
S5.3 Sedimentological analyses of profile Tek-3 .....	XX
S5.4 Sedimentological analyses of profile Tek-4 .....	XXII
S5.5 Sedimentological analyses of profile Tek-4-2 .....	XXIV
S5.6 Sedimentological analyses of profile Tek-5-2 .....	XXVI
S6.1 Location of the profiles AD29/30 .....	XXXI
S6.2 Correlation of LOI <sub>550</sub> and TOC, and LOI <sub>900</sub> and TIC .....	XXXII

S6.3 Sedimentological analyses of profile Del-2 ..... XXXIII  
S6.4 Sedimentological analyses of profile Del-4 ..... XXXVI  
S6.5 Sedimentological analyses of profile Del-5 ..... XXXVII  
S6.6 Sedimentological analyses of profile Del-6 ..... XXXIX



## List of tables

1.1 Overview of the four working packages .....	7
2.1 Chronological scheme for the Pergamon micro-region .....	16
3.1 Metadata of all sediment archives in this thesis .....	26
3.2 Classification of sediment proxies used in this thesis .....	30
3.3 Summary of the dataset used for the USPED model .....	34
3.4 Classification of the USPED model results .....	35
3.5 Metadata of the four local meteorological stations .....	36
3.6 Parameters used for the calculation of the cover factor .....	38
4.1 Geomorphometric derivatives used for the identification of landforms .....	54
4.2 Geomorphological parameters in the four geomorphological units .....	56
4.3 Mountain-front sinuosity index (Smf) and extension of colluvial deposits in the lower Bakırçay plain .....	66
5.1 Metadata of sediment profiles of the Tekkedere catchment .....	87
5.2 Equal interval classification of the sediment proxies for the Tekkedere sediments .....	88
5.3 AMS- <sup>14</sup> C dating samples from the Tekkedere catchment .....	91
5.4 Features of different sediment facies in the Tekkedere catchment .....	104
5.5 Summary of settlements and natural-social relationships in the Tekkedere valley .....	116
6.1 Metadata of sediment profiles from the Deliktaş alluvial fan .....	128
6.2 Characteristics of sediment sub-facies in the Deliktaş catchment .....	130
6.3 AMS- <sup>14</sup> C dating samples from the Deliktaş catchment .....	132
6.4 Summary of the (pre-)Holocene sediment characteristics, depositional processes, and landscape and settlement dynamics in the Deliktaş area .....	140
7.1 Comparison of the geomorphodynamics from various sources .....	166

S1.1 Summary of different names of mountains and Bakırçay river .....	I
S2.1 Summary of Mediterranean geomorphodynamics and dominating drivers .....	III
S4.1 Definition and classification rules of landform units for the geomorphological map .....	VII
S6.1 Archaeological sites and chronology from the Deliktaş area .....	XXIX
S6.2 Classification of the sediment proxies for the Deliktaş sediments .....	XXX
S7.1 Soil structure and permeability index according to the soil texture class .....	XLII
S7.2 Three-tier hierarchy of land cover classes and support practice factor .....	XLIII

## List of acronyms

m a.s.l.	meter above sea level
b.s.	below surface
ca.	circa
yr	year (synonym for a, annum)
ka	thousand years (kiloannum)
BC	before Christ (synonym for BCE, before the common era)
AD	anno domini (synonym for CE, common era)
BP	before present (before 1950)
cal yr BP	calibrated years before present
BOP	Beyşehir Occupation Phase (from ca. 3.2 to 1.2 ka BP) in SW Türkiye
DEM	digital elevation model
pH	potential of hydrogen, acidity
EC	electrical conductivity
MS	magnetic susceptibility
pXRF	portable energy dispersive X-ray fluorescence spectroscopy
LOI <sub>550</sub>	loss on ignition between 105 °C and 550 °C
LOI <sub>900</sub>	loss on ignition between 550 °C and 900 °C
TC	total carbon
TIC	total inorganic carbon
TOC	total organic carbon
MAD	median absolute deviation
IDW	inverse distance weighting



## Abstract

The Mediterranean landscapes are highly fragile and sensitive to changes in the natural and human ecosystems. While the general morphodynamic changes and their dominating driving factors have been well studied, regional peculiarities are still not fully understood, particularly in western Türkiye. This study focuses on the ancient city of Pergamon, which underwent a profound urban transformation during the Hellenistic–Roman periods, thereby influencing its micro-region in various aspects. Moreover, the Pergamon micro-region has a long history of human activities and occupation dating back to the Late Epipalaeolithic Period, with continuity since the Early Bronze Age. This doctoral project primarily aims to understand the spatiotemporal pattern of geomorphodynamics and their dominating drivers in the Pergamon micro-region since the Middle- to Late Holocene.

This cumulative thesis consists of four case studies that employ different methods on multiple temporal and spatial scales. (1) Geomorphometric calculations and visual interpretation of remote sensing data were used to map and analyze the present-day geomorphological characteristics of the Bakırçay and Madra river catchments, providing a micro-regional background for the subsequent research. (2) Two case studies involving radiocarbon-dated sediment sequences in the mountainous catchments of Tekkedere and Deliktaş were conducted to reconstruct the Holocene geomorphodynamics and obtain a better understanding of their driving factors from a small-scale perspective. (3) Back to a micro-regional scale, monthly rainfall data for the last 6000 years from the AWI-ESM climate model and spatiotemporal pattern of archaeological sites in the western lower Bakırçay catchment were incorporated to calculate the soil erosion and deposition risk during the Mid- to Late Holocene by applying the Unit Stream Power Erosion Deposition (USPED) model. In addition, the soil erosion and deposition situation in recent times and sedimentation rate calculated from an updated meta-data analysis of <sup>14</sup>C ages were applied for comparison.

The main highlights of the present-day geomorphological mapping and the reconstruction of the Mid- to Late Holocene geomorphodynamics are as follows. The present-day Pergamon micro-region exhibits a highly heterogeneous and complex landscape shaped by Miocene–Pleistocene tectonics, which formed the basic structure and provides essential resources for human settlements. The human impacts in the micro-region have influenced local geomorphodynamics. Archive-based reconstructions indicate two approximately simultaneous phases of increased geomorphodynamics that occurred during the Middle and Late Holocene in the alluvial fans of the Tekkedere and Deliktaş catchments, two

tributaries of the lower course of the Bakırçay river, despite the slight variation in the structures of the fan development. The burial of soils resulting from the fan growth (progradation) marked the initial increase in geomorphodynamic activities around 5–3.7 ka BP, approximately between the Early and Middle Bronze Age. This coincided with a supra-regional drying trend accompanied by rapid climate change events, and the amplification of the initially local human activities. However, strong effects of the Hellenistic–Roman transformation were not evident from the synchronous fan sediments. The valley bottom sediments in the Tekkedere catchments and the fan-edge sediments in the Deliktaş catchment deposited after ca. 1.5 ka BP might be associated with this assumed accelerated geomorphodynamics.

The USPED modeling results indicate the past and present spatial heterogeneity in the soil erosion and deposition risk within the western lower Bakırçay catchment. The present-day soil erosion risk is validated by field observations and is remarkably higher than that modelled for selected time slices over the last 6000 years. Throughout the Mid- to Late Holocene, the micro-regional geomorphodynamics most likely experienced five main phases, as supported by both the soil erosion and deposition risk estimated from the USPED modeling and the sedimentation rates estimated from a meta-data analysis of <sup>14</sup>C-ages (n = 140) from sediment archives in the micro-region (incorporated with samples from the Tekkedere and Deliktaş catchment, updated from Becker et al., (2020).

The second phase (ca. 5–3.7 ka BP) and the fourth phase (ca. 2.5–1.5 ka BP) were characterized by an apparent acceleration of geomorphodynamics. They are roughly consistent with the sedimentological evidence from the tributary catchments of Tekkedere and Deliktaş, and the sediment dynamics observed in the supra-regional studies of the eastern Mediterranean. Both climate change and human activities are suggested to mutually contribute to the geomorphodynamics. The weak correlation between rainfall fluctuations and the modeled soil erosion risk requires further validation with archive-based input climate data. The highest soil erosion risk occurring during the Hellenistic–Roman transformation reveals the potential time when the human impacts exceeded the climate pressure on the landscape.

Overall, this doctoral thesis emphasizes the importance of studying the human–climate–geomorphodynamic interactions across various spatiotemporal scales and employing multiple methods. The findings can be applied not only to the broader Pergamon micro-region but also to other regions. Furthermore, the thesis discusses essential improvements for future quantitative research, including the proxy-based reconstruction of rainfall and land use distribution, precise chronology, and model calibration and validation.

# Zusammenfassung

Die mediterranen Landschaften sind äußerst fragil und empfindlich gegenüber Veränderungen in den natürlichen und menschlichen Ökosystemen. Obwohl der allgemeine Trend geomorphologischer Veränderungen und ihre vorherrschenden treibenden Faktoren gut erforscht sind, sind (mikro-)regionale Besonderheiten immer noch nicht vollständig verstanden, insbesondere in der Westtürkei. Diese Studie konzentriert sich auf die antike Stadt Pergamon, die während der hellenistisch-römischen Zeit eine tiefgreifende städtische Transformation durchlief und damit auch ihre Mikroregion in vielerlei Hinsicht beeinflusste. Darüber hinaus hat die Mikroregion eine lange Geschichte menschlicher Aktivitäten und Besiedlung, die bis in die späte Epipaläolithikum-Periode zurückreicht und seit der frühen Bronzezeit andauert. Ziel dieser Doktorarbeit ist es primär, das räumlich-zeitliche Muster der Geomorphodynamik und ihre treibenden Faktoren vom Mittel- bis zum Spätholozän in der Pergamon-Mikroregion zu untersuchen.

Diese kumulative Arbeit besteht aus vier Artikeln, die verschiedene Methoden auf mehreren zeitlichen und räumlichen Skalen anwenden. (1) Für die Kartierung und Analyse der heutigen geomorphologischen Charakteristika in den Flusseinzugsgebieten des Bakırçay und des Madra wurden geomorphometrische Analysen und visuelle Interpretationen von Fernerkundungsdaten durchgeführt, die die Grundlage auf Ebene der Mikroregion Pergamon für die folgenden kleinskaligen Untersuchungen bilden. (2) Zwei Fallstudien basieren auf der Analyse radiokarbondatierter Sedimentsequenzen, die auf den Schwemmfächern von zwei Seitentälern (Deliktaş und Tekkedere) der die Landschaft prägenden westlichen unteren Bakırçay-Ebene mittels Rammkernsondierungen erbohrt wurden, um die Geomorphodynamik im ländlichen Raum und ihre Einflussfaktoren auf einer kleinräumigen Skala zu rekonstruieren. (3) Unter Einbeziehung räumlich interpolierter monatlicher Niederschlagsdaten für die letzten 6000 Jahre (AWI-ESM-Klimamodell) und dem raum-zeitlichen Verbreitungsmuster archäologischer Stätten in der westlichen unteren Bakırçay-Ebene wurde die mikroregionale Dimension des Bodenerosions- und Depositionsrisikos während des mittleren bis späten Holozäns mit dem Unit Stream Power Erosion Deposition (USPED)-Modell simuliert. Darüber hinaus wurden zum Vergleich das rezente Bodenerosions- und Ablagerungsrisiko sowie die Sedimentationsraten herangezogen, die aus einer aktualisierten Metadatenanalyse der <sup>14</sup>C-Alter aus bereits vorliegenden Sedimentprofilen berechnet wurden. Die wichtigsten Ergebnisse der geomorphologischen Kartierung und der Rekonstruktion der mittel- bis spätholozänen Geomorphodynamik lassen sich wie folgt zusammenfassen:

Die heutige Mikroregion Pergamon weist eine sehr heterogene und komplexe morphotektonische Landschaft auf. Die miozän-pleistozäne Tektonik prägt die Großformen des Reliefs, die wesentliche Ressourcen für menschliche Siedlungsaktivitäten bereitstellen. Die menschlichen Einflüsse in der Mikroregion verändern die lokale Geomorphodynamik.

Archivbasierte Rekonstruktionen weisen auf zwei annähernd gleichzeitige Phasen erhöhter Geomorphodynamik hin, die während des mittleren und späten Holozäns in den Schwemmfächer-Sedimenten der Einzugsgebiete des Tekkedere und des Deliktaş, zwei Nebenflüssen des Unterlaufs des Bakırçay-Flusses, trotz geringfügiger Unterschiede in der Entwicklung der beiden Schwemmfächer, zu sehen sind. Die Überdeckung von Böden durch die progradierenden Schwemmfächer markierte den ersten Anstieg der Mittel-/Spätholozänen Geomorphodynamik wahrscheinlich während der frühen und mittleren Bronzezeit (ungefährer 5–3,7 ka BP). Diese Entwicklung verlief annähernd parallel zu einer Phase überregionaler Aridisierung mit raschen Klimaveränderungen. Die einhergehende geomorphodynamische Entwicklung wurde durch den Beginn lokaler menschlicher Aktivitäten verstärkt. Die tiefgreifenden Auswirkungen der hellenistisch-römischen Transformation sind jedoch in den kontemporären Fächersedimenten nicht erkennbar. Die Talboden- und Fächerrandsedimente lagerten sich nach ca. 1,5 ka BP ab und könnten mit dieser angenommenen Geomorphodynamik verbunden sein.

Die USPED-Modellierung zeigt einen analogen Charakter der räumlichen heterogenen Entwicklung der Geomorphodynamik in der westlichen unteren Bakırçay-Ebene. Das Erosionsrisiko in der heutigen Zeit ist höher als in den letzten 6000 Jahren. Während des mittleren bis späten Holozäns durchlief die Geomorphodynamik der Mikroregion fünf Hauptphasen, die auch durch eine (aktualisierte) Meta-daten Analyse der <sup>14</sup>C-Alter aus den Sedimentarchiven der Mikro-region bestätigt wird. Die zweite (ca. 5–3,7 ka BP) und die vierte (ca. 2,5–1,5 ka BP) Phase mit einer offensichtlichen Verstärkung der Geomorphodynamik sind in etwa vergleichbar mit den Sedimentbefunden aus den Teileinzugsgebieten Tekkedere und Deliktaş und der für den östlichen Mittelmeerraum rekonstruierten Sedimentdynamik. Es ist davon auszugehen, dass sowohl klimatische Veränderungen als auch menschliche Aktivitäten zur veränderten Geomorphodynamik beitragen. Die schwache Korrelation der Niederschlagsschwankungen mit der Bodenerosion bedarf einer weiteren Validierung mit archivbasierten Eingangsklimadaten. Das höchste Erosionsrisiko während der hellenistisch-römischen Transformation zeigt, dass der menschliche Druck den Effekt des sich veränderten Klimas übersteigt.

Insgesamt unterstreicht diese Dissertation die Bedeutung der Untersuchung der Mensch-Klima-Geomorphodynamik-Interaktionen auf verschiedenen räumlichen und zeitlichen

Skalen und mit Hilfe mehrerer Methoden, was eine Anwendung auf die weitere Mikroregion Pergamon und sogar darüber hinaus ermöglicht. Wesentliche Verbesserungen in der Zukunft, um die Forschung quantitativ voranzutreiben, werden in der Dissertation zusätzlich diskutiert, einschließlich der proxy-basierten Rekonstruktion der Niederschlags- und Landnutzungsverteilung, der präzisen Chronologie sowie der Modellkalibrierung und -validierung.



# 1. General introduction

## 1.1 Background

Geomorphodynamics, denoting the major changes in geomorphological processes in this study, plays a crucial role in various aspects of land management, including soil fertility, agricultural productivity, water quality, and settlement pattern. Considerable research interest has been received in understanding the impacts of geomorphological changes in the past (e.g., Dotterweich et al., 2013). This is because the reconstruction of Holocene geomorphodynamics could provide valuable insights into the resolution of soil erosion problems, the facilitation of future landscape management, and the achievement of sustainable development goals (Allen et al., 2022).

Numerous studies have explored the overarching patterns of geomorphological changes and the potential drivers – however, the majority of these studies have local to regional validity. Different local scale case studies utilizing various methods and sedimentary archives often present contrasting scenarios (Mitasova et al., 2013). Consequently, many studies often face methodological constraints, leading to unclear or even opposite conclusions (Van Loo et al., 2016; Manning et al., 2020). During the Holocene, increased geomorphodynamics are often related to the dominance of climatic changes (Faust et al., 2004; Dotterweich, 2008) and human activities (Geeson et al., 2002; Fuchs et al., 2004; Glais et al., 2017), or both (Bintliff, 2002; Giraudi, 2018; Pérez-Lambán et al., 2018), while other drivers (e.g., volcanism and earthquakes) are only rarely considered. When and how the factor(s) influenced local landscapes remain contrasting results, particularly during the Middle Holocene (Roberts et al., 2011a).

Mediterranean region is one of the earliest and most important regions for settlement history in the world (Woodward, 2009; Lionello, 2012; Walsh, 2013). At the same time, this region has long-termed suffered from intensive soil erosion processes, including sheet, rill, and gully erosion, as well as shallow landslides, and the development of large and active badlands in both sub-humid and semi-arid areas (Geeson et al., 2002; García-Ruiz et al., 2013). Geomorphodynamic research in the Mediterranean region has shown distinct spatial differences, with sedimentary archives being less rich in the eastern Mediterranean compared to the western part (Dusar, 2011). Also, the Aegean region of Turkey, particularly the northwest part, has often been overlooked in regional comparisons (Finné et al., 2019; Roberts et al., 2019a; Walsh et al., 2019).

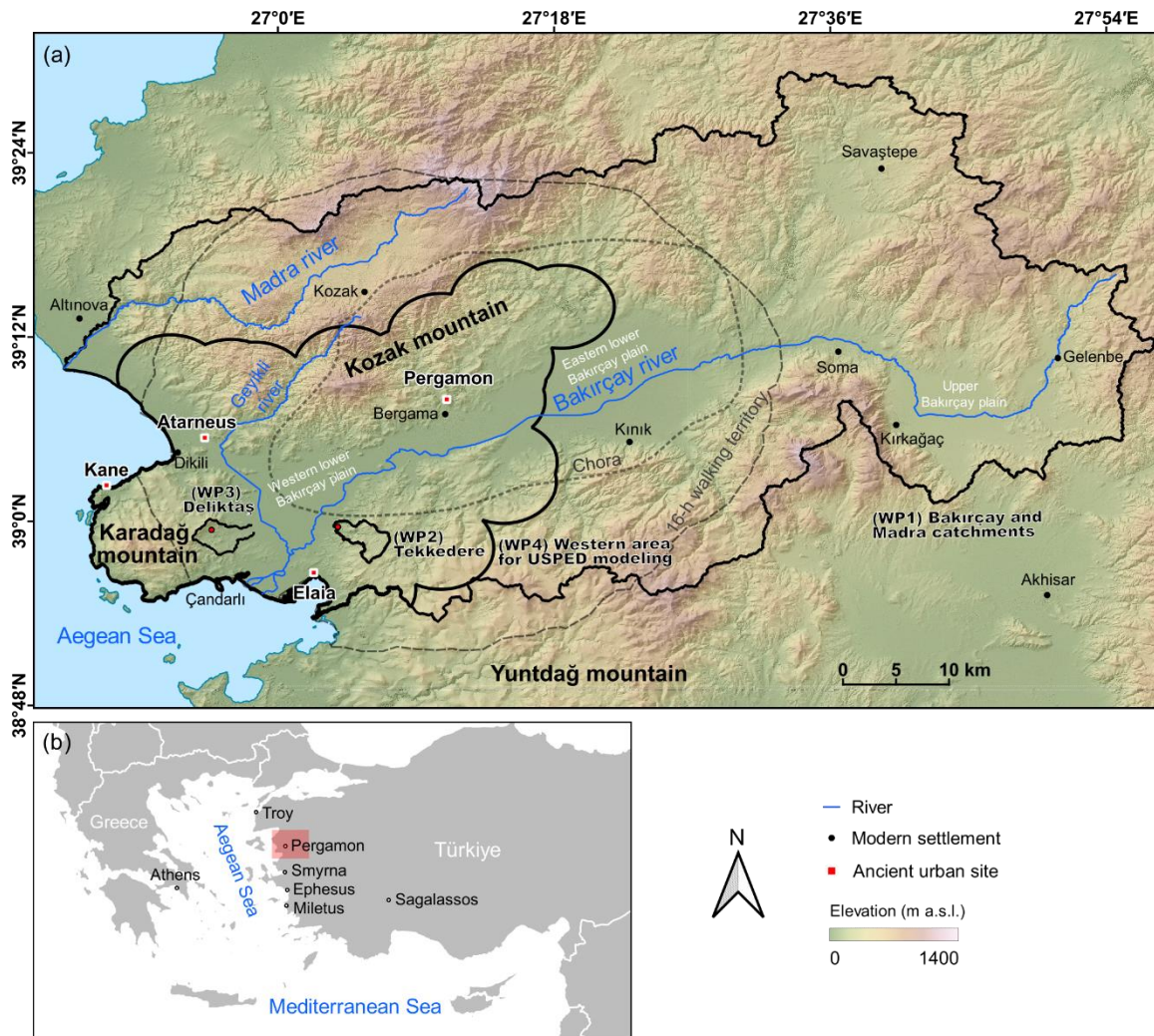


**Figure 1.1** (a) Topographical map (Data source: TanDEM-X, 12.5 m (Rizzoli et al., 2017; Wessel et al., 2018)) with the boundaries of the four working packages in the thesis and also the *chora* and 16-h walking territory (from Laabs and Knitter, 2021), showing the unfixed geographical boundaries of the Pergamon micro-region which depend on the research objectives and data availability. (b) The location of this study is in the eastern Mediterranean region (western Türkiye) with important ancient cities.

Hence, our study focuses on the surroundings of the Hellenistic–Roman city of Pergamon (now the modern city of Bergama, Figure 1.1) in western Türkiye. The city and its rural areas are broadly regarded as the term “Pergamon micro-region”, which mainly comprises the Bakırçay plain, the Kozak mountain (ancient Pindasos), the Yuntdağ mountain (ancient Aspordenon), the Karadağ mountain (ancient Kane), as well as the coastal areas along those mountains (Figure 1.1) (Ludwig, 2023). From a landscape archaeological view, the term “micro-region” is not defined by fixed (geographical) boundaries but by dynamic spaces of interaction between humans and the natural environment, which might show various extensions according to the level of interaction (e.g., economic, military, sociocultural) and the applied research approach with its theoretical framework (Ludwig, 2023). Nevertheless, the areas from the city to the coast have been subject to extensive

archaeological work by the team of Felix Pirson (2020 and references therein), and geoarchaeological investigations by the team of Brigitta Schütt (Knitter, 2013; Schneider et al., 2013; 2014; 2015; 2017; Becker et al., 2020a) and Helmut Brückner (Seeliger et al., 2014; Pint et al., 2015; Shumilovskikh et al., 2016; Seeliger et al., 2017; 2018; 2019; Shumilovskikh et al., 2022). They provide a wealth of information for studying the landscape history and its human–environment interplay. These previous geoarchaeological studies have various foci on only selected archaeological sites, for example, Atarneus, Elaia, and the western lower Bakırçay plain (Figure 1.1); the areas from the surrounding mountains including Yuntdağ and Karadağ mountains are not covered yet.

## 1.2 Research objectives

The thematic interests of this dissertation are to determine the Holocene phases and processes of the (accelerated) geomorphodynamics during the Holocene in the Pergamon micro-region, western Türkiye. This dissertation focuses on understanding the timing and interplaying of its major drivers, particularly, the interactions of the presence and dynamics of climate changes and human activities. The objectives of this thesis are as follows:

- analyze the present-day landform characteristics to establish a foundation for understanding past geomorphodynamics and human activities;
- provide a Holocene timeframe of geomorphodynamics, with a particular focus on the phase from Mid- to Late Holocene;
- identify the major periods characterized by increased geomorphodynamics;
- examine various driving factors of geomorphodynamics, with a specific emphasis on the effects of climate and settlement activities;
- compare findings across multiple spatial scales, ranging from small mountainous catchments to the micro-region, and extrapolate the discussion to the supra-region;
- employ a combination of archive-based and empirical-model-based reconstruction of landscape and geomorphodynamics;
- enrich geoarchaeological case studies in the eastern Mediterranean region;
- serve as a basis and motivation for future research and provide insights for studying other ancient (micro-)regions.

To address these research objectives, four working packages were conducted to investigate the following specific research questions.

Research questions of the first working package - chapter 4:

- What are the major characteristics of the present-day relief in the Bakırçay and Madra river catchments, as the two biggest catchments surrounding the ancient Pergamon?
- What are the differences observed among various landforms?
- What are the principal driving factors suggested in the scientific literature?
- How do human activities impact the landscape?

Research questions of the second working package - chapter 5:

- How did the Tekkedere valley, a tributary of the Bakırçay river, and its alluvial fan develop over the past 6500 years?
- What were the geomorphodynamics of the Tekkedere catchment during the studied time interval, particularly before and after ca. 4 and 2 ka BP?
- What were the potential factors controlling the increased geomorphodynamics, including regional climate change and local human impact, in relation to supra-regional Holocene records?

Research questions of the third working package - chapter 6:

- What were the Holocene geomorphodynamics in the Deliktaş catchment, a tributary of the Bakırçay river?
- How did the Deliktaş alluvial fan develop throughout the entire Holocene?
- What were the triggers and controlling factors for the varying intensities of geomorphodynamic processes, such as supra-regional climatic events and rural-to-urban human impacts?
- Did geomorphodynamics in the Deliktaş catchment vary from that in the Tekkedere catchment?

Research questions of the fourth working package - chapter 7:

- How feasible is it to apply a soil erosion and deposition model for a better understanding of the ancient human–environment interactions?
- What were the potential geomorphodynamic scenarios during the Mid- to Late Holocene for the Pergamon micro-region?
- How do demographic and climatic changes in the Pergamon micro-region correlate with geomorphodynamics?
- When did the landscape transition from being nature-dominated to human-dominated?
- How can further research improve the model?

## 1.3 Dissertation outline

In this dissertation, the geomorphodynamics of the Pergamon micro-region are analyzed, starting from the micro-regional to the local, and back to the micro-regional scale. Based

on the research objectives and specific questions, the dissertation contains eight chapters (Figure 1.2).

The general introduction provides the study background and research objectives. The second chapter presents the state of the art on the Holocene geomorphodynamics in the Mediterranean region and emphasizes the relevance of the Pergamon micro-region. Chapter 3 lists all the methods used in this doctoral thesis. Chapters 4–7 correspond to the four working packages (Table 1.1), following the structure of conventional scientific manuscripts in geomorphology (Lane, 2014).

Chapter 4 (working package 1) focuses on mapping and analyzing the heterogeneous characteristics of four major geomorphological units, covering the catchments of the Bakırçay and Madra rivers. Together with the literature review of other natural characteristics (geographical setting, tectonic, bedrock, soil, climate, and vegetation), this chapter also serves as the general background of the study area in a micro-regional view. Chapter 5 (working package 2) analyzes the alluvial fan and valley bottom sediment sequences from the Tekkedere catchment, a tributary of the Bakırçay river and a long-term settled catchment in the Yuntdağ mountain (the names of mountains might vary within papers in the following chapters and a full list of names used in other studies refers to Table S1.1). It provides insights into local-scale geomorphodynamics during the Mid- to Late Holocene. Chapter 6 (working package 3) investigates the Holocene alluvial sediments from the Deliktaş catchment, again a rural catchment with a topographic background different from that in the Tekkedere catchment. Chapter 7 (working package 4) simulates the spatiotemporal pattern and dynamic changes of soil erosion and deposition risk during the Mid–Late Holocene applying the Unit Stream Power Erosion Deposition (USPED) model, synthesizing the previous individual site studies to understand landscape processes over the last 6000 years. The last chapter provides the overall conclusions of the dissertation.

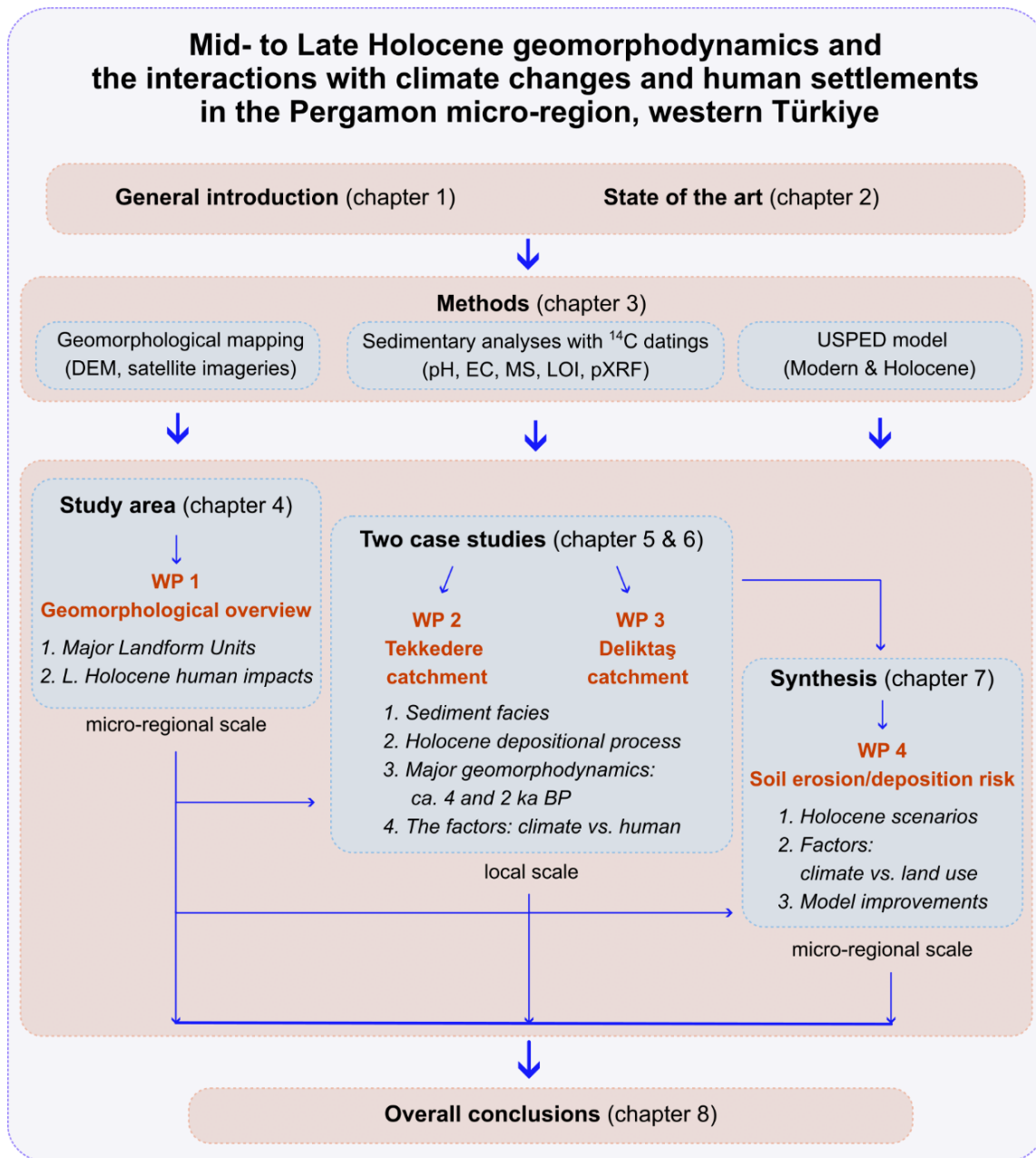


**Figure 1.2** The general concept and structure of the dissertation.

**Table 1.1** The overview of the four working packages (chapters 4–7).

Working package	Publication	Own contribution
WP1	<p><b>Main text:</b> Yang, X., Becker, F., Knitter, D., Schütt, B., 2021. An Overview of the Geomorphological Characteristics of the Pergamon Micro-Region (Bakırçay and Madra River Catchments, Aegean Region, West Turkey). <i>Land</i> 10, 1–27. <a href="https://doi.org/10.3390/land10070667">https://doi.org/10.3390/land10070667</a>.</p>	55%
WP2	<p><b>Main text:</b> Yang, X., Becker, F., Nykamp, M., Ludwig, B., Doğan, M., Doğan, T., Knitter, D., Schütt, B., 2023. Mid- to Late Holocene geomorphodynamics in a long-term settled mountain catchment in the Pergamon micro-region, western Turkey. <i>Quaternary Research</i> 114, 69–92. <a href="https://doi.org/10.1017/qua.2022.73">https://doi.org/10.1017/qua.2022.73</a>.</p> <p><b>Research data:</b> Yang, X., Becker, F., Nykamp, M., Schütt, B., 2022. Dataset of sediment analyses (pH, electrical conductivity, magnetic susceptibility, loss on ignition, and X-ray fluorescence) from the Tekkedere catchment in the Pergamon Micro-Region, western Turkey. In: Yang X (ed). <i>Pangaea</i>. <a href="https://doi.pangaea.de/10.1594/PANGAEA.944177">https://doi.pangaea.de/10.1594/PANGAEA.944177</a>.</p>	65%
WP3	<p><b>Main text:</b> Yang, X., Becker, F., Nykamp, M., Ludwig, B., Doğan, M., Doğan, T., Knitter, D., Schütt, B., 2023. Holocene geomorphodynamics of a rural catchment in the Pergamon micro-region (eastern Mediterranean). <i>The Holocene</i> 33, 1407–1427. <a href="https://doi.org/10.1177/09596836231185837">https://doi.org/10.1177/09596836231185837</a>.</p> <p><b>Research data:</b> Yang, X., Becker, F., Nykamp, M., Schütt, B., 2023. Dataset of sediment analyses (pH, electrical conductivity, magnetic susceptibility, loss on ignition, and X-ray fluorescence) from the Deliktaş catchment in the Pergamon micro-region, western Türkiye. In: Yang X (ed). <i>Pangaea</i>. <a href="https://doi.org/10.1594/PANGAEA.959672">https://doi.org/10.1594/PANGAEA.959672</a>.</p>	75%
WP4	<p><b>Main text:</b> Yang, X., Becker, F., Ludwig, B., Schütt, B., in preparation. Climate vs. human impacts on Mid- to Late Holocene geomorphodynamics on the western lower Bakırçay catchment (western Türkiye): an evaluation based on USPED modeling.</p>	90%



## **2. State of the art**

### **2.1 Holocene geomorphodynamics in the Mediterranean**

#### **2.1.1 Geomorphodynamics: interpretation and consequence**

Rohdenburg (1983) introduced the term geomorphodynamic activity to describe the destabilization of an ecosystem by regressive succession caused by repeated events of less intensive rainfall, whereas geomorphodynamic stability is associated with apparent soil formation. Becker et al. (2020a) explained the usage of this generic term geomorphodynamics for two reasons in their study of the meta-data analyses of <sup>14</sup>C ages from the western lower Bakırçay plain. First, the term involves different surface processes of erosion, deposition, and reworking. Second, they related the term to the change in the cumulative probability of <sup>14</sup>C-ages, sedimentation rate, or sediment facies in the sediment sequences. Although it has not been officially defined, the term geomorphodynamics is combined with “geo” and “morphodynamics”. In the Earth sciences, the latter is often associated with the study of the processes that shape the Earth's surface, such as weathering, erosion, sediment transport, deposition, and landform evolution. Hence, geomorphodynamics is equivalent to morphodynamics, with a clear focus on the geoscientific background.

In the field of geomorphology, the fundamental components of form (relief) – material (sediment) – process (morphodynamics) show complex interactions (Dikau et al., 2019). The geomorphological forms are the result of the relationship between the forces at the Earth's surface and the resistance of the subsurface material, which are transformed by the geomorphological process (Huggett, 2017). When the geomorphological resistance threshold exceeds that materials can be transported, a change in form results. The geomorphological form might have developed through several phases (multiphase) in the view of the geomorphogenetic systems (Dikau et al., 2019). The phases comprise different conditions of adjustment (dynamic equilibrium, quasi-equilibrium, or grade) and constant forms (steady state); the latter might contain a sub-set of dynamic equilibrium (Abrahams, 1968). Abrupt changes from the relatively steady state to the tendency of adjustment could be the responses of a system when the geomorphic thresholds are crossed (Schumm, 1973). The geomorphological forms and processes often only remain recognizable in the form of process-correlated materials; hence, sediment archives, as the relics of

geomorphological form and process, are essential for the reconstruction with the guide of scientific-theoretical approaches, methods, and closure procedures (Goudie, 2004; Huggett, 2017).

In this doctoral study, the term geomorphodynamics, under the consideration of the aforementioned definitions, refers to the predominant processes shaping geomorphological forms and materials, and how they are influenced by external variables (Dikau et al., 2019). Given the temporal scope of this study – the Holocene, its primary focus is on soil erosion (Kirchhoff et al., 2019) and associated paleoenvironmental changes (Kock et al., 2019; Nykamp et al., 2020). An acceleration in geomorphodynamics indicates a landscape becomes more sensitive and likely shifts from relatively stable conditions to severe soil erosion by overland flows in the upper course of a river and deposition/flooding processes in the lower course, resulting in a remarkable increase in sedimentation rates. Conversely, a landscape becoming more stable suggests a decrease in geomorphodynamics. In addition, geomorphodynamics are associated with the changes in sediment facies, both gradually and abruptly. Sediment facies in various terrestrial environments include fluvial (channel, floodplain), alluvial fan, colluvial, and lacustrine deposits with different sediment textures, reflecting contemporary energetic conditions (Goldberg and Macphail, 2006; Miall, 2006). Thus, sediment dynamics serve as an external manifestation of geomorphodynamics.

The acceleration of geomorphodynamic processes poses a notable impediment to soil productivity, vegetation growth, and in consequence, agricultural activity. Such acceleration can lead to the overexploitation of land surfaces, the abandonment of fertile areas, the onset of desertification, and, historically, even the decline of certain civilizations (Geeson et al., 2002; Butzer et al., 2008; Dotterweich, 2008, 2013; Van Loo et al., 2016; Fyfe et al., 2019; Walsh et al., 2019).

### **2.1.2 Methods to reconstruct geomorphodynamics**

Numerous approaches have been employed to reconstruct the past environment changes or sediment dynamics, including sedimentary analyses (Ackermann et al., 2014a; Dreibrodt et al., 2014; Roberts et al., 2019b), cumulative probability functions of <sup>14</sup>C-ages (Piccarreta et al., 2011; Dusaar et al., 2012; Becker et al., 2020a), remote sensing techniques (Wang et al., 2023), and soil erosion risk models (Harmon and Doe, 2001; Benavidez et al., 2018). Here, we focus on the archive-based and model-based methods.

**Archive-based methods.** Over the past century, sedimentary archives on or near archaeological sites have been increasingly studied (Weiberg and Finné, 2022) for the

reconstruction of the depositional processes and their environment (Dikau et al., 2019) including processes of soil formation (Bartz et al., 2017), soil erosion (Dusar et al., 2011), flooding (Benito et al., 2015; Wolf and Faust, 2015), and coast–delta dynamics (Anthony et al., 2014; Stock et al., 2020b). However, the synchronicity between archives and the geomorphic system response does not necessarily imply a cause–effect relationship (Gladfelter, 1977; Dusar et al., 2011), and vice versa. Therefore, the simple correlation is challenged by some scholars (Butzer, 2005). Sediment cascades within a catchment can buffer the response of the geomorphic system, leading to time lags and non-linear responses to potential drivers (Fryirs, 2013; Wolf and Faust, 2015). Furthermore, the chronologies of sediment archives and records of driving forces often lack sufficient accuracy and detail (Dusar et al., 2011; Verstraeten et al., 2017). The geomorphic processes and conditions are also highly influenced by the sampling location within the landform background (Ackermann et al., 2014b). Despite these constraints, archive-based methods are efficient in detecting the changes in the environment and remain crucial for geoarchaeological research (Goldberg and Macphail, 2006; Goldberg et al., 2017).

**Model-based methods.** Geomorphic numerical models are generally based on physical laws and mathematical equations (Dikau et al., 2019), and can provide insights into human–environment interactions, particularly when combined with quantitative field data and sedimentary analyses for calibration and validation (Verstraeten, 2014). Such research has been applied in various regions, including Europe (Notebaert et al., 2011), China (Chen et al., 2021), and the Mediterranean region (Kosmas et al., 1997). In recent decades, numerous models have been developed to predict the soil erosion distribution on a larger spatial scale, falling into three main categories — empirical/statistical, conceptual/rule-based models, and physics-based/process-oriented models, as summarized among others by Borrelli (2011), Mitasova (2013), and Alewell et al. (2019). In the eastern Mediterranean, Van Loo et al. (2016) adapted the WATEM/SEDEM geomorphic model, indicating that soil erosion in the vicinity of the Hellenistic–Roman city of Sagalassos was mainly driven by deforestation and anthropogenic activities over the past 4 millennia. Empirical approaches such as the Universal Soil Loss Equation (USLE) and its derived models are globally used due to their simplified parameterization and data accessibility, with USLE-type models being particularly widespread (Alewell et al., 2019). Among them, the Unit Stream Power Erosion Deposition (USPED) model can predict soil erosion and deposition more accurately than USLE applications (Warren et al., 2005).

### **2.1.3 The Mediterranean geomorphodynamics**

#### **The timing**

The Mediterranean region is regarded as a cradle of civilization for many ancient societies with important global socio-cultural impacts (Roberts et al., 2019a). However, many areas within the Mediterranean have experienced severe land degradation, particularly soil erosion, flooding (Benito et al., 2015), and sedimentation on various scales and geomorphological locations (Geeson et al., 2002; Aiello et al., 2015; Pérez-Lambán et al., 2018), which have changed throughout the Holocene. Mediterranean climate reveals an east–west division (Roberts et al., 2011a). The Holocene sediment dynamics in the Eastern Mediterranean can be summarized into three main phases: (1) 12–6/5 ka BP: moderate sediment dynamics; (2) 6/5–1.5 ka BP: stepwise increasing sediment dynamics; (3) 1.5–0 ka BP: dramatical decrease in sediment dynamics due to population decline, followed by a progressive increase (Dusar et al., 2011). The environment is an intricate, multi-dimensional system with diverse interdependent factors (Zangger, 1992). Hence, the onset and duration of increased or decreased geomorphodynamics are highly complex and the reconstruction results depend on the scales, geographical locations, and methods employed in the current studies, as observed in the Mediterranean region (summary in Table S2.1).

#### **General driving factors**

The landscape evolution in the Mediterranean region during the Holocene is the result of multiple potential drivers (Brunsden and Thornes, 1979). The geomorphological processes can be triggered by various external variables, including natural and anthropogenic factors (Fuchs, 2007; García-Ruiz et al., 2013; Morellón et al., 2016; Connor et al., 2019; Woodbridge et al., 2019). Natural triggers contain climate variations (Finné et al., 2019), tectonics such as volcanic eruptions, earthquakes, and associated landslides (Morellón et al., 2016; Bulkan et al., 2018), vegetation cover (Kosmas et al., 1997; Francke et al., 2019; Fyfe et al., 2019), sea level changes (Kayen, 1999; Seeliger et al., 2017; 2019), and the inherited characteristics of topography, surface soil, and bedrock.

### **2.1.4 Key debates: climate vs. human impacts**

#### **Dominant driver(s)**

The debate regarding the dominant contribution of either climatic changes (Dotterweich, 2008) or socio-economic stresses (Geeson et al., 2002; Glais et al., 2017), or both (Bintliff, 2002; Giraudi, 2018; Pérez-Lambán et al., 2018), on the Holocene landscape, has

persisted for decades (Vita-Finzi, 1969b; Van Andel et al., 1990; Butzer, 2005; Wilkinson, 2005; Fuchs, 2007; Cremaschi et al., 2016). Vita-Finzi (1969b) established a broad chronological framework identifying two significant phases of erosion: the Upper Paleolithic and the Historic Period. The latter was suggested to be primarily influenced by climate change (Vita-Finzi, 1995). However, this hypothesis has been challenged, suggesting that human activities played a dominant role in sediment fluxes during the historic period, as observed in antique Greece (Van Andel et al., 1990). In recent years, these two viewpoints have been criticized for their simplistic mono-causal explanations (Bintliff, 2002). Nowadays, scholars increasingly favor complex multi-causal explanations instead of deterministic mono-causality, acknowledging the interactions among environmental contexts, climate fluctuations and anomalies, and human impacts (Bintliff, 2002; Izdebski et al., 2016a; Stoddart et al., 2019; Degroot et al., 2022; Weiberg and Finné, 2022). Particularly in arid to semi-arid regions, increased human activities may intensify the influence of climate; extreme rainfall events triggered by climate fluctuations can lead to intensified erosion, which can, in turn, be amplified by human activities (Walsh et al., 2019).

The present climate in the Mediterranean region is semi-arid to dry/semi-humid, characterized by low annual precipitation levels, high rainfall seasonality (Woodward, 2009), and prolonged droughts with high evapotranspiration, followed by intense rainstorms (García-Ruiz et al., 2013). These climatic features have contributed to severe erosion on the frequently already highly degraded soils of steep upland slopes (Geeson et al., 2002; Borrelli et al., 2014). Locally, they may also lead to the deposition of habitable and arable sediments in bottomland areas (Leigh et al., 2019). Throughout the Holocene, the occurrence of global-scale rapid climate changes (RCCs) has been identified during several time intervals, including 9000–8000, 6000–5000, 4200–3800, 3500–2500, 1200–1000, and 600–150 calibrated years before present (cal yr BP) (Mayewski et al., 2004). A recent hydro-climatic study in the Mediterranean reveals that centennial-scale climate changes may have occurred around 6700–6300, 4500–4300, and 3500–3300 yr BP (Finné et al., 2019). Several RCCs have coincided with environmental stresses that have caused major disruptions to civilizations or offered opportunities for cultural reorganization (Wanner et al., 2008; Roberts et al., 2011b), particularly within a Mediterranean context (Bintliff, 2002; Casana, 2008; Fletcher and Zielhofer, 2013). Hence, the periods of RCCs also repeatedly align with some important socio-cultural transformations, such as the 4.2 event (transition from the Early to Middle Bronze Age) and the 3.2 event (transition from the Late Bronze Age to Iron Age).

Humans have exerted distinct impacts on their surroundings throughout (pre-)history, particularly since the widespread adoption of intensive agriculture (Efe, 1996). Human activities include settlement development, woodcutting, firing, grazing, farming, ploughing and cultivating, and slope terracing as an adaptation to water shortness and high soil erosion rates (García-Ruiz et al., 2013; Mazzini et al., 2016; Roberts et al., 2019a). Large parts of the Mediterranean have experienced substantial human impacts over the past several millennia, resulting in landscape degradation through severe soil erosion, which has been described as a “cultural Mediterranean landscape” (Naveh, 1982). For example, the impact of humans on the Greek landscape has intensified since the Late Bronze Age, coinciding with the introduction of more extensive herding and agricultural practices (Weiberg et al., 2019a). Deforestation activities have often led to dramatic increases in surface soil erosion and sedimentation (Walsh et al., 2019).

Regarding the interrelating effects of climate and human pressure on the landscape, Bellin et al. (2013) reviewed the Holocene sediment dynamics in SE Spain and found that phases of enhanced aridity consistently aligned with increased sediment dynamics, regardless of the intensity and type of human occupation. Conversely, humid conditions corresponded to varying levels of sediment dynamics as controlled by human impacts. However, Van Loo (2016) suggests a relatively weak relationship between precipitation and sediment delivery based on research in the Gravgaz basin, the environs of Sagalassos (Figure 1.1). Analogous findings have been observed in south Greece during the Early to Middle Holocene (Fuchs, 2007).

### **The timing**

In the Early Holocene, landscape changes were primarily influenced by general climatic changes and extreme climatic events (Dusar et al., 2011). Conversely, the Late Holocene was more strongly influenced by human disturbance, e.g., in the Levant (Palmisano et al., 2019) and the Balkans (Pope and van Andel, 1984; Francke et al., 2019). However, the effects of both factors during the transitional period between the Mid-Holocene and Late Holocene, remains unclear, known as the Mid-Holocene ‘mélange’ (Roberts et al., 2011a). In certain areas, human impacts might have become the most important factor since 8 ka BP, as observed in Greece (Jouffroy-Bapicot et al., 2021).

During the Early Holocene, early human communities started utilizing the landscape. However, the population density was relatively low compared with later periods, e.g., in the Near East (Palmisano et al., 2019), as well as in the Pergamon micro-region (only one site from the Epipalaeolithic to Neolithic periods (Aksan et al., 2022); Table 2.1). This suggests that increased geomorphodynamics during the Early Holocene were primarily

controlled by climatic factors rather than the rare contribution of human activities (Becker et al., 2020a). A fundamental change in the Mediterranean landscape occurred around 8.2 ka BP, associated with the pronouncedly cold and arid conditions known as the 8.2 event, as well as the introduction and spread of early farmers (Weninger et al., 2006). The 9.2 ka event was similar to the 8.2 event, albeit with a smaller magnitude in southwest Asia (Flohr et al., 2016).

A long-term trend of climatic drying and increasing rainfall instability began around 6000 years ago (Finné et al., 2019) or even earlier (Berger et al., 2016), despite the wetter conditions occurred in the Early to Middle Holocene (Hancock et al., 2023). This climatic trend persisted until around 3.3–2.7 ka BP and had detrimental effects on contemporary societies in the eastern Mediterranean region (Walker and Fattahi, 2011). Around 5 ka BP, intense flooding occurred across the Mediterranean, causing notable landscape changes that were sensitive to climate and environmental variations (Benito et al., 2015). However, local floodplain conditions might have remained relatively stable (Collins et al., 2005).

At the end of the Middle Holocene, the geomorphodynamics showed an evident decrease, associated with the 4.2 ka BP drought event (hereinafter 4.2 event), such as in the western lower Bakırçay plain (Becker et al., 2020a). In contrast, increased sediment dynamics, including flooding and erosion/deposition, were observed in the eastern Mediterranean region (Dusar et al., 2011). The 4.2 event, considered a global hydro-climatic anomaly (Walker et al., 2019) and sometimes referred to as a "global megadrought" (Weiss, 2016), had varying impacts on the Mediterranean landscapes. Particularly, recent studies show less impact of the 4.2 event on the ecosystem of the northern Mediterranean (Di Rita et al., 2022; Ön, 2023), which might apply to contemporary geomorphodynamics (Finné et al., 2011). In eastern Türkiye, the intensified fluvial incision after the 4.2 event was likely influenced by both climate and human factors (Collins et al., 2005).

During the Late Holocene, human activities, such as land clearing and the absence of soil conservation measurements, emerged as the dominant cause of landscape changes, as observed in Greece (Pope and van Andel, 1984). Since ca. 3 ka BP, the progressive population growth and human activities, including forest clearance, agriculture, and pastoralism, had distinct effects on the regional landscape in western Anatolia (Eastwood et al., 1998; Knipping et al., 2007; Dusar et al., 2011; Finné et al., 2011; Stock et al., 2020a), which is widely mentioned as the Beyşehir Occupation phase (BOP, ca. 3.5–1.5 ka BP) (Eastwood et al., 1998; Kaniewski et al., 2007; Bakker et al., 2011a).

**Table 2.1** A chronological scheme for the Pergamon micro-region (based on regional studies (Roberts et al., 2019b; Walsh et al., 2019; Becker et al., 2020a) and webservice iDAI.chronontology)) and raw settlement count (Data source: unpublished archaeological data, address to B. Ludwig for the latest data).

Period	Chronology	Raw settlement count (n) *
Late Epipalaeolithic Period	13.7 – 12.2 ka BP	1
Neolithic Period	10.5 – 8 ka BP	1
Chalcolithic Period	8 – 5 ka BP	0
Early Bronze Age	5 – 4 ka BP	25
Middle Bronze Age	4 – 3.7 ka BP	26
Late Bronze Age	3.7 – 3.2 ka BP	27
Iron Age	3.2 – 2.8 ka BP	14
Archaic Period	2.8 – 2.5 ka BP	21
Classical Period	2.5 – 2.3 ka BP	35
Hellenistic Period	330 – 27 BC	80
Roman Imperial Period	27 BC – 395 CE	64
Late Antiquity	ca. 5th century CE	47
Byzantine Period	ca. 6th – 13th century CE	36
Ottoman Period	ca. 14th century – 1923 CE	18

\* Note:

- 1) only the sites with chronology and coordinate were counted in our study;
- 2) if a site was originally determined in the Bronze Age, it is assigned to cover the Early, Middle, and Late Bronze Ages;
- 3) if a site was originally determined in the Iron Age, it is assigned to cover the Iron Age, Archaic, and Classical periods;
- 4) if a site was originally determined in the Hellenistic Period, it is assigned to cover from the Pergamenian Kingdom (331–133 BC) to 133–27 BC;
- 5) if a site was originally determined in either the Early, Middle, or Late Byzantine Period, it is assigned in the Byzantine Period;
- 6) the chronology for the Late Epipalaeolithic and Neolithic periods is only for the Ballık Cave (Aksan et al., 2022) which is not additionally used in the USPED model.

Geomorphodynamics in the western lower Bakırçay plain, draining the Pergamon micro-region, reached a peak at ca. 2.5 to 1.4 ka BP, corresponding to the Classical, Hellenistic, and Roman Imperial periods in the history of the Pergamon micro-region. During these periods substantial urbanization processes and demographic growth in cities and rural settlements occurred (Becker et al., 2020a; Ludwig, 2023). The controlling influence of

various human activities seems to decouple from the climatic fluctuations during the Late Holocene, for example, in the Levant (Palmisano et al., 2019).

## **2.2 The Pergamon micro-region**

### **2.2.1 Natural background**

The delineation of the Pergamon micro-region is not fixed to specific areas and differs depending on the disciplinary view. In physical geography, the catchment is regarded as a fundamental geomorphological unit and is frequently used as the primary landscape unit for hydrological, and environmental investigations including land management activities (Goudie, 2004). Consequently, this doctoral thesis centers the study areas on the catchments of Bakırçay and Madra rivers that encompass or overlap with the urban expanse of Pergamon; Figure 1.1). The ongoing (geo)archaeological investigations predominantly concentrate on these catchment areas (Becker et al., 2020 and references therein). Considerable attention has been directed towards the western part, encompassing the western lower Bakırçay plain, the Kozak, Yuntdağ, and Karadağ mountains, as well as the coastal areas. These studies have yielded substantial numerical data essential for the synthesis of the fourth case study.

The Pergamon micro-region exhibits considerable local variations in terms of bedrock (MTA, 2002), distribution of soil types (Gülersoy, 2008; Danacıoğlu and Tağıl, 2017), vegetation cover (Efe, 1996), and landforms, which has been summarized by Yang et al. (2021) (chapter 4). The area experiences a prevalent Mediterranean climate type (Csa) characterized by hot and dry summers and mild winters (Lionello, 2012).

During the settlement history intensive land use in the area caused a degradation of the vegetation. In the Yuntdağ mountains, the progressive degradation from forest to maquis/garrigue is suggested to be primarily driven by human activities and livestock resulting in reduced productivity and enhanced soil erosion (Efe, 1996). Geoarchaeological studies have also indicated locally increased geomorphodynamics during certain periods of the Holocene in the western lower Bakırçay plain, for example, fluvial sediment deposition (ca. 3.5 m thick) after the Bronze Age (Schneider et al., 2017), ca. 2 m thick after the antiquity (Schneider et al., 2015), and colluvial/alluvial sediments (6 m thick) in the last 2 thousand years (Schneider et al., 2013).

## 2.2.2 Archaeological research

During the Hellenistic and Roman periods the ancient city of Pergamon held great importance as one of the largest regional centers in Asia Minor; it played a crucial role in various aspects, including administration, crafts/industry, cult, trade, and security (Knitter et al., 2013). By the late 4<sup>th</sup> century BCE, Pergamon had already grown into a significant Hellenistic city or polis of considerable size (Pirson, 2017). During the Hellenistic period, Pergamon was the capital city of the Attalid dynasty, known as the Pergamene Empire, which ruled over western Anatolia during the 3<sup>rd</sup> and 2<sup>nd</sup> centuries BCE; as a result, Pergamon attained a high degree of power and supra-regional importance (Pirson, 2008; Pirson and Scholl, 2014). Unlike many ancient coastal cities, such as Troy, Smyrna (Izmir), Ephesus, and Miletus (Figure 1.1), Pergamon was situated on a hill (330 m a.s.l.), ca. 23 km inland from its nearest Aegean coast (Pirson, 2008) and facing to the south – the plain of the regional river, the Bakırçay river (ancient Kaikos). Its unique location was part of a deliberate spatial strategy that protected against potential sea-based attacks (Pirson, 2008) while maintaining connections with coastal cities and settlements in the surrounding areas (Ludwig, 2020b).

During the Roman Imperial Period (the 1<sup>st</sup> and 2<sup>nd</sup> centuries CE), Pergamon became a metropolis within the Roman province of Asia. The city underwent substantial expansion, extending from the city hill to its footslope, and doubled its size due to strong population growth (Radt, 2016; Pirson, 2017). According to estimation by the Greek physician and writer Galen (129–216 CE), the city and its surrounding region, known as the chora (Figure 1.1), were home to approximately 120,000 people (including slaves) during this period (Pirson, 2020). This marked a profound urban transformation and a shift in the city's political and social framework from the Hellenistic to the Roman Imperial period (Pirson, 2017, 2020). The term transformation is cited and defined as “the reshaping or transition of a form or pattern from one state to another” by Ludwig (2023). Hence, from a social perspective, a fundamental transformation is accompanied by erratic changes in political and economic development under long-term processes. After the Roman Imperial period, the city of Pergamon declined in importance during the Byzantine and Ottoman periods but was never fully abandoned and continued to develop (Ludwig, 2023). Presently, the city continues to extend downhill the antique Pergamon and has evolved into the modern town of Bergama; only the settlement of the antique Pergamon on the hilltop was abandoned.

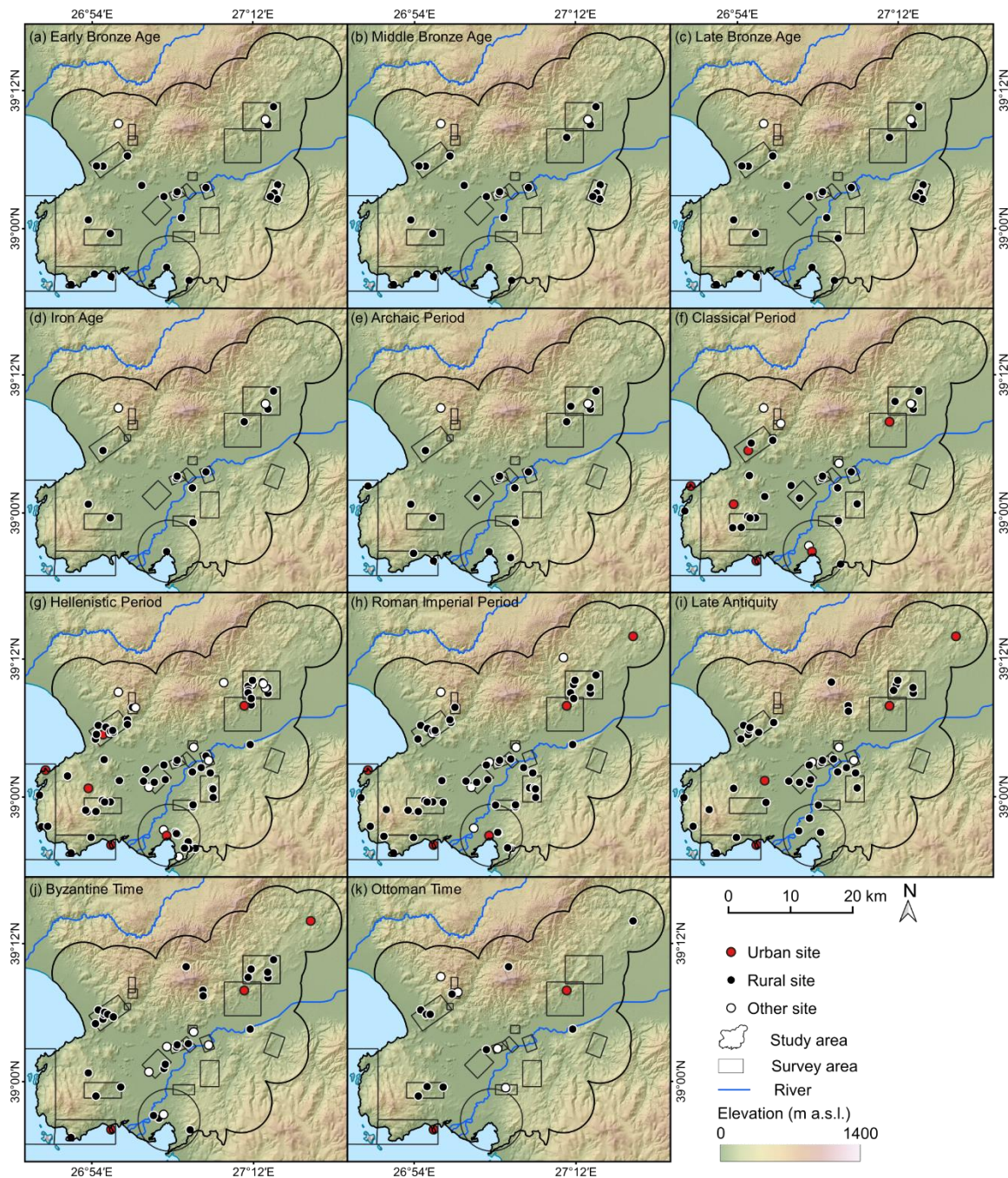


**Figure 2.1** The spatial and temporal distribution of the archaeological sites from the Early Bronze Age to the Ottoman Period (5 ka BP–1922) in the western Pergamon micro-region (Data source: unpublished archaeological data, address to B. Ludwig for the latest data). Note: the circle around the ancient harbor city of Elaia is the boundary of its archaeological survey area.

Pergamon has been archaeologically researched by the German Archaeological Institute since the early 20<sup>th</sup> century. The environ of Pergamon has been intensively investigated since 2006 when F. Pirson became the head of the Pergamon excavation (Pirson, 2017; Ludwig, 2023). The archaeological survey areas primarily cover the western part of Pergamon, including the western lower Bakırçay plain, the surrounding mountains, such as Kozak/Madra Dağı mountain (ancient Pindasos), Yuntdağ mountain (ancient Aspordenon), Karadağ

mountains (ancient Kane), and the coastal areas (Pirson, 2010; 2015; 2017) (Figure 2.1). Numerous urban settlements, large villas, small rural settlements, and other sites have been discovered and reported in this region (Zimmermann et al., 2015; Pavúk and Horejs, 2018). The oldest site excavated is the Ballık Cave in Kozak mountain (Aksan et al., 2022). Based on the radiocarbon dating, the site was used from the Late Epipalaeolithic (13.7–12.2 ka BP) to Neolithic (10.5–8 ka BP) periods (Aksan et al., 2022) (Table 2.1). Contemporarily, the site of Pergamon itself was not of any major importance (Aksan et al., 2022).

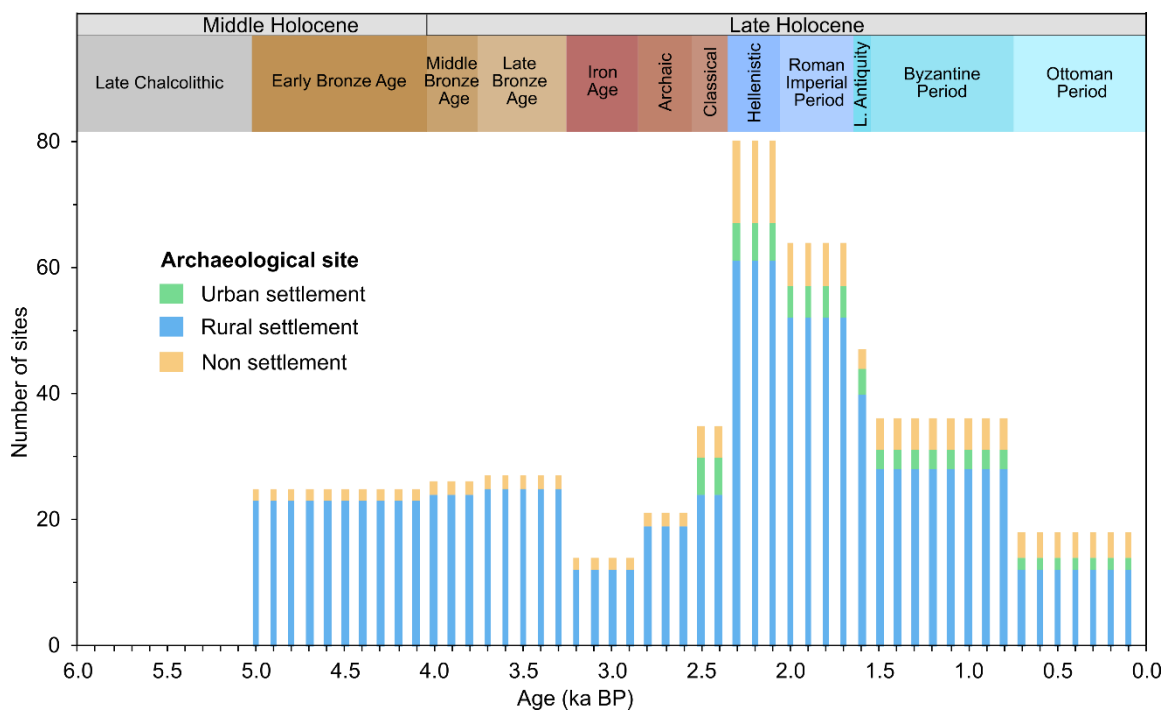


**Figure 2.2** The raw count of archaeological sites in each 100-year time span from the Late Chalcolithic to the Ottoman periods (6 ka BP–1922) in the western Pergamon micro-region (Data source: unpublished archaeological data, address to B. Ludwig for the latest data). Note: sites without chronology or coordinates were excluded from this dataset

Continuous settlement activities in the Pergamon micro-region started in the western lower Bakırçay plain, specifically at the small hill site of Yeni Yeldeğirmentepe, during the Late Chalcolithic (ca. 6 ka BP) to Early Bronze Age periods (4.7 to 4.4 ka BP) (Horejs, 2011b; Schneider et al., 2017). From the Early Bronze Age (5–4 ka BP) to the end of the Late Bronze Age (3.7–3.2 ka BP), numerous settlement sites were inhabited (Figures 2.1 and 2.2), coinciding with a period of denser population in Anatolia (Goldewijk et al., 2010). Most of the archaeological sites in the Pergamon micro-region were located on elevated areas, such as hilltops or their gentle slopes in the plains or the adjoining mountainous areas (Figure 2.1). For the first time, continuous settlement activities were observed at some important settlement sites, including Pergamon, Elaia, Pitane, Atarneus, Teuthrania, and Hatipler (Schneider et al.,

2014). From approximately 3.5 to 2.8 ka BP (Iron Age), the number of settlement sites in the Pergamon micro-region distinctly declined (Figure 2.2), but it progressively increased again, reaching its peak during the Hellenistic Period (Ludwig, 2023) (Figure 2.2).

During the Hellenistic–Roman Imperial period, the fundamental urban transformation in the city of Pergamon accordingly led to a series of changes in its micro-region, including the expansion of villages (Table 2.1), changes in land use, and resulting geomorphodynamics, as a result of the close interdependencies between Pergamon and its surroundings (Ludwig, 2023). The growing population in the city necessitated larger-scale agricultural and pastoral practices in the surrounding areas, often leading to increased rates of soil erosion in the rural landscape (Goodchild, 2013). The number of sites declined again during the Ottoman period, particularly for rural settlements (Figure 2.2) (Pirson and Zimmermann, 2014).

During the Archaic Period (ca. 2.8–2.5 ka BP), coinciding with the Beyşehir Occupation phase in the wider Aegean region, settlements located in the coastal areas started intensified overseas trade, including the later important harbor cities of Elaia (Pirson, 2014; Pirson et al., 2015), Pitane (Bes and Keweloh-Kaletta, 2022), and Kane (Fediuk et al., 2019) (Figure 1.1). These harbor cities received intensive development during the Hellenistic and Roman periods. Elaia was likely abandoned probably in Late Antiquity (Seeliger et al., 2014; 2019). The Hellenistic polis of Atarneus, situated on the foothill of the Kozak mountain, was in use probably from the Archaic Period to the beginning of the Roman Imperial Period (Schneider et al., 2013).



## **3. Material and methods**

This chapter compiles the methods that were used for the four working packages in the doctoral thesis (Yang et al., 2021; Yang et al., 2023a; Yang et al., 2023b) (Figure 1.2). The texts in this chapter are reworked and extended based on the texts in the four working packages; partially the original paragraphs from the publications (chapters 4, 5, and 6) are used.

The first working package (chapter 4) delineates the present-day geomorphological overview of the Bakırçay and Madra catchments, hence, geomorphological mapping and analyses were used (chapter 3.1). In the second and third working packages (chapters 5 and 6), field observation and work were conducted (chapter 3.2); sediment profiles from the valley bottom and alluvial fans from the Tekkedere and Deliktaş catchments were measured (chapter 3.3) and statistically analyzed (chapter 3.4); the chronology of the sediment profiles was framed by radiocarbon dating (chapter 3.5). To extrapolate the Mid- to Late Holocene geomorphodynamics in the western lower Bakırçay catchment (the fourth working package, chapter 7), a soil erosion and deposition model, the USPED model, was applied (chapter 3.6).

### **3.1 Geomorphological mapping and analyses**

#### **3.1.1 Survey of geomorphological features**

The major geomorphological features during recent times in the catchments of the Bakırçay and Madra rivers were documented and mapped using QGIS (v 3.8) (QGIS Development Team, 2020). This was supported by a literature review of old topographical maps and documents, field observations, visual interpretations of freely available high-resolution satellite images provided by Google Earth (<1 m resolution; DigitalGlobe, Inc., maps.google.com, last accessed 8 June 2020), and geomorphometric derivatives from TanDEM-X data (spatial horizontal resolution: 12 m (Rizzoli et al., 2017; Wessel et al., 2018)). The subdivisions with definition and classification rules of the landform units in the geomorphological map are summarized in Table S4.1 (Walstra et al., 2009). The major rivers in the catchments were digitalized from topographic and geological maps (Emre and Doğan, 2010; Emre et al., 2011a; Emre and Özalp, 2011; Emre et al., 2011b).

Field photographs and additional materials from each landform unit (Figures S4.1–S4.7) were used for the geomorphological interpretation and validation. The field observations were mainly conducted in the western and eastern lower Bakırçay plain and its surrounding mountains (the Kozak, Yuntdağ, and Karadağ mountains), whereas the geomorphological mapping from other areas was mostly validated based on the literature (e.g., Yilmaz et al., 2000; İnci, 2002; Karacik et al., 2007).

### **3.1.2 Extraction of basic geomorphometric parameters**

**Geomorphometric derivatives.** Based on a digital elevation model derived from the TanDEM-X data, selected geomorphometric analyses, slope, aspect, geomorphons, Topographic Position Index, and Topographic Wetness Index (Hengl and Reuter, 2009; Huggett, 2017), were conducted using various modules implemented in GRASS GIS (v 7.8) (GRASS Development Team, 2020) and SAGA GIS (v 2.1) (Conrad et al., 2015) in QGIS (v 3.8) (QGIS Development Team, 2020). Zonal statistical analyses of those geomorphometric derivatives in each geomorphological unit and subunit were processed using the Zonal statistics module in QGIS (v 3.8) (QGIS Development Team, 2020). The elevations received from the TanDEM-X were treated with caution because they are ellipsoidal heights and the undulation of the geoid averaging around 40 m at the coast (Rizzoli et al., 2017; Wessel et al., 2018).

Slope and aspect display the slope angle and orientation of a raster pixel, respectively, which was used by the module of `r.slope.aspect` (Hofierka et al., 2009). Geomorphons is a recognition approach for the classification and mapping of the ten most common landform elements (flat, peak, ridge, shoulder, spur, slope, pit, valley, footslope, and hollow), which was generated applying `r.geomorphon` (Jasiewicz and Stepinski, 2013) (the outer search radius: 1000 m; the inner search radius: 50 m; the flatness threshold: 3 degrees; settings for other derivatives remained at default values). The topographic Position Index shows the comparison of the raster pixel's elevation to the mean elevation of a specified neighborhood around that pixel, which was extracted by the module of topographic position index (TPI) (Guisan et al., 1999; Weiss, 2001). The Topographic Wetness Index shows the capacity of a raster pixel to accumulate water, which was generated by `r.topidx` (Beven and Kirkby, 1979; Moore et al., 1991; Mattivi et al., 2019).

**River longitudinal profiles and knickpoints.** River longitudinal profiles (Rhoads, 2020) were extracted for the major river courses of the Bakırçay catchment from the TanDEM-X data (Emre and Doğan, 2010; Emre et al., 2011a; Emre and Özalp, 2011; Emre et al., 2011b) to receive information on knick-points. Noise in the river longitudinal profiles

caused by reservoirs was manually corrected. Knickpoints were identified manually as inflexion points of the river longitudinal profiles.

**Mountain-front sinuosity index.** To assess the shape of the mountain front of the Kozak and Yuntdağ mountains, the mountain-front sinuosity index (Bull, 2007) was applied and calculated in QGIS (v 3.8) (QGIS Development Team, 2020).

$$Smf = \frac{Lmf}{Ls}$$

where  $Smf$  represents the mountain-front sinuosity index,  $Lmf$  is the planimetric length of a mountain front along the footslope which is at the topographic break in slope, and  $Ls$  is the length of a straight line at the former mountain front.

The low  $Smf$  value results likely indicate the straight mountain front produced by active tectonics, whereas, the high  $Smf$  value results suggest the sinuous or eroded front due to erosive processes and less active tectonics (Bull, 2007; Mahmood and Gloaguen, 2012).

**Topographic swath profiles.** To determine the topographic differences between the Kozak and Yuntdağ mountains, two swath profiles, i.e., the mean, maximum, and minimum elevation of equally spaced rectangles (here 500 × 6000 m) along the profile line (midline) (Telbisz et al., 2013), were extracted using GRASS GIS (v 7.8) modules (v.mkgrid, v.rast.stats, and v.to.points) via QGIS (v 3.8) (GRASS Development Team, 2020; QGIS Development Team, 2020).

## 3.2 Field work

During four field campaigns in the Pergamon micro-region (September 2019, October 2020, 2021, and 2022), the present-day geomorphological situations and geomorphic processes of the Bakırçay catchment were systematically investigated (Figure 4.4) according to Barsch (1985). Particularly, the mountainous catchments of Tekkedere and Deliktaş in the western lower Bakırçay catchment were detailed geomorphologically mapped (Figures 5.2 and 6.2) and sediments of their deposits were extracted.

The sediment archives sampled include three sediment outcrops from the Tekkedere valley bottom and five open sediment cores from each of the Tekkedere and Deliktaş alluvial fans (Table 3.1).

**Table 3.1** Metadata of the sediment archives in this thesis. In the Tekkedere catchment, three outcrops in the valley and five drilling cores on the alluvial fan were obtained; in the Deliktaş catchment, five drilling cores were obtained on the alluvial fan.

Catchment	Sediment sequence	Latitude (° N)	Longitude (° E)	Elevation (m a.s.l.)	Depth (cm)	Sediment samples (n)	<sup>14</sup> C samples (n)	Geomorphological position	Land use
Tekkedere	Tek-1	38.99164	27.08685	88.7	176	14	3	Valley (channel bank)	Olive grove
	Tek-2	38.98832	27.08677	70.8	158	11	2	Valley (channel bank)	Olive grove
	Tek-3	38.99120	27.08701	84.0	220	19	1	Valley (channel bank)	Olive grove
	Tek-4	38.99268	27.05971	16.6	200	0	0	Alluvial fan (apex)	Olive grove
	Tek-4-2	38.99341	27.05418	11.5	700	32	2	Alluvial fan (middle)	Arable land
	Tek-5	38.99472	27.05216	9.1	786	48	7	Alluvial fan (middle)	Arable land
	Tek-5-2	38.99554	27.04988	7.4	400	17	3	Alluvial fan (middle)	Arable land
	Tek-6	38.99688	27.04662	6.3	800	50	2	Alluvial fan (toe)	Arable land
Deliktaş	Del-2	38.99649	26.97883	6.0	500	33	3	Alluvial fan (distal area)	Arable land
	Del-3	38.99484	26.97604	7.1	700	46	3	Alluvial fan (middle area)	Arable land
	Del-4	38.99339	26.97326	9.3	800	39	1	Alluvial fan (middle area)	Arable land
	Del-5	38.99110	26.96710	12.5	444	28	2	Alluvial fan (proximal area)	Arable land
	Del-6	38.99000	26.96794	12.2	500	25	3	Alluvial fan (proximal area)	Arable land

In September 2019, the sediment outcrops in the Tekkedere valley were sampled due to the occurrence of archaeological sites in this area. The outcrops in the olive grove were along a bank of creek B, a major tributary of the Tekkedere stream (Figure 5.2). The sediment profiles were firstly cleaned and macroscopically described. Sediment samples (3–5 cm thick pieces; n = 44) were collected for geochemical analyses corresponding to their position of unit boundary and thickness. Sediment profiles were carefully checked for charcoal pieces, shells, and organic-rich bulk samples for radiocarbon dating (n = 6).

In October 2020, the sediment cores (thicknesses up to 8 m) were extracted along transects from the apex to the toe of the Tekkedere alluvial fan by vibracoring (Wacker BHF 30 S, with open cores of 5 cm diameter) (Becker et al., 2022b) (Figure 5.2). None of the profiles reached the underlying bedrock. Sediment samples (n = 147) and radiocarbon dating samples (n = 14) were collected from the sediments of the Tekkedere alluvial fan (Table 3.1).

On the Deliktaş alluvial fan, five sediment cores (thicknesses up to 8 m) were extracted following the same protocol in October 2021 (Figure 6.2). Sediment samples (n = 171) and radiocarbon dating samples (n = 12) were taken from the sediments of the Deliktaş alluvial fan (Table 3.1).

Lithostratigraphy of all the sediment profiles (outcrops and cores) was macroscopically documented on-site including sediment depositional structure (Stow, 2005), unit thickness, sediment texture and fabric (Blair and McPherson, 1999), sediment color (Munsell soil color), hydromorphic features, biological modification, and the occurrence of artifacts (Jahn et al., 2006). The degree of reaction to 9.9 % HCl (no, slightly, moderately, strongly) was applied to estimate the amount of calcium carbonate ( $\text{CaCO}_3$ ) (Jahn et al., 2006).

### **3.3 Laboratory analyses of the sediments**

Sediment samples from the Tekkedere valley and alluvial fans of Tekkedere and Deliktaş were prepared and analyzed in the field laboratory of the Bergama archaeological excavation house to provide indicators for sediment origins, erosional and (post-) depositional processes (Buggle et al., 2011; Ülgen et al., 2012; Croudace and Rothwell, 2015), paleosol occurrence (Niwa et al., 2011; Nykamp et al., 2020) and human activity (Goldberg and Macphail, 2006). Before the measurement, samples were air-dried for more than 48 h and the aggregates were crushed in a porcelain mortar. For subsequent analyses, the fine fraction ( $\varnothing < 2$  mm) was separated from the coarse component by dry sieving. Sediment samples were analyzed on six bulk parameters:

### 3.3.1 Mass percentage of the coarse components

For the Deliktaş alluvial fan sediments the separated coarse components ( $\varnothing \geq 2$  mm) and fine fractions ( $\varnothing < 2$  mm) were weighted to calculate the mass percentage of the coarse components.

### 3.3.2 Electrical conductivity and pH

The electrical conductivity (EC) and pH values of the sediments were measured in the water-saturated sediments (1:2.5 solutions of 5 g sediments and 12.5 mL distilled water) with a TDS/EC/pH/TEMP meter (PEZ9908; resolution: 0.01 pH, 1  $\mu\text{S cm}^{-1}$  EC). Reaction class terms and the pH range are based on the USDA soil survey manual (Soil Science Division Staff, 2017) (Table 3.2). Average values of 2–5 non-consecutive measurements of pH and EC were reported.

### 3.3.3 Loss on ignition

Approximately 10 g homogenized sediments were measured on the loss on ignition (Dean, 1974; Heiri et al., 2001; Santisteban et al., 2004). The air-dried weighted samples were firstly filled in weighted crucibles and heated in a microwave oven at 105 °C for 4 hours. After cooling to room temperature in a desiccator, they were weighted again and ignited in a muffle furnace at 550 °C for another 4 hours.  $\text{LOI}_{550}$  was calculated as the weight difference of a sample treated by both temperatures and is used for the estimation of organic matter content (Heiri et al., 2001; Santisteban et al., 2004) following the equation:

$$\text{LOI}_{550} = \frac{DW_{105} - DW_{550}}{DW_{105}}$$

where  $\text{LOI}_{550}$  represents loss on ignition at 550 °C (mass-%),  $DW_{105}$  represents the oven dry weight of the sample (g), and  $DW_{550}$  represents the dry weight of the sample after heating to 550 °C (g).

The in-lab reference material was measured with every 20 samples to control variability, which is reproducible with a median  $\text{LOI}_{550}$  value of 5.6 mass-% (median absolute deviation (MAD): 0.2 mass-%). Values of  $\text{LOI}_{550}$  were compared with the measured total organic carbon contents (TOC) (Figure S6.2) of sediments from the western lower Bakırçay plain ( $n = 86$ ,  $R^2 = 0.71$ ,  $\alpha < 0.05$ ; Figure S6.1). The TOC values were quantified by a LECO TruSpec CHN analyzer and a Shimadzu TOC-L CPH system. The strong

positive relationships between LOI<sub>550</sub> and the TOC (Figure S6.2) indicate that LOI<sub>550</sub> in this region is capable of estimating organic matter content.

### 3.3.4 Magnetic susceptibility

The magnetic susceptibility of sediments was measured using a Bartington magnetic susceptibility system (MS3 meter and MS2B dual-frequency sensor; measuring resolution:  $2 \times 10^{-6}$  SI and range: 26 SI) via the *Bartsoft* software. The volume-specific magnetic susceptibility ( $\kappa$ ) at low frequency (LF, 0.465 kHz) of weighed samples filled in 12 cm<sup>3</sup> plastic pots was determined with triple repetition. The in-lab reference material was measured with every 20 samples for quality control. The mass-specific susceptibility at the low frequency ( $X_{LF}$ ,  $10^{-8}$  m<sup>3</sup> kg<sup>-1</sup>) was calculated (Dearing, 1994; Dearing et al., 1996). The confidence intervals of sample median  $X_{LF}$  values were estimated by simple quantile bootstrapping (B = 1,000) in R (v 3.6) (R Core Team, 2021).

In addition, Samples from the Tek-5 profile (n = 48) were measured five times with a MS2B meter. The results are highly comparable to 88 % of samples used via the MS3 meter (correlation of the sediment measured in both meters: median = 0.97). The median of the volume-specific susceptibility of the 10 mL calibration sample is  $2620 \cdot 10^{-5}$  SI (MAD:  $0.25 \cdot 10^{-5}$  SI; accuracy: 1%).

### 3.3.5 Element composition based on pXRF

The element composition of sediment samples from the profiles of Tek-5, Tek-5-2, and Tek-6 on the Tekkedere alluvial fan and Del-2, Del-3, and Del-5 on the Deliktaş alluvial fan was analyzed applying a portable energy-dispersive X-ray fluorescence spectrometer (p-ED-XRF; Thermo Fisher Scientific NITON XL3t-900 GOLDD+; analytical range: Mg to U) and measuring each sample for 120 s in the manufacture's "Mining Cu/Zn" mode with main, high, low, and light filters (50, 50, 15/20, and 8 kV, respectively; 30 s measurement time each filter). The certified reference material (LKSD-4) (Lynch, 1990) and the acid-purified silica sand were taken as standards to ensure the measurement quality. The repeatability of the selected samples was determined.

## 3.4 Statistical analyses of sediment data

Results of laboratory sediment analyses are reported in median values and median absolute deviation values (MAD, in parentheses) which were categorized using the classification summarized in Table 3.2. Reported relationships between the variables

were established based on Spearman's correlation coefficient and related tests ( $\alpha = .05$ ). The assumption of (bivariate) normality is tested by applying the Shapiro-Wilk test (*ggpubr v0.6.0* (Kassambara, 2023) and *corrplot v0.92* (Wei and Simko, 2021) in R (v 4.2) (R Core Team, 2022).

Raw and processed data and the R code (R Core Team, 2021) for the data processing are provided in the published datasets at PANGAEA, both for the studies of Tekkedere (Yang et al., 2022) and the Deliktaş (Yang et al., 2023c).

**Table 3.2** The classification of sediment proxies used in this thesis (except pH (Soil Science Division Staff, 2017)).

class	$\geq 2\text{mm}$ (mass%)	pH		EC ( $\mu\text{S cm}^{-1}$ )	$X_{\text{LF}}$ ( $10^{-8} \text{ m}^3 \text{ kg}^{-1}$ )	$\text{LOI}_{550}$ (mass%)
class 1 (very low)	0–20	6.5–7.3	neutral	84–227	4–32	0.7–2.1
class 2 (low)	20–40	7.3–7.8	slightly alkaline	227–371	32–60	2.1–3.5
class 3 (medium)	40–60	7.8–8.4	moderately alkaline	371–515	60–87	3.5–4.9
class 4 (high)	60–80	8.4–9	strongly alkaline	515–659	87–115	4.9–6.2
class 5 (very high)	80–100	$\geq 9$	very strongly alkaline	659–803	115–143	6.2–7.6

### 3.5 Radiocarbon dating

The chronology of the sediment profiles from the valley bottom and alluvial fans in the Tekkedere and Deliktaş catchments was developed by accelerator mass spectrometry (AMS) radiocarbon dating ( $^{14}\text{C}$ ) using accelerator mass spectrometry (AMS) at the TÜBİTAK National 1 MV AMS Laboratory (Doğan et al., 2021). Dated materials contain charcoals, the mixture of mainly charcoal with adjacent sediments (if %C of the macroscopically separatable charcoal is  $<1\text{--}2 \text{ mg}$ ), organic-rich bulk samples, and the terrestrial snail shell. Macroscopic plants and rootlets were removed from the samples before the standard pretreatment procedure (acid-base-acid (ABA) protocol) was applied (Fowler et al., 1986; Bronk Ramsey, 2008; Brock et al., 2010). Fragile charcoal remnants with an amount of charcoal below ca. 10 mg were only treated with acid wash (Fowler et al., 1986; Brock et al., 2010).

The IntCal20 calibration curve (Reimer et al., 2020) and the *rcarbon* package (Crema and Bevan, 2021) were used to calibrate the radiocarbon ages in R (v 4.2) (R Core Team, 2022). Confidence intervals of 95% are reported for the calibrated ages. The age-depth modeling of samples from profiles Del-2, Del-3, and Del-6 are calculated based on the *clam* R-package (v2.5.0) (Blaauw, 2010).

The potential differences between the dating results and the sediment deposition age from a hillslope–fluvial–alluvial system due to the reworking of the sediments and dating materials (Blong et al., 2023) were discussed with the sediment cascade model (Lang and Hönscheidt, 1999) in chapters 5 and 6. In addition, the dating results from the TÜBİTAK Laboratory were reported when the samples show carbon content over 500 µg and passed the quality control (Doğan et al., 2021).

### 3.6 USPED model

To estimate the annual average rate of baseline soil erosion and deposition both for the recent times and the Mid- to Late Holocene, an empirical model – the Unit Stream Power Erosion Deposition (USPED) model (Moore and Burch, 1986) was used, following the procedure by Mitasova et al. (1996; 2013) and Aiello et al. (2015) (Figure 3.1). It incorporates the input factors of topography, precipitation, soil, land cover, and management practices (Mitasova and Mitas, 1999a; Aiello et al., 2015), which improves the RUSLE sub-factors by accounting for the overland flow and sediment transportation (Benavidez et al., 2018).

The equations employed for the calculation of the sediment transport capacity applying the USPED model are as follows (Mitasova and Mitas, 1999a; Aiello et al., 2015):

$$T_{(r)} = R \times C \times LS \times K \times P \quad (1)$$

where,

Parameter	Description	Unit
$T_{(r)}$	is the sediment transport capacity	dimensionless
R	is the rainfall–runoff erosivity factor	MJ mm ha <sup>-1</sup> h <sup>-1</sup> year <sup>-1</sup>
C	is the cover and management factor	dimensionless
LS	is the topographic factor	dimensionless
K	is the soil erodibility factor	t h MJ <sup>-1</sup> mm <sup>-1</sup>
P	is the support practice factor	dimensionless

Based on equation (1), the net soil erosion and deposition rates are calculated:

$$ED_{(r)} = (T_{(r)} \times s) = \frac{d(T_{(r)} \times \cos\alpha)}{dx} + \frac{d(T_{(r)} \times \sin\alpha)}{dy} \quad (2)$$

where,

Parameter	Description	Unit
$ED_{(r)}$	is the net soil erosion and deposition rate	t ha <sup>-1</sup> year <sup>-1</sup>
$\alpha$	is the aspect of terrain surface	degree

All input data (Table 3.3) were assigned to the Universal Transverse Mercator (UTM) projection system, cropped to the same extent, and resampled to a pixel size of 100 m using R (v 4.2) (R Core Team, 2022), GRASS GIS (v 7.8) (GRASS Development Team, 2020), and QGIS (v 3.22) (QGIS Development Team, 2023).

To capture the general trend of geomorphodynamics over the past 6000 years, the results were averaged to 100-year time intervals. The outcome values received from the USPED model were classified into nine soil erosion and deposition risk groups (Table 3.4) and the percentage of areas (in km<sup>2</sup>) in each group during the last 6 thousand years was calculated.

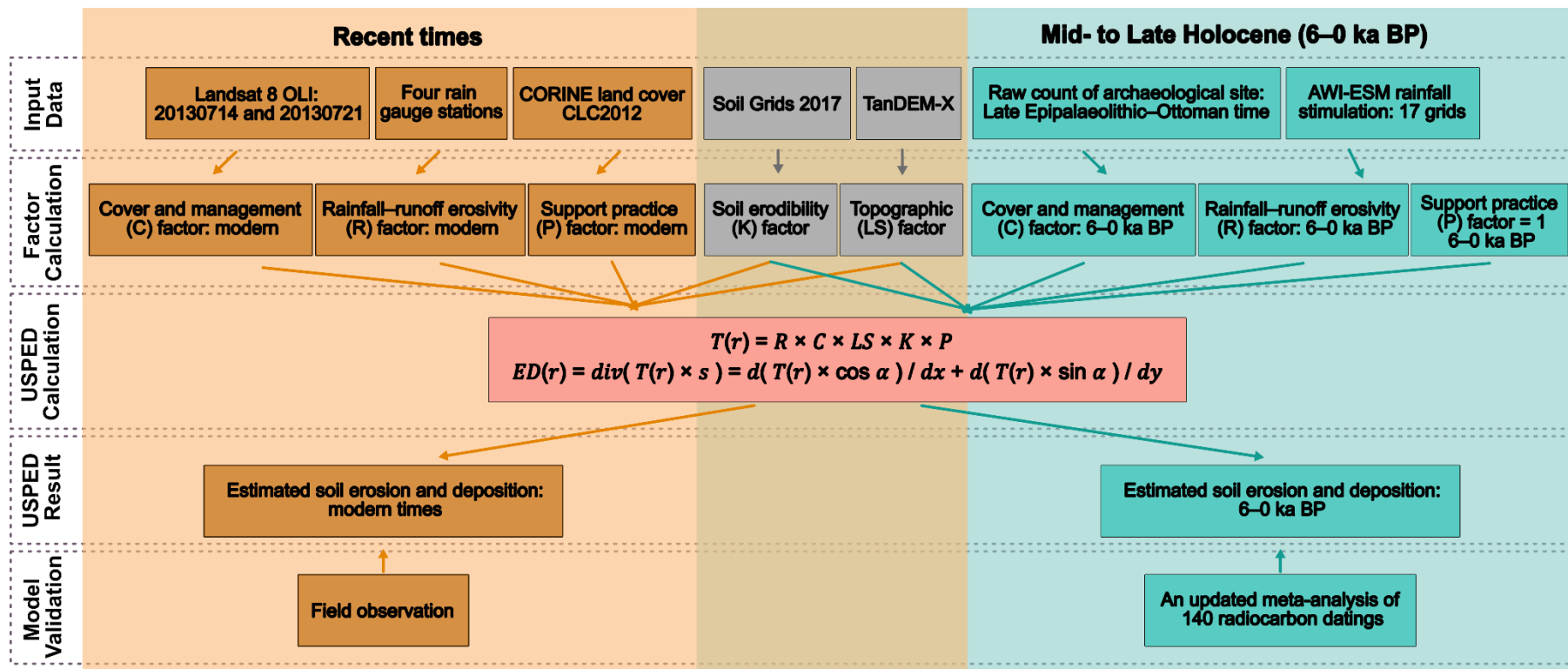


**Figure 3.1** The flow chart of the USPED model for estimating soil erosion and deposition risk in recent times and during the last 6000 years in the Pergamon micro-region. The data input refers to Table 3.3.

**Table 3.3** The summary of the dataset used for the USPED model.

Factor	Data	Description	Spatial resolution	Temporal resolution	Time range	Data source *
R	Modern rainfall	Dikili, Bergama, Soma, and Ahkisar rain gauge stations	-	Monthly	1998–2013	(Danacıoğlu and Tağıl, 2019)
	Holocene rainfall	AWI-ESM rainfall simulation (17 grids)	ca. 160 km	Monthly	6000–0 yr BP (BP: before 1950)	(Shi et al., 2022a; 2022b)
C	Landsat 8 OLI	two scenes acquired on 20130714 and 20130721	30 m	-	-	<a href="https://earthexplorer.usgs.gov/">https://earthexplorer.usgs.gov/</a>
	Holocene land use	estimated by the raw count of archaeological sites	-	-	Neolithic to Turkish period	Archaeological investigation
LS	TanDEM-X	topography data for elevation, aspect, and slope	12.5 m	-	-	(Rizzoli et al., 2017; Wessel et al., 2018)
K	Soil Grids soil data 2017	clay, silt, sand, coarse fragments, and organic carbon at 0, 5, 15, and 30 cm b.s.	250 m	-	-	(Hengl et al., 2017)
P	CLC2012	CORINE land cover dataset	100 m	-	2011–2012	(Cole et al., 2018)

**Table 3.4** The classification of the soil erosion and deposition risk based on the USPED model.

USPED value (t ha <sup>-1</sup> year <sup>-1</sup> )	Class
< -10	extreme soil erosion risk
-10 ~ -5	high soil erosion risk
-5 ~ -1	medium soil erosion risk
-1 ~ -0.001	low soil erosion risk
-0.001 ~ 0.001	stable
0.001 ~ 1	low soil deposition risk
1 ~ 5	medium soil deposition risk
5 ~ 10	high soil deposition risk
> 10	extreme soil deposition risk

### 3.6.1 Rainfall–runoff erosivity factor (R)

The rainfall–runoff erosivity factor (R) represents the ability of rainfall and runoff (e.g., from snowmelt water) to initiate soil erosion (Wischmeier and Smith, 1978; Benavidez et al., 2018). It was estimated using the modified Fournier index (MFI) (Equations 3 and 4) (Demirci and Karaburun, 2012).

$$MFI = \sum_{j=1}^N \sum_{i=1}^{12} \frac{p_{ij}^2}{p_j} \quad (3)$$

$$R = 4.17MFI - 152 \quad (4) \quad \text{Buyukcekmece, Türkiye (Demirci and Karaburun, 2012)}$$

where,  $P_{ij}$  (mm) represents the average monthly precipitation for the  $i$ -th month and  $j$ -th year, and  $P_j$  is the annual precipitation for the  $j$ -th year. Equation (4) proposed by Demirci and Karaburun (2012) was selected because their study area is also located in Türkiye.

**Recent times.** Monthly precipitation data between 1998 and 2013 were collected from four local meteorological stations provided by Danacıoğlu and Tağıl (2019) (Table 3.5) to estimate the R factor value for recent times. Two rain gauge stations (Dikili and Bergama) are immediately located within the study area (Figure 7.1), while the two nearby stations (Soma and Akhisar; Figure 1.1) were also included. The spatial distribution of the annual

rainfall data was interpolated from the point data of these stations using inverse distance weighting (IDW) and ordinary kriging methods.

**Mid- to Late Holocene.** For the period of 6–0 ka BP (BP: before 1950), the simulated monthly rainfall data of the AWI-ESM, a state-of-the-art Earth system model that was incorporated in the latest Paleoclimate Modelling Intercomparison Project phase 4 (PMIP4) (Shi et al., 2022a; 2022b) were applied; spatial resolution for one grid/cell accounted ca. 160 × 160 km<sup>2</sup> (Shi et al., 2022b). The IDW and ordinary kriging interpolation were applied on the nearest 17 grids of the Mid- to Late Holocene annual rainfall data (temporal resolution: monthly; time range: 6-0 ka BP; Figure 7.1b) to obtain the spatial distribution of the R factor in the Pergamon micro-region. The simulation of the rainfall factor during the last 6000 years ran for the slices of every 100 years, representing a centennial-scale archaeological period (e.g., approximately only a century for the Late Antiquity in the study area), to reduce computational requirements. Hence, rainfall extreme events occurring on a decadal or shorter timescale were excluded. The results were also compared with the Z score value of climatic conditions in the Mediterranean region by Finné et al. (2019) for the quality control of the rainfall data.

**Table 3.5** Metadata of the four local meteorological stations. \* MAD: median absolute deviation.

Station name	Bergama	Dikili	Soma	Akhisar
Latitude (° N)	27.18	26.89	27.61	27.84
Longitude (° E)	39.12	39.07	39.19	38.92
Elevation (m a.s.l.)	45	3	144	93
Measured period	1998–2013	1998–2013	1998–2013	1998–2013
Median annual precipitation (MAD*)	651 (183)	626 (135)	635 (118)	576 (121)
Median precipitation during May – Oct. (MAD*)	558 (133)	536 (127)	488 (102)	454 (76)
Median precipitation during Nov. – April (MAD*)	126 (51)	117 (56)	133 (57)	123 (44)

### 3.6.2 Cover and management factor (C)

The cover and management (C) factor represents the non-dimensional ratio of soil loss from an area with specified cover and management to that from an identical area under continuously tilled fallow land (Wischmeier and Smith, 1978). It quantifies the impact of

vegetation cover on reducing soil erosion. Higher vegetation cover results in a lower C factor and, consequently, less soil loss risk. Frequently, the C factor is estimated through normalized difference vegetation index (NDVI) derived from satellite imageries (Aiello et al., 2015; Borrelli et al., 2015), or land use and cover data (Benavidez et al., 2018).

**Recent times.** We used the NDVI approach to estimate the C factor during recent times. Two scenes acquired from Landsat 8 OLI on 20130714 and 20130721 (spatial resolution: 30 m; Table 3.3) were chosen because of the low cloud cover. They also represent the annual average NDVI values according to the time-based trend of the NDVI relevant to 8 vegetated land cover classes in Italy (Aiello et al., 2015). The NDVI raster layer for the study area was generated by seamless mosaicking the two scenes and using the following band math equation of band 4 (Red, b4) and band 5 (NIR, b5) in ENVI (v5.3) as follows:

$$NDVI = \frac{(float(b5) - b4)}{(b4 + b5)} \quad (5)$$

$$C = 0.431 - 0.805 \times NDVI \quad (6) \quad \text{Aiello et al. (2015)}$$

The C factor values should range between 0 and 1. Following the suggestions by Borrelli et al. (2015), for pixels with NDVI exceeding 0.535, the C factor values were assigned to 0.003 (a small value close to 0, instead of less than 0) using Reclassify by Table in QGIS (v 3.22) (QGIS Development Team, 2023).

**Mid- to Late Holocene.** The spatial and temporal changes of the cover factor during the Mid- to Late Holocene were estimated based on the human settlement patterns because the raw count and distribution of archaeological sites could investigate the long-term regional trends of the human population (Palmisano et al., 2017; Berger et al., 2019) and the intensity of human activities on the surrounding landscape (Yu et al., 2016). That is to say that different land uses around different settlement sites are supposed to have varying human impacts. Although the estimation may not correspond exactly to the actual C factor values, the relative intensity of the C factor throughout the Mid- to Late Holocene is more important than the precise values.

Only the archaeological sites with known coordinates and chronologies based on the archaeological findings (n = 242) were incorporated (Table 2.1). Based on criteria such as the size and function in the chronological scheme (e.g., Horejs, 2010a; Pirson, 2014; Zimmermann et al., 2015; Ludwig, 2023, and references therein), these sites were classified into three categories: urban, rural, and other sites. Urban sites were assumed to have a higher intensity of landscape exploitation compared to rural or other sites

(Stoddart et al., 2019). The urban sites in the western lower catchments include Pergamon, Elaia, Atarneus, Pitane, Hatipler Kalesi, Gryneion, Aigai, Allianoi, Apollonis / Doidye, Kane (Kanai), Kyme, Perperene, and Thyateira. They only remained as urban sites for a certain time. The rural site contains settlements, watch towers, and fortifications. The other site represents non-settlement sites which also have a limited impact on the surroundings.

The extension of residential, agricultural, and pastoral land use for each site category is different and their corresponding assigned C factor values are listed in Table 3.6. The average residential area in the radius (m) was estimated based on the archaeological survey in this area. For example, the residential area around the urban sites was obtained based on the largest size of Pergamon (Pirson, 2020) and Aterneus (Schneider et al., 2014); the residential area around the rural sites was based on the characters of Tekkedere and Deliktaş settlements (Ludwig, 2019, 2023). The areas for agricultural and pastoral use were determined based on residential sizes according to the calculation developed by Hughes et al. (2018).

**Table 3.6** Parameters used for the application of the C factor. \* The other site in this study represents non-settlement sites which also have a limited impact on the surroundings.

Site category	Average residential area in radius (m)	Average agricultural area in radius (m)	Average pastoral area in radius (m)
Urban site	300	5000	6000
Rural site	100	1800	2500
Other site *	10	750	1750
<b>Assigned C factor</b>	0.09	0.25	0.05

In addition, areas with slope gradients larger than 30° being unsuitable for settlements were excluded (cf. Günther et al., 2021) from the spatial extent of residential, agricultural, and pastoral use. The walking distance for agricultural and pastoral use around the settlement sites is comparable to the application of a modular agent-based modeling platform for socio-ecological dynamics in the Tekkedere settlement (agricultural area: up to 1.5 km from the settlement; pastoral area: 10–15 km from the settlement (Günther et al., 2021)). The unsuitability of floods in the Bakırçay plain which is suggested to be preferred by the pastoralist herders over the more elevated or mountainous regions (Günther et al., 2021) is not considered. The influence of altitude limit and soil/bedrock type on land use (Goodchild, 2007, 2013) was also ignored. The estimated C factor values for different agricultural use was assigned based on the values for degraded land around

Sagalassos, a Hellenistic–Roman city in western Türkiye (Van Loo et al., 2016). The estimated C factor values for the residential and pastoral areas were deduced from the research in Southern Ethiopia (Girma and Gebre, 2020). The remaining non-degraded area was assigned to be 0.0005 as its C factor value (Van Loo et al., 2016).

### 3.6.3 Topographic factor (LS)

Topographical characteristics involve slope length (L) and steepness (S) (Wischmeier and Smith, 1978), playing a crucial role in soil erosion and deposition risk (Benavidez et al., 2018). Steeper and longer slopes generally have a higher risk of soil erosion. To apply the topographic factor (LS) to complex terrains on a watershed scale rather than the original unit plot and field scale, modifications have been made to the original LS factor by taking flow accumulation and slope into account (Benavidez et al., 2018).

**Recent times.** In this study, the TanDEM-X data (Rizzoli et al., 2017; Wessel et al., 2018) were used to perform the LS factor calculation in QGIS (v 3.22) (QGIS Development Team, 2023) as follows (Mitasova et al., 1996; Mitas and Mitasova, 1998):

$$LS = A^m \times (\sin\beta)^n \quad (7)$$

where, A represents the upslope contributing area per unit width, which is equal to the product of flow accumulation and cell size,  $\beta$  denotes the slope in degrees, and m and n are constants of which the values depend on the prevailing soil erosion type (m = 1.6, n = 1.3 for rill erosion, and m = n = 1 for sheet erosion). In this study, sheet erosion was chosen because the semi-arid Mediterranean landscape allows water infiltration (Van Loo et al., 2016).

**Mid- to Late Holocene.** Considering the assumed minimal elevation changes during the Holocene in the study area compared to the present-day situation (cf. Mitasova et al., 2013), the LS factor was assumed to remain constant throughout the time. This is also suggested in a comparable study conducted around the archaeological site of Sagalassos (Van Loo et al., 2016).

### 3.6.4 Soil erodibility factor (K)

The soil erodibility (K) factor refers to the inherent properties of soils that determine the susceptibility to particle detachment and transportation by rainfall and runoff (Wischmeier et al., 1971). High K factor values reveal a high erosional susceptibility of the soil (Benavidez et al., 2018).

**Recent times.** In this study, a set of equations developed by Auerswald et al. (2014) was used to calculate the K factor, which fully emulates the soil erodibility nomograph introduced by Wischmeier et al. (1971). These equations account for various parameters of soil characters, including the relative content of silt and very fine sand, the relative clay content, the content of organic matter, soil structure plus permeability, soil with rock fragments, high organic matter soils, and soils with high silt content or low erodibility (Auerswald et al., 2014). The raster format data of soil data were obtained from Soil Grids (Hengl et al., 2017) at depths of 0, 5, 15, and 30 cm (EPSG: 4326; spatial resolution: 250 m; Table 3.3), including:

- 1) sand (50–1000  $\mu\text{m}$ ), silt (2–50  $\mu\text{m}$ ), and clay (< 2  $\mu\text{m}$ ) (weight %);
- 2) coarse fragments (volumetric %);
- 3) soil organic carbon content ( $\text{g kg}^{-1}$ ).

To obtain the average K factor value within the 0–30 cm depth interval, Equation 8 was applied (Hengl et al., 2017):

$$S = \frac{(5 - 0) \times (S0 + S5) + (15 - 5) \times (S5 + S15) + (30 - 15) \times (S15 + S30)}{30 \times 2} \quad (8)$$

where, S5, S15, and S30 represent the values from the 0–5, 5–15, and 15–30 cm soil depth intervals, respectively. Due to data scarcity for the very fine sand, the relative content of silt plus very fine sand (2–100  $\mu\text{m}$ ) was estimated as the sum of 100% silt content plus 20% sand content (Auerswald et al., 2014). The content of organic matter (in %) was assumed to be 1.72×0.1 times the soil organic carbon content ( $\text{g kg}^{-1}$ ). The soil texture class was determined using the sand, silt, and clay raster layers using the *soiltexture* R package (<https://obrl-soil.github.io/soil-texture-rasters/>, last access: June 2020). The soil classification was based on the USDA soil texture triangle (Soil Survey Division Staff, 1993). The soil structure and permeability index were assigned based on Table S7.1, which was modified from Bagarello et al. (2009). All the required parameters were input into the set of equations by Auerswald et al. (2014) in R to obtain the K factor in SI units ( $\text{t h MJ}^{-1} \text{mm}^{-1}$ ) (Torri et al., 1997). The accuracy of the dataset and results obtained from this procedure were compared with field-based soil samples in the Bakırçay River catchment by Danacıoğlu and Tağıl (2017).

**Mid- to Late Holocene.** During the Holocene, it is assumed that soil characteristics remained relatively constant. Therefore, the same K factor value for recent times was applied for the modeling during the last 6000 years. However, it should be noted that using the recent soil data is not entirely sufficient for predicting ancient soil conditions due to soil loss or degradation (Van Loo et al., 2016).

### 3.6.5 Support practice factor (P)

The support practice (P) factor is a dimensionless measure of prevention that represents the ratio of soil loss under a certain support practice (such as contouring, strip cropping, or terracing) with straight-row farming up and down the slope (Wischmeier and Smith, 1978). It describes how different land uses influence soil erosion and deposition (Benavidez et al., 2018). The P factor ranges from 0 to 1; a higher value indicates less effective soil conservation and greater soil loss.

**Recent times.** In this study, the P factor for recent times was estimated based on the Corine land cover data (Cole et al., 2018). Different land cover was assigned with different P factor values (Table S7.2).

**Mid- to Late Holocene.** Considering the assumption that in the study area no special support practices were implemented during the Holocene, a value of 1.0 for the P factor was assigned throughout the last 6000 years, as also suggested by Benavidez et al. (2018) and references therein.

### 3.6.6 Model validation

To validate the performance of the USPED modeling in recent times, field observations were conducted in the Tekkedere and Deliktaş catchments, focusing on the areas characterized by high soil erosion (Figure 7.2). By comparing the soil erosion and deposition risk in recent times with the risk over the past 6000 years, a better understanding of the model's accuracy and its ability to capture long-term trends are highlighted.

The results of the USPED model for the Holocene soil erosion and deposition risk were primarily compared with a combination of reconstructed sedimentation rate based on an updated meta-data analysis (Becker et al., 2020a) and sediment archives from the Tekkedere and Deliktaş catchments (Figure 3.1). The updated meta-data analysis of the cumulative probability functions was applied to the  $^{14}\text{C}$ -ages ( $n = 140$ ) obtained from 38 sediment sequences, primarily from the colluvial and alluvial environments in the western lower Bakırçay plain (Becker et al., 2020a).



## 4. The geomorphological characteristics of the Pergamon micro-region

Working package 1

**An overview of the geomorphological characteristics of the Pergamon micro-region (Bakırçay and Madra river catchments, Aegean region, west turkey)**

**Published manuscript:** Yang, X., Becker, F., Knitter, D., Schütt, B., 2021. An Overview of the Geomorphological Characteristics of the Pergamon Micro-Region (Bakırçay and Madra River Catchments, Aegean Region, West Turkey). *Land* 10, 1–27.

<https://doi.org/10.3390/land10070667>.

This article is an open access article distributed under the terms and conditions of the Creative Commons Attribution (CC BY) license (<https://creativecommons.org/licenses/by/4.0/>).

**Supplementary materials:** see Supplementary materials – To chapter 4 (working package 1). The supplementary materials were originally published online at <https://www.mdpi.com/article/10.3390/land10070667/s1>.

**Keywords:** geomorphological map; geomorphometry; geomorphodynamics; human–environment interaction

**Abstract:** Current landforms are the basis for understanding past geomorphodynamics and human activities. Based on multiple materials and methods, including geomorphometric analyses of a digital elevation model and visual interpretations of satellite images, different landscape units of the Bakırçay and Madra River catchments in the environs of ancient Pergamon are described. The area was mainly shaped by tectonics that formed a horst-and-graben structure; small Miocene horsts and NE-trending subgrabens in the Kozak and Yunt Dağı Mountains were separated by the NEE-trending Plio-Pleistocene Bergama Graben. The asymmetry in relief, drainage network, and sediment accumulation between the Kozak Mountains to the north and the Yunt Dağı Mountains to the south of the lower Bakırçay plain characterize the Pergamon Micro-Region. The regional relief characteristics, with wide flat basin and plateau areas, are suitable for agriculture. Complemented by its richness in natural resources, the Pergamon Micro-Region became a preferred settlement area, with evidence of human impact since the Hellenistic–Roman period at the latest. As a consequence of settlement activities, several landscape engineering measures were implemented simultaneously with a parallel change in morphodynamics.

## 4.1 Introduction

The Aegean Region of Turkey (Ege Bölümü) is characterized by a number of mountain ranges below ca. 2500 m a.s.l. that are dissected by several large east–west oriented valleys (Figure 4.1B) (Kayan, 1999). Sediments transported and deposited by rivers caused the development of alluvial plains and large prograding deltas (Kayan, 1999; Kayan and Vardar, 2007a; Kuzucuoğlu et al., 2019b). Abundant prehistoric and historic settlements were built on and along these valleys and deltas; for example, Troy in the Karamenderes valley (Kraft et al., 1980; Kayan, 1997; Kraft et al., 2003; Kayan, 2019); Pergamon and its rural settlements in the Bakırçay valley (Knitter et al., 2013; Schneider et al., 2013; Schneider et al., 2014; Schneider et al., 2015; Schneider et al., 2017); Phocaea and Smyrna at the former mouth of the Gediz River (Kayan, 1997); Ephesus in the Küçük Menderes valley (Kayan, 1997; Kraft et al., 2007; 2011; Stock et al., 2013); and Miletus in the Büyük Menderes valley (Kayan, 1997; Brückner et al., 2006; Knitter et al., 2013).

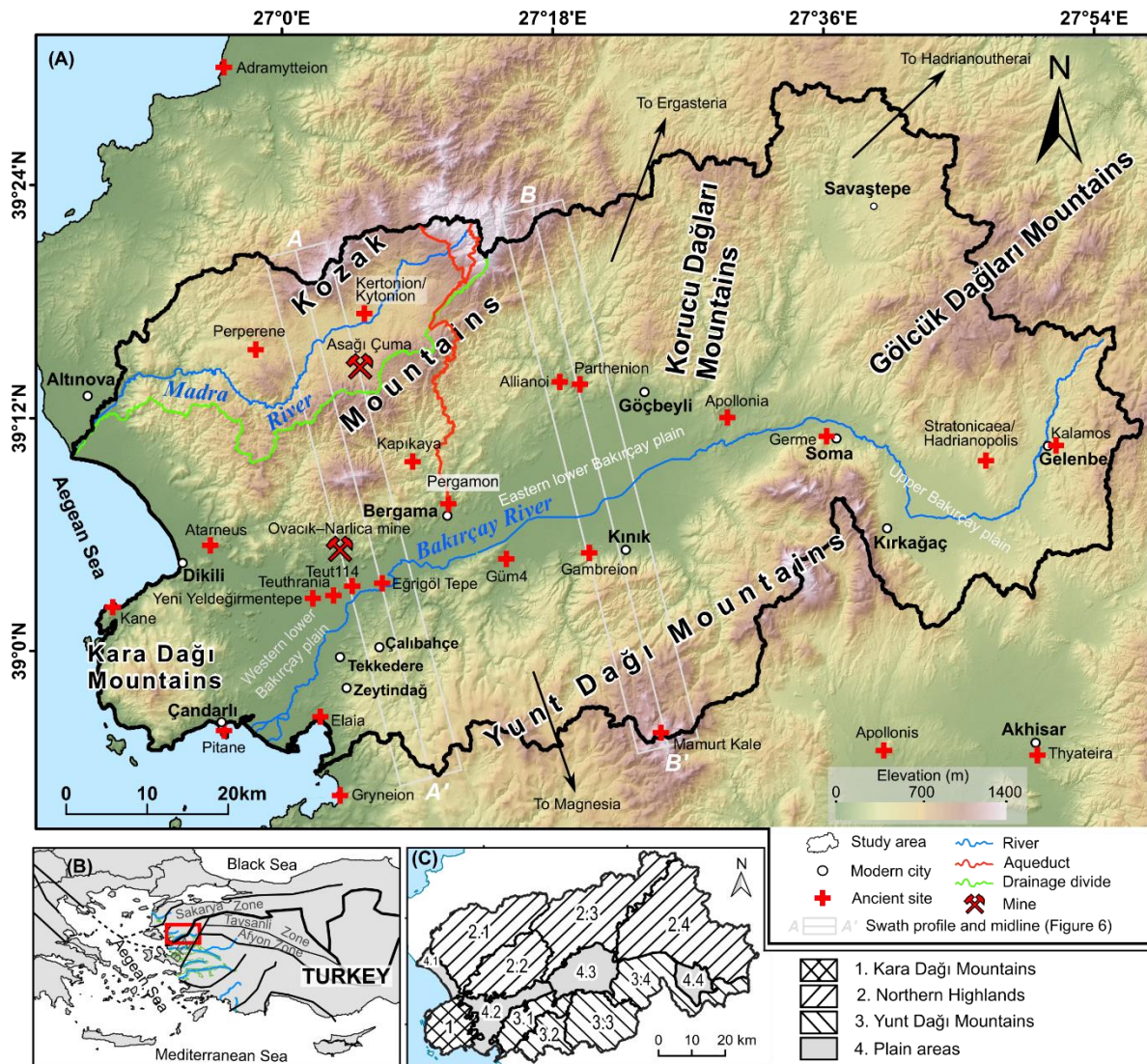


**Figure 4.1 (A)** Overview map of the Pergamon Micro-Region (Bakırçay and Madra River catchments and the adjacent coastal areas). Data: (1) ancient site (Horejs, 2011a; Knitter, 2013; Schneider et al., 2014; Schneider et al., 2015; Schneider et al., 2017; Ludwig, 2020b); (2) aqueduct: The Atlas Project of Roman Aqueducts (<https://www.romaq.org/the-project/aqueducts/article/692#tab-details>, last accessed 8 June 2021) (Radt, 2016) (p. 150); (3) mine site (Yılmaz et al., 2007; Russell, 2013b); (4) elevation data: TanDEM-X digital elevation model (12-m horizontal resolution) (Rizzoli et al., 2017; Wessel et al., 2018). **(B)** The location of the study area (red rectangle), highlighted with the major westward-trending rivers (blue lines) and their alluvial plains (green polygons) along the Aegean coastal region of west Turkey (modified from Kayan (1999)), and the major tectonic structures (shown as black thin lines in the west of Anatolia and dashed lines linked to the sutures across the Aegean Sea) and tectonic zones (black thick line: the İzmir–Ankara Suture Zone; BFZ: Bornova Flysch Zone) modified from Okay (2008)). **(C)** Geomorphological units and subunits of the Pergamon Micro-Region.

The current study focuses on one of these valleys, the Bakırçay valley, which is directly related to the Pergamon Micro-Region. This microregion has been settled at least since the Neolithic period (Pavúk and Horejs, 2018). The site of Pergamon, on the hilltop northeast of modern Bergama (Figure 4.1A), had already become a polis by the fourth century BC and then became the capital of the Kingdom of Pergamon in 281–133 BC.

Pergamon doubled its size prior to the beginning of the third century and subsequently the decline had already set in (Pirson, 2015; Laabs and Knitter, 2021). The Hellenistic–Roman urban center of Pergamon (a UNESCO World Heritage site) and its micro-region have been intensively studied, predominantly from the archaeological point of view, since the end of the 19th century (Lolling, 1879; Philippson, 1912; Kökten, 1949; Sommerey, 2008; Horejs, 2010b; Pirson, 2015; Pirson et al., 2016). More recently, geoarchaeological research has been integrated, focusing on selected archaeological sites and related subbasins along the western lower Bakırçay plain (Schneider et al., 2013; Seeliger et al., 2013; Schneider et al., 2014; Seeliger et al., 2014; Pint et al., 2015; Schneider et al., 2015; Shumilovskikh et al., 2016; Schneider et al., 2017; Seeliger et al., 2017; Seeliger et al., 2019; Becker et al., 2020a; Mecking et al., 2020) and the neighboring Madra River delta (Lambrianides and Spencer, 2007).

The majority of prehistoric and ancient settlements in the Pergamon Micro-Region were located in the transitional areas between the mountains and alluvial plains or along flat unconfined valleys (Figure 4.1A) (Horejs, 2011a; Knitter, 2013; Knitter et al., 2013; Schneider et al., 2014; Schneider et al., 2015; Schneider et al., 2017; Ludwig, 2020b). These areas appear to be particularly suitable for the foundation of human settlements and for local supplies and route networks. They are relatively flood-protected, adjacent to fertile plains for agriculture and to mountainous hinterland for horticulture and pastoralism (Knitter, 2013; Schneider et al., 2014; Ludwig, 2020b). Examples include the Greek polis Atarneus (from the sixth to the fourth century BC) in the southwestern Kozak Mountains (Schneider et al., 2013; Schneider et al., 2014) and the Late Chalcolithic/Byzantine settlement Güm4 in the northern Yunt Dağı Mountains (Figure 4.1A) (Horejs, 2011a; Knitter, 2013). However, some of the original flood-safe areas became prone to flooding because of continuous aggradation of the lower Bakırçay plain and occasionally flood episodes, e.g., the site Teut114 after the 1st century CE (Schneider et al., 2015) and the Late Chalcolithic to Bronze Age settlement Yeni Yeldeğirmentepe (Schneider et al., 2017) in the western lower Bakırçay plain. In addition to the settlements adjacent to the main Bakırçay alluvial plain, prehistoric sites were located on or close to the coast during the Middle Holocene, when alluvial and colluvial conditions began to dominate the littoral areas (Kayan, 1999). The settlements on the Madra River delta and around the Bakırçay River delta are prominent examples (Lambrianides and Spencer, 2007; Seeliger et al., 2013; Seeliger et al., 2019). Flourishing in a sheltered position, the Greco-Roman harbor city of Elaia (Figure 4.1A) avoided the presumably high sedimentation of the Bakırçay River (Seeliger et al., 2013; Seeliger et al., 2019). Several ancient human settlements and archaeological remains have been documented in the mountains adjoining the lower

Bakırçay plain (Pirson et al., 2016; Pirson, 2019; Ludwig, 2020b), which, however, lack systematic geoarchaeological research.

Previous geomorphological and sedimentological studies indicate not only the environmental potential for human activities, but also the Holocene local morphodynamics in the western lower Bakırçay plain and the adjacent piedmonts. Moreover, a meta-data analysis of the  $^{14}\text{C}$ -ages from site-related sediment sequences reconstructed several phases of increased geomorphodynamics during the Holocene, which are presumably related to multiple triggers such as climate, population dynamics, and local settlement history (Becker et al., 2020a).

Large spatial-scale geological studies in western Anatolia—regarding the Miocene-Quaternary grabens and their deposits (Yilmaz et al., 2000; İnci, 2002; Kaya et al., 2007; Sanğu et al., 2020), Miocene volcanism (Borsi et al., 1972; Karacik et al., 2007), and river responses to Quaternary tectonics (Kuzucuoğlu, 1995; Kayan, 1999; Okay, 2008)—indicate a complex tectonic-dominated landscape of uplands (mainly as horsts) and plains (mainly as grabens).

The morphological complexity of a landscape in a catchment subsequently influences the sediment connectivity (Baartman et al., 2013). Landscape configuration controls where and how long the sediments are stored (Fryirs et al., 2007; Fryirs, 2013). Wider valleys have larger accommodation spaces for sediments to be stored within the catchment and less in the basin outlet (Fryirs, 2013), which could promote landscape stability. Combined factors of neotectonics (Sanğu et al., 2020), cycles of climate (Finné et al., 2019) and sea level changes (Kayan, 1999; Seeliger et al., 2017), vegetation degradation, and increased human activities (Shumilovskikh et al., 2016; Becker et al., 2020a) are able to increase sediment and landscape dynamics (Fryirs et al., 2007; Fryirs, 2013), and, consequently, shape the local geomorphology (Dusar et al., 2011; Roberts et al., 2019a).

An identification of geomorphological characteristics forms the basis for a reconstruction of geomorphodynamics, which allows insights to be gained into the distribution of human activities in a landscape, including ancient human settlements and route networks. Despite the previously mentioned site-related geoarchaeological, regional, and supra-regional geological and paleoenvironmental studies, geomorphological characterizations of the Bakırçay and Madra River catchments in the environs of ancient Pergamon are currently lacking. Therefore, our main objectives are (a) to provide a catchment-scale overview and (sub)unit comparison of current landforms in the Bakırçay and Madra River catchments based on geomorphological mapping and geomorphometric analyses; and (b) to assess potential drivers of landscape dynamics and to infer the consequences for

different landscape units. On this basis, the attractiveness and appropriateness of the Pergamon Micro-Region as a preferred settlement area since Hellenistic times are sketched.

## **4.2 Natural Characteristics of the Pergamon Micro-Region**

### **4.2.1 Geographical Setting**

The study area comprises the Bakırçay River catchment (ca. 3382 km<sup>2</sup>) and the neighboring Madra River catchment (ca. 382 km<sup>2</sup>), and the adjacent coastal areas along the Aegean Sea (Figure 4.1A). It includes the major part of the Pergamon Micro-Region (Laabs and Knitter, 2021), where important natural resources (such as stone as a building material, clay for ceramic production, soil for agricultural production, and water as a daily necessity) have been utilized to supply the city of Pergamon (Lambrianides and Spencer, 2007; Tassios, 2007; Ludwig, 2020b). Located between 38°54'–39°29' N and 26°48'–27°57' E, this area extends approximately 100 km in E–W direction and 66 km in N–S direction, covering an area of ca. 4124 km<sup>2</sup>.

To the north, the divide between the Bakırçay and Madra River catchments (Figure 4.1A) runs along the southern range of the Kozak Mountains (Kuzucuoğlu, 1995; Macklin et al., 1995; Seeliger et al., 2014) (in other studies, the mountains are also mentioned as Mount Kozak (Yılmaz et al., 2000), Madra Mountain (Lambrianides and Spencer, 2007), Madra Dağı (Ludwig, 2020b; Sanğu et al., 2020) or Pindasos (Laabs and Knitter, 2021)), the Korucu Dağları Mountains, and the Gölcük Dağları Mountains (MTA, 2002). To the south, the divide of the Bakırçay River runs along the northern range of the Yunt Dağı Mountains (Figure 4.1A) (i.e., Yüntdağ Mountains (Yılmaz et al., 2000; Seeliger et al., 2013), Yüntdağ Mountain Complex (Seeliger et al., 2019), Yunt Mountains (Sanğu et al., 2020), Yunt Dağı (Ludwig, 2020b) or Aspordenon (Laabs and Knitter, 2021)). The Kara Dağı Mountains (i.e., Kara Dağ massif (Schneider et al., 2014) or Dikili–Çandarlı high (Karacik et al., 2007)) on the Kane Peninsula (Ludwig, 2020b) are located west of the Bakırçay plain (Seeliger et al., 2019).

The Bakırçay River (the ancient Kaikos) is one of the E–W oriented graben-related rivers of the Aegean Region in Turkey (Aksu et al., 1987; Kayan, 1988; Aksu et al., 1990; Kayan, 1997) (Figure 4.1B). It originates from the Kocadağ (in the Gölcük Dağları Mountains; Figure 4.1A). After flowing through the upper and the (eastern and western) lower

Bakırçay alluvial plain, it enters into the Aegean Sea and develops a delta between Zeytindağ (west Yunt Dağı Mountains) and Çandarlı (south Kara Dağı Mountains) (Figure 4.1A). Its natural channel pattern changes from braided in the middle reaches to meandering in its lower reaches (Aksu et al., 1987; Schneider et al., 2017). The Madra River drains through the intramountainous basin of the Kozak interior plain and it incises the steep valley in the western Kozak Mountains (Figure 4.1A). After passing through the Altınova–Dikili littoral plain, deposits of the Madra River form a delta in the Aegean Sea (Lambrianides and Spencer, 2007), smaller than the Bakırçay delta.

#### **4.2.2 Tectonic, Bedrock, and Soil**

Geologically, the study area belongs to the westward-drifting Aegean–Anatolian microplate (Okay, 2008; Vacchi et al., 2014), comprised by the Sakarya Zone in the north and Bornova Flysch Zone in the south (Figure 4.1B) (Okay, 2008). Among these continental zones is the NE-trending İzmir–Ankara Suture Zone (IASZ) (Figure 4.1B) (Okay, 2008; Sanğu et al., 2020). NE-trending dextral strike slip faults of the North Anatolian Fault System and N–NW-trending extension of the Aegean Extensional System simultaneously controlled the tectonic structures in this area (Sanğu et al., 2020). Several horsts and grabens formed under the tectonic paleostress, e.g., the Kozak Horst, the Miocene Zeytindağ and Örenli–Eğiller grabens, and the Plio-Pleistocene Bergama and Ayvalik–Lesvos grabens (Figure 4.2) (Altunkaynak and Yılmaz, 1998; Kuzucuoğlu et al., 2019a; Sanğu et al., 2020). The Bergama Graben continues to subside at an average rate less than 1 cm per 1000 years (Aksu et al., 1987; Seeliger et al., 2017). The tectonic stress caused severe earthquakes during the last two millennia, for example, the Çandarlı earthquake in 105 CE (Emre et al., 2005), the Dikili earthquake in 1939, and the Göçbeyli earthquake in 1919, the magnitudes of the latter two being  $\geq 6.5$  (Paradisopoulou et al., 2010) (Figure 4.2). Within its western sector, several Miocene volcanic domes (Turkish tepe, hills) rise from the Bakırçay plain (Borsi et al., 1972). Faults are mainly found in three zones, viz., the Altınova–Dikili fault zone (Figure 4.2: ①), the Zeytindağ–Bergama fault zone (Figure 4.2: ②), and the Soma–Kırkağaç fault zone (Figure 4.2: ③) (Emre and Doğan, 2010; Emre et al., 2011a; Emre and Özalp, 2011; Emre et al., 2011b). The latter two zones are dominated by normal faults that were active during the Holocene (Figure 4.2).

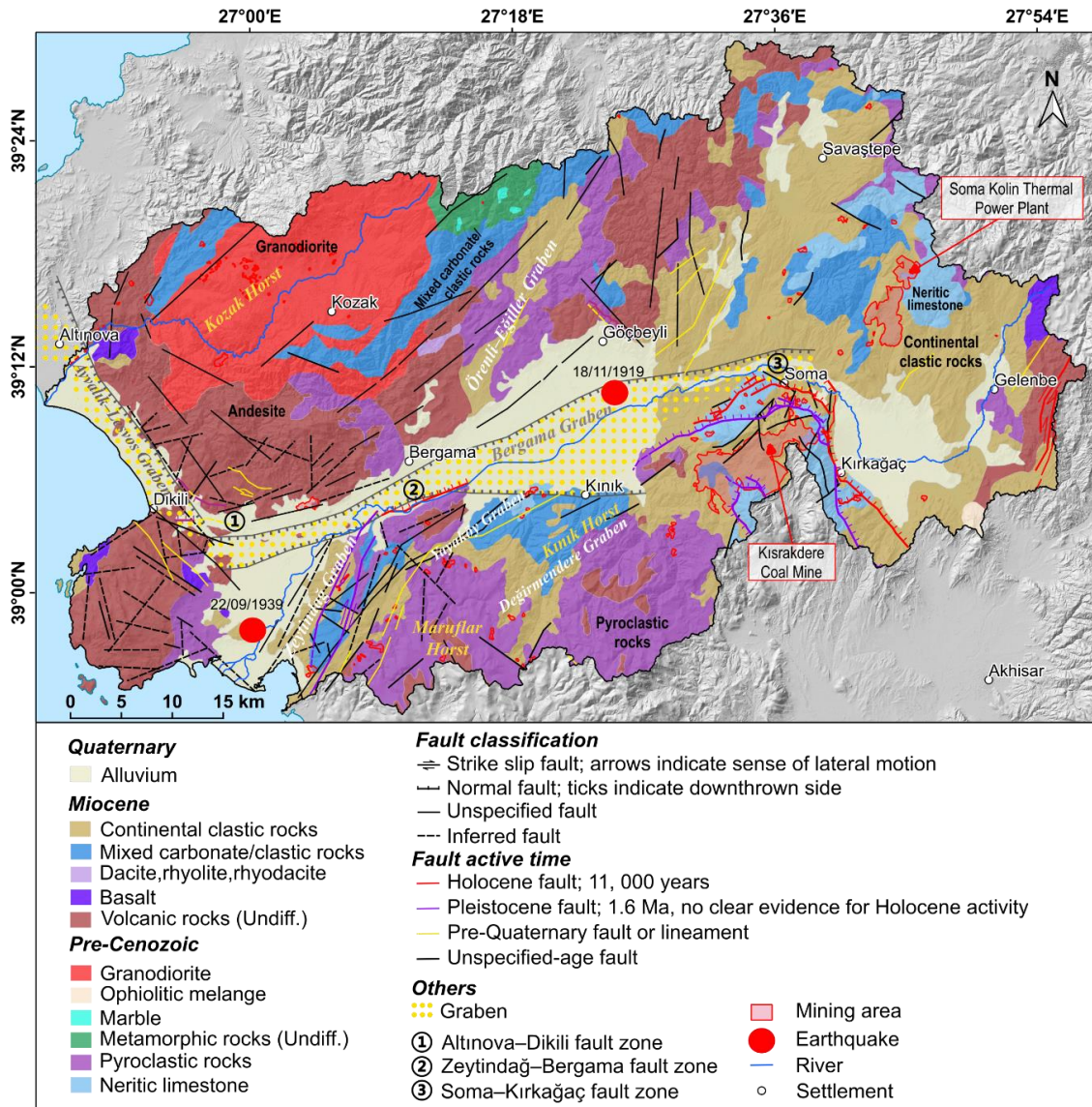


**Figure 4.2** Geological map of the Bakırçay and Madra River catchments and their adjacent coastal areas. Data: 1) bedrock: Geological Map of Turkey, 1:500,000 (İzmir) (MTA, 2002); 2) fault: 1:250,000 scale Turkey Active Fault Maps (Emre and Doğan, 2010; Emre et al., 2011a; Emre and Özalp, 2011; Emre et al., 2011b) and the unspecified-age fault (black line) (Yılmaz et al., 2000; MTA, 2002; Ölgün, 2004); 3) location of graben, horst, and fault zones (Yılmaz et al., 2000); 4) mining area: Google Earth satellite images (WorldView-2, last accessed 8 June 2020); 5) earthquake epicenter of  $M \geq 6.5$  since 1900 (Paradisopoulou et al., 2010).

Pre-Miocene granodioritic rocks form the core of the Kozak Mountains and are surrounded by Mesozoic metamorphic rocks, Miocene carbonate rocks, and volcanic formations (MTA, 2002) (Figure 4.2). The volcanic units are dominated by andesites, basalts, and pyroclastic rocks. The latter rock can also be found at the western Yunt Dağı Mountains, e.g., the Maruflar Horst (Figure 4.2). Miocene continental clastic rocks were deposited at the outer belt of the Kozak Horst, mostly covering the old carbonate rocks in the Gölcük Dağları Mountains and some at the depressions in the Yunt Dağı Mountains (MTA, 2002) (Figure 4.2).

The formation of different soils in this area mainly depends on lithology and vegetation cover (Erlat, 2007). The predominant soil types are Cambisols–Leptosols in the mountains and Fluvisols in the alluvial plains (Danacioğlu and Tağıl, 2017; Kapur et al., 2017). Beyond these, brown forest soils, which dominantly formed on granodiorite parent materials, are the most common soil type in the Kozak Mountains; Rendzinas are mainly distributed on calcareous-rich sedimentary bedrocks (Erlat, 2007). In the area along Soma–Kırkağaç, Luvisols prevail (Danacioğlu and Tağıl, 2017; Kapur et al., 2017).

### 4.2.3 Climate

Located in the Aegean Region, the study area has a typical Mediterranean subhumid climate (Akman and Ketenoğlu, 1986). The area is characterized by dry and hot summers, and mild and wet winters (“Csa” climate according to the Köppen–Geiger classification (Peel et al., 2007)). Between 1981 and 2010, the annual temperature averaged 16.2 °C in Dikili and 14.7 °C in Bergama, and the annual precipitation averaged 711 mm in Dikili and 749 mm in Bergama (Figure 4.3). At both locations, most rain falls in December and January, reaching 140 mm per month; the dry period spans from May to October (Figure 4.3). The maximum precipitation recorded at the meteorological station in Dikili between 1939 and 1996 totaled 183 mm within 24 h (Erlat, 2007).

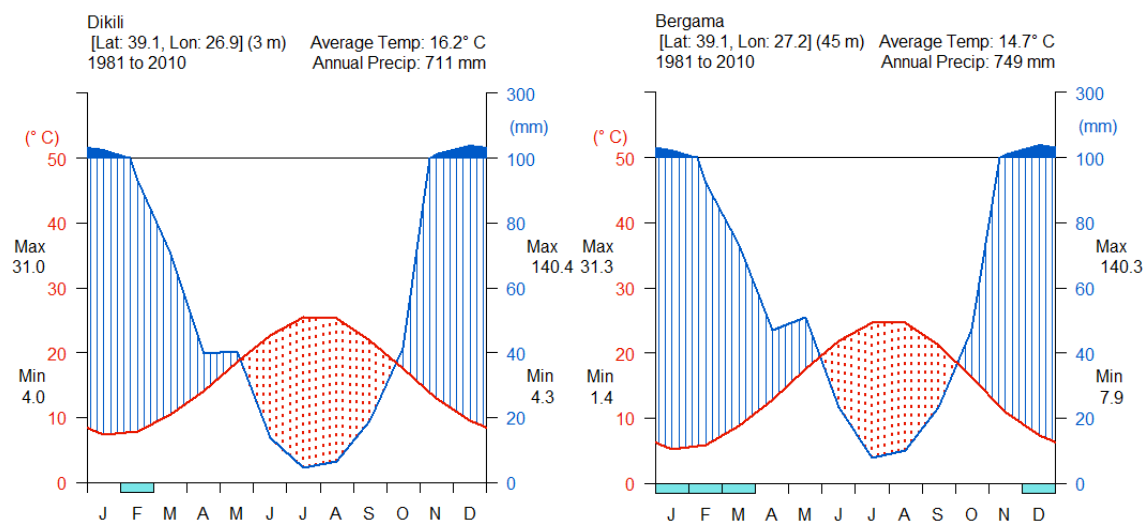


**Figure 4.3** Climate diagrams of Dikili and Bergama (reference period: 1981–2010), showing Mediterranean subhumid climate with arid conditions prevailing during summer months and extreme rainfall during winter months. Data: Climatic Research Unit (CRU) (database: [http://data.ceda.ac.uk/badc/cru/data/cru\\_ts/cru\\_ts\\_4.01/data](http://data.ceda.ac.uk/badc/cru/data/cru_ts/cru_ts_4.01/data), last accessed 8 November 2020) (Harris et al., 2014).

Between 9 and 3 ka BP, climate conditions in the eastern Mediterranean became gradually drier after the relatively wet early Holocene; the period between 6 and 3 ka BP

appears to have been the driest period during the Holocene (Finné et al., 2019). More rapid (centennial-scale) climate change events were interspersed around 6.7–6.3 ka BP, 4.5–4.3 ka BP, and 3.5–3.3 ka BP in the Mediterranean (Finné et al., 2019). During the past three millennia, the hydroclimate became slightly wetter (Roberts et al., 2019a). Climate changes, particularly rapid climate change events, are assumed to be in chronological agreement with major archaeological turnover events in the Aegean/Levantine region (Rohling et al., 2019).

#### **4.2.4 Vegetation**

During the early Holocene (9500–8500 yr BP), the landscape ecology in the Mediterranean region remained stable with the forest extent reaching a maximum (Roberts et al., 2019a). The gradual decline in forest between 7500 and 3000 yr BP was impacted both by climate change and human activities; subsequently, the landscape has continued to be subject to anthropogenic pressure (Roberts et al., 2019a). Now, the remnants of the natural vegetation cover have retreated to steep valley sites (Figure S4.6, Corine Land Cover data (Cole et al., 2018)), appearing predominantly as contracted vegetation (Erlat, 2007).

Present-day vegetation cover in the study area is Thermo-Mediterranean (Akman and Ketenoğlu, 1986) or Eu-Mediterranean type (Shumilovskikh et al., 2016). Forest communities and shrub formations (woody shrubs with evergreen leaves: maquis, and xerophyte bushes and thorns: garrigue) of the Mediterranean region are widespread in the mountainous areas (Kuzucuoğlu et al., 2019b). Dense forest (mainly coniferous forest) is dominant in elevations above 500 m a.s.l. at the outer belt of the Kozak intramountainous basin and the eastern Yunt Dağı Mountains (Figure S4.6). Stone pine forests (*Pinus pinea*) occur in the Kozak Mountains in elevations between 600 and 700 m a.s.l. (Erlat, 2007). Shrub and herbaceous vegetation associations are widespread in the Kara Dağı Mountains at 200 and 500 m a.s.l. The western slopes of the Kozak Mountains and the Maruflar Horst (in Yunt Dağı Mountains) are intensively used for grazing (Lambrianides and Spencer, 2007; Schneider et al., 2014) (Figure S4.6). The Zeytindağ Graben (the western Yunt Dağı Mountains) and the margins of the upper Bakırçay plain (Soma–Kırkağaç area) are largely cultivated with olive trees (Figure S4.6). Common vegetation of the Bakırçay and Madra alluvial plains comprises cash crops, mainly cotton and vegetables (Erlat, 2007; Kuzucuoğlu et al., 2019b). Sporadically, crops are also cultivated in intramountainous basins and infilled valleys (Figure S4.6).

## **4.3 Materials and Methods**

### **4.3.1 Survey of Geomorphological Features**

Major geomorphological features were mapped using QGIS 3.8 (QGIS Development Team, 2020), supported by a literature review, field observations, visual interpretations of freely available high-resolution satellite images provided by Google Earth (<1 m resolution; DigitalGlobe, Inc., maps.google.com, last accessed 8 June 2020), and geomorphometric derivatives from TanDEM-X data (Rizzoli et al., 2017; Wessel et al., 2018) (Section 3.2.). Their subdivisions with definition and classification rules are summarized in Table S4.1 (Walstra et al., 2009). The materials used for interpretation and field photos of each landform unit are provided in Supplementary materials Figures S4.1–S4.7.

Rivers were digitalized from topographic and geological maps (Emre and Doğan, 2010; Emre et al., 2011a; Emre and Özalp, 2011; Emre et al., 2011b). Please note that the field observations were mainly conducted in the lower Bakırçay plain and its surrounding mountains, whereas the validation of the results from other areas is mostly based on the literature (e.g., Yilmaz et al., 2000; İnci, 2002; Karacik et al., 2007).

### **4.3.2 Extraction of Basic Geomorphometric Parameters**

Based on a digital elevation model derived from TanDEM-X data (12 m horizontal resolution; please note that the elevations received from the TanDEM-X are ellipsoidal heights; the undulation of the geoid is around 40 m at the coast (Rizzoli et al., 2017; Wessel et al., 2018)), selected geomorphometric analyses (Hengl and Reuter, 2009) were conducted using various modules implemented in GRASS GIS (GRASS Development Team, 2020) and SAGA GIS (v 2.1) (Conrad et al., 2015) in QGIS 3.8 (QGIS Development Team, 2020). Computed geomorphometric derivatives were shaded relief, slope, geomorphons, aspect, Topographic Position Index and Topographic Wetness Index (Table 4.1). Zonal statistical analyses of geomorphological subunits were processed using the Zonal statistics module in QGIS 3.8 (QGIS Development Team, 2020).

To obtain information on the major channel courses, river longitudinal profiles (Rhoads, 2020) (pp. 294–312) were extracted for several major river courses from the TanDEM-X data (Emre and Doğan, 2010; Emre et al., 2011a; Emre and Özalp, 2011; Emre et al., 2011b). Noise in the river longitudinal profiles caused by reservoirs was manually excluded. Knickpoints were identified manually as inflexion points of the river longitudinal profiles.

**Table 4.1** Geomorphometric derivatives (based on TanDEM-X data (Rizzoli et al., 2017; Wessel et al., 2018)) used for the identification of landforms in this study.

Derivate	Module	Interpretation
Shaded relief	Hillshade	Shaded relief representation of the terrain surface.
Slope	r.slope.aspect (Hofierka et al., 2009)	The slope angle of a raster pixel.
Geomorphons	r.geomorphon * (Jasiewicz and Stepinski, 2013)	A recognition approach for the classification and mapping of the ten most common landform elements.
Aspect	r.slope.aspect (Hofierka et al., 2009)	The slope orientation of a raster pixel.
Topographic Position Index	topographic position index (TPI) (Guisan et al., 1999; Weiss, 2001)	Comparison of each raster pixel's elevation to the mean elevation of a specified neighborhood around that pixel.
Topographic Wetness Index	r.topidx (Beven and Kirkby, 1979; Moore et al., 1991; Mattivi et al., 2019)	The capacity of a raster pixel to accumulate water.

\* Regarding the parameters of r.geomorphon in this study, the outer search radius was set to be 1000 m, the inner search radius 50 m, and the flatness threshold 3 degrees. Geomorphon classes in the main text are shown in italics. Settings for other derivatives remained at default values.

To assess the shape of a mountain front, the mountain-front sinuosity index ( $S_{mf} = L_{mf} / L_s$ ; where  $L_{mf}$  is the planimetric length of a mountain front along the footslope which is at the topographic break in slope, and  $L_s$  is the length of a straight line at the former mountain front) was applied and calculated in QGIS 3.8 (QGIS Development Team, 2020). This represents the straight mountain front produced by active tectonics when the  $S_{mf}$  value is low, and sinuous or eroded front due to erosive processes and less active tectonics when the  $S_{mf}$  value is high (Bull, 2007; Mahmood and Gloaguen, 2012).

Two swath profiles (Figure 4.1A: profiles A–A' and B–B'), i.e. the mean, maximum, and minimum elevation of equally spaced rectangles (here 500 × 6000 m) along the profile line (midline) (Telbisz et al., 2013), were calculated using GRASS GIS modules (v.mkgrid, v.rast.stats, and v.to.points) via QGIS 3.8 to determine topographic differences.

## 4.4 Results

### 4.4.1 General Geomorphological Characteristics

The relief of the Bakırçay and Madra River catchments and their adjacent coastal areas can be grouped into three major landform types: (1) upland landforms including ridge, slope with debris cover and with bare rock, and valley with or without fluvial infill, (2) lowland landforms, and (3) anthropogenic landforms (Figure 4.4).

In the mountainous areas, upland landforms prevail, of which ridges and slopes with debris cover dominate. Outcropping bare rocks occur locally. Most of the perennial and intermittent river valleys are filled with fluvial deposits, whereas their tributary valleys in general have distinctly steeper inclining stream beds than the receiving streams and lack fluvial infills. Furthermore, anthropogenic landforms including reservoirs, mines, and agricultural terraces are widespread in the mountainous area. Alluvial landforms refer to the plains aggraded by the Bakırçay River; paleochannels in the lower Bakırçay plain document the anastomosing character of the Bakırçay River before straightening and embanking. To drain the lower Bakırçay plain, a wide network of canals was installed. The coastal areas are characterized by littoral plains and the deltas of Bakırçay and Madra Rivers. In the transition to the plain areas, the footslopes are fringed by colluvial deposits, locally interfingering with fan deposits from mountain rivers.

The entire area of the Bakırçay and Madra River catchments has a mean elevation of ca. 377 m ( $\sigma = 233$  m) with an elevation range of ca. 1432 m (Table 4.2). Corresponding to the mountainous relief, slope inclination averages around  $12^\circ$  with steep slopes regularly exceeding  $10^\circ$  in the mountains and flat–gentle terrain less than  $3^\circ$  in the plain areas (Table 4.2; Figure 4.5A). Landform units as displayed by geomorphons are dominated by slopes and spurs in the mountainous areas whereas the geomorphon *flat* prevails in plain areas (Figure 4.5B). All of these geomorphometric parameters clearly show spatial diversities in different (sub)units (Figures 4.5 and S4.7).

Our results show extensive asymmetrical features of Bakırçay and Madra River catchments, as evident in their geomorphometric characteristics. In particular, the asymmetry between the Northern Highlands and the Yunt Dağı Mountains surrounding the (western and eastern) lower Bakırçay plain is pronounced (Figure 4.6). The swath profile characterizes the asymmetry between the mountains surrounding the western lower Bakırçay plain (Figure 4.6: profile A-A'), viz., the Kozak Mountains to the north, and the western Yunt Dağı Mountains to the south. The eastern lower Bakırçay plain, with the

Northern Highlands adjoining to the north and the eastern Yunt Dağı Mountains adjoining to the south (Figure 4.6: profile B-B'), is also asymmetrical, although with less-distinct geomorphological features.

**Table 4.2** Geomorphological parameters in the four geomorphological units and their subunits of the study area (see Figure 4.1C for the (sub)units).

Geomorphological (Sub)Units	Area (km <sup>2</sup> ) (Percentage)	Mean Elevation* (m) (Elevation Range (m))	Slope (°) (σ)	TWI (σ)	
Total area	4124 (100%)	377 (1432)	11.6 (9)	6.4 (1.7)	
Kara Dağı Mountains	198 (5%)	221 (860)	11.3 (8)	6.7 (1.7)	
Northern Highlands	2	2320 (56%)	452 (1387)	13.7 (9)	6.1 (1.7)
	2.1	516 (13%)	529 (1337)	13.7 (8)	5.9 (1.7)
	2.2	332 (8%)	437 (1110)	18.3 (9)	5.8 (1.7)
	2.3	644 (16%)	436 (1171)	14.8 (8)	6.1 (1.6)
	2.4	829 (20%)	423 (880)	10.9 (8)	6.5 (1.7)
Yunt Dağı Mountains	3	988 (24%)	411 (1249)	12.9 (9)	6.4 (1.7)
	3.1	179 (4%)	187 (423)	9.6 (6)	6.6 (1.7)
	3.2	145 (4%)	516 (1038)	11.1 (7)	6.2 (1.6)
	3.3	310 (8%)	427 (1152)	15.5 (8)	6.4 (1.8)
	3.4	354 (9%)	423 (742)	12.9 (10)	6.9 (1.5)
Plain areas	4	618 (15%)	92 (349)	1.9 (3)	6.9 (1.8)
	4.1	64 (2%)	53 (183)	2.1 (3)	6.9 (1.8)
	4.2	219 (5%)	55 (229)	2.2 (3)	6.9 (1.8)
	4.3	240 (6%)	88 (182)	1.4 (4)	6.9 (1.7)
	4.4	94 (2%)	213 (133)	1.7 (2)	7.0 (1.8)

\*Elevation: ellipsoidal height, based on TanDEM-X data (Rizzoli et al., 2017; Wessel et al., 2018).

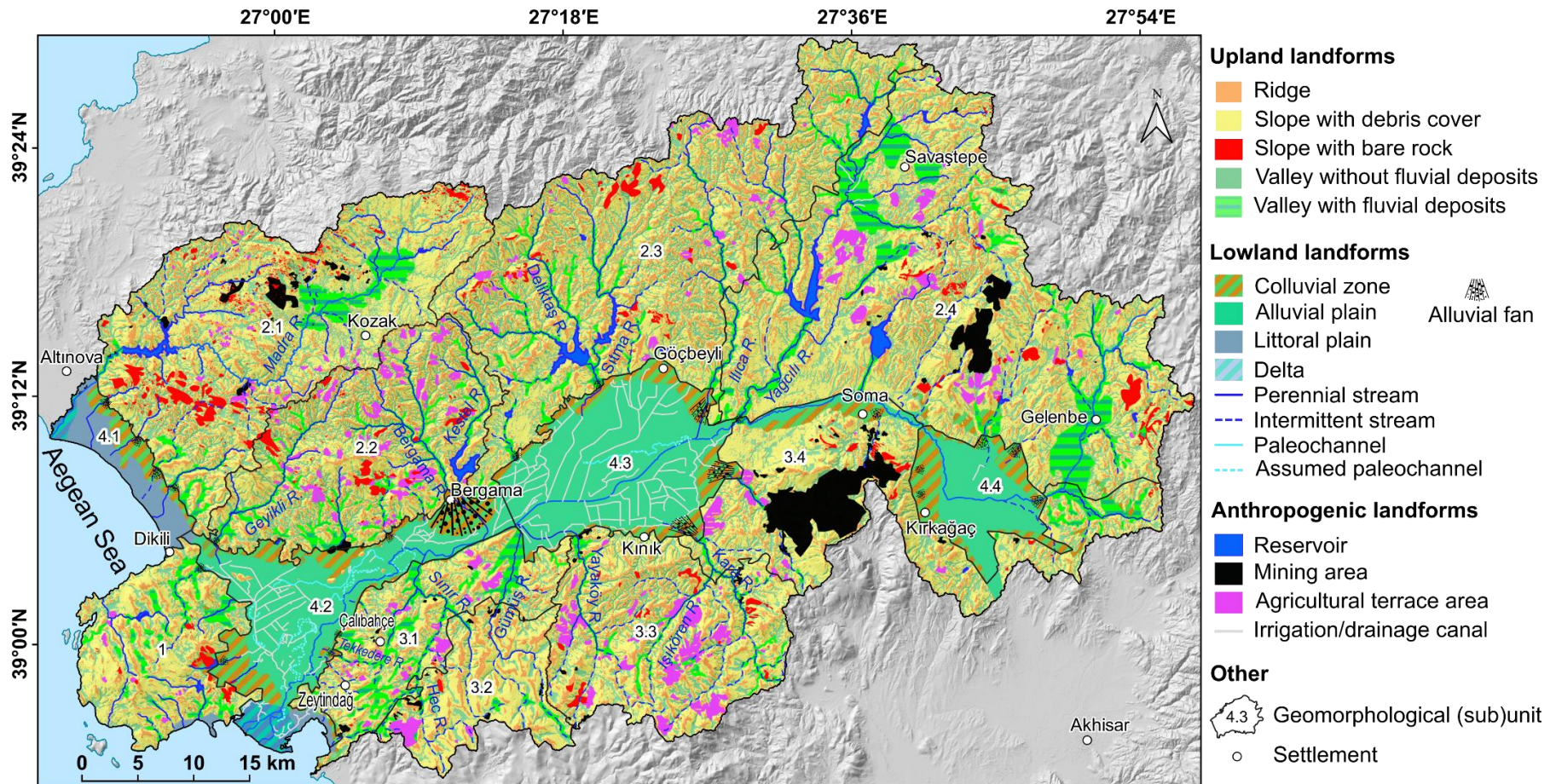


**Figure 4.4** Geomorphological map of the Bakırçay and Madra River catchments according to the classification rules in Table S4.1 (Walstra et al., 2009). Note that paleochannels and terraces are not exhaustive. Geomorphological (sub)units are indicated by numbers; for territorial extent of the geomorphological (sub)units see Figure 4.1C.

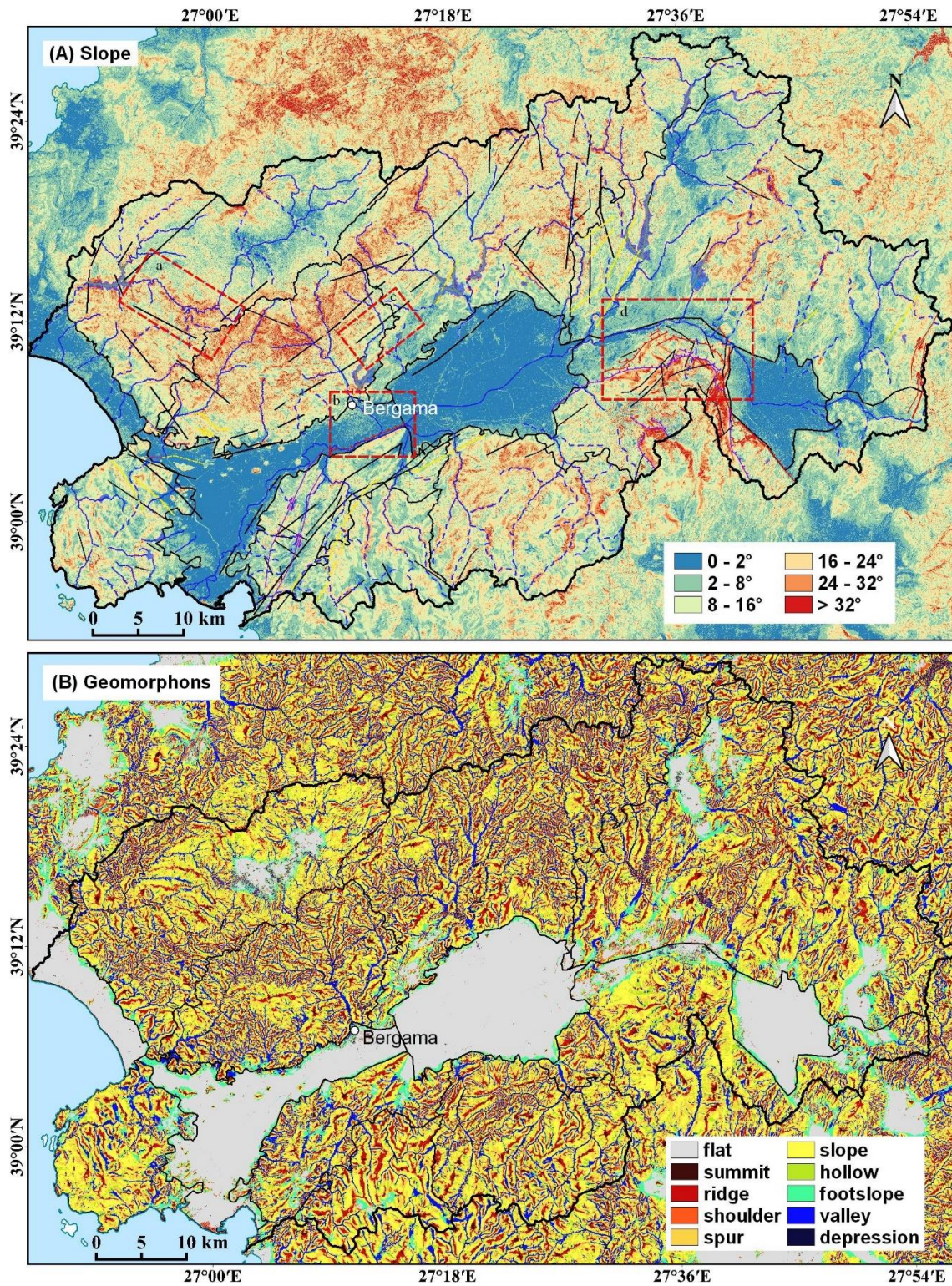


**Figure 4.5** Morphometric characters of the Bakırçay and Madra River catchments. (A) Slope with perennial streams (streams were based on (Emre and Doğan, 2010; Emre et al., 2011a; Emre and Özalp, 2011; Emre et al., 2011b)) and faults (fault legends see Figure 4.2; the red dashed rectangles denote the geomorphological features under the impacts of tectonics, see the Discussion section). (B) Geomorphons. See Figure 4.1C for the geomorphological (sub)units.

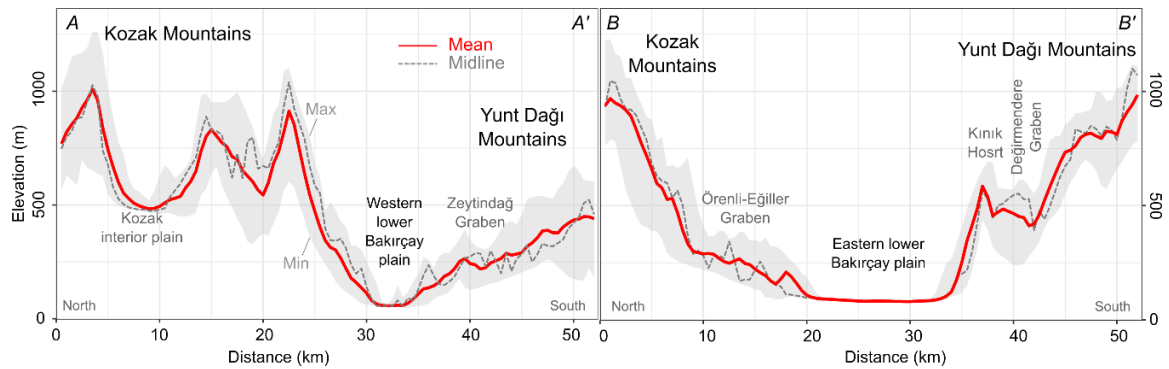


**Figure 4.6** Swath profiles (for location see Figure 4.1A), indicating distinctly asymmetrical geomorphological characteristics between the Northern Highlands and Yunt Dağı Mountains surrounding the western lower Bakırçay plain (A-A') and the eastern lower Bakırçay plain (B-B'). Note: 20x vertical exaggeration.

## 4.4.2 Major Geomorphological Units

Corresponding to the major lithological (Figure 4.2) and geomorphological characteristics (Figure 4.4), the study area was divided into the four major geomorphological units—1—Kara Dağı Mountains, 2—Northern Highlands, 3—Yunt Dağı Mountains, and 4—Plain areas—with a total of thirteen subunits (Figure 4.1C).

### 4.4.2.1 Geomorphological Unit 1—Kara Dağı Mountains

Geomorphological unit 1 corresponds to the Kara Dağı Mountains and covers an area of 198 km<sup>2</sup> (~5% of the study area; Table 4.2); this unit is not further subdivided. The Kara Dağı Mountains are dome-shaped, with the highest elevation at its central southwestern part (ca. 860 m a.s.l.) and circumferentially gently decreasing slopes (Figure 4.1A). In its eastern part, slopes generally incline less than 16°, whereas in its western part slopes reach inclinations up to 30° (Figure 4.5A). In its eastern part, narrow elongated valleys less than 1 km wide cut through a rolling landscape of slopes and ridges; extended slope areas occur at the western part of the Kara Dağı Mountains at its dip to the Aegean (Figure 4.5B). Agricultural terraces locally occur along the elongated valley flanks; these valleys are mostly infilled with shallow fluvial and colluvial deposits (Figure 4.4). Bare rocks are dominantly exposed at the southeastern upslope areas, whereas the downslope connecting footslope is covered by colluvial deposits, interfingering with littoral deposits of the Bay of Elaia (Figure 4.4).

### 4.4.2.2 Geomorphological Unit 2—Northern Highlands

Geomorphological unit 2 corresponds to the Northern Highlands, which include the major Kozak Mountains (subunits 2.1 and 2.2), Korucu Dağları Mountains (subunit 2.3), Golcük

Dağları Mountains (subunit 2.4), and their intramountainous basins (Figure 4.1A). This is the largest geomorphological unit in the study area, covering more than half of its area (Table 4.2). Subunits 2.1–2.3 were separated based on the major drainage divides, whereas subunit 2.4 was delineated according to differences in parent rocks with sedimentary rocks characterizing subunit 2.4, and mainly volcanic and pyroclastic rocks characterizing subunit 2.3. The Madra River (subunit 2.1) directly flows through the Altınova–Dikili littoral plain into the Aegean Sea.

**Geomorphological subunits 2.1 and 2.2** correspond to the Kozak Mountains with the Madra River catchment draining the northern part of the Kozak Mountains delineated as subunit 2.1. The Kozak Mountains have a mean elevation of around 530 m a.s.l. in subunit 2.1 and 440 m a.s.l. in subunit 2.2, with a total elevation range c. 1400 m (Table 4.2). Slope inclinations average 18° (Table 4.2) and locally reach a maximum of 80° (Figure 4.5A). Within the Kozak Mountains, the Kozak interior plain at 500–600 m a.s.l. altitude is located as a NE-striking intramountainous basin. The basin floor is filled by sediments with the fluvial deposits of the Madra River forming overlying strata (Figure 4.4) (Kuzucuoğlu, 1995). Relief of the Kozak interior plain is shallow (<3°), corresponding to its high values of the Topographic Wetness Index (TWI) (Figure S4.7: C). The predominating geomorphons are ridges, spurs, slopes, hollows, and valleys in the mountainous areas beyond the Kozak interior plain (Figures 4.5B and 4.7). The high heterogeneity of the relief is also displayed by small scale changes in the values of the Topographic Position Index (TPI) (Figure S4.7: B).

Headwater areas of Madra, Geyikli, Bergama, and Kestel Rivers rise from the Kozak Mountains (Figure 4.4). Due to year-round spring discharge, these rivers sourcing from Kozak Mountains are perennial. River courses of Madra River and Kestel River show clear rectangular drainage patterns (Kuzucuoğlu, 1995; Lambrianides and Spencer, 2007) (Figure 4.5A: a). The Madra River is dammed midstream at the transition of the Kozak Mountains into the coastal plain (Figure 4.4). Valley slopes are only rarely terraced, with agricultural terraces predominantly occurring at the Kozak Mountains' southern slopes (subunit 2.2) (Figure 4.4). Tributaries sourcing from the Kozak Mountains are short and intermittent, with valley infills predominantly found along their lower courses (Figure 4.4). Longitudinal profiles of the river courses (subunit 2.2) have a distinct concavity with steep upstream channel gradients that rapidly decrease at the mountain's foot zone and achieve a stretched characteristic in the downstream part (Figure 4.8), whereas flowing through the Kozak Mountains, repeatedly occurring knickpoints mark riffles and rapids (Figure 4.8).

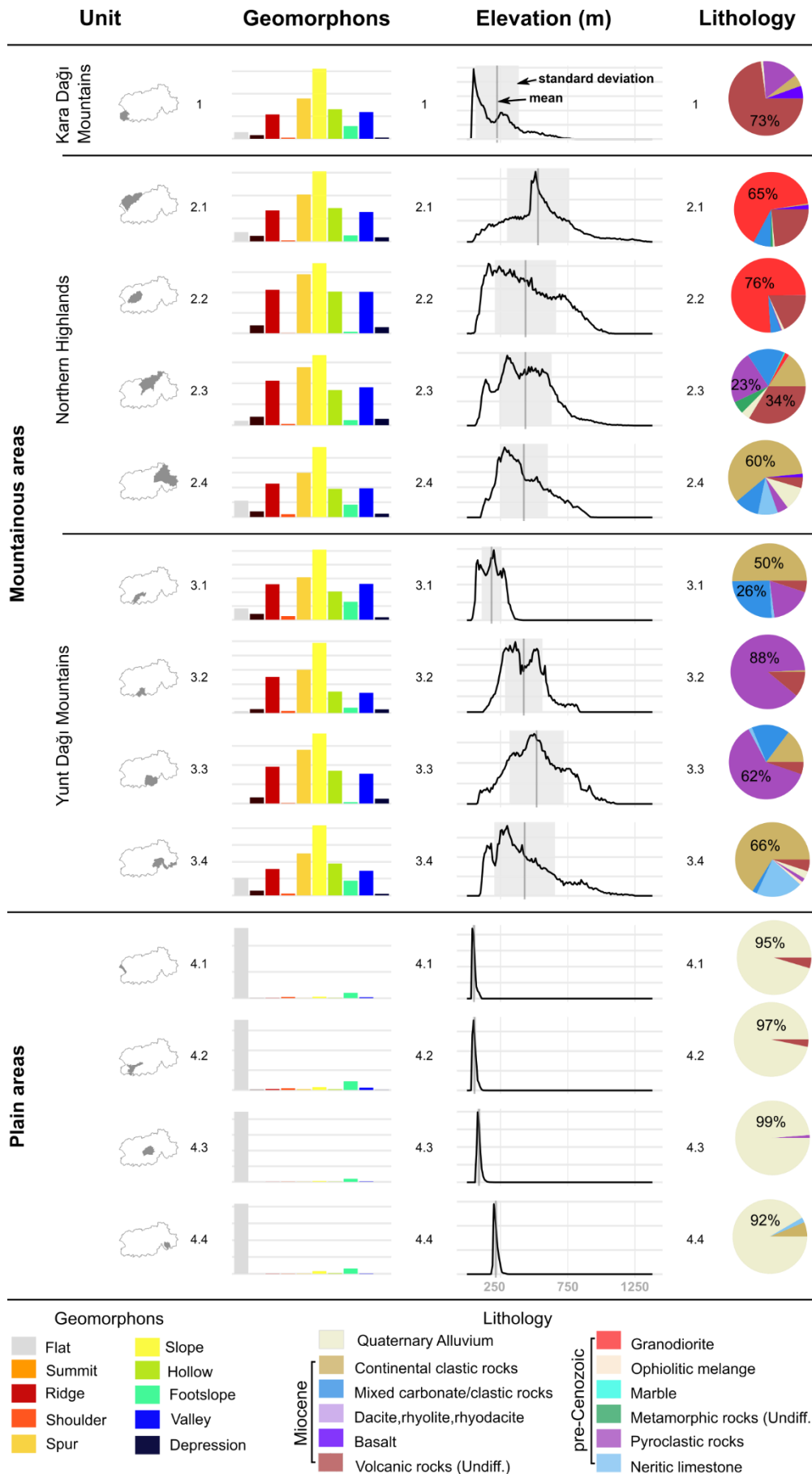
Along the southwestern ridges of the Kozak Mountains, extended areas with outcropping bedrock occur (Figure 4.4). These locations frequently coincide with small extraction areas and small stone quarries spread particularly across the northern slopes of the Kozak interior plain (subunit 2.1). Due to the plutonic rocks forming the northern and western part of the Kozak mountains, outcropping bedrock corresponds to granite boulders and their weathering products (Figure 3.S4: A). The Ovacik Gold Mine (Yilmaz et al., 2010) is located at the southern footslopes of the Kozak Mountains at the transition to the western lower Bakırçay plain (Figure 4.2).

**Geomorphological subunits 2.3 and 2.4** exhibit a NE-striking depression–mountain–depression pattern, including the major morphotectonic landforms (from west to east): the Örenli–Eğiller Graben, Korucu Dağları Mountains, Savaştepe interior plain, Gölcük Dağları Mountains, and Gelenbe interior plain (Figures 4.1A and 4.2). The Örenli–Eğiller Graben (100–300 m a.s.l.) is characterized by a slightly rolling landscape with an average inclination of  $<6^\circ$  and an average TWI of 7; the graben floor is covered by fluvial and colluvial deposits with locally occurring landslides. Graben flanks, and the Kozak Mountains to the northwest and the Korucu Dağları Mountains to the east, have a strong relief, with c.  $15^\circ$  average inclination (subunit 2.3; Figure 4.5A). The basin structures of the Savaştepe interior plain and Gelenbe interior plain are located at an elevation of c. 250 m a.s.l.; like the Kozak interior plain, they are filled with fluvial and colluvial deposits, resulting in a shallow relief with an average TWI of 7.1 (Figure S4.7: C). Outcropping bare rocks are widely scattered across the mountainous areas of subunits 2.3 and 2.4 (Figure 4.4).

Tributaries of Bakırçay River with sources in the Korucu Dağları Mountains (subunit 2.3) and the Gölcük Dağları Mountains (subunit 2.4) show concave longitudinal channel profiles which are typical for mountainous tributaries with very steep upper courses repeatedly interrupted by knickpoints (Figure 4.8). A clear relationship between the concavity degree and the ratio of the channel length to the altitude of the headwater area can be observed, indicating stronger morphodynamics for Deliktas and Sitma Rivers than for Ilica and Yağcılı Rivers.

---

**Figure 4.7** Distribution of the morphometric and lithologic characteristics of the Bakırçay and Madra River catchments outlining geomorphological subunit distribution of geomorphons and elevation; y-axis shows the total number of pixels per geomorphon and per altitude range. Pie charts show the distribution of lithology.



Reservoirs have been built at the middle-lower reaches of the major streams (Deliktaş, Sıtma, and Yağcılı) (Figure 4.4), some of which collect runoff from drainage basin areas up to 450 km<sup>2</sup> in size, e.g., the Sevişler reservoir on the Yağcılı River between the Korucu Dağları and Gölcük Dağları Mountains (Tosun et al., 2020) (Figure 4.4). A large mining area is located next to the Soma–Kolin Thermal Power Plant in the Korucu Dağları Mountains (subunit 2.4; Figures 4.2 and 4.4) covering an area of c. 15 km<sup>2</sup>. Agricultural terraces mainly occur on the Gölcük Dağları Mountains (subunit 2.3; Figure 4.4).

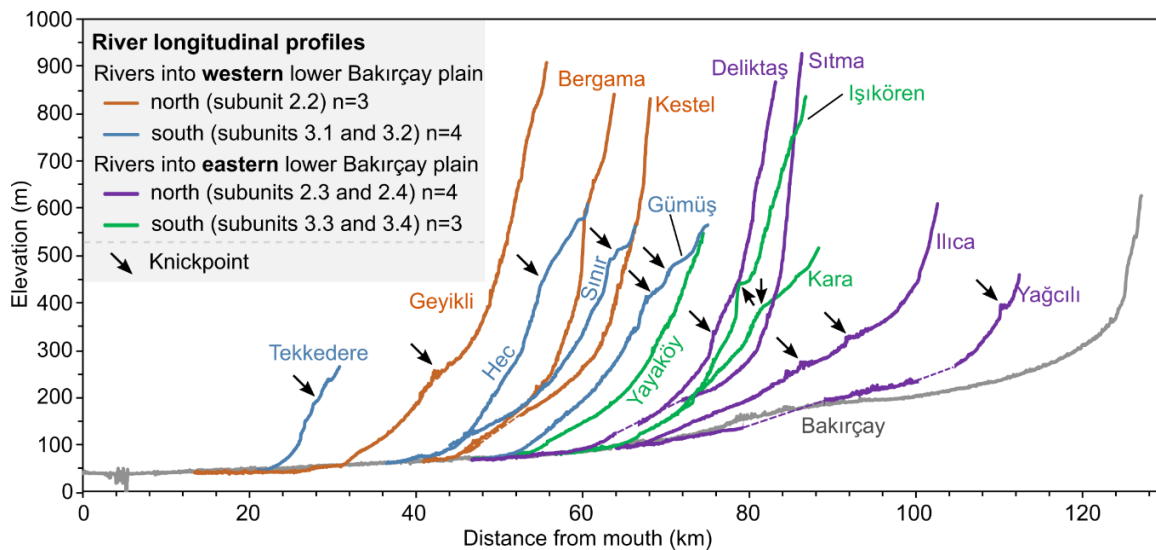


**Figure 4.8** Longitudinal profiles of channel courses and major knickpoints in the Northern Highlands (geomorphological units 2.2–2.4) and Yunt Dağı Mountains (geomorphological units 3.1–3.4) enclosing the lower Bakırçay plain (see Figure 4.4 for the river courses). Note: c. 50x vertical exaggeration; reservoirs were manually modified with dashed lines.

#### 4.4.2.3 Geomorphological Unit 3—Yunt Dağı Mountains

Geomorphological unit 3 corresponds to the northern part of the Yunt Dağı Mountains and incorporates about one-quarter of the research area (Table 4.2). Including the Maruflar Horst, the ridges along the divide reach elevations >1200 m a.s.l. (Table 4.2) and are widely composed of pyroclastic rocks (88% of its area). The Zeytindağ and Yayaköy grabens (subunit 3.1; Figure 4.2) confine the Maruflar Horst to the NW and N, both being infilled by Quaternary fluvial deposits (Figure 4.4). In the NE of Maruflar Horst, Değirmendere Graben and Kınık Horst (subunit 3.3) display the basin–range structure, building the transition into Bergama Graben. The Kınık Horst corresponds to a block of uplifted Miocene carbonates, whereas adjacent eastern Yunt Dağı Mountains (subunit 3.4) are mainly built of continental clastic rocks (Figures 4.2 and 4.7).

**Geomorphological subunit 3.1.** The ground level of the Zeytindağ and Yayaköy grabens (subunit 3.1) is at 180–190 m a.s.l. altitude; Quaternary graben infills cause a moderate relief with inclinations  $<10^\circ$  (Table 4.2; Figure 4.5A). Streams are generally short and intermittent, especially those close to Çalibahçe and Zeytindağ (Figure 4.4). Additionally, agricultural terraces and mining areas widely spread throughout the area (Figure 4.4).

**Geomorphological subunit 3.2.** The Maruflar Horst (subunit 3.2) has a mean elevation of c. 516 m and forms the highest area of the Yunt Dağı Mountains. The horst is in the headwater areas characterized by small flats and footslopes (areas of less than 2 km<sup>2</sup>), and wide and elongated ridges and slopes being up to c. 3 km wide (Figure 4.5B). In the headwater areas, valleys are saucer-shaped and infilled by shallow fluvial deposits. Valleys are deeply incised and still under active incision at the confluence into the Zeytindağ and Yayaköy grabens. At the lower courses of the Sınır and Gümüş Rivers, in particular, the valley floors widen and are infilled by fan deposits; fans gently incline and cover areas of c. 2 km<sup>2</sup> (Sınır) and 5 km<sup>2</sup> (Gümüş) (Figure 4.4). Agricultural terraces occur predominantly on the uphill graben shoulders of Zeytindağ and Yayaköy grabens.

Channel courses in the western Yunt Dağı Mountains (subunits 3.1 and 3.2) show distinct convex shapes of their longitudinal profiles in the upstream areas, tracing the transition of saucer-shaped valleys in plateau-like environments of the headwater areas to the graben flanks (Figure 4.8). Repeatedly occurring knickpoints mark fault lines crossed by the river courses (see Gümüş, Tekkedere, and Sınır Rivers in Figure 4.8).

**Geomorphological subunit 3.3.** The basin–range structure of Kınık Horst and Değirmendere Graben (subunit 3.3) covers an elevation range of 1152 m;  $15.5^\circ$  average slope inclination documents the strong relief (Table 4.2). Landform units are characterized by short and narrow ridges, slopes, and valleys, whereas there is a lack of flats (Figure 4.7); overall, the landscape of Kınık Horst and Değirmendere Graben is highly heterogeneous (Figure 4.5B). Corresponding to the strong relief, valleys are deeply incised, with fluvial deposits only occurring in basin-like valley openings, such as in the lower course of Yayaköy River (Figure 4.4). The size of most of these basins is less than 1 km<sup>2</sup>. Slopes are widely covered by debris and only locally bare rocks crop out (Figure 4.4); correspondingly, agricultural terraces are widely distributed.

**Geomorphological subunit 3.4.** The eastern Yunt Dağı Mountains (subunit 3.4) are characterized by steep slopes of more than  $30^\circ$  inclination, particularly at the areas adjoining to the Soma valley and upper Bakırçay plain (Figure 4.5A). The slopes are widely covered by debris, whereas bare rocks only locally crop out. Soma valley, with its 1–2 km wide valley floor, is also part of subunit 3.4, expressed by a distinct occurrence of

flats (Figure 4.5B). Kısırkdere Coal Mine, with a quarrying area of more than 40 km<sup>2</sup>, is located in the central eastern Yunt Dağı Mountains (Figure S4.4: E). Agricultural terraces occur only rarely (Figure 4.4).

Longitudinal profiles of channel courses in the eastern Yunt Dağı Mountains (subunit 3.3 and part of subunit 3.4) have a concave shape, locally interrupted by convex knickpoints, e.g., Kara and Işıkören Rivers (Figure 4.8). In particular, the longitudinal channel profile of the Işıkören River is marked by strong inclinations at the upper and middle courses, and a distinct knickpoint in the middle course.

#### **4.4.2.4 Geomorphological Unit 4—Plains**

The plain areas (geomorphological unit 4) are widely flat with inclinations of less than 3° (Figure 4.5A). Fluvial, colluvial, and littoral Quaternary deposits cover the plain areas (Figure 4.4). Subunit 4.1 corresponds to the littoral area. Subunits 4.2–4.4 display the alluvial plains of the Bakırçay River, separated by the Bergama fan and Soma valley into the western lower Bakırçay plain (subunit 4.2), eastern lower Bakırçay plain (subunit 4.3), and upper Bakırçay plain (subunit 4.4). The width of the lower Bakırçay plain in its central part (around the Bergama fan) is 2–3 km, while it increases to c. 10 km in the western lower Bakırçay plain (subunit 4.2) and c. 13 km in the eastern lower Bakırçay plain (subunit 4.3).

The headwater areas of Bakırçay River are located in the Gölcük Dağları Mountains from where the river course heads southward until reaching the basin of the upper Bakırçay plain (subunit 4.3). In the upper Bakırçay plain, the river flows westward before turning north when reaching the eastern spur of the Yunt Dağı Mountains. In particular, the Bakırçay River close to Soma flows along a meandering valley, which is predetermined by the adjoining mountain ranges and the local fault systems.

Downstream of Soma, the valley opens to the lower Bakırçay plain. Bakırçay River flows in a WSW direction in the eastern lower Bakırçay plain (subunit 4.3) and turns to SW after passing the Bergama fan (western lower Bakırçay River plain; subunit 4.2). Throughout the lower Bakırçay plain, the Bakırçay River flows almost along the footslopes of the Yunt Dağı Mountains.

At the transition of the western lower Bakırçay plain into the Aegean Sea, the delta of Bakırçay River with an area of 14 km<sup>2</sup> is developed between the modern settlement of Çandarlı (subunit 1) and the Bay of Elaia, which is separated from the delta by the Bozyertepe ridge, a spur of the Yunt Dağı Mountains (subunit 3.1) (Seeliger et al., 2019).

**Geomorphological subunit 4.1.** The Altınova–Dikili littoral plain adjoins the footslopes of the western Kozak Mountains. Correspondingly, the area is composed of a 1–2 km wide zone covered by coastal deposits interfingering with colluvial deposits along the western footslopes of the Kozak Mountains (Figure 4.4). Fluvial deposits from the Madra River aggrade and gradually form the Madra River delta downstream from the modern settlement of Altınova (Lambrianides and Spencer, 2007). The littoral plain also connects to the western lower Bakırçay plain (subunit 4.2) through a narrow corridor close to Dikili.

**Table 4.3** Mountain-front sinuosity index (Smf) and extension of colluvial deposits in the lower Bakırçay plain.

Location		Lmf (m)	Ls (m)	Smf	Extension of Colluvial Deposits (km)
Western lower Bakırçay plain	north	76.29	27.97	2.73	0.5–2
	south	48.17	22.32	2.16	<0.5
Eastern lower Bakırçay plain	north	53.83	20.11	2.68	<0.5 (west part);
	south	60.80	20.29	3.00	0.5–3 (east part)

**Geomorphological subunit 4.2.** At the northern transition zone between the Kozak Mountains and the western lower Bakırçay plain, colluvial deposits and alluvial fans cover the foot zone of the Kozak Mountains, reaching a width of 2 km (Table 4.3). In contrast, at the southern boundary of the western lower Bakırçay plain, the colluvium along the footslope of the Yunt Dağı Mountains has a maximum width of 500 m (Figure 4.4). In addition, the mountain-front sinuosity index (Smf) of the Kozak Mountains and Yunt Dağı Mountains differs, with a distinctly lower value for the Yunt Dağı Mountains (2.16) than for the Kozak Mountain front (2.73) (Table 4.3). In the northern part of the Bergama Graben, small dome-shaped volcanic hills occur (Figure 4.2), e.g., the Kalarga Tepe and Eğrigöl Tepe.

The Bergama fan separates the western lower Bakırçay plain from the eastern lower Bakırçay plain. The city of Bergama was founded in the root-zone of the fan and provides its name. The Bergama fan covers an area of approximately 14 km<sup>2</sup> and receives sediments from the Kozak Mountains by the Bergama River and Kestel River, which have a combined drainage basin area of 156 km<sup>2</sup>. Other fans deposited in the western lower Bakırçay plain mostly cover areas of 1–2 km<sup>2</sup> and are deposited by Bakırçay tributaries with drainage basin areas <120 km<sup>2</sup>. In the western lower Bakırçay plain, widespread river regulation measures occur, including canals, stream straightening (e.g., the Doğramacı

canal of the Geyikli River), and construction of river embankments up to 5 m high (Schneider et al., 2015). Abandoned channels and cut-off meanders occur predominantly close to the straightened and embanked river courses (Figure 4.4). The extensive drainage of wide areas of the lower Bakırçay plain influences local runoff regimes and water budget.

**Geomorphological subunit 4.3.** In the eastern lower Bakırçay plain (ca. 88 m; Table 4.2), colluvial deposits at the eastern transition zone from Göçbeyli to Kınık are up to 3 km wide, whereas in the western transition areas they are generally less than 0.5 km wide (Table 4.3). Alluvial fans with areas of 2–5 km<sup>2</sup> primarily occur in the east of the zone (Figure 4.4). The sinuosity value of the eastern Yunt Dağı Mountains' front (3.00) is slightly higher than that of the Northern Highlands (2.68) (Table 4.3).

**Geomorphological subunit 4.4.** The mean elevation of the upper Bakırçay plain (subunit 4.4) averages ca. 213 m (Table 4.2). The slopes to the Akhisar plain of the Gediz River catchment are gentle, thus they can be easily connected (Philipson, 1912; Ludwig, 2020b). At the footslopes along the upper Bakırçay plain, abundant colluvial sediments were deposited (Figure 4.4), building a two-kilometer-wide transition zone at the east (from Soma to Kırkağaç) and decreasing in extent to the west. Alluvial fans of Bakırçay River tributaries have areas of less than 1 km<sup>2</sup>. Only a few canals are found in the upper Bakırçay plain.

## 4.5 Discussion

The distinct asymmetry of the topography in the Bakırçay and Madra River catchments (Figure 4.6) is an expression of the strong impact of tectonic movements. Locally varying rates of uplift and sinking due to tectonic compression and divergence resulted in a small-chambered relief with sharp borders between the different geomorphological units. These effects are amplified by the inclination of the rock strata forming the mountainous areas due to their locally highly variable characteristics of strike and dip. This diverse landscape promotes the usage suitability since the Holocene.

### 4.5.1 Development of the Major Landform Units

The **Kozak Mountains** (geomorphological subunits 2.1 and 2.2) are characterized by high average elevation and steep slopes (Figure 4.6: A-A'), a NW-trending large-scale bare rock association, and rectangular drainage courses. The mountains comprise Miocene volcanic centers characterized by andesitic volcanism, which surround the plutonic core

of the Kozak interior plain (Karaoğlu, 2014). In parallel, compressional forces from the westward drift of the Anatolian plate during the Miocene caused an uplift of the area (Borsi et al., 1972; Kuzucuoğlu et al., 2019b). During the Miocene, Pliocene, and early Quaternary, the uplift of the Kozak Horst and subsidence of surrounding grabens shaped the Kozak Mountains (Figure 4.2) (Kuzucuoğlu, 1995; Yilmaz et al., 2000; Kayan and Vardar, 2007b). The bare rock association dominating on the western ridges of the Kozak Mountains (subunit 2.1, Figure 4.4) is associated with the NW–SE-striking Altınova–Dikili fault zone (Emre et al., 2011b) (Figure 4.2). Steep slopes are deeply fissured, resulting in a high infiltration capacity and shallow soils (Erlat, 2007). The rectangular flow pattern of the Madra River is controlled by the local fault system (Figure 4.5A) and the Mio-Pliocene lava flows (Kuzucuoğlu, 1995). In addition to lithological differences between pyroclastic and continental clastic rocks (MTA, 2002) (Figure 4.2), the rectangular drainage pattern of the Kestel River can also be attributed to the fault system (Emre et al., 2011b) (Figure 4.5A: c).

A peculiarity of the Kozak Mountains is the wide and flat Kozak interior plain (geomorphological subunit 2.1), a large intramountainous basin filled by Quaternary sediments. Granodiorite boulders in the northern margin of the Kozak interior plain document spheroidal weathering (Figure S4.4: A), building a typical granite landform (Gutiérrez and Gutiérrez, 2016). In addition, the slopes formed in the granodioritic bedrock result in frequently outcropping bare rock covered by a thin layer of weathering products. Comparable interior plains as large sediment sinks can be found at Savaştepe and Gelenbe in geomorphological subunit 2.4 (Mustafaoğlu and Dağ, 2012). The formation of the Savaştepe interior plain can be linked to the NE-trending İzmir–Ankara Suture Zone (Figure 4.2) (Okay, 2008; Sanğu et al., 2020).

Compared to the Yunt Dağı Mountains (see below), colluvial and alluvial fan deposits at the footslopes of the Kozak Mountains are largely extended, being directly related to the drainage basin size and relief, which indicate high soil erosion dynamics (Bull, 1977; Lague, 2014; Clarke, 2015; Rhoads, 2020). The upper parts of the Geyikli, Bergama, and Kestel Rivers' longitudinal profiles, which each have headwater areas located in the Kozak Mountains (Figure 4.8), clearly indicate high relief, resulting in strong incision processes (Ahnert, 1970; Schlunegger and Hinderer, 2003). The knickpoints along the longitudinal profiles are indicative of faults if the bedrock remains unchanged (Das, 2018; Rhoads, 2020).

In the western **Yunt Dağı Mountains**' hinterland, Maruflar Horst (subunit 3.2) developed in a manner geologically similar to the Kozak Horst (Yilmaz et al., 2000); the bedrock of

Maruflar Horst is dominated by pyroclastic rocks formed by Early–Middle Miocene volcanism (Yilmaz et al., 2000; MTA, 2002).

The **Zeytindağ and Yayaköy grabens** (subunit 3.1) form local sedimentary sinks. The NE–trending Zeytindağ Graben to the south of the Bakırçay plain—together with Örenli–Eğiller Graben to the north—developed under the Late Miocene east–west extension between the Kozak Horst and Göçbeyli Horst (Yilmaz et al., 2000). The formation of the orthogonal Bergama Graben during the Pliocene separated the Zeytindağ–Örenli–Eğiller Graben into two units (Yilmaz et al., 2000), both having the typical topographical characteristics of graben structures with flat infilled graben floors and step faults along the graben shoulders (Becker et al., 2020b) (p. 74). The straight mountain fronts of the Yunt Dağı Mountains display regional tectonics, particularly the Holocene normal faults, e.g., the Sindel normal fault (Emre et al., 2011a) (Figure 4.5A: b).

In comparison to the Kozak Mountains, the gentler relief in the western Yunt Dağı Mountains is expressed in less-pronounced channel gradients (Ozdemir and Bird, 2008) (Figure 4.8). The convex-upward shape of the Bakırçay tributaries draining the Yunt Dağı Mountains indicates the plateau-like relief in the headwater area, whereas the repeatedly superimposed concavities in their longitudinal profiles show their high incision with rapid adjustment close to the Bakırçay plain (Das, 2018). Fluvial sediments can only be found along the river courses in local sinks wherever there is a break in inclination corresponding to the system of sediment cascades (Fryirs et al., 2007; Baartman et al., 2013; Fryirs, 2013). Overall, the Bakırçay tributaries flowing from the Yunt Dağı Mountains show an immature stage of channel development (Rhoads, 2020), with frequently occurring knickpoints indicating Quaternary faults (Emre and Doğan, 2010; Emre et al., 2011b) (Figure 4.2). Where perennial streams such as Sınır and Gümüş Rivers merge into the Bakırçay plain, alluvial fans are only very slightly convex-shaped, due to the shallow inclination of the tributaries' river courses and the corresponding shallow relief of their drainage basins (Knitter, 2013).

In the north of the eastern Lower Bakırçay Plain, the NE-trending **Örenli–Eğiller Graben** (Figure 4.2) exhibits similar elevation distribution and gentle slopes to the Zeytindağ Graben (subunit 3.1) (Yilmaz et al., 2000). The basis of Örenli–Eğiller Graben forms a sink, preventing most of the sediment eroded from the mountains from reaching the eastern lower Bakırçay plain (Figure 4.4). The steep channels of the upper Deliktaş and Sıtma Rivers indicate the lasting uplift of Kozak Horst (Rhoads, 2020) (p. 306). The Ilica and Yağcılı Rivers show less steep longitudinal channel profiles than Deliktaş and Sıtma Rivers, indicating lower uplift rates in their headwater areas than at Kozak Horst (Rhoads,

2020). Knickpoints along Ilıca and Yağcılı River course profiles imply fault lines of the İzmir–Ankara Suture Zone (Okay, 2008). Due to the large drainage basins of Ilıca, Yağcılı, Deliktaş, and Sıtma Rivers, extended alluvial fans formed at their confluence into the eastern lower Bakırçay plain (Figure 4.4).

The **Kınık Horst** (subunit 3.3) in the south surmounts the eastern lower Bakırçay plain by approximately 500 m and steep slopes characterize its transition to the eastern lower Bakırçay plain (Figure 4.6: profile B–B'). Its sinuous mountain front ( $S_{mf} = 3.00$ ; Table 4.3) indicates low to moderate tectonic activities (Bagha et al., 2014). Only a narrow verge at the footslope of Kınık Horst is covered by colluvial deposits (Figure 4.4). The two alluvial fans of the Yayaköy and Kara Rivers occur because their drainage basin sizes are distinctly larger than those deposited at the footslopes of the western Yunt Dağı Mountains. The rivers deeply incised into Kınık Horst; the lack of intermediate sediment storage areas resulted in large fan areas being slightly disproportionate to the size of their drainage basins.

**Kara Dağı Mountains** to the west of the lower Bakırçay plain have a Miocene volcanic center (Karaoğlu, 2014) and form as Kane peninsula reaching into the Aegean Sea. The N–S trending valleys and ridges in the Kara Dağı Mountains (Figure 4.4) correspond to Cenozoic NNW–SSE striking faults (Ölgen, 2004; Karacik et al., 2007; Emre and Doğan, 2010; Emre and Özalp, 2011) (Figure 4.2). Extensive colluvial deposits in the southeast of the Kara Dağı Mountains in the transition zone to the western lower Bakırçay plain are indicative of high erosion activities resulting in deeply incised valleys following faults (Karacik et al., 2007).

The **lower Bakırçay plain** develops in the east–west trending Bergama Graben. Alluvial deposits of the Bakırçay River, in addition to colluvial and alluvial fan deposits from the adjoining mountains, are continuously aggrading the lower Bakırçay plain. Separating the upper and lower Bakırçay plain, Soma valley with a long and narrow shape is controlled by a series of high-angle oblique-slip normal faults, active since the Pleistocene, with small lateral components that strike NE–SW, NW–E, N–S, and E–W (İnci, 2002; Emre et al., 2011a; Sanğu et al., 2020) (Figure 4.2). The west extension of N-trending faults (Emre et al., 2011a) between Soma and Kırkağaç forms a linear structure of steep slopes facing west.

Formation of the Bergama Graben started from the Early Pliocene (Yılmaz et al., 2000; Sanğu et al., 2020). During the Quaternary, two NNE- to NE-trending dextral oblique-slip fault segments at Zeytindağ–Bergama and Kınık–Turgutalp deformed the former Bergama Graben into a transtensional pull-apart basin striking NE–SW with sediments up

to 120 m thick (Sanğu et al., 2020). Due to the influence of the former fault zone, the Zeytindağ Graben and the surrounding ridges (subunit 3.1) were moved to the NE (towards the city of Bergama), causing the constriction between the eastern and western lower Bakırçay plain (Yılmaz et al., 2000; Sanğu et al., 2020). Here, the straight channel pattern of the Bakırçay River (Figure 4.5A: b) displays the tectonic influence on the river course. Presumably due to the continuous uplift of the Kozak Mountains, the Bakırçay River flows close to the footslopes of the Yunt Dağı Mountains, contributing to the asymmetry of the plain (Yılmaz et al., 2000).

An exceptional landform in the Plain Areas is the **Bergama alluvial fan**, which is formed from deposits of the Kestel and Bergama Rivers in the Northern Highlands. Mountainous relief (Bull, 1977), and seasonally high discharges allow high transport rates for the bedload deposited at the longitudinal gradient change at the transition from the Kozak Mountains to the Bakırçay Plain (Bull, 1977).

Widespread **paleochannels** in the lower Bakırçay plain indicate the formerly anastomosing channel pattern of the Bakırçay River, with strong deposition and redeposition dynamics during seasonal flood flows at least since ancient history (Schneider et al., 2015; 2017). During the Early–Middle Holocene, the Bakırçay floodplain was assumed to be narrower than today (Schneider et al., 2017).

The most prominent **coastal landforms** in the study area are the Altınova–Dikili littoral plain and the deltas of the Madra and Bakırçay Rivers. The littoral plain is part of the NW-trending Ayvalık–Lesvos Graben which subsided during the Quaternary (Kayan and Vardar, 2007b) (p. 19). Similar to the southern Kozak Mountains (section 5.1.1), the tectonic movement caused steep slopes, which today merge into the coastal plain by colluvium deposited at the footslope (Kuzucuoğlu, 1995; Kayan, 1999). The Altınova–Dikili coastal area is dominated by Pliocene–Pleistocene alluvial fans based on torrential deposits that extend into the Aegean Sea (Kayan and Vardar, 2007a, b). These coarse-detrital fan deposits were flooded by the Holocene marine transgression after 7000–6000 yr BP (Kayan and Vardar, 2007b) and were subsequently overlain by alluvial delta deposits of Madra River and Karakoç River (the latter is located c. 5 km north to the Madra River) (Seeliger et al., 2017).

The corridor between the Altınova–Dikili littoral plain and the Bakırçay plain can be linked to the active tectonic activities at the Altınova–Dikili fault zone (Figure 4.2: ①) (Özürlan et al., 2006). Tectonic activities along the fault zone are also responsible for the thermal springs occurring in this area, e.g., the Kaynarca thermal spring that emerged after the 1939 earthquake (Özürlan et al., 2006). In addition to these effects of tectonics, the

development of coastal areas was highly impacted by regional sea-level changes (Kayan, 1999; Marriner and Morhange, 2007; Brückner et al., 2010) and caused the deposition of interbedded coastal swamp–sandy marine sediments and terrestrial alluvial–deltaic deposits (Lambrianides and Spencer, 2007; Seeliger et al., 2019).

#### **4.5.2 Usage Suitability and Human Impact during the Late Holocene**

Prehistoric and ancient settlements in the Pergamon Micro-Region are dominantly found in the flat–gently inclining transition areas between the mountains and plains (Figure 4.1A) (Knitter, 2013; Knitter et al., 2013). Those areas are easily accessible to diverse resources (including water, food, and building materials) and have geographical strategic significances (such as flood-safe and through-traffic). Fertile plain areas provide the largest portion of the food supply of the micro-region (Laabs and Knitter, 2021). Throughout **the Bakırçay plain**, settlements prefer flood-safe places, such as the piedmonts along the footslopes of the adjoining mountain areas (Schneider et al., 2015). In the western lower Bakırçay plain, some archaeological sites also occur close to the elevated volcanic cones, e.g., the site Yeni Yeldeğirmentepe (Figure 4.1A) (Schneider et al., 2017). The slightly rolling and flood-safe piedmonts at the footslopes of the mountains are currently the preferred locations for pathway and road networks (Ludwig, 2020b). Low-angle colluvial deposits attracted colonization and foundation of cities, e.g., modern cities of Soma (ancient Germe), Kırkağaç, and Kınık (Figure 4.1A) (Ludwig, 2020b). However, the flood-safe areas are not always “safe”. Fluvial aggradation during Holocene transgression may occasionally flood the ancient human occupations (Schneider et al., 2015), agricultural fields, and roads, which may hinder the continuous usage of plain areas.

The strong relief of the **Kozak Mountains** is widely unsuitable for settlements, and only the gently inclined colluvial deposits adjoining the Bakırçay plain are favored for agriculture (Schneider et al., 2013; Schneider et al., 2014). An exception is the hill-top settlement of Kale Ağılı (ancient polis Atarneus) in the lower Geyikli drainage basin (Figure 4.1A), which benefited from its prominent topographical location and advantages such as a strategic position in terms of visual control, easy access to timber from a mountainous hinterland and fertile agricultural land in the environs (Schneider et al., 2014). The foot-zone of the Kozak Mountains is a preferred area for the through-traffic between the coast and Bergama, i.e., between the ancient polis of Atarneus and Pergamon (Figure 4.1A) (Ludwig, 2020b). In addition, the flat relief and fertile fluvial sediments on the Kozak interior plain provide ideal conditions for agriculture (Figure S4.6). During antiquity, human

settlements were found in the area, e.g., Perperene and Kytonion (Figure 4.1A) (Ludwig, 2020b). Similarly, the low inclinations and infilled unconsolidated sediments make the Örenli–Eğiller Graben suitable for agriculture (Figure S4.6) and settlements (Figure 4.1A) (Ludwig, 2020b). The Kozak Mountains have been incised by large rivers (Madra and Bergama Rivers) that are integral parts of the road network, with connections among the Kozak interior plain (further to Adramytteion), the coastal areas, and ancient Pergamon (Figure 4.1A) already existing in ancient times (Ludwig, 2020b). In addition, the İlica, Yağcılı, Deliktaş, and Sıtma Rivers in the Northern Highlands formed deeply incised valleys that provided natural pathways connecting Pergamon with ancient settlements to the northeast and east, such as Ergasteria and Hadrianoutherai (Figure 4.1A) (Ludwig, 2020b).

The **Bergama fan** is a terrestrial landform of high morphodynamics, characterized by frequent sheet-flow and rapid stream–channel shifts, which hampered settlement activities. However, after the incision of the Bergama River into its own deposits, the channel course stabilized, and the flooding risk was reduced. Consequently, natural advantages, including access to water (surface water and groundwater) for drinking and farming, fertile soils for food, and spaces for living, attract humans to settle (Bull, 1977; Boyer et al., 2006). Some scholars regard the major reasons for founding ancient Pergamon adjacent to the Bergama fan were the fan’s physiographic endowment, good accessibility of natural resources, and good strategic location (Von Diest, 1889; Philippson, 1912; Zimmermann, 2011). In spite of the possible access of water from the Bergama alluvial fan, gigantic size of aqueducts in the ancient Pergamon were constructed for continuous water supply as a basic feature of civilized life during the Hellenistic-Roman times, such as the aqueduct from the Kozak Mountains to the Acropolis of the Pergamon (Figure 4.1A) built by Eumenes II (197–159 BC). The construction benefited from not only the political, economic, and technical developments (Tassios, 2007; Radt, 2016), but also the geographical advantage of having the water source area in the topographically high Kozak Mountains.

For the Pergamon Micro-Region, most recent archaeological surveys in the gentle areas of the **Yunt Dağı Mountains** assume a large potential for human occupation (Knitter, 2013; Knitter et al., 2013; Pirson, 2019; Becker et al., 2020b). Olive cultivation in the western Zeytindağ Graben has been reported since at least ~2.8 ka BP (Shumilovskikh et al., 2016). The local sediment sinks in the Yunt Dağı Mountains, including the fertile intramountainous basins and flat basin-like extended valleys at the river outlets, favor the development of small-scale settlements and agriculture, e.g., in the Tekkedere, Çalibahçe, and Gümüş valleys (Figure 4.1A), in different archaeological periods at least since the

Late Chalcolithic period (Horejs, 2010b; Knitter, 2013; Knitter et al., 2013; Pirson, 2019; Becker et al., 2020b). In the Yunt Dağı Mountains, small flats with infilled saucer-shaped valleys served for the founding of small hamlets. The soils formed on the fluvial deposits of the saucer-shaped valleys attracted farming; the hamlets were also able to be used as rest areas for travelers on the route from Pergamon to southern cities such as Apollonis and Magnesia (Figure 4.1A) (Ludwig, 2020b), proving the importance of the areas adjoining the plain for traffic purposes. However, due to the active tectonics, such as earthquakes and the resulting landslides, the settlements in the west Yunt Dağı Mountains may be abandoned and relocated occasionally (Becker et al., 2020b).

The **Kara Dağı Mountains** make the Bakırçay valley unique along the Anatolian Aegean coast because they restrict the connection between the Bakırçay plain and the Aegean Sea to two narrow corridors (Schneider, 2014) (p. 15). Settlement areas in the Kara Dağı Mountains predominantly occur along the coastal zone and close to small rivers (Pirson, 2015, 2019; Ludwig, 2020b). The fertile delta plains of Bakırçay and Madra Rivers favor agricultural activities (Lambrianides and Spencer, 2007), and their marshy ground also makes them widely unsuitable as settlement areas and for through-traffic. The site of the Hellenistic–Roman harbor city of Elaia (Pint et al., 2015; Seeliger et al., 2019) was chosen due to its protected location in the lee of the Kara Dağı Mountains. However, the shallow area of the Bay of Elaia was already silted during Roman times due to the high sediment load of the Bakırçay River and the adjacent slopes (Seeliger et al., 2019).

Currently, human activities in the Bakırçay and Madra River catchments and their adjacent coastal areas are not only affected by the characteristics of the natural environments, but also directly shape landforms and locally dominate the landscape.

Hydrologic constructions for water storage are common in the Northern Highlands. These constructions have affected discharge and resulted in reduced sediment transport and alluviation within the lower Bakırçay plain and coastal areas since the 20th century (Kayan, 1999; Schneider et al., 2013; Schneider et al., 2015). Mechanized, industrial-scale agriculture is conducted on the entire eastern and western lower Bakırçay plain due to (a) river regulation and straightening, (b) drainage by a network of ditches, and (c) flood protection resulting from the construction of dams along the course of the Bakırçay River (Knitter, 2013).

Rich mineral resources such as coal (İnci, 2002; Karayiğit et al., 2017; Oskay et al., 2019) and gold (Yılmaz et al., 2007; Dill et al., 2015) are widely extracted (Yılmaz et al., 2010; Russell, 2013a, b; Hökerek and Özçelik, 2015), resulting in the formation of mining areas of varying sizes throughout the study area. Coal mining areas are located in the eastern

part of the area (Figure 4.2), i.e., the Soma coal basin, which is one of the largest economic lignite-bearing alluvial basins in Turkey, with lignite and kerogen as the main products (İnci, 2002; Hökerek and Özçelik, 2015). A gold and silver mine is located at Ovacık–Narlıca in the south of the Kozak Mountains (Figure 4.1A), where the precious metals formed during the Early Miocene (Yılmaz et al., 2007; Yılmaz et al., 2010). Mining activities in this area started around 600 BCE under the rule of King Croesus and were further exploited during the Roman period (c. 400 CE) (Yılmaz et al., 2007). The modern Ovacık Gold Mine has been active since ca. 1990. Stone or sand quarries are widely distributed throughout the study area and are mostly small in size. The stone quarry at Asağı Çuma (Figure 4.1A) has been used at least since the Hellenistic period (Russell, 2013a, b). Mining of perlite, a weathering product emerging from the hydration of obsidian, is conducted in the western Yunt Dağı Mountains (Knitter, 2013).

Agricultural terraces implemented for slope stabilization and water harvesting are widespread on the slopes of the intramountainous basins and along the slopes of Bakırçay and Madra tributaries; today they are preferably used for olive groves (Pirson, 2019; Becker et al., 2020b) (Figure S4.6). Ancient agricultural terraces from the Aegean Region date to at least Greco-Roman times (Grove and Rackham, 2003; Price and Nixon, 2005).

## 4.6 Conclusions

The Bakırçay and Madra River catchments and adjacent coastal areas form major parts of the Pergamon Micro-Region, corresponding to the environs of the UNESCO World Heritage site of Pergamon (modern Bergama). The landform characteristic of this area is highly influenced by tectonic processes and structural components. Overall, the Pergamon Micro-Region is an impressive example of a complex morphotectonic landscape, attributed to interfingering factors of tectonics, lithology, sea-level change, and human impact on erosion and sedimentation processes. Cenozoic tectonics and volcanism formed the basic horst and graben structures. Plio-Pleistocene tensional forces and crustal stretching formed the Bergama Graben and the adjoining horsts with their intramountainous basins. The Kozak Mountains to the north of the lower Bakırçay plain, and the Yunt Dağı Mountains to its south, show remarkably asymmetrical geomorphological features displaying these tectonic influences. The continuous uplift of the Kozak Horst resulted locally in a mountainous relief. Extensive interior plains served as local sediment sinks, which vary in size within highland areas. Rich mineral resources, such as coal, gold and silver, and perlite, are present and have been continuously mined

since antiquity, forming extensive quarrying areas. Overall, Quaternary tectonics resulted in a widely immature relief, which remains highly dynamic in the present day.

Due to the availability of several natural resources, the Pergamon Micro-Region was a preferred settlement area in early times. The infills of the intramountainous basins and graben structures provide suitable grounds for agriculture. Perennial streams sourced in the adjoining mountainous areas provide year-round water. Widespread andesitic rocks are an appropriate construction material. The forest areas in the adjoining mountains provided sufficient amounts of wood for construction needs and charcoal production. The topography of the Bergama Graben is characterized by two small seaside accesses and potentially flood-safe footslopes of the adjoining graben flanks, thus providing a high degree of protection for the settlements on the Bakırçay plain. However, as early as during antiquity, unsuitable land use triggered an enhancement in morphodynamics, resulting in the extended colluvial deposition and an increase in the major river sediment load, causing an aggradation of the alluvial plains and a progression of the delta areas, and, finally, the silting up of the Elaia harbor area.

## 5. Sediment analyses from Tekkedere catchment

Working package 2

### **Mid- to Late Holocene geomorphodynamics in a long-term settled mountain catchment in the Pergamon micro-region, western Turkey**

**Published manuscript:** Yang, X., Becker, F., Nykamp, M., Ludwig, B., Doğan, M., Doğan, T., Knitter, D., Schütt, B., 2023. Mid- to Late Holocene geomorphodynamics in a long-term settled mountain catchment in the Pergamon micro-region, western Turkey. *Quaternary Research* 114, 69–92. <https://doi.org/10.1017/qua.2022.73>.

This article is an open access article distributed under the terms and conditions of the Creative Commons Attribution (CC BY) license (<https://creativecommons.org/licenses/by/4.0/>).

**Supplementary materials:** see Supplementary materials – To chapter 5 (working package 2). The supplementary materials were originally published online at <https://doi.org/10.1017/qua.2022.73>.

**Research data:** Yang X., Becker F., Nykamp M., Schütt, B., 2022. Dataset of sediment analyses (pH, electrical conductivity, magnetic susceptibility, loss on ignition, and X-ray fluorescence) from the Tekkedere catchment in the Pergamon Micro-Region, western Turkey. In: Yang X (ed). *Pangaea*. <https://doi.pangaea.de/10.1594/PANGAEA.944177>.

This research data is an open access data distributed under the terms and conditions of the Creative Commons Attribution (CC BY) license (<https://creativecommons.org/licenses/by/4.0/>).

**Keywords:** sediment dynamics; floodplain-alluvial fan interplay; settlement pattern; Bakırçay river; geoarchaeology

**Abstract:** From 300 BC to AD 300, the city of Pergamon underwent a profound urban transformation that impacted the rural settlement patterns and the concomitant geomorphodynamics. We present a geoarchaeological study in a long-term settled catchment in the Pergamon micro-region, to disentangle the Holocene geomorphodynamics and triggering factors, e.g., climate change and human activities. The analyses of eight radiocarbon-dated sediment profiles from the Tekkedere alluvial fan and its catchment indicate four principal sedimentation phases. Phase 1 (ca. 6.2 to 5–4 ka BP) is dominated by the floodplain aggradation of the receiving Bakırçay river, which is followed by the formation of floodplain soils (phase 2). Substantial geomorphodynamic changes occurred around 4 ka BP (phase 3) when the edge of the floodplain was buried by fan sediments of the tributary Tekkedere creek. This is attributed to supraregional aridization and rapid climate change events, superimposed by the onset of local human activities. Repeated cycles of coarse- and fine-textured fan sediments with age inversions after ca. 3.8 ka BP and valley infills younger than 1300 yr BP indicate the strong erosion and redeposition of sediments in phase 4. This increased geomorphodynamics may coincide with the changing settlement pattern and thus reflect human-environment interactions.

## 5.1 Introduction

Holocene environmental changes and the interplay between natural conditions and human activities are intensely discussed research topics (Constante et al., 2010; Bellin et al., 2013; Ackermann et al., 2014a), which covers, e.g., soil erosion, natural hazard as well as settlement location decision (Black et al., 2011). The complex causes of changing geomorphodynamics in Mediterranean landscapes are debated for more than 50 years (Vita-Finzi, 1969b; Butzer, 2005; Duser et al., 2011; Walsh et al., 2019; Jouffroy-Bapicot et al., 2021). The main issue is to which degree geomorphological changes are triggered by environmental fluctuations (Avni et al., 2006; Jalut et al., 2009; Roberts et al., 2011a), human decisions, and socio-economic conditions (Van Andel et al., 1990; Remondo et al., 2005; Roberts, 2019), or the complex interaction of those (Brisset et al., 2013; Verstraeten et al., 2017; May et al., 2021). Hence, disentangling the related factors is not always straightforward (Fuchs, 2007; Walsh et al., 2019). Past human settlement strategies are, conversely, to some extent related to the geomorphic location and process (Kondolf and Piégay, 2011; Aucelli et al., 2018). River terraces and piedmonts are, for example, often the preferred settlement locations (e.g., Kidder et al., 2008; Knitter, 2013; Lü et al., 2019).

In the eastern Mediterranean, the meta-data analyses of Holocene terrestrial sediment archives indicate several phases of increased geomorphodynamics (Dusar et al., 2011; Walsh et al., 2019), which especially occur during the periods when human impacts on the environment became more important. This general trend, however, might not be equally seen in all Mediterranean areas due to diverse settlement patterns and landscape sensitivities. A ground check in small valleys occupied by remote settlements and under the background of large urban centers could thus provide advanced and multi-layered insights.

A suitable study area for such a ground check is the ancient city of Pergamon and its micro-region. As one of the most important and biggest cities in Asia Minor (Pirson, 2017), it experienced a profound transformation from the Hellenism to Roman Imperial Period (300 BC–AD 300) (Pirson, 2020). During this time, the urban area of Pergamon doubled (Wulf, 1994) coming along with a significant increase in population and an intensive public building program (Pirson, 2020). The population probably reached 180,000 people in the whole Pergamon micro-region (Zimmermann, 2011). The contemporary demilitarization of Pergamon's hinterland increased the importance of rural settlements (Figure 4.1) where possibly around 70% of the population lived (Pavúk and Horejs, 2018; Pirson, 2020; Laabs and Knitter, 2021). In the micro-region, diverse archaeological sites (e.g., settlements, farms, and luxury agricultural estates) were located in different geomorphological settings, including plains, plain-mountain transitional areas, intra-mountain basins, and small tributary valleys (Horejs, 2011a, 2014; Pirson, 2020, 2022). These landforms are potentially favorable for small settlements because of the proximity to fertile floodplains for agriculture and mountains for horticulture or pastoralism (Sommerer, 2008; Yang et al., 2021). Rural areas were also highly influenced by the rising demand for agricultural products during the transformation period (Knitter, 2013; Laabs and Knitter, 2021). Hence, the investigation of rural catchments is an integral part to develop a complete picture of the Pergamon history both on very local and micro-regional scales.

Previous geoarchaeological studies in the micro-region have different foci on selected archaeological sites, including the geomorphological investigation of prehistory settlement locations in the Gümüş catchment (Knitter, 2013); the Geyikli valley (Schneider et al., 2013) and the landscape evolution around a hill-top settlement (Schneider et al., 2014); the Bakırçay floodplain dynamics related to archaeological sites (Schneider et al., 2015; 2017); the ancient harbor city of Elaia with studies of its development and paleoenvironmental conditions (Seeliger et al., 2013; 2014; Pint et al., 2015; Shumilovskikh et al., 2016; Seeliger et al., 2017; 2019); the marine seismic investigation

of the ancient harbor of Kane (Fediuk et al., 2019); geophysical investigations on a monumental tumulus (Mecking et al., 2020).



**Figure 5.1** Topography and previous geoarchaeological study sites of the Pergamon micro-region. The inset map indicates the location of this study in the Aegean coastal region of western Turkey. Abbreviations: T. (Tepe), Yeni Y.T. (Yeni Yeldeğirmentepe), Sultant. (Sultantepe).

Notwithstanding the relatively intensive research program, no study in the micro-region covers a continuously occupied settlement chamber that allows for the reconstruction of local geomorphodynamics in the *longue durée*. In addition, the micro-region shows remarkable diversities in relief, drainage network, and sediment accumulation in different landscape units (Yang et al., 2021), but not all of these landforms have been geoarchaeologically studied. The meta-data analyses of  $^{14}\text{C}$ -ages from the western Pergamon micro-region suggest past geomorphodynamics are more or less associated with the general — but spatially more fragmented — settlement history of the region (Becker et al., 2020a). Hence, additional research especially in the Yunt Dağı mountains (the south part of the micro-region) is required to fill the gap and develop a deeper understanding of the whole area.

Tekkedere catchment is therefore selected as our study area to understand human-environment interactions in the Pergamon micro-region. Archaeological remains suggest the lower Tekkedere valley was continuously settled since the Middle Bronze Age (since ca. 1700 BC) (Ludwig, 2020a; Michalski, 2021). Its settlement history thus covers the main phases of intensified human impacts on Mediterranean landscapes during the Late Holocene (Dusar et al., 2011).

As the backbone of geoarchaeology, sediments and soils hold enormous information on landscape evolution and human usage history through various sediment analyses and chronological datings (Goldberg and Macphail, 2006). Different sediment archives might react separately to certain triggers on multiple temporal and spatial scales (e.g., Goldberg and Macphail, 2006; Dusar et al., 2011; Nykamp et al., 2021). Among them, alluvial (and colluvial) deposits near ancient settlements in lower-order watersheds hold the benefit of a more direct interpretation of causal relationships between human disturbance and sediment accumulation (Dotterweich, 2008; Dusar et al., 2011). With the availability of archaeological data, climatic and anthropogenic influences on geomorphodynamics can be more easily differentiated (Pérez-Lambán et al., 2018).

Our main objectives are a) reconstructing the geomorphodynamics of the Tekkedere valley and its alluvial fan using sediment analyses and radiocarbon dating and b) elucidating the potential drivers of the increasing geomorphodynamics, including the regional climate change and the local human impact (changing settlement pattern), in relation to supraregional Holocene records. The term geomorphodynamics used in this study refers to the changes of the Earth's surface and related processes (Sauer and Ries, 2008; Becker et al., 2020a). In particular, it covers erosion and deposition in the terrestrial environments in our study.

## **5.2 Study area**

### **5.2.1 Natural setting**

Tekkedere catchment (ca. 13 km<sup>2</sup> drainage basin area) is a mountainous sub-catchment (second order) of the western lower Bakırçay river catchment (Figure 5.1). The Bakırçay catchment (3382 km<sup>2</sup>) is under the territory of the Pergamon micro-region (Yang et al., 2021). It is one of the most fundamental river networks in Aegean Anatolia (Kayan, 1999; Yang et al., 2021). The modern climate is a typical Mediterranean subhumid climate that is characterized by dry and hot summers, and mild and wet winters (Peel et al., 2007).

The average annual precipitation was 749 mm and the temperature was 14.7 °C during 1981–2010 in Bergama (the modern name of Pergamon) (Yang et al., 2021).

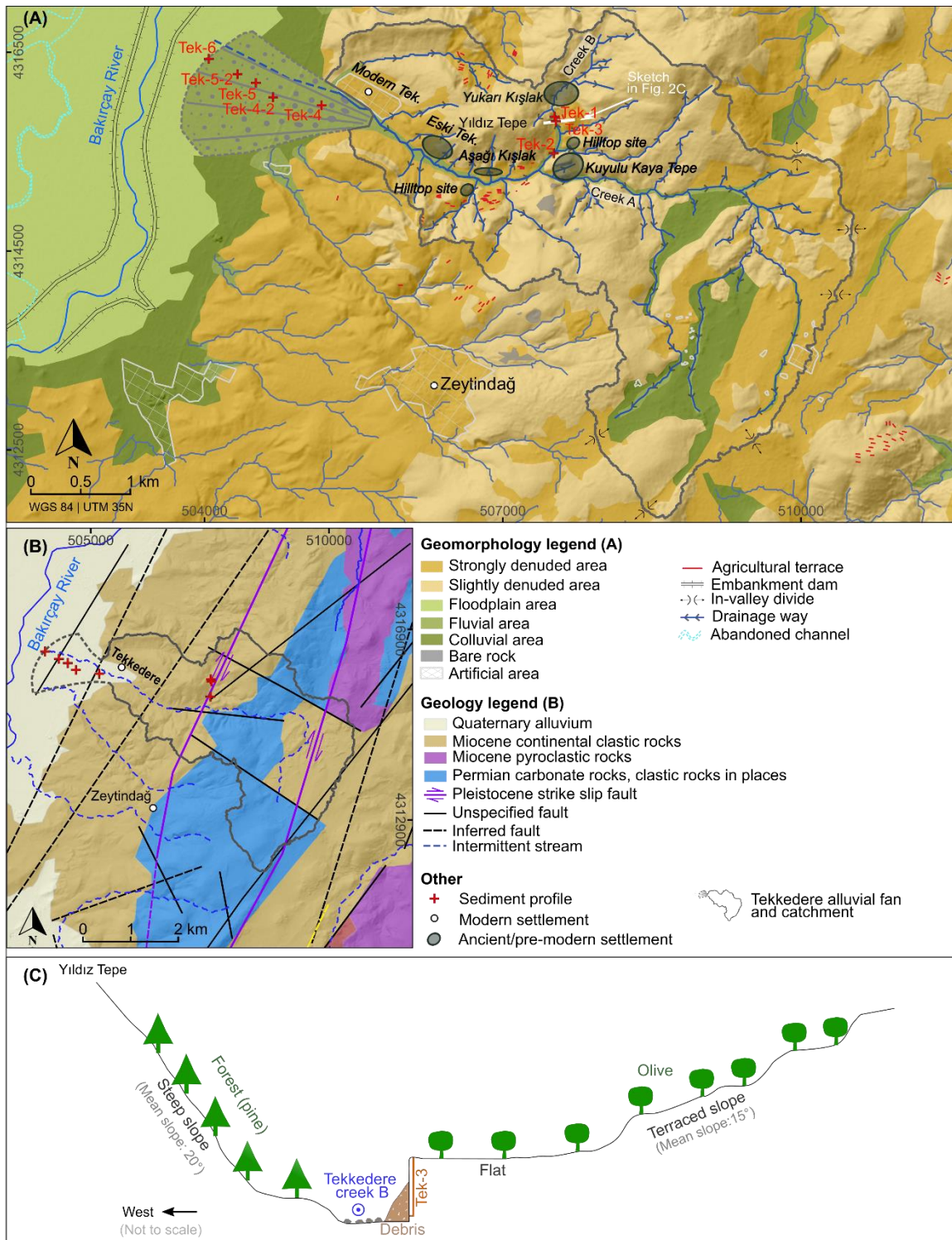


**Figure 5.2** Overview of the Tekkedere area. (A) Geomorphological map of the Tekkedere area complemented by the locations of the settlements and sediment profiles (Ludwig, 2019; 2020a; Michalski, 2021). (B) Geological map of the Tekkedere area (modified after Yang et al. (2021) based on (MTA, 2002; Emre et al., 2011a; 2011b)). (C) Schematic cross-section through the Tekkedere creek B (located at the sediment profile Tek-3).

The Tekkedere catchment is adjacent to the major route network between the city of Pergamon and its ancient harbor of Elaia (Pirson, 2008; Ludwig, 2020b) with short travel distances (around 18 km and 7 km, respectively) (Figure 5.1). Modern Tekkedere village is also close to ancient settlements of Teuthrania (Kalarga Tepe, ca. 8 km in the north) (Gehrke, 2014; Zimmermann et al., 2015; Williamson, 2016), Halisarna (Eğrigöl Tepe, ca. 9 km in the northeast) (Pirson, 2008; Zimmermann et al., 2015; Pavúk and Horejs, 2018), and the ancient polis of Atarneus (16 km in the northwest) (Pirson and Zimmermann, 2014; Zimmermann et al., 2015).

Geologically, the Pergamon micro-region is located in the western Extensional Province of Anatolia, which is regarded as one of the most rapidly extending regions on Earth (Özpolat et al., 2022). Under the tectonic stress, the NE-striking Miocene Zeytindağ and Örenli–Eğiller grabens and the Plio-Pleistocene Bergama Graben have formed (Bozkurt, 2003; Yang et al., 2021). The grabens of Zeytindağ and Bergama (Bakırçay) are ongoing subsiding with a subsidence rate lower than 1 mm/yr which results in the steadily rising of the local sea level during the Holocene (Seeliger et al., 2017). Part of the Zeytindağ Graben (Yilmaz et al., 2000) (Figure 5.1), the upper Tekkedere catchment is characterized by slightly rolling plains and shallow depressions (Yang et al., 2021). Within the catchment, Pleistocene tectonics formed NE-trending strike-slip faults (Yilmaz et al., 2000; Emre et al., 2011a; 2011b); more (unspecified or inferred) faults are reported with the occurrence of NE- or NW-trending (modified after Yang et al. (2021) based on MTA (2002)) (Figure 5.2B). The bedrock in the catchment is composed of Miocene continental clastic rocks (ca. 61 % of the catchment), Permian carbonate rocks with occasionally occurring clastic rocks (ca. 38 % of the catchment), and pyroclastic rocks (ca. 1 % of the catchment) (MTA, 2002) (Figure 5.2B). Reddish-brown and red Mediterranean soils develop on the clastic and pyroclastic rocks, whereas Rendzinas form on the carbonate rocks (Danacıoğlu and Tağıl, 2017).

Tekkedere creek encompasses several intermittent drainage systems (Figure 5.2A) with a torrential flow regime, which are similar to the small rivers along the Aegean coast (Kayan and Vardar, 2007b). There are two major creeks in the catchment. Creek A, the longest drainage way in the valley, flows from the intramountainous basin of the headwater area to the gorge, south of Kuyulu Kaya Tepe (summit ca. 160 m a.s.l.). Creek B drains the northern part of the catchment (east of the Yıldız Tepe, summit ca. 210 m a.s.l.) and joins with creek A at the west of the Kuyulu Kaya Tepe, which continues westwards as the Tekkedere creek. The creek is channelized on its alluvial fan and drains into the Bakırçay river just 12 km upstream of its mouth into the Aegean Sea.

The slopes of the lower valley (including the valley of creek B) are asymmetrical (Ludwig, 2019) (Figure 5.2C). Its northern slopes are steeply inclined (16–37°, mean = 20°) whereas the southern slopes are gentler (10–30°, mean = 15°). Strong denudation and soil erosion are the prevailing geomorphological processes on the southern slopes, partly confined by agricultural terraces grown with olives (Figure 5.2A and C) (Becker et al., 2020b). Where soils are fully eroded, scattered bare rocks crop out, mainly on the southern slopes (Figure 5.2A) (Ludwig, 2019). The Kuyulu Kaya Tepe has large areas of outcropping bedrocks with screes covering its southern foot slopes.

Locally, the tributaries of Tekkedere creek are incised for more than 1 m into the valley infills (Figure 5.2C). The valley bottom widens in its lower course where the modern Tekkedere village is built at its right riverbank (Figure 5.2A). The Tekkedere alluvial fan forms at the opening area from the valley to the Bakırçay floodplain, covers an area of ca. 2 km<sup>2</sup> (length: ca. 2 km; width: ca. 1.4 km), and is the largest alluvial fan in the foreland of the western Yunt Dağı mountains. The altitude difference from the fan's apex to its toe amounts to 18 m which is calculated based on TanDEM-X data (Wessel et al., 2018). At present, the toe of the fan is located only ca. 500 m east of the current Bakırçay river channel (Figure 5.2A).

While arable lands with the cropping of vegetables and grains dominate the land use in the headwater area of Tekkedere valley, coniferous forests, transitional woodland–shrubland covers, and olive groves on agricultural terraces characterize the vegetation cover on the slopes of the middle valley (Figure S5.1 based on Corine Land Cover data (Cole et al., 2018) and field observation). In the lower part, pine forests cover the northern slopes (Yıldız Tepe), whereas olives are mainly cultivated on the southern slopes and the valley bottom. On the Tekkedere alluvial fan, olive cultivation characterizes its upper part. Downslope the fan's apex, cropping of cotton and vegetables predominate, and fig and citrus fruit trees occur sporadically.

A palynological study around Elaia indicates the vicinity of Tekkedere was dominated by natural deciduous oak forests between 7.6 and 3 ka BP (Shumilovskikh et al., 2016). Deforestation occurred as a consequence of the increased layout of olive groves and the development of macchia shrublands under rising grazing pressure since the Hellenistic Period, reaching a maximum during 2.1–1.8 ka BP. Alongside the hillslopes, semi-natural forests (mainly pines) developed during the past millennium (Shumilovskikh et al., 2016). The abundance of grains and the fertility of the area were described by ancient geographers and historians (Sommerer, 2008; Pirson and Zimmermann, 2014). Recent studies, however, suggest that Pergamon's demand for grain, at least in the Roman

Imperial Period, cannot be covered without imports or environmental modifications (e.g., agricultural terracing) (Kobes, 1999; Günther et al., 2021; Laabs and Knitter, 2021).

### **5.2.2 Settlement history**

Since 2018, archaeological surveys have been conducted in the Tekkedere catchment by the German Archaeological Institute (Deutsches Archäologisches Institut, DAI) (Ludwig, 2019; 2020a). The findings give evidence for at least six archaeological sites in the catchment (Figure 5.2A), which develops an almost uninterrupted settlement continuity and changing settlement patterns since the late Middle Bronze Age (ca. 1700 BC) (Ludwig, 2019; 2020a; Michalski, 2021).

Ceramic remains on and around the hill site of Kuyulu Kaya Tepe (Um19 Fst 02) (Figure 5.2A) indicate settlement activities continued from the late Middle Bronze Age to the end of Early Byzantine time (ca. 3.7–1.2 ka BP) (Ludwig, 2019; Michalski, 2021). Building remains including several cisterns are found on the rock plateau (Ludwig, 2019). The foot slopes of Kuyulu Kaya Tepe were situated by a small rural settlement, which probably reached its peak during the Classic period. Considering that the Kuyulu Kaya Tepe surmounts the surroundings by ca. 40 m and is characterized by steep slopes with outcropping bedrocks towards creek A, the site, especially the hill site on the rock plateau, might have been used as a fortress to overlook or control the entire Tekkedere valley and large parts of the western lower Bakırçay plain (Ludwig, 2020a) (Figure 5.2A).

Two small hilltop sites (UM19 Fst 04 and 13), a few hundred meters to the north and west of the Kuyulu Kaya Tepe in the creek B (Figure 5.2A) with a high concentration of ceramics and bricks, suggest human activities existed during the Classic period (Ludwig, 2020a).

Predecessor settlement of the modern Tekkedere village was likely first established as the upper settlement (Yukarı Kışlak; UM18 Fst 01 or UM19 Fst 09), ca. 1 km north of the Kuyulu Kaya Tepe in the creek B (Ludwig, 2019) (Figure 5.2A). Based on the archaeological results, the upper settlement is assumed to have a duration from the late antiquity to the Byzantine time (Ludwig, 2020a). The settlement was replaced by the smaller lower settlement (Aşağı Kışlak; UM19 Fst 14) which was situated in the middle of the lower valley (Ludwig, 2020a; Tozan, 2022) (Figure 5.2A). When the lower settlement was abandoned, the old Tekkedere settlement (Eski Tekkedere) was built further downstream (Tozan, 2022). The old Tekkedere settlement was given up mostly due to an earthquake-triggered landslide, which was previously assumed to occur in the middle of the 19<sup>th</sup> century (Ludwig, 2020a). Based on the information provided by the locals, it was the earthquake that took place around Dikili, Zeytindağ, and Bergama in 1939

(Paradisopoulou et al., 2010; Çelik et al., 2019). Residents left and developed the modern Tekkedere village which is built directly to the west of the old Tekkedere settlement (Ludwig, 2020a).

## **5.3 Methods**

### **5.3.1 Fieldwork**

Three sediment outcrops along the banks of creek B were described and sampled in September 2019 (Becker et al., 2020b) and five sediment cores were extracted and brought to the surface along a transect from the apex to the toe of the alluvial fan by vibracoring (Wacker BHF 30 S, with open cores of 5 cm diameter) in October 2020 (Becker et al., 2022b) (Figure 5.2A and Table 5.1). None of the profiles reached the underlying bedrock.

Lithostratigraphy was documented as comprising sediment color (Munsell soil color), unit thickness, sediment depositional structure (Stow, 2005), sediment texture and fabric (Blair and McPherson, 1999), hydromorphic feature, biological modification, and occurrence of artifacts (Jahn et al., 2006). The degree of reaction to 9.9 % HCl was applied as an indicator for the amount of calcium carbonate ( $\text{CaCO}_3$ ) (Jahn et al., 2006). A summary classification of the sediment description can be found in Yang et al. (2022). Sediment samples (3–5 cm thick pieces;  $n = 191$ ) were collected for geochemical analyses corresponding to their position of unit boundary and thickness. Sediment profiles were carefully checked for charcoal pieces and bulk samples that contain organic matter for radiocarbon dating.

**Table 5.1** Metadata of sediment outcrops in the valley (n = 3) and drilling cores on the alluvial fan (n = 5) of the Tekkedere catchment (WGS 84).

Sediment sequence	Latitude (° N)	Longitude (° E)	Elevation (m a.s.l.)	Depth (cm)	Samples (n)	Geomorphological position	Land use
Tek-1	38.99164	27.08685	88.7	176	14	Valley (channel bank)	Olive grove
Tek-2	38.98832	27.08677	70.8	158	11	Valley (channel bank)	Olive grove
Tek-3	38.99120	27.08701	84.0	220	19	Valley (channel bank)	Olive grove
Tek-4	38.99268	27.05971	16.6	200	0	Alluvial fan (apex)	Olive grove
Tek-4-2	38.99341	27.05418	11.5	700	32	Alluvial fan (middle)	Arable land
Tek-5	38.99472	27.05216	9.1	786	48	Alluvial fan (middle)	Arable land
Tek-5-2	38.99554	27.04988	7.4	400	17	Alluvial fan (middle)	Arable land
Tek-6	38.99688	27.04662	6.3	800	50	Alluvial fan (toe)	Arable land

## 5.3.2 Laboratory work

### 5.3.2.1 Sediment analyses

Geochemical analyses of sediments could effectively assist in distinguishing the occurrence of past soil formation and the difference in natural and cultural processes (Goldberg et al., 2017). Sediment samples were analyzed in the laboratory of the Bergama archaeological excavation house. Before the measurement, samples were air-dried for more than 48 h and the aggregates were crushed in a porcelain mortar. For subsequent analyses, the fine fraction ( $\varnothing < 2$  mm) was separated from the coarse component by dry sieving.

The pH and electrical conductivity (EC) values were obtained in the water-saturated sediments (1:2.5 solutions of 5 g sediments and 12.5 mL distilled water) with a TDS/EC/pH/TEMP meter (EZ9908; resolution: 0.01 pH, 1  $\mu\text{S cm}^{-1}$  EC). Reaction class terms and the pH range are based on the soil survey manual (Soil Science Division Staff, 2017) (Table 5.2). The pH value in sediment solutions is highly related to the buffering process of organic acids and is indicative of paleosol occurrence (Nykamp et al., 2020) and human activity (Goldberg et al., 2017). The EC value provides a hint of readily soluble salts which crystallize from chemical weathering or soil water evaporites (Nykamp et al., 2020).

**Table 5.2** The equal interval classification of the sediment proxies (except pH (Soil Science Division Staff, 2017)).<sup>a</sup>

Class	pH		EC ( $\mu\text{S/cm}$ )	$X_{\text{LF}}$ ( $10^{-8}$ m <sup>3</sup> /kg)	LOI <sub>550</sub> (mass%)
Class 1 (very low)	6.5–7.3	neutral	84–227	4–32	0.7–2.1
Class 2 (low)	7.3–7.8	slightly alkaline	227–371	32–60	2.1–3.5
Class 3 (medium)	7.8–8.4	moderately alkaline	371–515	60–87	3.5–4.9
Class 4 (high)	8.4–9	strongly alkaline	515–659	87–115	4.9–6.2
Class 5 (very high)	$\geq 9$	very strongly alkaline	659–803	115–143	6.2–7.6

<sup>a</sup> EC, electrical conductivity; LOI<sub>550</sub>, loss on ignition at 550°C;  $X_{\text{LF}}$ , mass-specific susceptibility at the low frequency.

Approximately 10 g of oven-dried (105 °C) sediments were measured on the loss on ignition at 550 °C (LOI<sub>550</sub>) (Dean, 1974; Heiri et al., 2001). LOI<sub>550</sub> was calculated as the

weight difference of a sample treated by both temperatures and is used for the estimation of organic matter content (Heiri et al., 2001; Santisteban et al., 2004). The in-lab reference material was measured with every 20 samples to control variability, which is reproducible with a median LOI<sub>550</sub> value of 5.6 mass-% (median absolute deviation (MAD): 0.2 mass-%). Often, a higher LOI<sub>550</sub> value is associated with oxidation accumulation, pointing to soil horizons, the stability of land surface, and the intensity of human activity (Goldberg and Macphail, 2006; Panin et al., 2021).

The magnetic susceptibility of sediments was measured using a Bartington magnetic susceptibility system (MS3 meter and MS2B dual-frequency sensor; measuring resolution:  $2 \times 10^{-6}$  SI and range: 26 SI) via the *Bartsoft* software. The volume-specific magnetic susceptibility ( $\kappa$ ) at low frequency (LF, 0.46 kHz) of weighed samples filled in 12 cm<sup>3</sup> plastic pots was determined with triple repetition. The mass-specific susceptibility at the low frequency ( $X_{LF}$ ,  $10^{-8}$  m<sup>3</sup> kg<sup>-1</sup>) was calculated according to Dearing (Dearing, 1994; Dearing et al., 1996). The confidence intervals of sample median  $X_{LF}$  values were estimated by simple quantile bootstrapping (B = 1,000) in R (version 3.6) (R Core Team, 2021). In addition, we used the MS2B meter to measure the Tek-5 samples (n = 48) five times. The results are highly comparable to 88 % of samples used via the MS3 meter (correlation of the sediment measured in both meters: median = 0.97). The median of the volume-specific susceptibility of the 10 mL calibration sample is  $2620 \times 10^{-5}$  SI (MAD:  $0.25 \times 10^{-5}$  SI; accuracy: 1%). Higher  $X_{LF}$  values are generally related to the formation of clay minerals under a higher weathering process (Maher and Thompson, 1991; Blundell et al., 2009; Sherriff, 2014).

The element composition of sediment samples from the profiles of Tek-5, Tek-5-2, and Tek-6 was analyzed using a portable energy-dispersive X-ray fluorescence spectrometer (p-ED-XRF; Thermo Fisher Scientific NITON XL3t) measuring each sample for 120 s in the manufacture's "Mining Cu/Zn" mode with main, high, low, and light filters (50, 50, 15/20, and 8 kV, respectively). The certified reference material (LKSD-4) (Lynch, 1990) and the acid-purified silica sand were taken as standards to ensure the measurement quality. The reproducibility of selected elements (Zr, Rb, Ti, and Ca) for LKSD-4 and silica sand are in a range of 22%–34% and 6%–11%, respectively. Two element ratios were calculated for the sediment characterization. The Zr/Rb ratio is used as a proxy for grain size variability (Dinelli et al., 2007) and the Ca/Ti ratio as an indicator for synsedimentary weathering as well for the precipitation of secondary carbonates (Ülgen et al., 2012).

The sediment proxies in this study are reported in median and median absolute deviation (MAD, in parentheses) values and are grouped using an equal interval classification of

the data (Table 5.2). Raw/processed data and R code (R Core Team, 2021) could be found in the dataset of Pangaea (Yang et al., 2022).

### **5.3.2.2 Radiocarbon dating**

In our study, radiocarbon dating would be the optimum solution for the development of a chronological framework due to the scarcity of available materials for alternative methods. The samples were conducted by accelerator mass spectrometry (AMS) radiocarbon dating ( $^{14}\text{C}$ ) at the TÜBİTAK National 1 MV AMS Laboratory (Doğan et al., 2021). Dated materials ( $n = 20$ ) include charcoals, the mixture of mainly charcoal with adjacent sediments (if %C of the macroscopically separatable charcoal is  $<1-2$  mg), organic-rich bulk samples, and one terrestrial snail shell (Table 5.3).

Macroscopic plants and rootlets have been removed from the samples before the standard pretreatment procedure (acid-base-acid (ABA) protocol) was applied (Fowler et al., 1986; Bronk Ramsey, 2008; Brock et al., 2010). Fragile charcoal remnants with an amount of charcoal below ca. 10 mg were only treated with acid wash (Fowler et al., 1986; Brock et al., 2010). The radiocarbon ages were calibrated via the *IntCal20* calibration curve (Reimer et al., 2020) and the *rcarbon* package (Crema and Bevan, 2021) in R (version 3.6) (R Core Team, 2021). We report a 95 % probability range of the calibrated age.

**Table 5.3** The AMS-<sup>14</sup>C dating samples from the Tekkedere valley (n = 6) and Tekkedere alluvial fan (n = 14), pretreatment procedure, sediment facies of the sample location and their dating results and calibration (calibration curve: *IntCal20* (Reimer et al., 2020)).

Sediment profile	Depth/cm bs (Unit ID) <sup>a</sup>	Lab.ID (TÜBİTAK*)	Dated material <sup>b</sup>	Pretreatment Procedure <sup>c</sup>	Sediment facies <sup>d</sup>	Radiocarbon age <sup>14</sup> C yr BP ± σ	cal yr BP		BC/AD (95%)
							Median	95 % probability	
	40 (⑤)	1143	Charcoal	ABA	Ab	318 ± 23	388	456–308	AD 1494–1642
Tek-1	144 (②)	1145	Shell	Acid Splash	Aa	663 ± 24	628	668–560	AD 1282–1390
	172 (①)	1142	Charcoal	ABA	Ab	627 ± 24	599	653–554	AD 1297–1396
Tek-2	65 (④)	1144	Charcoal	ABA	sAa	899 ± 23	791	904–732	AD 1046–1218
	75-80 (④)	1141	Charcoal	ABA	sAa	910 ± 24	827	908–737	AD 1042–1213
Tek-3	125 (③)	1140	Charcoal	ABA	Ab	1243 ± 26	1183	1271–1072	AD 679–878
Tek-4-2	161 (⑥)	1646	C/S	ABA	Bb	4164 ± 28	4708	4829–4581	2880–2632 BC
	469 (②)	1647	C/S	Acid wash	sBa	4283 ± 45	4852	4971–4653	3022–2704 BC

Sediment profile	Depth/cm bs (Unit ID) <sup>a</sup>	Lab.ID (TÜBITAK*)	Dated material <sup>b</sup>	Pretreatment Procedure <sup>c</sup>	Sediment facies <sup>d</sup>	Radiocarbon age <sup>14</sup> C yr BP ± σ	cal yr BP		BC/AD (95%)
							Median	95 % probability	
	221 (⑥)	1648	C/S	Acid wash	Ba	5680 ± 31	6457	6556–6396	4607–4447 BC
	260–265 (⑥)	1649	C/S	Acid wash	Ba	4719 ± 29	5447	5575–5325	3626–3376 BC
	363 (⑤)	1650	C/S	Acid wash	Bb	3399 ± 27	3634	3812–3566	1863–1617 BC
Tek-5	427 (④)	1651	Bulk soil	Acid wash	sCf	4330 ± 30	4892	4968–4841	3019–2892 BC
	435 (④)	1652	C/S	Acid wash	sCf	4635 ± 27	5412	5462–5309	3513–3360 BC
	478 (③)	1653	Bulk soil	Acid wash	sCf	5347 ± 30	6128	6270–6002	4321–4053 BC
	781 (①)	1654	Charcoal	ABA	Cf	4502 ± 31	5162	5301–5045	3352–3096 BC
	273 (②)	1655	Charcoal	Acid wash	Ba	2542 ± 26	2627	2743–2499	794–550 BC
Tek-5-2	285-286 (①)	1656	Bulk soil	Acid wash	sCf	3734 ± 31	4086	4224–3982	2275–2033 BC
	354 (①)	1657	C/S	ABA	Cf	5046 ± 28	5823	5901–5718	3952–3769 BC
	459–460 (②)	1658	Bulk soil	Acid wash	Cs	4308 ± 29	4861	4959–4833	3010–2884 BC
Tek-6	665–666 (②)	1659	Bulk soil	Acid wash	Cs	5294 ± 29	6082	6187–5947	4238–3998 BC

<sup>a</sup> cm bs, cm below surface. Numbers in circles correspond to unit numbers in Figures. 5.3–5.5.

<sup>b</sup> C/S refers to mixed materials (charcoal and accompanying sediments).

<sup>c</sup> ABA refers to standard acid-base-acid protocol.

<sup>d</sup> See Table 5.4 for descriptions.

## 5.4 Sediment characteristics

The analyzed sediment profiles are located in two different landforms: the valley infill of the tributary creek B and the Tekkedere alluvial fan (Table 5.1). Profile Tek-2 from the valley infill and profiles of Tek-5 and Tek-6 from the fan are taken as key profiles and are presented in detail. More profiles in the Supplementary material show comparable sediment characteristics. The calculation of the median value (To chapter 5 – working package 2) of sediment proxies from different profiles' sedimentary units is provided in the dataset (Yang et al., 2022). Taken together, the samples' age ranges between ca. 6.6 and 0.3 cal ka BP (Table 5.3).

### 5.4.1 Tekkedere valley infill: Key-profile Tek-2

Profile Tek-2 has a total thickness of 158 cm and its six lithostratigraphic units are dominated by alternating units of silts/sands and pebbles (Figure 5.3). Except for the upper two units (units 5 and 6), the lithostratigraphic units 1–4 show sharp contacts. Roots occur commonly above 100 cm b.s. The sediment matrix is strongly calcareous and moderately alkaline (pH: 8.1 (0.1)). Electrical conductivity values (EC: 95 (10)  $\mu\text{S cm}^{-1}$ ) are very low (class 1, Table 5.2) and only slightly increased in unit 4.  $X_{\text{LF}}$  (24 (9)  $10^{-8} \text{ m}^3 \text{ kg}^{-1}$ , class 1) and  $\text{LOI}_{550}$  (4.1 (0.6) mass-%, class 3) peak in the same unit.

Basal unit 1 (158–135 cm b.s.) is characterized by yellowish brown, highly compacted silty sand with few embedded medium pebbles ( $\varnothing < 2 \text{ cm}$ ). Some pebbles show a grayish weathering rind.

Unit 2 (135–116 cm b.s.) shows clast-supported fabric. The clasts consist of yellowish brown, disorganized pebbles with few fine cobbles ( $\varnothing < 11 \text{ cm}$ ). The matrix is sandy silt with adhesions of secondary precipitated carbonates and very few fine roots.

Unit 3 (116–84 cm b.s.) is characterized by normally graded fabric. The sediment texture changes from strong yellowish silty sand with few angular, disorganized fine to coarse pebbles ( $\varnothing < 3 \text{ cm}$ ) at the base of the unit, to light gray silty sand at the top. Clasts are partly carbonated and slightly weathered. Very few fine to coarse roots occur throughout the unit. The analytical values of sediment samples ( $n = 4$ ) from units 1–3 remain roughly constant. Sediments are moderately alkaline (pH: 8.2 (0)). EC (94 (4)  $\mu\text{S cm}^{-1}$ , class 1) and  $X_{\text{LF}}$  (14 (3)  $10^{-8} \text{ m}^3 \text{ kg}^{-1}$ , class 1) are very low.  $\text{LOI}_{550}$  (3.4 (0.2) mass-%, class 2) is low.

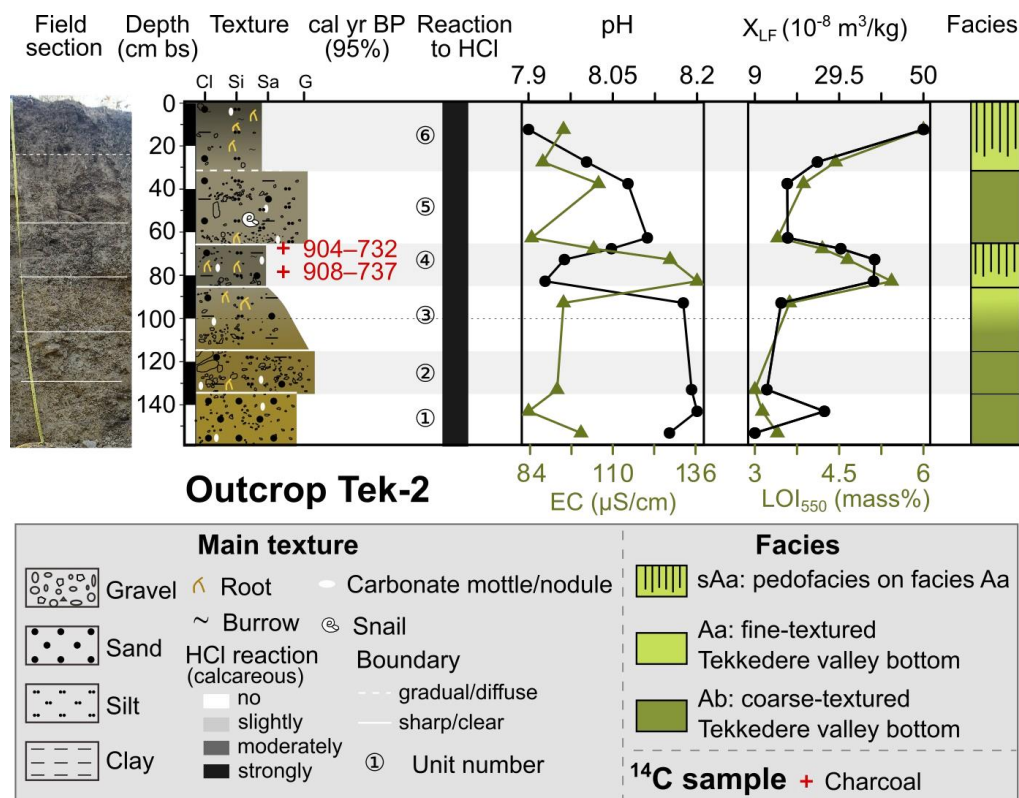


**Figure 5.3** The lithostratigraphy, radiocarbon dates, and sedimentological analyses of sediment outcrop Tek-2. The color of the sediment texture column represents the color observed in the field; the shaded band represents the different units and the dashed line refers to the depth in every meter. cm bs, cm below surface; EC, electrical conductivity; LOI<sub>550</sub>, loss on ignition at 550°C; X<sub>LF</sub>, mass-specific susceptibility at the low frequency.

Unit 4 (84–65 cm b.s.) is composed of light grayish, slightly sandy silt with few fine pebbles. Fine roots and burrows are abundant. Sediments are moderately alkaline and enhanced in solutes (EC: 128 (9)  $\mu\text{S cm}^{-1}$ , class 1,  $n = 3$ ). X<sub>LF</sub> amounts to 38 (0)  $10^{-8} \text{ m}^3 \text{ kg}^{-1}$  (class 2,  $n = 3$ ), and LOI<sub>550</sub> totals to 4.9 (0.5) mass-% (class 4,  $n = 3$ ). Two charcoal pieces (at 65 cm b.s. and 75–80 cm b.s.) date the unit 4 around 908–732 cal yr BP (Table 5.3 and Figure 5.3).

Unit 5 (65–32 cm b.s.) is characterized by light grayish, silty sand with embedded pebbles to fine cobbles ( $\varnothing < 7 \text{ cm}$ ). A thin rooted clast-supported layer of fine pebbles is interbedded at 65–60 cm b.s. A shell of a land snail occurs at 55 cm b.s. EC, X<sub>LF</sub>, and LOI<sub>550</sub> values ( $n = 2$ ) widely correspond to the values of units 1–3.

Unit 6 (32–0 cm b.s.) corresponds to the modern plow horizon. It consists of dark to light brown sandy silt with very few fine to coarse pebbles ( $\varnothing < 3 \text{ cm}$ ). The unit has abundant roots and common burrows. The samples ( $n = 2$ ) show slightly decreased pH values (7.9 (0.1)) and increased X<sub>LF</sub> (37 (13)  $10^{-8} \text{ m}^3 \text{ kg}^{-1}$ , class 2) and LOI<sub>550</sub> (5.5 (0.8) mass-%, class 4) values.

### 5.4.2 Tekkedere mid-fan: Key-profile Tek-5

Profile Tek-5 was obtained from the middle position of the Tekkedere alluvial fan (Figure 5.2A). The extracted 786-cm-thick sediment sequence is divided into eight units (Figure 5.4). The lower part of the profile (below 426 cm b.s., units 1–4) is mainly characterized by layers of dark grayish or brownish silts with very few embedded fine pebbles, whereas units of brownish silts and sands with variable contents of pebbles prevail in the upper half of the profile (units 5–8). Concentrations of secondary precipitated carbonates and manganese mottles or small nodules occur almost throughout the whole profile.

Sediment samples ( $n = 48$ ) in the profile Tek-5 are slightly to strongly alkaline (pH: 8.0 (0.1)). EC indicates an overall very low amount of solutes ( $195 (43) \mu\text{S cm}^{-1}$ , class 1,  $n = 48$ ) with slightly increased values in units 1–4 ( $237 (35) \mu\text{S cm}^{-1}$ , class 2,  $n = 25$ ).  $X_{\text{LF}}$  shows a median value of  $27 (7) 10^{-8} \text{ m}^3 \text{ kg}^{-1}$  (class 1,  $n = 48$ ) with relatively low results in units 1–4 ( $20 (8) 10^{-8} \text{ m}^3 \text{ kg}^{-1}$ , class 1,  $n = 25$ ) and relatively high results in units 5–8 ( $32 (7) 10^{-8} \text{ m}^3 \text{ kg}^{-1}$ , class 2,  $n = 23$ ).  $\text{LOI}_{550}$  has a median value of 3.5 (0.9) mass-% (class 3,  $n = 48$ ) in the profile with slightly higher values in units 1–4 (4.4 (0.7) mass-%, class 3,  $n = 25$ ) than in units 5–8 (3.2 (0.4) mass-%, class 2,  $n = 23$ ). Element ratios of Ca/Ti and Zr/Rb also display marked differences between the upper and lower half of the profile. Variabilities of both Ca/Ti (14.70 (2.1),  $n = 25$ ) and Zr/Rb (1.50 (0.2),  $n = 25$ ) in units 1–4 are slightly smaller than in units 5–8 where Ca/Ti has a median value of 19.99 (4.4,  $n = 23$ ) and Zr/Rb 1.71 (0.2,  $n = 23$ ) (Figure 5.4). Beside the sedimentological differences between the two parts of the profile, differences are also identified among the units. Dating results in Tek-5 ( $n = 7$ , from ca. 6.6 cal ka BP at 221 cm b.s. to 3.6 cal ka BP at 363 cm b.s.) show markedly repeated age inversions (Table 5.3 and Figure 5.4).

Unit 1 (786–693 cm b.s.) consists of very dark gray (10 YR 3/1), moderately to strongly calcareous sandy silt. An intermediate sandy layer occurs at 751–740 cm b.s. Common carbonate nodules and few manganese mottles exist. Fine pieces of snail shells were found around 765 cm b.s. The charcoal sample from the bottom of the profile (781 cm b.s.) dates to 5301–5045 cal yr BP (Table 5.3). The transition from unit 1 to 2 takes place gradually.

Unit 2 (693–607 cm b.s.) contains two layers of dark yellowish brown (10 YR 4/3) sandy silt with an intercalated layer of very dark grayish brown (10 YR 3/2) sandy silt at 658–662 cm b.s. Sediments are strongly calcareous. Few blackish manganese and reddish iron nodules ( $\varnothing < 1$  cm) and common carbonate nodules occur in the lower third of the unit. The sediment boundary between units 2 and 3 is gradual.

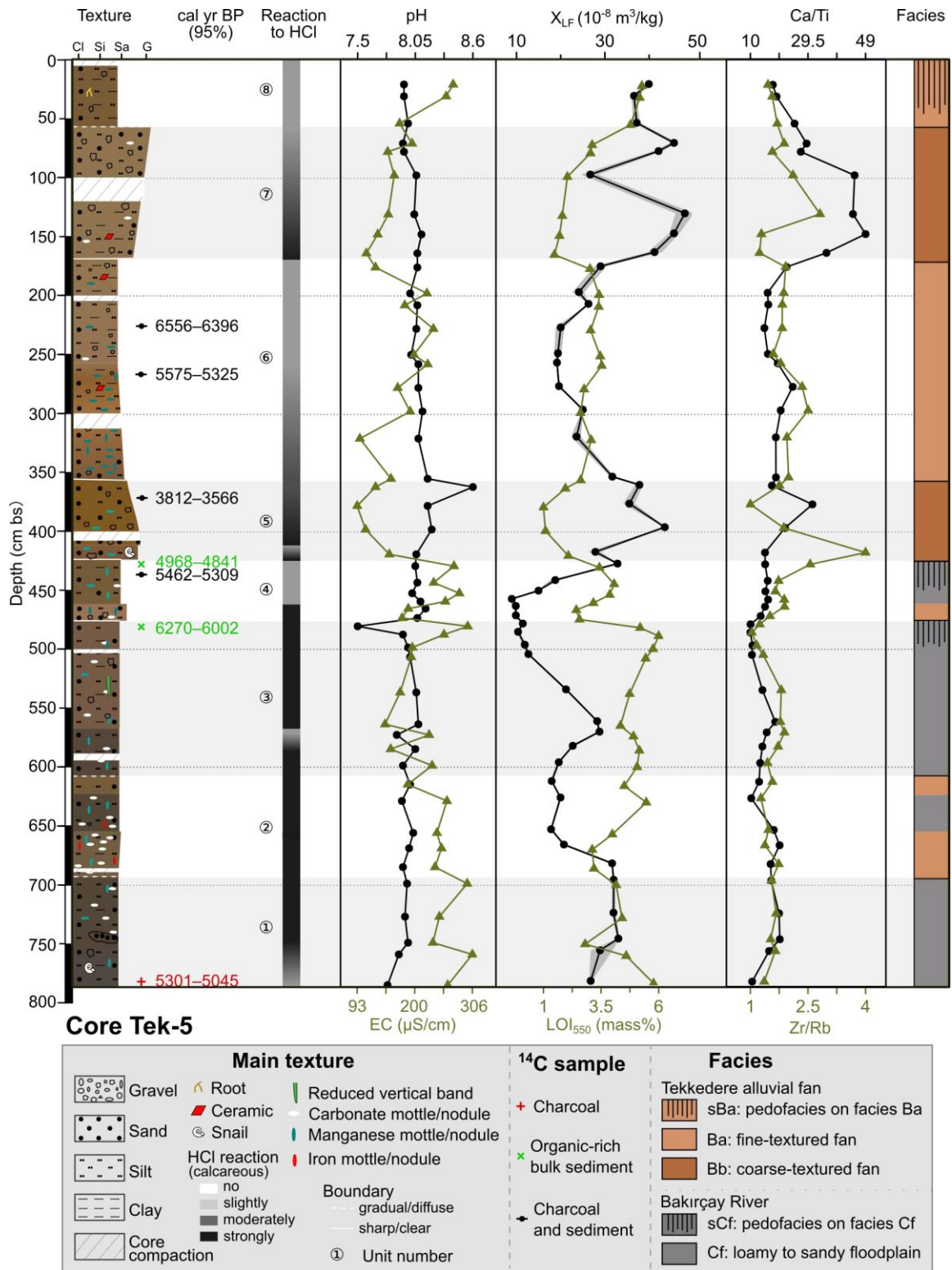


**Figure 5.4** The lithostratigraphy, radiocarbon dates, and sediment analyses of sediment core Tek-5. The confidence intervals of the sample median mass-specific susceptibility at the low frequency ( $X_{LF}$ ) values are estimated by simple quantile bootstrapping ( $B = 1,000$ ). cm bs, cm below surface; EC, electrical conductivity; LOI<sub>550</sub>, loss on ignition at 550°C.

Unit 3 (607–477 cm b.s.) consists of strongly calcareous sandy silt with very few fine pebbles. The color changes from dark brown (7.5 YR 3/2) at the bottom to brown (7.5 YR

4/3) at the top. Few fine carbonate nodules and manganese mottles are incorporated. One vertical greenish mottled structure occurs at 530–520 cm b.s.

Bulk parameters of  $LOI_{550}$  and  $X_{LF}$  display strong oscillations in median values of the three units (Figure 5.4). In unit 1,  $X_{LF}$  has a median value of  $32 (2) 10^{-8} \text{ m}^3 \text{ kg}^{-1}$  (class 2,  $n = 5$ ), and the median value of  $LOI_{550}$  ranges into class 3 (4.4 (0.2) mass-%). With decreasing depth in unit 2,  $LOI_{550}$  values slightly increase while simultaneously values for  $X_{LF}$  slightly decrease (Figure 5.4). Small peaks in  $X_{LF}$  and  $LOI_{550}$  occur at the intermediate layer of unit 2. In unit 3,  $X_{LF}$  values ( $n = 9$ ) peak at 570 cm b.s. ( $29 10^{-8} \text{ m}^3 \text{ kg}^{-1}$ , class 1) and gradually decrease to the top reaching a minimum value ( $10 10^{-8} \text{ m}^3 \text{ kg}^{-1}$ , class 1) at 480 cm b.s.  $LOI_{550}$  values gradually increase from 5 to 5.8 mass-% (class 4) with decreasing depth. At the top of unit 3 (478 cm b.s.), the organic-rich bulk sample dates to 6270–6002 cal yr BP. The boundary between unit 3 and overlying unit 4 is sharp.

Unit 4 (477–426 cm b.s.) is composed of brown (7.5 YR 5/4), poorly compacted and strongly calcareous, slightly fine pebbly, silty sand in the lower part (477–463 cm b.s.) and dark yellowish brown (10 YR 4/4), heavily compacted, moderately calcareous sandy silt in the upper part (463–426 cm b.s.). Some pebbles are carbonated. Few fine manganese nodules and very few fine carbonate concretions were found.

The median pH value of water-saturated sediments in unit 4 is around 8.1 ( $n = 6$ ) and is in the same range as the underlying units (moderately alkaline). Also, EC values are comparable to those in the underlying sediments but underly remarkable oscillations ( $245 (32) \mu\text{S cm}^{-1}$ , class 2,  $n = 6$ ).  $LOI_{550}$  is low in the lower layer of unit 4 (2.7 mass-%, class 2, at 477–463 cm b.s.) and it increases to the unit top, peaking at 444 cm b.s. (4.1 mass-%, class 3).  $X_{LF}$  has a median value of around  $13 (3) 10^{-8} \text{ m}^3 \text{ kg}^{-1}$  (class 1,  $n = 6$ ) and constantly increases from  $10 10^{-8} \text{ m}^3 \text{ kg}^{-1}$  (class 1) at the bottom to  $33 10^{-8} \text{ m}^3 \text{ kg}^{-1}$  (class 2) at the top. Graphs of element ratios (Ca/Ti and Zr/Rb) widely run parallelly, altogether showing low values in the lower strata (units 1–4, Figure 5.4). At the top of unit 4, a bulk sample from 427 cm b.s. dates to 4958–4841 cal yr BP and a mixed charcoal/sediment sample from 435 cm b.s. dates to 5462–5309 cal yr BP. The boundary to overlying unit 5 is sharp.

Unit 5 (426–358 cm b.s.) consists of dark yellowish brown (10 YR 4/6), normally graded sediments. Sediment texture changes from very soft, subangular to subrounded medium pebbly ( $\varnothing < 2 \text{ cm}$ ) sand at the base to silty sand at the top. A snail fragment occurs at 420 cm b.s. The sediments are moderately to strongly calcareous and contain very few blackish manganese mottles. The pH peaks at the top of unit 5 (pH: 8.6, strongly alkaline, at 363 cm b.s.). Within unit 5 ( $n = 4$ ), EC ( $118 (17) \mu\text{S cm}^{-1}$ , class 1) and  $LOI_{550}$  (1.9 (0.4)

mass-%, class 1) drop to their lowest values, whereas  $X_{LF}$  ( $37 (4) 10^{-8} \text{ m}^3 \text{ kg}^{-1}$ , class 2) shows high values in comparison with the underlying and overlying units. Element ratios of Ca/Ti (19.2 (3.4)) and Zr/Rb (1.7 (0.4)) also slightly increase compared to the lower units. The mixed charcoal/sediment sample at 363 cm b.s. dates to 3812–3566 cal yr BP. The boundary to overlying unit 6 is sharp.

Unit 6 (358–169 cm b.s.) consists of soft, moderately calcareous, and normally graded sediments. The texture changes from strongly brown (7.5 YR 4/4) sandy silt at the bottom to brown (7.5 YR 5/6) slightly sandy silt at the top. Few fine pebbles ( $\varnothing < 1 \text{ cm}$ ) occur and very few of them are carbonated. Greyish to blackish manganese mottles commonly exist throughout the unit, particularly at 358–313 cm b.s. Fine brick/ceramic fragments were found at 180 and 273 cm b.s.

The measured bulk parameters ( $n = 10$ ) remain constant in this unit and show clear differences with the underlying unit 5 and the overlying unit 7. Sediments are moderately alkaline (pH: 8.1 (0.1)). EC shows alternating, but in total increased values ( $186 (33) \mu\text{S cm}^{-1}$ , class 1).  $X_{LF}$  values display a distinct trough ( $24 (4) 10^{-8} \text{ m}^3 \text{ kg}^{-1}$ , class 2) compared to the underlying unit 5 ( $37 (4) 10^{-8} \text{ m}^3 \text{ kg}^{-1}$ , class 2,  $n = 4$ ) and overlying unit 7 ( $44 (2) 10^{-8} \text{ m}^3 \text{ kg}^{-1}$ , class 2,  $n = 6$ ).  $\text{LOI}_{550}$  (3.2 (0.3) mass-%, class 2) remains relatively stable and is higher than the underlying (1.9 (0.4) mass-%, class 1,  $n = 4$ ) and overlying unit (2.2 (0.3) mass-%, class 2,  $n = 6$ ). Element ratios (Ca/Ti and Zr/Rb) remain roughly the same and show relatively lower values compared to the underlying and overlying units. The two datings of mixed charcoal/sediment samples show distinct age inversions. The sample from 260–265 cm b.s. dates to 5575–5325 cal yr BP. The sample from 221 cm b.s. dates to 6556–6396 cal yr BP and, thus, is older than the underlying age samples. The transition between unit 6 and unit 7 is sharp.

Unit 7 (169–58 cm b.s.) is characterized by yellowish brown (10 YR 5/4), slightly compacted, and inversely graded sediments. Sediment texture changes from fine pebbly silty sand at the bottom, to sandy, subangular subrounded medium pebbles at the top. The pebbly sediments at the top are matrix-supported and poorly sorted. Sediments in this unit are strongly calcareous and contain very few carbonate nodules. A ceramic piece occurs at 149–140 cm b.s. and a small brick fragment at 150–147 cm b.s. Geochemical samples ( $n = 6$ ) indicate relatively low EC ( $150 (15) \mu\text{S cm}^{-1}$ , class 1) and  $\text{LOI}_{550}$  values (2.2 (0.3) mass-%, class 2) compared to those in the overlying and underlying units. Overall,  $\text{LOI}_{550}$  values gradually increase from the bottom (1.8 mass-%, class 1) to the top (3.3 mass-%, class 2). Along with the whole extracted profile, values of  $X_{LF}$  ( $44 (2) 10^{-8} \text{ m}^3 \text{ kg}^{-1}$ , class 2) and the element ratio of Ca/Ti (40.05 (6.9)) reach their maximum in unit 7.

Also, the Zr/Rb has a peak of 2.55 at 130 cm b.s. The boundary to the overlying unit 8 is gradual.

Unit 8 (58–0 cm b.s.) corresponds to the present-day plow horizon and contains dark yellowish brown (10 YR 4/4), moderately calcareous, slightly sandy silt with very few embedded fine pebbles and roots. The pH values remain stable all over units 6–8 (moderately alkaline). EC values steadily increase from the bottom to the top of unit 8, reaching  $271 \mu\text{S cm}^{-1}$  (class 2) at the surface.  $\text{LOI}_{550}$  contents have a median value of 5.1 (0.1) mass-% (class 4,  $n = 3$ ).  $X_{\text{LF}}$  values ( $37 (0) 10^{-8} \text{ m}^3 \text{ kg}^{-1}$ , class 2,  $n = 3$ ) are slightly lower than the underlying unit 7. Element ratios ( $n = 3$ ) of Ca/Ti (18.57 (1.3)) and Zr/Rb (1.50 (0.1)) are in the same range as unit 6 and are distinctly lower than unit 7.

### 5.4.3 Tekkedere fan toe: Key-profile Tek-6

Profile Tek-6 was extracted from the toe of the Tekkedere alluvial fan. It has a total thickness of 800 cm and seven units (Figure 5.5). This profile is characterized by a thick (2.5 m) unit of blackish greyish clayey silt (unit 2) in its lower part, overlain by normally graded sediments (units 3–4) in the middle part and brownish fine-textured sediments (units 5–7) in the upper 2 m. Sediments of Tek-6 are moderately to strongly calcareous.

The pH values in the lower half of the profile (below 427 cm b.s., units 1–2) are constant at 8.4 (0.1,  $n = 30$ ) corresponding to a moderately alkaline environment. Sediments from 400 cm b.s. to the profile surface gradually change to slightly alkaline (pH is 7.9 at 33 cm b.s.). The graphs of EC ( $343 (108) \mu\text{S cm}^{-1}$ , class 2,  $n = 50$ ) and  $\text{LOI}_{550}$  values (3.9 (2.1) mass-%, class 3,  $n = 50$ ) run inversely to the graph of pH values. The lowest EC and  $\text{LOI}_{550}$  values are observed at the middle profile (427–224 cm b.s.). The graph of  $X_{\text{LF}}$  values ( $56 (29) 10^{-8} \text{ m}^3 \text{ kg}^{-1}$ , class 2,  $n = 50$ ) roughly shows the same trend as pH and peaks of  $109 (10) 10^{-8} \text{ m}^3 \text{ kg}^{-1}$  (class 4) in the middle part of the profile (427–224 cm b.s.,  $n = 11$ ). The element ratio of Ca/Ti has a median value of 12.94 (3.9) and Zr/Rb 1.20 (0.2) with a distinct Ca/Ti peak at 677 cm b.s. and a distinct Zr/Rb peak at 400 cm b.s.

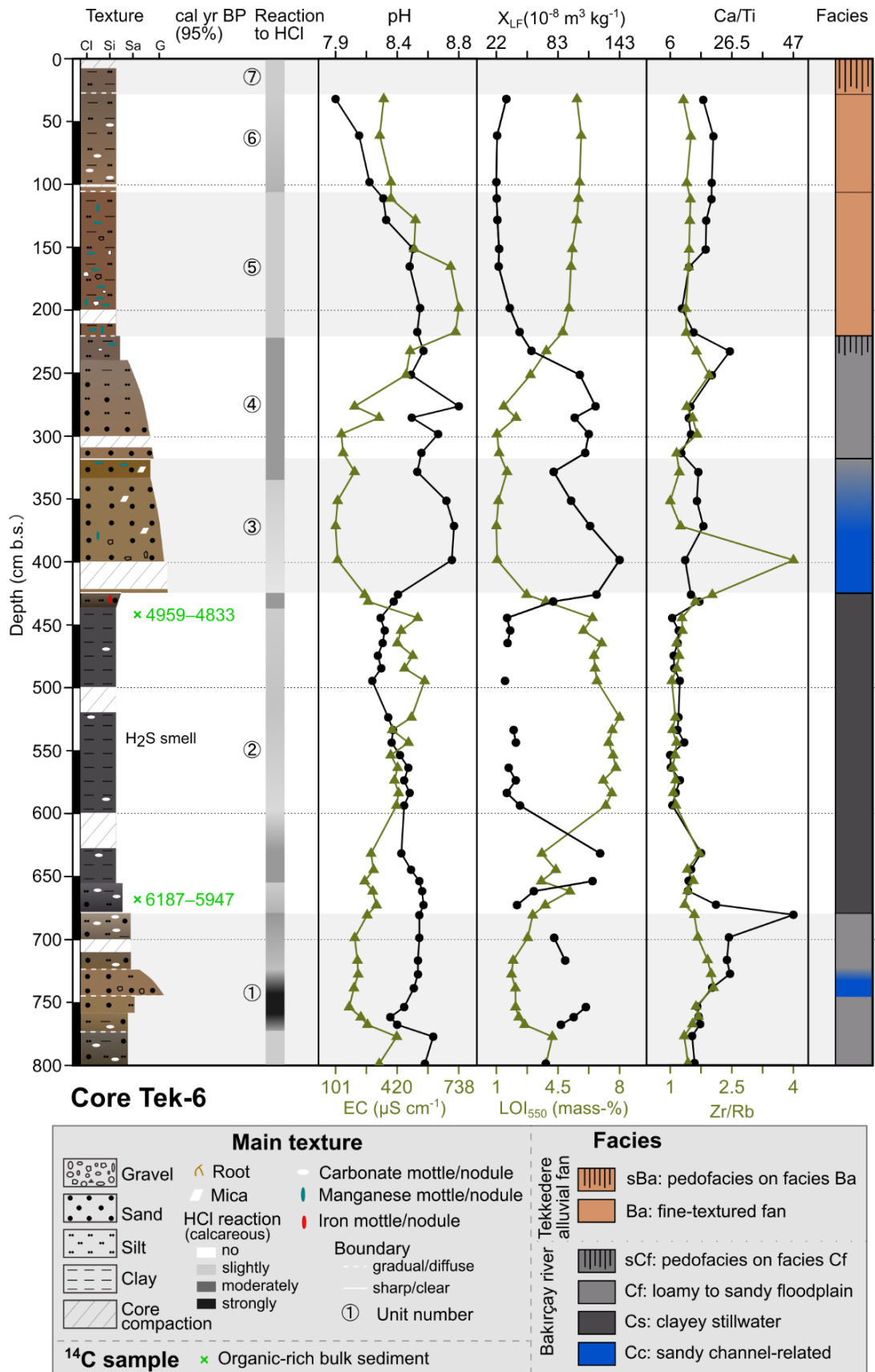


**Figure 5.5** The lithostratigraphy, radiocarbon dates, and sediment analyses of sediment core Tek-6. cm bs, cm below surface; EC, electrical conductivity; LOI<sub>550</sub>, loss on ignition at 550°C;  $X_{LF}$ , mass-specific susceptibility at the low frequency.

Unit 1 (800–677 cm b.s.) is composed of four thin layers of sandy to silty sediments varying in colors (Figure 5.5). Brown sediments at 747–725 cm b.s. are normally graded, of which texture gradually changes from coarse sand with few medium pebbles ( $\varnothing < 3$  cm, angular to subrounded) at the bottom, to silty sand at the top. The uppermost layer (725–677 cm b.s.) consists of brown to yellowish gray sandy silt with few weathered carbonate concretions. The yellowish-gray color of the sediment likely results from the weathered carbonate. At 770–725 cm b.s., sediments are strongly calcareous. The graphs of measured bulk parameters have comparable trends with a slight decrease of pH, EC, and  $LOI_{550}$  values occurring around 770 cm b.s. The Ca/Ti ratio has a median value of 17.75 (4.2,  $n = 10$ ) and a peak of 21 at the top of this unit (around 673 cm b.s.). The ratio of Zr/Rb has a median value of 1.45 (0.2,  $n = 10$ ). The boundaries among the layers in this unit are gradual and unit 1 sharply transits to unit 2.

Unit 2 (677–427 cm b.s.) is characterized by poorly compacted, blackish greyish clayey silt. Color slightly varies between dark greenish gray (Gley 1 3/5GY, 600–500 cm b.s.) and very dark gray (Gley 1 3/N, 500–436 cm b.s.). The sediments are moderately calcareous at 657–628 cm b.s. and slightly calcareous at 600–436 cm b.s. Beside a single carbonate nest around 585 cm b.s. and few carbonate concretions at 677–657 cm b.s., only very few carbonate concretions occur in this unit. Sediments at 677–657 cm b.s. are clayey sandy silt which are slightly coarser than the upper part (657–436 cm b.s.). The latter is characterized by a very strong emanation of an  $H_2S$  smell after adding 9.9 % HCl, indicating the presence of Fe sulfides under reducing conditions (Jahn et al., 2006). At 436–427 cm b.s., sediments are moderately calcareous, poor in clay content, and contain very few fine reddish iron mottles.

The pH values ( $n = 20$ ) gradually decrease from 8.5 (strongly alkaline) at the base to 8.2 (moderate alkaline) at the top. Values of EC ( $n = 20$ ) gradually increase from ca.  $300 \mu S cm^{-1}$  (class 2) at the bottom to  $500 \mu S cm^{-1}$  (class 3) at its top.  $X_{LF}$  values remain low ( $35 (3) 10^{-8} m^3 kg^{-1}$ , class 2,  $n = 14$ ) at 600–440 cm b.s., where  $LOI_{550}$  values reach the maximum (6.7 (0.5) mass-%, class 5,  $n = 20$ ) of the whole profile. Element ratios of Ca/Ti (8.65 (2.0),  $n = 20$ ) and Zr/Rb (0.94 (0.1),  $n = 20$ ) remain low. Two organic-rich bulk samples from 665 cm b.s. and 460 cm b.s. date to 6187–5947 cal yr BP and 4959–4833 cal yr BP, respectively. The sediment boundary between units 2 and 3 is sharp.

Unit 3 (427–320 cm b.s.) shows slightly calcareous and normally graded sediments. The texture gradually changes from light olive brown (2.5 Y 5/3), pebbly coarse sand at the base, to medium–coarse sand in the middle, and to dark yellowish brown (10 YR 4/6) fine sand at the top. Very few manganese mottles and few micas occur in the upper part of

the unit (320–315 cm b.s.). Sediments are strongly alkaline (pH: 8.7 (0.1),  $n = 5$ ). Median values ( $n = 5$ ) of EC (112 (11)  $\mu\text{S cm}^{-1}$ , class 1) and  $\text{LOI}_{550}$  (0.8 (0.1) mass-%, class 1) remain the lowest of the whole profile. Values of  $X_{\text{LF}}$  (114 (19)  $10^{-8} \text{ m}^3 \text{ kg}^{-1}$ , class 4,  $n = 5$ ) peak at ca. 400 cm b.s. (143  $10^{-8} \text{ m}^3 \text{ kg}^{-1}$ , class 5), and gradually decrease to 80  $10^{-8} \text{ m}^3 \text{ kg}^{-1}$  (class 3) at the top. Ca/Ti values (14.68 (2.0),  $n = 5$ ) are slightly higher than in unit 2. Zr/Rb ratio peaks around 400 cm b.s. (3.91) and decreases to the top. The boundary from unit 3 to the overlying unit 4 is sharp.

Unit 4 (320–224 cm b.s.) continues the trend of decreasing grain size with decreasing depth. The moderately calcareous sediments consist of brown (7.5 YR 5/4) coarse sand at the bottom, sandy silt at the middle, and dark reddish gray (5 YR 4/2) sandy clayey silt at the top. Weathered fragments of carbonate rocks occur at 239–232 cm b.s. and very few manganese mottles at 244–224 cm b.s. Sediments are strongly alkaline (pH: 8.5 (0.1),  $n = 6$ ). EC values gradually increase from 140  $\mu\text{S cm}^{-1}$  (class 1) at the base to 487  $\mu\text{S cm}^{-1}$  (class 3) at the top. Median  $X_{\text{LF}}$  values (106 (7)  $10^{-8} \text{ m}^3 \text{ kg}^{-1}$ , class 4,  $n = 6$ ) remain in the same range as the underlying unit 3. Also,  $\text{LOI}_{550}$  has a median value of around 1.5 (0.7) mass-% (class 1,  $n = 6$ ) and shows the same range as unit 3. Ca/Ti ratio (12.63 (1.9),  $n = 6$ ) and Zr/Rb ratio (1.40 (0.1),  $n = 6$ ) undergo a slight increase from the bottom to the top and display small peaks in the upper part. The boundary to overlying unit 5 is gradual.

Unit 5 (224–107 cm b.s.) shows reddish brown (5 YR 4/4), strongly compacted clayey silt with very few embedded fine pebbles. Manganese mottles commonly exist in this unit with slightly decreasing abundance from the bottom to the top. Sediments are slightly calcareous and very few fine to medium carbonate fragments occur at 200–150 cm b.s. The boundary to overlying unit 6 has a gradual contact.

Unit 6 (107–29 cm b.s.) consists of brown (7.5 YR 5/4), slightly calcareous clayey silt. The compactness and carbonate content decrease with decreasing depth. Sediments from units 5 and 6 are moderately alkaline with decreasing pH values from the bottom to the top. EC values gradually decrease from ca. 730  $\mu\text{S cm}^{-1}$  (class 5) in unit 4 to 330  $\mu\text{S cm}^{-1}$  (class 2) in unit 6. Median  $X_{\text{LF}}$  values in units 5 and 6 are low without remarkable oscillations (24 (1)  $10^{-8} \text{ m}^3 \text{ kg}^{-1}$ , class 1,  $n = 9$ ).  $\text{LOI}_{550}$  values in both units are relatively high (5.2 (0.2) mass-%, class 4,  $n = 9$ ) compared to the underlying units 3–4 (1.1 (0.4) mass-%, class 1,  $n = 11$ ). Ca/Ti ratio (17.58 (1.7),  $n = 9$ ) is high and Zr/Rb ratio (1.22 (0.1),  $n = 9$ ) is low in units 5 and 6. Unit 6 gradually transits to unit 7.

Unit 7 (29–0 cm b.s.) corresponds to the present-day plow horizon, which consists of brown (7.5 YR 4/2), heavily compacted clayey silt.

## 5.5 Sediment facies

Similar to previous studies in the Pergamon micro-region (Schneider et al., 2014; 2015), sediment facies in the eight Tekkedere profiles are identified based on their geomorphological setting, field observation, sediment texture, and measured sediment characteristics (Blair and McPherson, 1994; Brown, 1997; Goldberg and Macphail, 2006; Miall, 2006, 2014).

### 5.5.1 Facies A: Tekkedere valley bottom sediments

Sediments that infilled the Tekkedere valley, i.e., profiles Tek-1 (Figure S5.2), Tek-2 (Figure 5.3), and Tek-3 (Figure S5.3), are classified as facies A (Tekkedere valley bottom sediments). Facies A is further subdivided into fine-textured (facies Aa) and coarse-textured (facies Ab) deposits (Table 5.4). They were predominantly deposited by fluvial processes of the Tekkedere creek (Figure 5.2A and C), as evidenced by the sediment lithology and topographical location (Goldberg and Macphail, 2006). Fluvial sediments are partly interfingering with colluvial deposits characterized by massive bedding and poor sorting (Mills, 1979; Brown, 1997; Miall, 2014). The development of fine- and coarse-textured valley bottom sediments in Tekkedere is different from the Gümüş valley which is dominated by fine-grained sediments (Knitter, 2013).

Facies Aa (fine-textured sediments) contains low coarse fractions (grains <2 mm are less than 10 %), whereas facies Ab (coarse-textured) shows distinctively higher coarse contents (reaching 60 %) (Figure 5.3). Compared to facies Aa, facies Ab is mostly more alkaline and shows lower EC and LOI<sub>550</sub> values. Parts of the fine-textured sediments present typical post-sedimentary and pedogenic features, including common animal burrows and roots, relatively dark color, low pH, high EC, and increased LOI<sub>550</sub> values. They document processes of humification and consequently are classified as buried topsoil horizons (pedofacies sAa, Table 5.4) (Goldberg and Macphail, 2006), such as the buried soil horizon of unit 4 in Tek-2 (Figure 5.3). This facies indicates a poorly developed soil horizon, pointing to a short period of reduced land erosion activity (Dusar et al., 2011).

**Table 5.4** The features of different sediment facies in the Tekkedere catchment.

Facies		Description <sup>a</sup>
Tekkedere valley bottom sediments (A)	Aa	fine-textured valley bottom sediments, containing less than 10 % coarse fraction (>2 mm)
	sAa	buried topsoil horizons on the fine-textured valley bottom sediments (facies Aa) with high bioturbation and higher EC and LOI <sub>550</sub> values compared to facies Aa
	Ab	coarse-textured valley bottom sediments, with coarse fraction contents in the range of 10–60 %; mostly more alkaline; decreased EC and LOI <sub>550</sub> values
Tekkedere alluvial fan sediments (B)	Ba	fine-textured alluvial fan sediments, characterized by clayey to silty sediments with a low portion of pebbles; often increased in EC and LOI <sub>550</sub> values; low X <sub>LF</sub> and element ratios of Ca/Ti and Zr/Rb
	sBa	buried topsoil horizons on the fine-textured alluvial fan sediments (facies Ba), with a distinct increase in LOI <sub>550</sub> values compared to facies Ba
	Bb	coarse-textured alluvial fan sediments, containing more coarse components (mainly sands with fine to medium pebbles) with less Fe–Mn mottles; very low EC and LOI <sub>550</sub> values; increased in X <sub>LF</sub> and element ratios of Ca/Ti and Zr/Rb
Bakırçay river sediments (C)	Cc	channel-related sediments of the Bakırçay river, containing fining upwards pebbly sand with remarkably low LOI <sub>550</sub> values and relatively high Zr/Rb ratio
	Cf	floodplain sediments of the Bakırçay river, dominated by sandy silt; compared to the Tekkedere alluvial fan sediments (facies B), LOI <sub>550</sub> and EC values are generally higher, whereas the X <sub>LF</sub> , element ratios of Ca/Ti and Zr/Rb are lower
	sCf	buried topsoil horizons on the Bakırçay floodplain sediments (facies Cf), with increased LOI <sub>550</sub> values compared to facies Cf
	Cs	still water sediments of a poorly drained environment on the Bakırçay floodplain, containing dark gray silty clay with very high LOI <sub>550</sub> values; strong H <sub>2</sub> S smell after adding 9.9 % HCl

<sup>a</sup> EC, electrical conductivity; LOI<sub>550</sub>, loss on ignition at 550°C; X<sub>LF</sub>, mass-specific susceptibility at the low frequency.

### 5.5.2 Facies B: Tekkedere alluvial fan sediments

The deposition of the Tekkedere alluvial fan is predominantly formed by brownish fan sediments (facies B). Facies B is also differentiated into fine-texture (facies Ba) and coarse-texture (facies Bb) deposits (Table 5.4) with distinct characteristics of alluvial fan deposits (Blair and McPherson, 2009; Bowman, 2019). Facies Ba is inferred from the generally fine composition of grain size (clayey to silty sediments with a low portion of pebbles), often increased EC and LOI<sub>550</sub> values, and very low results of  $X_{LF}$ , Ca/Ti, and Zr/Rb ratios. In contrast, facies Bb contains more coarse components (sands with fine to medium pebbles) and fewer Fe–Mn mottles than facies Ba, e.g., units 5 and 7 in Tek-5 (Figure 5.4). Facies Bb usually shows very low EC and LOI<sub>550</sub> values, but increased  $X_{LF}$  and element ratios.

Following the alluvial fan's longitudinal profile (the transect from the fan apex to toe, Figure 5.6), two major cycles of fine- and coarse-textured fan sediments can be identified in the mid-fan position, i.e., profiles Tek-5 and Tek-4-2. In general, the texture of facies Ba and Bb fines from the apex to the toe of the alluvial fan, and in parallel the thickness of layers declines (Figure 5.6), which is also reported on the alluvial fans in western Turkey (Özpolat et al., 2020). Besides, the thin layers of facies Ba, which only vertically discontinuously occur in the lower part of Tek-5, can be linked with the fine-textured sediments below 463 cm b.s. in Tek-4-2 (Figure 5.6).

Increased LOI<sub>550</sub> values in units 2 and 5 of Tek-4-2 (Figure S5.5) indicate the evidence of buried topsoil horizons developed on the fine-textured alluvial fan deposits, reaching a thickness up to 30 cm (facies sBa, Figure 5.6 and Table 5.4) (Soil Survey Staff, 1999; Kapur et al., 2017; Macphail and Goldberg, 2017).

### 5.5.3 Facies C: Bakırçay river sediments

Given that the position of the fan toe is proximal to the Bakırçay river, the dark-colored and organic-rich sediments in the lower part of the profiles extracted at the middle–distal part of the fan (profiles Tek-5, Tek-5-2, and Tek-6) are interpreted as the Bakırçay river deposits (facies C) (Figure 5.6) (cf. Goldberg and Macphail, 2006; Miall, 2006). Most of these sediments correspond to sandy silts, whereas coarse sands and angular pebbles almost lack. The element ratio of Ca/Ti in facies C is generally lower than in facies B, likely associated with the differences in the occurrence and distribution of carbonate rocks in the drainage basins of Bakırçay and Tekkedere (MTA, 2002; Yang et al., 2021) (Figure 5.2B).

Field observation in the present-day Bakırçay floodplain indicates sub-environments of the abandoned channel, paleo-oxbow, and overbank, which are comparable to the Büyük Menderes floodplain in western Turkey (Özpolat et al., 2020). Based on sediment characters and the occurrence in the proximity of the present-day floodplain, the sandy silty sediments are interpreted as Bakırçay river floodplain deposits (facies Cf, Table 5.4) (cf. Miall, 2006). These floodplain deposits can be observed in units 1 and 3 of Tek-5 (Figure 5.4), unit 1 of Tek-5-2 (Figure S5.6), and units 1 and 4 of Tek-6 (Figure 5.5). In the lower part of profile Tek-5 (mid-fan position), the floodplain deposits (facies Cf) are interfingering with layers of fine-textured alluvial fan sediments (facies Ba), i.e., units 2 and 4 in Tek-5 (Figures 5.4 and 5.6). None of the alluvial fan sediments (facies B) occur in the lower parts of Tek-5-2 and Tek-6 (the toe of the Tekkedere fan).

The 2.5-m-thick unit of dark gray silty clay with very high LOI<sub>550</sub> values (unit 2 in Tek-6, Figure 5.5) is interpreted as still water sediments (facies Cs, Table 5.4) of an oxbow lake or a (secondary) channel (Miall, 2006; Charlton, 2007; Miall, 2014). Sediments overlying the facies Cs in Tek-6 show a distinct fining-upward feature, from pebbly sand (unit 3) to sandy silt (unit 4) (Figure 5.5). This gradual change in grain size reflects a reduction in the sediment transportation ability of the Bakırçay river. The decreasing fluvial activity points out a high-energy channel-related environment (facies Cc) transferred to a low-energy floodplain (facies Cf) (Miall, 2006). In the middle part of unit 1 in Tek-6, a similar feature of abandoned channel-related deposits (facies Cc) can be observed but less thick and distinct (Figure 5.6). In general, the gradual change in vertical lithostratigraphy indicates a meandering pattern (Miall, 2006). This is supported by Aksu et al., (1987) who suggest a strongly meandering channel pattern of the Bakırçay in its lower course during the Late Quaternary.

Redoximorphic features of Mn–Fe nodules as well as secondary precipitated carbonates prevailing in the Bakırçay floodplain deposits reflect the effect of a post-sedimentary seasonally fluctuating groundwater table (Goldberg and Macphail, 2006). These post-depositional processes have also been reported in several locations in the lower Bakırçay basin (Schneider et al., 2014; 2015; 2017).

Boundaries between the facies of the Bakırçay river floodplain (facies Cf) and the overlying facies of the Tekkedere alluvial fan (facies B) in the profiles Tek-5, Tek-5-2, and Tek-6 are roughly at the same absolute elevation (ca. 4–5 m a.s.l., Figure 5.6). At these boundaries, the floodplain deposits frequently show weakly developed thin fossil soil horizons (facies sCf, Table 5.4 and Figure 5.6), i.e., the buried paleosols in the upper part of units 3 and 4 in Tek-5 (Figure 5.4), unit 1 in Tek-5-2 (Figure S5.6), and unit 4 in Tek-6

(Figure 5.5). Comparable to the soil facies sAa in the Tekkedere valley bottom, this pedofacies sCf with its immature A horizon documents a past soil formation and stable surface on the floodplain.

## **5.6 Middle and Late Holocene geomorphodynamics**

The lithostratigraphic analyses and the radiocarbon ages indicate four major phases of geomorphodynamics from the Middle to Late Holocene (Figures 5.6 and 5.7).

### **5.6.1 Phase 1 (ca. 6.2 to 5–4 cal ka BP): Aggradation of the Bakırçay floodplain**

Sediment dynamics during the first phase are mainly related to the deposition of Bakırçay river sediments (facies C), e.g., the floodplain aggradation. Proximal to the current Bakırçay channel, the paleo-floodplain (facies Cf) at the location of Tek-6 was first dissected by a (secondary) channel (facies Cc) (Figure 5.6). The channel was then filled by sediments with the fining upward feature. Hereafter, a still water environment (facies Cs) existed for more than a millennium (from 6.1 to 4.9 cal ka BP, Table 5.3). It was then dissected by a younger channel (facies Cc) and successively covered with silty floodplain deposits (facies Cf). The upper floodplain layers (facies Cf) in profile Tek-6 are linked to the floodplain sediments in Tek-5-2 based on the same absolute elevation at ca. 4–5 m a.s.l (Figure 5.6). More distal to the current Bakırçay river, floodplain deposits (facies Cf) in Tek-5 interfinger with the sediments originating from the Tekkedere catchment (facies Ba), which indicates the location of Tek-5 marks a former overlapping zone of the peripheral Bakırçay plain and the Tekkedere fan.

The beginning of the Bakırçay floodplain aggradation in the area of the present-day Tekkedere fan predates ca. 6.2 cal ka BP. This is revealed by the radiocarbon sample from the bottom of the still water sediment in Tek-6 (6187–5947 cal yr BP at 665 cm b.s., Table 5.3). Accordingly, the underlying floodplain (facies Cf) and the secondary channel (facies Cc) deposits were older than 6.2 cal ka BP. The Bakırçay floodplain sediments continued to deposit in the distal part of the current Tekkedere alluvial fan at least until 5301–5045 cal yr BP, which is indicated by the charcoal sample at 781 cm b.s. in Tek-5 (Table 5.3). Although it has to be considered that radiocarbon dates of charcoals are often interpreted as the maximum depositional age due to the possible reworking of the samples before their last deposition (Lang and Hönscheidt, 1999; Chiverrell et al., 2007; Nykamp et al., 2020), the aforementioned charcoal, because of its considerable size (ca. 0.5 cm

Ø, larger than other charcoal pieces) and its deposition in fine floodplain sediments, is considered to have been deposited in a rather short time after its burning. Hence, it is acceptable to use the charcoal date as the depositional age of the surrounding sediments.

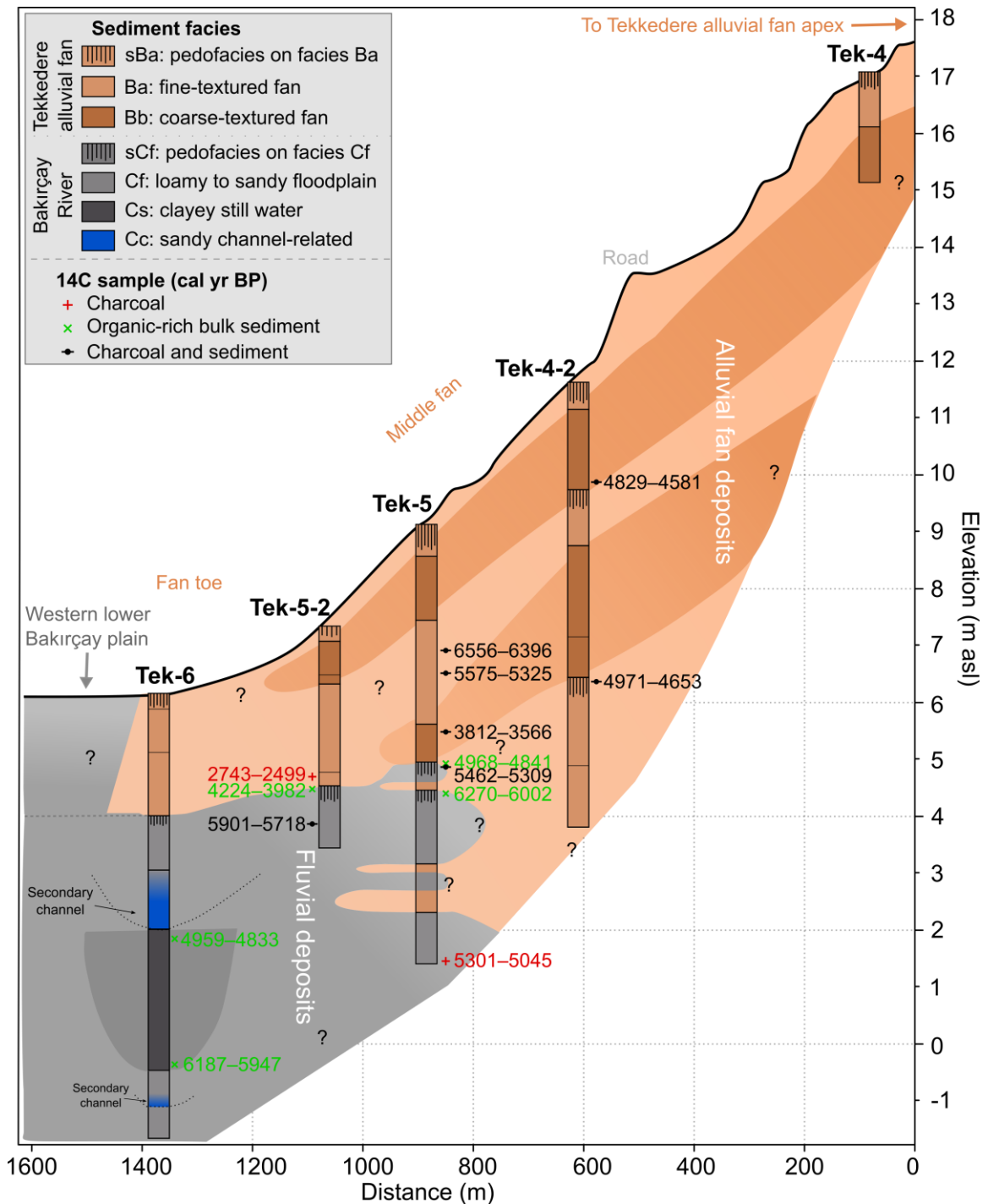


**Figure 5.6** Longitudinal profile along with the Tekkedere alluvial fan (91 × vertical exaggerations) with sediment cores. Display of the thickness of the different units corresponds to height scale, and sediment architectures are based on the sediment units of the different cores. Embedded calibrated radiocarbon ages provide an overview of sediment ages and age inversions. m asl, m above sea level.

The termination of floodplain aggradation in the first phase is marked by the formation of soil horizons (Figure 5.6). The dating of the end of phase 1 is precarious due to several age inversions and the specific characteristics of different dated materials. In Tek-5, the dating results of the two samples from 478 cm b.s. (6270–6002 cal yr BP) and 435 cm b.s. (5462–5309 cal yr BP) are most likely overestimated (Figure 5.6), because the charcoal sample taken from the bottom of the profile (781 cm b.s., 5301–5045 cal yr BP) represents a maximum depositional age of the overlying deposits. We, therefore, suggest the dating samples from the soil horizons (around 430 cm b.s. in Tek-5) incorporated older materials, such as reworked and washed terrestrial soils and organics (Fowler et al., 1986; Strunk et al., 2020). However, an alternative interpretation of dating results from bulk soil samples is possible. Due to the open system of soil formations (Scharpenseel and Schiffmann, 1977; Wang et al., 1996; Kovda et al., 2001), radiocarbon ages of organic-rich bulk samples have been considered as the minimum ages since the initiation of soil formations (Scharpenseel and Schiffmann, 1977; Wang et al., 1996). In this sense, the time of the soil formation and the deposition of the parent material should be even older than the dating result of the bulk sample at 478 cm b.s. of Tek-5 (6270–6002 cal yr BP). Nonetheless, this is inconsistent with the charcoal dating result.

The date of the bulk sample at 427 cm b.s. (4968–4841 cal yr BP) in Tek-5 (Figure 5.6) indicates an age of the soil formation that continued after ca. 5.0 cal ka BP. The bulk sample from the buried surface of the floodplain (facies sCf, 4224–3982 cal yr BP at 285 cm b.s.) in Tek-5-2 suggests the floodplain aggradation occurred before 4 cal ka BP. In Tek-6, the uppermost layer of still water sediments dated to 4959–4833 cal yr BP represents the maximum burial age of the floodplain at this location. Thus, based on the dating results from the three profiles, the depositional termination of the Bakırçay river sediments in the area of the recent Tekkedere fan started before ca. 6.2 cal ka BP and ended between ca. 5 and 4 cal ka BP. Concurrently, the fine-textured Tekkedere alluvial fan deposits (facies Ba) accumulated at least to the location of Tek-4-2 and interfingered with Bakırçay river sediments at the location of Tek-5.

The dominant deposition of Bakırçay river sediments over Tekkedere fan deposits was mainly controlled by supraregional factors. It is assumed that the extensive aggradation of the Bakırçay river is associated with the rising sea level around the Elaia Bay in the Aegean part of Turkey that slightly slowed down but continued after 6 ka BP (Kayhan, 1999; Seeliger et al., 2017; 2019), resulting in the rise of erosional base level (Robustelli et al., 2009). In addition, during the Middle Holocene, the prevailing wetter-than-today humid climate in Anatolia and the Balkans (Figure 5.7: rainfall in Turkey (Eastwood et al., 2007; Finné et al., 2019)) fostered fluvial dynamics (Walsh et al., 2019). Evidence for the

increased sediment load and discharge of the Bakırçay river in the Tekkedere area (i.e., maximum floodplain extension, a thousand-year-long still water environment, and shifted secondary channels) coincides with this Middle Holocene humid period. These fluvial dynamics are not only observed in Tekkedere but also in more areas in the Pergamon micro-region (Schneider et al., 2015; 2017; Becker et al., 2020a) and the eastern Mediterranean region (Dusar et al., 2011; Benito et al., 2015; Glais et al., 2017; Bulkan et al., 2018; Ocakoğlu et al., 2019).

Simultaneously, we could assume that under the Middle Holocene humid climate and high forest cover (Shumilovskikh et al., 2016) (Figure 5.7), erosion sensitivity and sediment dynamics were low which explains the middle Tekkedere alluvial fan (Tek-4-2 and Tek-5) during this phase only consisted of fine-textured sediments and had a low spatial extent (Figure 5.6). The interfingering layers of floodplain and alluvial fan deposits in profile Tek-5 are attributed to torrential runoff events in the Tekkedere valley, possibly corresponding to short-term relatively arid events as also recorded in Anatolia, e.g., at the Gediz Graben during 5.7–4.2 cal ka BP (Bulkan et al., 2018), the Kureyşler area at ca. 7.0–5.3 cal ka BP (Ocakoğlu et al., 2019), and the Tecer lake at ca. 5.3–5 ka BP (Kuzucuoğlu et al., 2011).

Human impacts on geomorphodynamics in the Tekkedere drainage basin during phase 1 might be neglectable. The settlements may have existed in the Pergamon micro-region since the Neolithic, e.g., the Yeni Yeldeğirmen-tepe (Schneider et al., 2017) and many sites in the western lower Bakırçay catchment (Horejs, 2010a, 2011a, 2014; Pirson and Zimmermann, 2014; Pirson, 2022), but there was likely no occupation or land use in Tekkedere during this time (Figure 5.7) (Michalski, 2021).

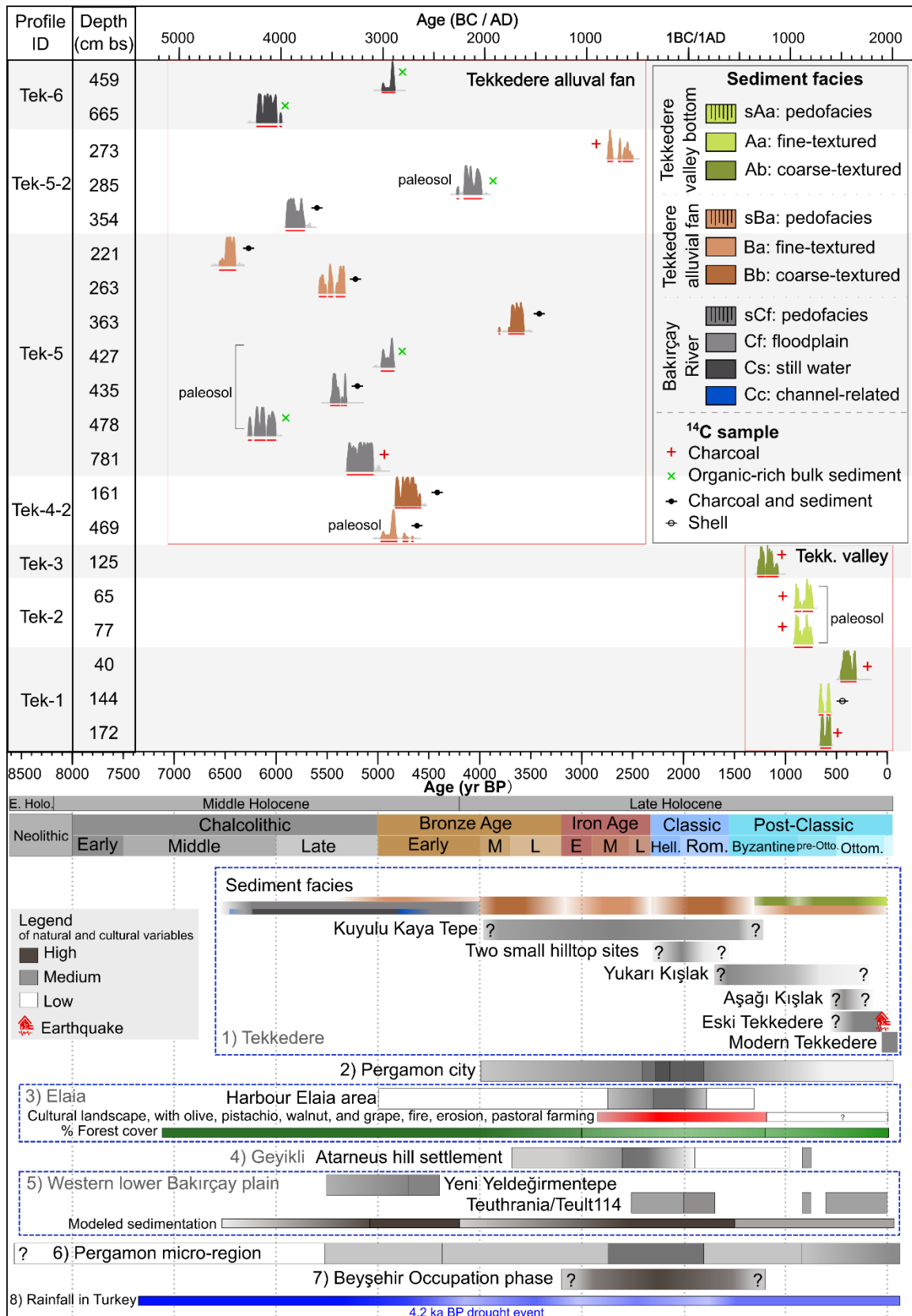
### **5.6.2 Phase 2 (between ca. 5 and 4 cal ka BP): Formation of floodplain soils**

In all three sediment profiles where Bakırçay river sediments were extracted, i.e., Tek-5, Tek-5-2, and Tek-6, organic-rich topsoil horizons (facies sCf) developed on the floodplain deposits (facies Cf) (Figure 5.6). The formation of the floodplain soil horizons is marked as the second phase of geomorphodynamics which indicates no or negligible accumulation of materials and thus a phase of relative stability. Phase 2 is suggested to occur between ca. 5 and 4 cal ka BP which is dated by the bulk samples at 427 cm b.s. (4968–4841 cal yr BP) in Tek-5 and 285 cm b.s. (4224–3982 cal yr BP) in Tek-5-2 (Figure 5.6).

Reduced flooding activities, as well as low accumulation of fan sediments, are the direct reasons for the soil formation, similar to the case study in the Central Ebro Basin (NE Spain) (Pérez-Lambán et al., 2018) and in the wider Mediterranean region (Collins et al., 2005; Vött et al., 2006; Dugar et al., 2011). The trend to floodplain stabilization or slow aggradation is in accordance with the climatic drying since 5.2 ka BP, particularly when the drier conditions dominated after 4500 yr BP (Finné et al., 2019). The climatic erosion sensitivity, hence, became relatively low (Dugar et al., 2011). In addition, the human disturbance in the Tekkedere catchment and the immediate vicinity might be also neglectable in the second phase (Figure 5.7), which altogether, promotes the development of the soil horizons.

---

**Figure 5.7** The calibrated radiocarbon ages of the samples from the Tekkedere area and the natural and cultural variables in the Pergamon micro-region. Data set: 1) Tekkedere: sediment facies (this study), preliminary results of the human occupation (Ludwig, 2020a; Michalski, 2021; Tozan, 2022) and earthquake in 1939 (Paradisopoulou et al., 2010; Çelik et al., 2019; Pirson, 2020; Tozan, 2022); 2) preliminary results of occupation in Pergamon city (Pirson, 2017); 3) Elaia: preliminary results of occupation (Pirson, 2014; Pirson et al., 2015; Feuser et al., 2020) and landscape, forest cover (Shumilovskikh et al., 2016; Seeliger et al., 2019); 4) Geyikli: preliminary results of occupation in Atarneus hill settlement (Schneider et al., 2013; 2014; Zimmermann et al., 2015); 5) Western lower Bakırçay plain: preliminary results of occupation in Yeni Yeldeğirmenetepe (Horejs, 2010b, 2011b; Schneider et al., 2017) and Teuthrania/Teult114 (Schneider et al., 2015; Williamson, 2016), modeled sedimentation (Becker et al., 2020a); 6) preliminary results of occupation in Pergamon micro-region (only valid for its western part) (Horejs, 2010a, 2011a, 2014; Pirson and Zimmermann, 2014); 7) Beyşehir Occupation phase (Eastwood et al., 1998); 8) Rainfall in Turkey (Finné et al., 2019). Abbreviations: E, Early; M, Middle; L, Late; Hell., Hellenistic Period; Rom., Roman Imperial Period; pre-Otto., pre-Ottoman; Ottom., Ottoman.



### **5.6.3 Phase 3 (ca. 4–3.8 cal ka BP): Transition from floodplain to fan environment/onset of human impacts**

The third depositional phase is characterized by the predominant deposition on the Tekkedere alluvial fan (facies B) that covered the floodplain soils (facies sCf; phase 2) and a terminal accumulation of the Bakırçay floodplain (facies C; phase 1). The mixed charcoal/sediment sample (3812–3566 cal yr BP, 363 cm b.s.) from the alluvial fan deposit overlying the buried soil in Tek-5 suggests the maximum depositional age of the fan sediment at this location (Figure 5.6). Therefore, the transition from the floodplain (and floodplain soils) environment to the Tekkedere alluvial fan presumably took place between ca. 4 and 3.8 cal ka BP. The charcoal sample taken from the overlying fan sediments dates much later (2743–2499 cal yr BP, 273 cm b.s.) in Tek-5-2 which reveals a younger coverage of fan sediments at the distal location.

This remarkable transition corresponds to the Middle/Late Holocene boundary and marks a substantial geomorphodynamic change in the area. Factors that trigger this transition from phases 1–2 to phase 3 likely include 1) the 4.2 ka BP drought event (Bini et al., 2019; Finné et al., 2019), 2) the onset of settlement activities in the catchment area (Figure 5.7) (Ludwig, 2020a; Michalski, 2021), and 3) the internal behavior of the fluvial system (Schumm, 1977), e.g., the (secondary) channels of the Bakırçay river shifted to the west.

The 4.2 ka BP drought event, generally corresponding to the period from 4.3–3.8 ka BP, shows drier conditions throughout the Mediterranean winters, in addition to already dry summers (Bini et al., 2019). Because of its global significance, it defines a formal boundary between the Middle and Late Holocene (Walker et al., 2019). More studies suggest this climate oscillation is not just one single dry event, but a highly dynamic succession of dry and wet events (Bini et al., 2019), which interprets the worldwide development of seasonal rainfalls, vegetation cover change (Shumilovskikh et al., 2016; Di Rita et al., 2022), and ensuing torrential runoff and high-frequency environmental instabilities (Türkeş and Erlat, 2005; Kuzucuoğlu et al., 2011; Dreibrodt et al., 2014; Oçakoğlu et al., 2019; Lawrence et al., 2021). The change from dominating floodplain aggradation to enlarged fan development as observed in Tekkedere, therefore, probably corresponds to the global effect of the 4.2 ka BP drought event.

In addition to a general climate change, after the onset of the Late Holocene, human activities started at the Kuyulu Kaya Tepe in the Tekkedere valley (Figures 5.2A and 5.7) (Ludwig, 2020a; Michalski, 2021). The subsequent continuous occupation, and agricultural and olive cultivation in the Tekkedere drainage basin (Ludwig, 2019; 2020a;

Michalski, 2021; Tozan, 2022) accompanied by a generally dry climate caused the reduction of forest cover, as is evident from the past vegetation change in Elaia (Shumilovskikh et al., 2016) (Figure 5.7), which in turn accelerated the soil erosion processes and hillslope dynamics in the Tekkedere area.

In the Pergamon micro-region, the meta-data analyses of previous studies suggest the modeled sediment facies and reconstructed geomorphodynamics in the western lower Bakırçay plain remarkably changed at ca. 4 ka BP, in relation to both triggers of climate change and continuous human settlements (Becker et al., 2020a). In Elaia, terrestrial input is the first time observed to cover the marine sediments after ca. 4 cal ka BP, associated with human-induced catchment erosion (Pint et al., 2015). An analogous environmental change is marked at 4.2 ka BP in Mediterranean French where soil development was buried by rainfall-induced and ongoing human-exacerbated erosion (Brisset et al., 2013). In our study, it is still a challenge to distinguish the dominating trigger between the climate and humans on the increased geomorphodynamics during this period.

Notwithstanding the climatic drying and intensifying human activities on both Tekkedere and Bakırçay catchments, the important contribution of the Tekkedere alluvial fan sediments over the Bakırçay floodplains is assumed due to different landscape sensitivity (Yang et al., 2021), sediment (dis)connectivity and reaction time (Goldberg and Macphail, 2006; Fryirs et al., 2007; Fryirs, 2013; Becker et al., 2020a). In addition, the internal shift in channel patterns is observed in the Bakırçay plain (Schneider et al., 2015; Becker et al., 2020b; 2022b) and the Büyük Menderes plain (western Turkey) (Özpolat et al., 2020), which cannot be excluded for the location of the recent Tekkedere fan. However, no direct evidence is available.

#### **5.6.4 Phase 4 (after ca. 3.8 ka BP): Alluvial fan dynamics and changing human settlement pattern**

During the ensuing Late Holocene, the geomorphodynamics in the Tekkedere catchment generally increased and varied spatiotemporally compared to the former phases. The increased geomorphodynamics are evident in the overall spatial enlargement of the alluvial fan coverage, the recurring coarse-textured fan deposits, age inversions (Figure 5.6), and the lack of older valley bottom sediments. The alternating fine- and coarse-textured sediments (facies Ba and Bb) with occasionally developed soils (facies sBa) correspond to event layers and temporary landscape stability.

During the last phase, the alluvial fan sediments and particularly the coarse-textured materials, were for the first time deposited at the mid-toe part of the current alluvial fan (Figure 5.6). This reveals that more sediments were produced at the unstable land surface and transported along the valley bottom. Radiocarbon dating results of the alluvial fan sediments (facies B) show several age inversions (Tek-5 and Tek-4-2, Figure 5.6), reflecting the reworking of older deposits stored in temporal sinks due to the intensified sediment erosion in the catchment. This corresponds to the sediment cascade model (Lang and Hönscheidt, 1999) which has been reported in more studies in the Mediterranean region (Vita-Finzi, 1969b; Van Andel et al., 1990; Nykamp et al., 2021; Cartelle et al., 2022).

A comparison of local, regional, and supraregional records, a general trend of aridization, rapid climate change (RCC) events, and human activities are the major triggers for the Late Holocene changing geomorphodynamics (Figure 5.7) (Constante et al., 2010; Duser et al., 2011; 2012; Shumilovskikh et al., 2016; Finné et al., 2019; Roberts et al., 2019a; 2019b; Becker et al., 2020a). In general, the Late Holocene hydro-climate becomes drier than the Early–Middle Holocene (Eastwood et al., 2007; Finné et al., 2019; Bozyiğit et al., 2022). It shows various fluctuations in different regions of the Mediterranean region (Duser et al., 2011; Finné et al., 2019). Centennial-scale climate oscillations between aridity and humidity during the Late Holocene have been widely reported in Anatolia where the Earth's surface responded to the rapid events accordingly both in coastal and hinterland areas (Kuzucuoğlu et al., 2011; Bulkan et al., 2018; Bassukas et al., 2021; Bozyiğit et al., 2022). A study in central Turkey indicates an alternation of humid (c. 3.9–3.8 ka BP; 3.65–3.55 ka BP; 3.4–3.4 ka BP) and dry (3.8–3.65 ka BP; 3.5–3.4 ka BP; 3.25–3.0 ka BP) episodes, followed by erosion crisis in 2.8–2 ka BP and drying episode in the Roman climatic optimum (ca. 2–1.5 ka BP) (Kuzucuoğlu et al., 2011). In southwest Turkey, stable isotope analyses further suggest a wetter condition during the Classical and Early Byzantine times (Eastwood et al., 2007). The climatic drying trend, amplified by the RCC events in the wider eastern Mediterranean region presumably triggered the repetition of the sediment dynamics in the Tekkedere catchment.

Settlement activities in the Tekkedere valley continued from the hilltop of the Kuyulu Kaya Tepe since the late Middle Bronze Age (Michalski, 2021). The location of settlement sites changed to flatter areas in the lower valley (Figures 5.2A and 5.7) (Ludwig, 2020a; Tozan, 2022). Strategies for settlement occupation and drivers of settlement abandonment (or the changing settlement pattern) vary in different geographical locations and societies throughout time and are hence controlled by environmental and societal factors (Butzer, 2005; Boyer et al., 2006; McLeman, 2011; Butzer, 2012). Environmental triggers

encompass various types of natural hazards such as rapid climate change events, (flash) floods, earthquakes, landslides, volcanic eruptions, and the ensuing geomorphodynamics (soil erosion and mass movements) (Black et al., 2011; Dusar et al., 2011; Palmisano et al., 2021; Zhang et al., 2021; Kennett et al., 2022). The last reason might be important in the Tekkedere catchment.

**Table 5.5** The summary of settlements and natural-social relationships in the Tekkedere valley.

Settlements	Chronology	Geomorphological position	Erosion sensitivity	Hazards / sediment dynamics	View, traffic, agriculture accessibility
Kuyulu Kaya Tepe	Late Middle Bronze Age to the end of Early Byzantine time	Rock plateau and foot slopes	Medium	Repeated high/low dynamics	Likely a fortress
Two small hilltop sites	Hellenistic Period to the Roman Imperial Period	Top of small hills	Medium-high	Likely high dynamics	Low
Yukarı Kışlak (upper settlement)	Late antiquity and likely to the Byzantine time	Across the upper valley of creek B (valley bottom and slopes)	Medium	Likely from low to high dynamics	<div style="display: flex; align-items: center; justify-content: center;"> <span style="margin-right: 5px;">Low</span> <span style="font-size: 2em;">↓</span> <span style="margin-left: 5px;">High</span> </div>
Aşağı Kışlak (lower settlement)	Unknown, likely between the occupation of Yukarı Kışlak and Eski Tekkedere	Northern slopes of the middle valley	High	Likely high dynamics	
Eski Tekkedere (old Tekkedere)	Before 1939	Northern slopes of the middle valley	High	Earthquake-triggered landslide	
Modern Tekkedere	Since 1939	Northern slopes of the lower valley	High	Unknown	

The recurring cycles of increased geomorphodynamics during the Late Holocene are presumably triggered by the past settlement locations around steep slopes in the mountainous part of the Tekkedere catchment (Figure 5.2). These settlement areas are geomorphologically sensitive to climate change and intensified land use. Hence, soil erosion and sediment dynamics may occur rapidly in the most sensitive areas, in particular, during the recent two millennia (Table 5.5). Conceivably, erosion on the land surface further results in unfavorable areas for agricultural, arboricultural, and settlement use. For

this reason, a concomitant change for a more suitable settlement location, e.g., fertile and less landscape-sensitive Tekkedere valley bottom and Bakırçay floodplain, is understandable. The nearest analogous studies are reported in Elaia (Pint et al., 2015; Seeliger et al., 2019) which suggest the harbor was abandoned in the Late Roman period, in relation to the progressive erosional processes and the resultant siltation.

In addition to soil erosion, earthquakes would also be an important trigger for the shifting occupation of settlements in the Tekkedere catchment. In the Pergamon micro-region, at least nine earthquakes have been documented during the last two millennia (Nalbant et al., 1998; Emre et al., 2005; McHugh et al., 2006; Paradisopoulou et al., 2010; Schneider et al., 2014; Seeliger et al., 2017). Particularly, the abandonment of the old Tekkedere settlement (Eski Tekkedere) and its relocation to the modern village took place due to the earthquake-triggered landslide in September–November 1939 (Figure 5.7 and Table 5.5) (Paradisopoulou et al., 2010; Çelik et al., 2019).

In addition to the geomorphodynamics, rapid events of cold and dry climates, or heavy and unstable rainfall have been reported to cause settlement abandonment (Weiss, 2016; Bini et al., 2019). The rural settlements in the Pergamon micro-region were built on elevated locations under the consideration of flood threat (Knitter, 2013; Schneider et al., 2015). In general, these extreme natural hazards lead to a relatively short-distance settlement relocation (Black et al., 2011), which interprets the settlement mobility in Tekkedere.

Notwithstanding the potential natural triggers, socio-cultural factors also influenced settlement dynamics in Tekkedere. In the case of Kuyulu Kaya Tepe, political-administrative reasons in the Late Hellenistic–Early Roman Period (3<sup>rd</sup>–2<sup>nd</sup> centuries BC) probably led to the razing of the fortified rock plateau (Table 5.5). The demilitarization also happened in the neighboring hilltop settlements of Teuthrania and Eğrigöl Tepe (in the lower Bakırçay plain), and Atarneus (the Geyikli river area) (Figure 5.1) (Schneider et al., 2014; Zimmermann et al., 2015; Williamson, 2016; Pirson, 2017; Ludwig, 2020a). The reasons for the final abandonment of the Kuyulu Kaya Tepe settlement in Byzantine times are obscure and a combination of human impacts and changing environmental conditions may have played a role. The gradual moving of the settlements downstream of the Tekkedere valley might be under the consideration of accessibility of major traffic routes and agricultural areas (Table 5.5). Other studies may suggest settlement abandonment and migration are only attributed to the consideration of, e.g., military strategies and socio-cultural dynamics (Butzer, 2012; Schneider et al., 2014; Weiberg et al., 2019b) or at least

the environmental and societal factors in combination (Black et al., 2011; Brown and Walsh, 2017).

Beyond Tekkedere, intensified sediment dynamics have been indicated from several alluvial fans and colluvium in the western lower Bakırçay plain since the Early Iron Age (Becker et al., 2020a) (Figure 5.7). Since then, the large settlements gradually rose and the population increased, e.g., Pergamon, Elaia, Teuthrania, Halisarna, and Atarneus (Pirson, 2008; Pirson and Zimmermann, 2014; Zimmermann et al., 2015; Pavúk and Horejs, 2018; Feuser et al., 2020) (Figure 5.7). Among them, the urban transformation of Pergamon from Hellenistic to the Roman Imperial Period is of the most significance (Pirson, 2020). To meet the increasing demand for cultivated crops and woods as food and construction materials (Kobes, 1999; Laabs and Knitter, 2021), Pergamon has remarkably impacted land use in rural areas, such as Tekkedere. Likewise, the ancient harbor cities (Elaia and Kane) and the monumental tumulus encountered human reshaping and construction of the land surface (Fediuk et al., 2019; Seeliger et al., 2019; Mecking et al., 2020).

Increasing landscape instability after land abandonment due to the concomitant absence of landscape management (cf. Schneider et al., 2014; Weiberg et al., 2021) is negatable for Tekkedere valley, because here, a continuous occupation is recorded for roughly the last four millennia. The same reason may also apply to the difference in geomorphodynamics between the Tekkedere and Geyikli valleys. The depositional system in Geyikli is reported to remain generally stable during the last 4000 years (Schneider et al., 2014), which is assumably related to the limited human impacts during ca. 2.3–1.9 ka BP (Schneider et al., 2013).

Throughout western Anatolia particularly during the Beyşehir Occupation phase (Classical and Early Byzantine times, ca. 3.2–1.3 ka BP, Figure 5.7) (Kaniewski et al., 2007), human impacts (forest clearance, fire activities, and grazing) have remarkably influenced the local landscape (Eastwood et al., 1998; Knipping et al., 2007; Duser et al., 2011; Finné et al., 2011; Schneider et al., 2013; Stock et al., 2020a). Likewise, continuous human activities since the Bronze Age (ca. 3.7 ka BP) may strongly disturb the landscape stability in Tekkedere and contributed to the ensuing colluviation, valley infill, and alluvial fan deposition in the western Yunt Dağı mountains. The palynological archives from Elaia (Shumilovskikh et al., 2016), the olive cultivation (Tozan, 2022) accompanied by deforestation, and the occurrence of ceramic fragments in profile Tek-5 (Figure 5.4) point to the increased human activities in the Tekkedere catchment, though the duration and

intensity of the activities in different locations of the valley are currently unclear (Ludwig, 2020a; Michalski, 2021; Tozan, 2022) (Figure 5.7).

The infills of the Tekkedere valley bottom (facies A) date younger than ca. 1300 yr BP, which again reveals the old materials have been removed in the former increased geomorphodynamics and were followed by the ongoing phase of sediment accumulation and a corresponding phase of increased erosion. The dynamics of fine- and coarse-textured sediments (facies Aa and Ab) and the local initial soil formation (facies sAa) in the Tekkedere valley bottom also suggest the erosion and stability repeated and varied spatiotemporally in the catchment during the last 1300 years. A similar process resulted in substantial siltation is reported in Elaia which continued during ca. 1.8–1.1 cal ka BP (Seeliger et al., 2013; Shumilovskikh et al., 2016; Seeliger et al., 2019). The onset of the modern trend towards aridity about 1300 years ago in southwest Turkey (Eastwood et al., 2007), the transition to the Little Ice Age (Kuzucuoğlu et al., 2011), and the various use of the local settlements in Tekkedere (Figure 5.7) altogether have the potential to influence the geomorphodynamics during the last millennium.

## 5.7 Conclusions

The geoarchaeological investigation of the Tekkedere alluvial fan and its catchment is the first detailed study that focuses on the Mid- to Late Holocene geomorphodynamics through alluvial sediments from a long-term settled valley in the hinterland of a major ancient city in western Turkey, i.e., the city of Pergamon. Sediment analyses, facies interpretation, and radiocarbon dating results suggest four principal phases of changing geomorphodynamics after 6.2 cal ka BP. In the first phase, before ca. 5–4 cal ka BP, the aggradation of the Bakırçay plain dominated the local geomorphodynamics, i.e., the deposition of still water sediments, channel beds, and floodplain sediments. This period is generally characterized by the rising sea level and the relatively humid Middle Holocene climate in western Anatolia. Alluvial soils that formed on the Bakırçay floodplain during phase 2 reflect a decline of the Bakırçay floodplain aggradation and low sediment dynamics in the Tekkedere catchment during a climatic phase of decreasing humidity between ca. 5 and 4 cal ka BP. The deposition of alluvial fan sediments from the Tekkedere valley was of low significance before ca. 4 cal ka BP. In the transition from the Middle to Late Holocene, the floodplain soils were buried by Tekkedere alluvial fan deposits (phase 3), pointing to the notably intensified geomorphodynamics in the Tekkedere catchment in comparison to the first two phases. This notable change is attributed to the supraregional trend of aridization and rapid climate change events

between 5 and 3 ka BP, superimposed by the onset of local human activities from the late Middle Bronze Age (ca. 3.7 ka BP) in the catchment. In the last phase, the indications of the enlarged fan coverage, the repetition of fine- and coarse-textured fan deposits, and the reworking of older sediments suggested by age inversions and young valley infills, reveal the increased geomorphodynamics during the Late Holocene. This increase is associated with the varying environmental conditions and natural hazards, soil erosion, and earthquake-triggered landslides, which largely affected the local geomorphodynamics and the consequent settlement activities.

A clear relationship between the climate variations, the changing settlement patterns, and geomorphodynamics especially during the Late Holocene remains unclear due to several age inversions that make the timing of erosion events challenging. Nonetheless, the evidence from Tekkedere suggests that the urban transformation of large settlements (e.g., Pergamon and Elaia) from Hellenism to the Roman Imperial Period contributed to the landscape change in rural areas, though the small catchment of Tekkedere reacted more sensitively to human activities than the higher order catchment of the Bakırçay river. The ongoing pressure from local land use promotes the accumulation of the relatively young valley infills.

## 6. Sediment analyses from Deliktaş catchment

Working package 3

### Holocene geomorphodynamics of a rural catchment in the Pergamon micro-region (eastern Mediterranean)

**Published manuscript:** Yang, X., Becker, F., Nykamp, M., Ludwig, B., Doğan, M., Schütt, B., 2023. Holocene geomorphodynamics of a rural catchment in the Pergamon micro-region (eastern Mediterranean). *The Holocene* 33, 1407–1427.

<https://doi.org/10.1177/09596836231185837>.

This article is an open access article distributed under the terms and conditions of the Creative Commons Attribution (CC BY) license (<https://creativecommons.org/licenses/by/4.0/>).

**Supplementary materials:** see Supplementary materials – To chapter 6 (working package 3). The supplementary materials were originally published online at <https://doi.org/10.1177/09596836231185837>.

**Research data:** Yang X., Becker F., Nykamp M., Schütt, B., 2023. Dataset of sediment analyses (pH, electrical conductivity, magnetic susceptibility, loss on ignition, and X-ray fluorescence) from the Deliktaş catchment in the Pergamon micro-region, western Türkiye. In: Yang X (ed). *Pangaea*. <https://doi.org/10.1594/PANGAEA.959672>.

This research data is an open access data distributed under the terms and conditions of the Creative Commons Attribution (CC BY) license (<https://creativecommons.org/licenses/by/4.0/>).

**Keywords:** alluvial fan; sediment dynamics; human-environment interactions; Bakırçay river; Mediterranean area; Holocene

**Abstract:** The Pergamon micro-region (western Türkiye) has experienced several phases of increased geomorphodynamics during the Holocene. However, the role of local–regional human activities during a transformation between Hellenism and the Roman Imperial period and supra-regional climate fluctuations is still under discussion. Five sediment profiles from the alluvial fan of the rural Deliktaş catchment are analyzed and radiocarbon-dated to provide a sedimentological record covering the Holocene. Our results indicate seven phases of changing sediment dynamics. Five Holocene cycles of coarse- and fine-textured fan sediment deposition covered the paleochannel deposits of the Çaylak creek, and the floodplain sediments of the receiving Geyikli river which aggraded towards the piedmont during the Mid-Holocene. The landscape became stable on the Deliktaş fan and Geyikli floodplain at least ca. 4–3.4 cal ka BP as indicated by paleosols. These paleosols were again buried by fan sediments marking the first phase of accelerated geomorphodynamics during the Late Holocene. Both the local onset of human activities and the regional Mid-Holocene aridization with rapid climate changes play a role. The increased number of archaeological sites and high human pressure on the environment during the Hellenistic–Roman transformation in the Deliktaş area and Pergamon micro-region were hypothesized to contribute to a phase of increased geomorphodynamic activity during the last 2.5 ka. This, however, is less apparent in our record. Our study emphasizes the importance of both, the climatic system and rural-urban cultural history, on landscape development, suggesting potential responses of locally diverse geomorphodynamics on regional-scale transformation in the eastern Mediterranean.

## 6.1 Introduction

In the micro-region of the ancient city of Pergamon (Figure 6.1), known as a Hellenistic and Roman Imperial supra-regional administrative and cultural center (Knitter et al., 2013; Pirson, 2020), archaeological remains reveal human occupation since ca. 11 ka BP (Aksan et al., 2022). After the Attalid kingdom bequeathed Pergamon to Rome in the 2nd century BCE, the micro-region underwent a profound transformation characterized by population growth, doubling of the urban area, a vigorous public building program, a change of settlement structure, and demilitarization (Wulf, 1994; Zimmermann, 2011; Pirson, 2017, 2020; Laabs and Knitter, 2021; Ludwig, 2023). This transformation increased the intensity of human impacts on land use both in and around the city and its villages (Günther et al., 2021; Laabs and Knitter, 2021). Beyond, sediment archives from the micro-region indicate local-scale changing geomorphodynamics during the Middle and Late Holocene (Schneider et al., 2013; 2014; 2015; Seeliger et al., 2019; Yang et al.,

2023a), roughly corresponding to the fluctuations in hydroclimate, vegetation, and settlement activities in the micro-region and its neighboring areas (Becker et al., 2020a). The intensified geomorphodynamics, in essence, correspond to soil erosion processes, as pointed out also for many areas in the eastern Mediterranean (Dusar et al., 2011; Roberts et al., 2019a; Walsh et al., 2019). However, the diversity of landforms (Yang et al., 2021), local tectonics (Paradisopoulou et al., 2010; Kuzucuoğlu et al., 2019a), human activities, and regionally varying climatic changes caused intra-regional differences in landscape development (Dusar et al., 2011).



**Figure 6.1** Topographical map with the locations of selected archaeological sites (Ludwig, 2020b) and modern settlements in the Pergamon micro-region. The inset map indicates the location of this study in the Aegean coastal region of western Türkiye.

The eastern Mediterranean experienced a marked drying trend from around 4.6 ka BP (Finné et al., 2011) and several distinct rapid climate changes with locally varying intensity and timing (Weiss, 2016; Bini et al., 2019). The 4.2 ka BP drought event (between ca. 4.2 and 3.9 ka BP) (Roberts et al., 2011a; Bini et al., 2019) and the later 3.2 ka BP drought event (two phases: 3.5–3.3 and 3.1–2.9 ka BP) (Manning et al., 2020; Hazell et al., 2022) are widely regarded as the most important rapid climate change events during the Mid–Late Holocene (Bini et al., 2019; Di Rita et al., 2022). The influence of these events on the diverse landscapes in the eastern Mediterranean region (including the Pergamon micro-region) is not yet fully understood.

Located in the western Pergamon micro-region, the Karadağ mountain forms a peninsula, to the north, west, and south surrounded by the Aegean Sea. To the east, it verges on the

floodplain of the lower Geyikli river, a major tributary of the Bakırçay river. The Deliktaş catchment drains the landside part of the Karadağ mountain (Figure 6.1). Widespread rills and gullies document severe soil erosion processes in the areas today covered by typical Mediterranean shrubland. Area-wide archaeological surveys document that this area has been inhabited by humans at least since the Bronze Age; the number of settlement sites markedly increased during the Hellenistic–Roman Imperial period (Ludwig et al., 2022). Sequential subsurface stratigraphy correlative to the erosion processes in the transition zone of the Deliktaş fan and the Geyikli floodplain provides a suitable archive to document regional environmental variability of different spatial scales, which might be influenced by the drainage basin size and geology as well as their responses to climatic, tectonic, base-level changes (Van Dijk et al., 2012) and human influence (Coulthard et al., 2002; Duser et al., 2011).

The overall objectives of this paper are to better understand (a) the complexity of local geomorphodynamics in the Pergamon micro-region, and (b) possible triggers of varying intensities of geomorphodynamic processes, i.e., supra-regional climatic events and local to regional settlement activities. Comparing our findings with studies from the wider eastern Mediterranean allows us to decipher the effects of climate and humans as spatiotemporally varying forces on the Mediterranean landscape forming processes that are subject to debate for already more than 50 years (e.g., Vita-Finzi, 1969b; Duser et al., 2011; Jouffroy-Bapicot et al., 2021, and references therein). Beyond, this study will provide insights into how local landscapes respond to the (urban) transformation in the Mediterranean region.

## **6.2 Study site**

### **6.2.1 Natural setting**

The Deliktaş catchment (ca. 15 km<sup>2</sup>) is located in the eastern Karadağ mountain (Figure 6.1) at the western tip of the graben-controlled Bakırçay plain (Karacik et al., 2007; Yang et al., 2021). The modern climate is typical Mediterranean subhumid, characterized by prominent seasonality with dry and hot summers and mild and wet winters (Peel et al., 2007; Bakker et al., 2013). The close-by station in Dikili (Figure 6.1) recorded an annual precipitation of 711 mm and an annual temperature of 16.2 °C (1981-2010) (Yang et al., 2021).

The Pergamon micro-region is located in one of the most rapidly extending regions on Earth (Özpolat et al., 2022), thus, being tectonically highly active, with at least nine

earthquakes documented during the last two millennia (Nalbant et al., 1998; Emre et al., 2005; McHugh et al., 2006; Paradisopoulou et al., 2010; Schneider et al., 2014). A seismic landslide caused the abandonment of a rural settlement during the 20<sup>th</sup> century (Ludwig, 2020a). Pleistocene tectonics formed NW-trending normal faults within the Deliktaş catchment (Karacik et al., 2007). At present, the NE-trending Bakırçay (Bergama) graben is subsiding at a rate  $<1 \text{ mm yr}^{-1}$  (Seeliger et al., 2017). Situated in the Dikili-Çandarlı volcanic suite of the western Anatolian Miocene volcanism, the Deliktaş catchment is dominated by upper Miocene–Pliocene rhyolite domes of the Çandarlı group (Karacik et al., 2007) where lime-free brown soils developed (Danacıoğlu and Tağıl, 2017).

A field survey showed very strong geomorphodynamics all over the Deliktaş catchment (Figure 6.2). Slopes in the upper catchment are steep (average ca.  $30^\circ$ , calculated from TanDEM-X data with 12.5 m resolution) and dissected by intermittent drainage ways, mainly gullies (Becker et al., 2022a) (Figure 6.2b and c). Bare rocks crop out predominantly on the steep slopes in the headwater area where stony soils are ubiquitous (Figure 6.2c). The Çaylak creek flows eastwards into the Geyikli river, a major tributary of the Bakırçay river (Figure 6.1). At the transition from the Karadağ mountain to the Geyikli floodplain, the Çaylak creek deposits an alluvial fan (size:  $1 \text{ km}^2$ ; length: 1.6 km; slope:  $1^\circ$ ; Figure 6.2).

Shrubs characterize the present-day vegetation cover of the Deliktaş area (Figure S6.1). Grasslands predominate in the northern part of the catchment; coniferous woodlands and olive groves prevail in its southern part (Figure 6.2c and d). From 7.6 to 3 ka BP natural deciduous oak forests prevailed around the nearby ancient harbor city of Elaia (Figure 6.1) (Shumilovskikh et al., 2016). A rather open landscape existed between 3.5 and 3.4 ka BP around the Kara Göl crater lake (Figure 6.1) (Shumilovskikh et al., 2022). Arboriculture (olive, pistachio, and walnut) extended during the Late Holocene, parallel to the spread of pastoral and tillage agriculture, likely reaching a maximum during 2.1–1.8 ka BP (Shumilovskikh et al., 2016; 2022). The spread of olives might also correspond with the contemporarily favorable climate conditions (Di Rita and Magri, 2009; Florenzano et al., 2017). In the past 1000 years, semi-natural forests (mainly pine) dominated whereas oak forests decreased (Shumilovskikh et al., 2016; 2022); olives are still cultivated. Overgrazing occurs in mountainous areas (Shumilovskikh et al., 2022).

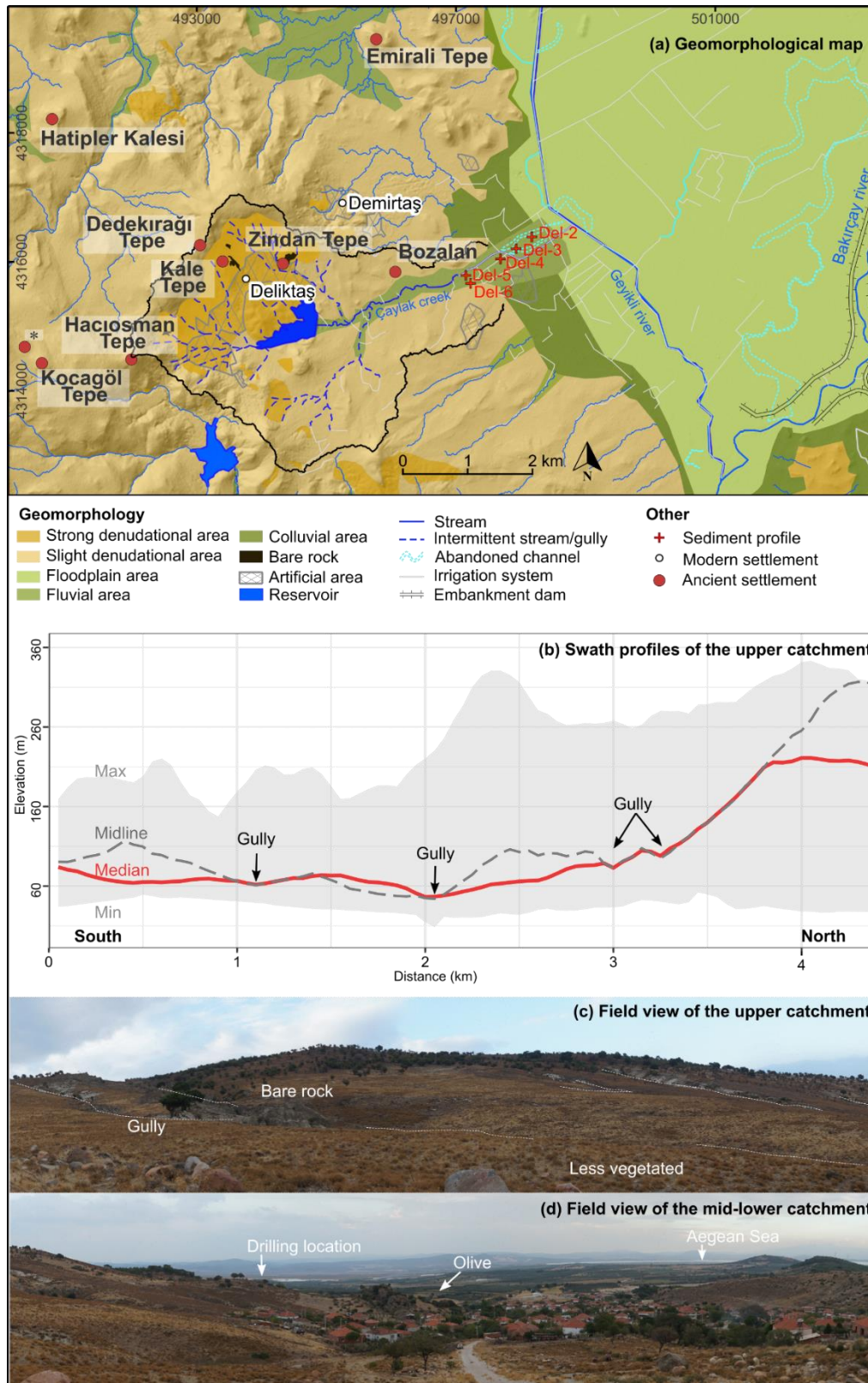


**Figure 6.2** (a) Geomorphological map of the Deliktaş catchment complemented by the locations of the sediment profiles and ancient settlements (Ludwig et al., 2022). Note: \* represents an unnamed archaeological site. (b) Swath profiles of the upper Deliktaş catchment. (c) Field view of the upper catchment. (d) Field view of the mid-lower catchment. (Field pictures in c and d were taken on 10 Oct 2021 by the first author, which, together with figure b, were modified from Becker et al. (2022a)).

## 6.2.2 Settlement history

The archaeological survey in the Deliktaş catchment and its surroundings indicates settlement activities have started since the Bronze Age (two sites: Zindan Tepe and Hatipler Kalesi) (Figure 6.2; Table S6.1) (Ludwig et al., 2022). The number of archaeological sites increased ( $n = 9$ ) at the onset of the Classical period and remained high during the Hellenistic and Roman Imperial periods (ca. 500 BC–400 AD; Table S6.1) (Ludwig et al., 2022). Successively, only three sites were settled during the Late Antiquity, Byzantine, and Ottoman periods (Table S6.1).

Hilltop sites, e.g., Zindan Tepe, were likely used as fortresses because they have an impressive view over the Bakırçay plain and to the cities of Pergamon, Elaia, and Pitane (Ludwig et al., 2022). Additionally, buildings in higher areas, e.g., Dedekırağı Tepe and Haciosman Tepe, are interpreted as watchtowers or tower houses as part of agricultural estates (Ludwig et al., 2022). The Deliktaş catchment is located adjacent to the major route network which connects the harbors of Pitane and Elaia with various sites in the Karadağ mountain (Laufer, 2015; Fediuk et al., 2019; Ludwig, 2020b) (Figure 6.1).

## 6.3 Methods

### 6.3.1 Field work

Five sediment profiles (thicknesses up to 8 m) were obtained along a transect from the proximal to distal area of the Deliktaş alluvial fan by vibracoring with open cores (5 cm diameter) in October 2021 (Figure 6.2; Table 6.1). The macroscopic sediment description included layer thickness, sediment color, depositional structure, texture and fabric, hydromorphic features, biological modification, and occurrence of artifacts (see also Yang et al. (2022)). Sediment samples ( $n = 171$ ) were taken according to stratigraphic layers; samples for radiocarbon dating ( $n = 12$ ; Table 6.3) were also collected.

**Table 6.1** Metadata of sediment cores extracted from the Deliktaş alluvial fan (n = 5).

Sediment profile	Latitude (° N)	Longitude (° E)	Elevation (m a.s.l.)	Depth (cm b.s.)	Samples (n)	Geomorphological position
Del-2	38.99649	26.97883	6.0	500	33	Alluvial fan (distal area)
Del-3	38.99484	26.97604	7.1	700	46	Alluvial fan (middle area)
Del-4	38.99339	26.97326	9.3	800	39	Alluvial fan (middle area)
Del-5	38.99110	26.96710	12.5	444	28	Alluvial fan (proximal area)
Del-6	38.99000	26.96794	12.2	500	25	Alluvial fan (proximal area)

## 6.3.2 Laboratory work

### 6.3.2.1 Sediment analyses

Sediment samples were analyzed on six bulk parameters in the laboratory of the Bergama archaeological excavation house to provide indicators for sediment origins, erosional and (post-) depositional processes (Buggle et al., 2011; Ülgen et al., 2012; Croudace and Rothwell, 2015), paleosol occurrence (Niwa et al., 2011; Nykamp et al., 2020) and human activity (Goldberg and Macphail, 2006). The aggregates of the air-dried samples were crushed. Coarse components ( $\varnothing \geq 2$  mm) were separated from fine fractions ( $\varnothing < 2$  mm) and weighted to calculate the mass percentage of the coarse components. Electrical conductivity (EC) and pH values of the sediments were measured at least 2 times in a suspension of 5 g dried sediments in 12.5 mL distilled water by applying a PEZ9908 meter (resolution: 0.01 pH, 1  $\mu\text{S cm}^{-1}$  EC). The pH classification refers to the USDA soil survey manual (Soil Science Division Staff, 2017) (Table S6.2). Mass-specific magnetic susceptibility of the sediments was determined by triplicate measurements of weighted samples at low frequency ( $X_{\text{LF}}$ ,  $10^{-8}$  m<sup>3</sup> kg<sup>-1</sup>) in 12 cm<sup>3</sup> plastic pots with a Bartington magnetic susceptibility system (MS3 meter and MS2B dual frequency sensor) (Dearing, 1994; Dearing et al., 1996). Loss on ignition (LOI<sub>550</sub>) as a proxy for organic matter content was measured by igniting 10 g sample materials at 550 °C for four hours in a muffle furnace after oven-drying the sediment (4 h at 105 °C) (Dean, 1974; Heiri et al., 2001;

Santisteban et al., 2004). Strong positive relationships between LOI<sub>550</sub> and the total organic carbon content (Figure S6.2) of sediments from the western lower Bakırçay plain (Figure S6.1) indicate LOI<sub>550</sub> in this region is capable to estimate organic matter content.

The elemental composition of samples from Del-2, Del-3, and Del-5 was analyzed using a portable energy-dispersive X-ray fluorescence spectrometer (p-ED-XRF; Thermo Fisher Scientific NITON XL3t-900 GOLDD+; analytical range: Mg to U) applying the “Mining Cu/Zn” mode with four filters (30 s measurement time each filter). Quality was controlled by measuring certified reference materials and acid-purified silica sand (Table S6.3). For elemental sediment characterization, we report the element ratios of Ca/Ti and K/Si.

Results of laboratory analyses are reported as median and median absolute deviation (MAD, in brackets) and categorized using the classifications in Table S6.2. Reported relationships between the variables were established based on Spearman’s correlation coefficient and related tests ( $\alpha = .05$ ). The assumption of (bivariate) normality is tested by applying the Shapiro-Wilk test (*ggpubr v0.6.0* (Kassambara, 2023) and *corrplot v0.92* (Wei and Simko, 2021)) in R (R Core Team, 2022). Raw and processed data are provided in a published dataset at PANGAEA (Yang et al., 2023c).

### 6.3.2.2 Radiocarbon dating

The sediment chronology is developed by radiocarbon dating (<sup>14</sup>C) of charcoal or a mixture of charcoal and adhering sediments (the latter if %C of the macroscopically separable charcoal is <1–2 mg) using accelerator mass spectrometry (AMS) at the TÜBİTAK National 1 MV AMS Laboratory (Doğan et al., 2021). Macroscopic plant remains and rootlets were removed before the samples were acid-washed (Fowler et al., 1986; Brock et al., 2010). The IntCal20 calibration curve (Reimer et al., 2020) and the *rcarbon* package (Crema and Bevan, 2021) were used to calibrate the radiocarbon ages in R (R Core Team, 2022). Confidence intervals of 95% are reported for the calibrated ages. The age-depth modeling of samples from profiles Del-2, Del-3, and Del-6 are calculated based on the *clam* R-package (v2.5.0) (Blaauw, 2010).

## 6.4 Sediment facies

Sediments extracted along the transect on the Deliktaş fan are categorized into seven sub-facies based on their macroscopical/lithological and (bulk-)chemical characteristics. These sub-facies are summarized into facies B, alluvial fan facies, and facies C, floodplain facies (Table 6.2). The classification resembles the facies described in Tekkedere alluvial fan (Yang et al., 2023a), following the conventional sedimentological terminology of

alluvial fan (Blair and McPherson, 1994, 2009; Moscariello, 2018) and floodplain deposits (Miall, 2006, 2014).

**Table 6.2** The characteristics of sediment sub-facies in the Deliktaş catchment (cf. Yang et al., 2023a).

Facies	Sub-facies	Description
Deliktaş alluvial fan sediments (B)	Ba	fine-textured alluvial fan sediments characterized by clayey to silty sediments with occasionally distributed pebbles; often high in EC and LOI <sub>550</sub> values; low X <sub>LF</sub> and element ratio of K/Si
	sBa	recent or buried topsoil horizons developed on sub-facies Ba clay/silt, a distinct increase in LOI <sub>550</sub> values compared to sub-facies Ba
	Bb	coarse-textured alluvial fan sediments more coarse components (mainly fine pebbly sand) with typically lower values of LOI <sub>550</sub> and increased values of K/Si compared to sub-facies Ba
	Bc	channel deposits layers of massive, clast-supported, subangular to subrounded fine–medium pebbles
Geyikli river sediments (C)	Cf	floodplain sediments of the Geyikli river clayey to silty deposits; compared to sub-facies B, this sub-facies is slightly more alkaline and organic richer; enhanced Ca/Ti ratio and solutes (secondary carbonate precipitation); common Fe-Mn mottling (strongly influenced by the groundwater variation from the Geyikli floodplain)
	sCf	buried topsoil horizons developed on sub-facies Cf silty clays, with increased LOI <sub>550</sub> values, compared to sub-facies Cf
	Csh	extreme flood events of the Geyikli river thin layers (ca. 10 cm thick) of (fine pebbly) coarse sand intercalated within sub-facies Cf

#### 6.4.1 Facies B: Deliktaş alluvial fan sediments

The Deliktaş alluvial fan facies B contains four sub-facies (Table 6.2). Clayey to silty deposits with occasionally distributed pebbles are classified as fine-textured alluvial fan sediments (sub-facies Ba) which show generally high EC and LOI<sub>550</sub> values, low X<sub>LF</sub> values, and low element K/Si ratios. Repeatedly sub-facies Ba is topped by a layer with distinctly increased LOI<sub>550</sub> values indicating recent or buried top-soil horizons (sub-facies sBa). Sub-facies Bb is composed of fine-pebbly sands with typically, compared to sub-

facies Ba, low LOI<sub>550</sub> values and increased K/Si ratio, corresponding to coarse-textured alluvial fan sediments. Massive, subangular to subrounded fine–medium pebbles represent channel deposits (sub-facies Bc) (Miall, 2006).

#### **6.4.2 Facies C: Geyikli river sediments**

Facies C, the Geyikli river sediments, includes three sub-facies (Table 6.2). Dark brown clayey to silty deposits, slightly alkaline and rich in organic matter are classified as sub-facies Cf, corresponding to floodplain sediments of the Geyikli river. Thin layers (ca. 10 cm thick) of coarse sand to fine pebble (sub-facies Csh) intercalate with these floodplain sediments and correspond to stronger flood events compared to sub-facies Cf (Miall, 2006). Silty clays with high LOI<sub>550</sub> values overlying sub-facies Cf represent buried top-soil horizons developed on the floodplain sediments (sub-facies sCf).

### **6.5 Sediment profiles**

The sediment profiles show alternating layers of alluvial fan deposits, which are generally coarser in the profiles extracted from the proximal fan and finer downslope. At the distal part, fan deposits interfinger with floodplain deposits of the Geyikli river. Sediment core Del-3 serves as a key profile and is presented in detail (Figure 6.3). The other sediment profiles are presented in overview and compared with the key profile Del-3; detailed documentation is provided in the Supplementary materials (To chapter 6 – working package 3). Radiocarbon datings document that fan deposition started at least in the Early Holocene and continued during the entire Holocene, and the Geyikli floodplain deposits occurred during the Middle Holocene (Figure 6.3; Table 6.3).

**Table 6.3** The AMS-<sup>14</sup>C dating samples from the Deliktaş alluvial fan (n = 12), pre-treatment procedure, sediment sub-facies of the sample location, and their dating results and calibration (calibration curve: IntCal20 (Reimer et al., 2020)). Dated material: C/S refers to mixed materials (charcoal and adhering sediment); sub-facies characteristics are in Table 6.2.

Sediment profiles	Depth cm b.s. (Unit ID)	Lab. ID (TÜBİTAK*)	Dated material	Sub-facies	<sup>14</sup> C ± σ	cal BP		CE/BCE (95%)
						Median	95% probability	
Del-2	226 (⑤)	2202	C/S	sCf	3215±26	3423	3478–3378	1529–1429 BCE
	322 (③)	2203	charcoal	Cf	4092±40	4605	4817–4444	2868–2495 BCE
	459 (①)	2204	C/S	Cf	6152±30	7056	7157–6956	5208–5007 BCE
Del-3	117 (⑦)	2205	C/S	Ba	3348±27	3570	3683–3486	1734–1537 BCE
	285 (⑤)	2206	charcoal	Ba	4735±73	5466	5587–5320	3638–3371 BCE
	569 (②)	2207	C/S	Bb	7843±76	8655	8982–8451	7033–6502 BCE
Del-4	85 (⑤)	2208	C/S	Ba	2227±31	2227	2336–2148	387–199 BCE
Del-5	77 (⑤)	2209	C/S	Ba	3666±97	4001	4290–3699	2341–1750 BCE
	230 (③)	2210	C/S	sBa	3541±37	3828	3960–3699	2011–1750 BCE
Del-6	77 (④)	2211	charcoal	Ba	421±21	495	515–343	1435–1607 CE
	166 (③)	2212	charcoal	sBa	1290±22	1225	1283–1177	667–773 CE
	333 (②)	2213	charcoal	Bb	1598±23	1470	1529–1411	421–539 CE

### 6.5.1 Key profile Del-3

Key profile Del-3 was taken from the middle part of the Deliktaş fan and is 700 cm thick. It is subdivided into 9 lithostratigraphic units (Figure 6.3). A pebble-dominated unit at the bottom (unit 1; channel deposits, sub-facies Bc) is overlain by repetitions of sandy (units 2, 4, 6, and 8; coarse-textured alluvial fan deposits, sub-facies Bb) and silty-clayey (units 3, 5, 7, and 9; fine-textured alluvial fan deposits, sub-facies Ba) sediments. A radiocarbon sample from unit 2 dates into the Early Holocene (ca. 8.7 cal ka BP at 569 cm b.s.; Table 6.3). At approximately 1 m depth below the surface (unit 7, 117 cm b.s.) fan deposits are of Late Holocene age dating to ca. 3.6 cal ka BP. Accordingly, in the approximately 4.5 ka between the Early Holocene and the beginning Late Holocene about 4 m of sediments were accumulated. The charcoal-based radiocarbon age extracted from unit 5 (285 cm b.s.) with an age of 5.4 ka BP is in line with the aggradation rates.

In total, 46 samples were extracted from Del-3. Graphs displaying the amount of coarse fraction (particles  $\varnothing \geq 2$  mm; 0–61 mass%) and K/Si ratios run highly parallel ( $p < .001$ ,  $\rho = 0.64$ ), and show inverse trends to the graphs of EC ( $\varnothing \geq 2$  mm and EC:  $p = 0.05$ ,  $\rho = -0.29$ ; K/Si and EC:  $p < .001$ ,  $\rho = -0.58$ ) and  $\text{LOI}_{550}$  values ( $\varnothing \geq 2$  mm and  $\text{LOI}_{550}$ :  $p < .001$ ,  $\rho = -0.71$ ; K/Si and  $\text{LOI}_{550}$ :  $p < .001$ ,  $\rho = -0.73$ ; Figure 6.3). Values of pH remain roughly constant at 7.8 below 353 cm b.s. (units 1–4), slightly increase to 8.5 at 60 cm b.s., and drop rapidly to 6.9 near the surface.  $X_{LF}$  values decrease slightly oscillating from  $71 \cdot 10^{-8} \text{ m}^3 \text{ kg}^{-1}$  (class 3) in unit 1 to  $36 \cdot 10^{-8} \text{ m}^3 \text{ kg}^{-1}$  (class 2) in unit 4 and remain constantly low at ca.  $23 \cdot 10^{-8} \text{ m}^3 \text{ kg}^{-1}$  (class 1) in units 5–9. The element ratio of Ca/Ti remains relatively constant with values between 3 and 5. Altogether, sediments are poor in carbonates; only few carbonate precipitations occur around 280 cm b.s.

**Unit 1 (700–647 cm b.s., n = 3)** is characterized by matrix-supported, poorly sorted, coarse sand and (sub)rounded fine–coarse pebbles. Water-saturated sediments below 660 cm b.s. indicate the level of the current groundwater table. This unit has a sharp boundary to overlying unit 2. Three sediment samples show a distinctively decreasing content of coarse components (from 61 to 16 mass%) with decreasing depth; in parallel, K/Si ratios constantly decrease. This pebbly unit is interpreted as channel sediments (sub-facies Bc).

**Unit 2 (647–528 cm b.s., n = 7)** contains dark yellowish brown (10 YR 4/4) fine–medium sand with few fine pebbles and Fe-Mn mottles. It gradually transits to unit 3. The mixed charcoal/sediment sample at 569 cm b.s. dates to 8982–8451 cal yr BP (Table 6.3). EC values remain distinctly low (around  $78 \mu\text{S cm}^{-1}$ ) in units 1–2.  $X_{LF}$  values reach the highest number of Del-3 at the bottom of unit 2 ( $98 \cdot 10^{-8} \text{ m}^3 \text{ kg}^{-1}$ ) and decrease gradually to the unit

top ( $46 \cdot 10^{-8} \text{ m}^3 \text{ kg}^{-1}$ ).  $\text{LOI}_{550}$  values constantly increase from 1.7 mass% at the bottom of unit 1 to 3 mass% at the top of unit 2. K/Si ratios slightly decrease from 0.092 to 0.088 with decreasing depth. This sandy unit corresponds to the coarse-textured alluvial fan facies (sub-facies Bb).

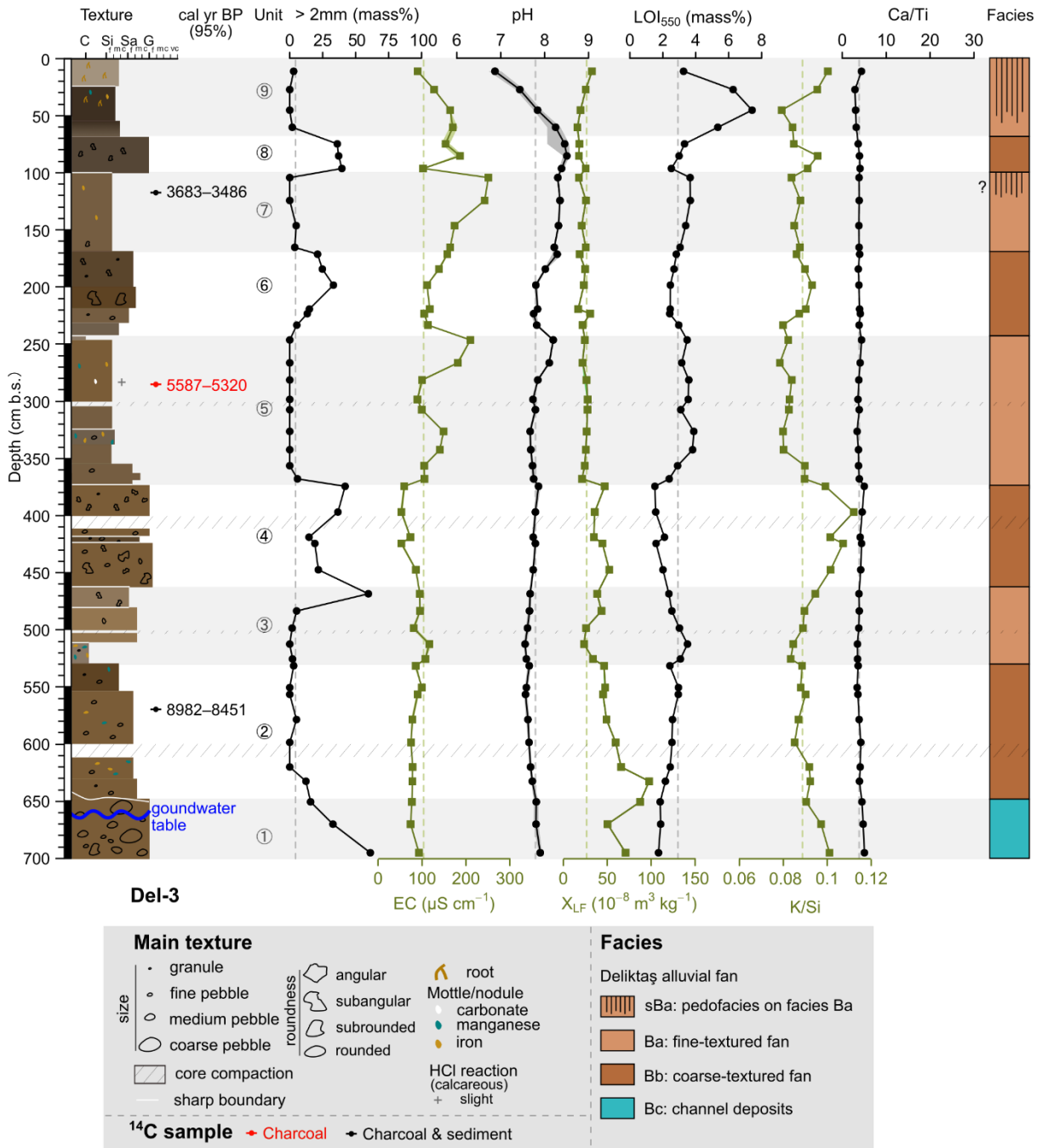


**Figure 6.3** The lithostratigraphy, radiocarbon datings, sediment bulk characters, and sediment facies of profile Del-3. 1) colors of the sediment texture column represent the color observed in the field; 2) shaded bands separate different units; 3) the vertical dashed lines of each sedimentary analysis represent the median values of the whole profile.

**Unit 3 (528–461 cm b.s., n = 5)** is composed of yellowish brown (10 YR 5/4) fine to medium sand in the upper layers and Fe-Mn mottled silty clay in the lower layers; few subrounded fine–medium pebbles occur. The boundary to overlying unit 4 is sharply marked by an increased content of coarse clasts ( $\text{\O} \geq 2$  mm). EC (96 (10)  $\mu\text{S cm}^{-1}$ ) and  $\text{LOI}_{550}$  (2.95 (0.4) mass%) in unit 3 are slightly higher than those in underlying units, however, predominantly marked by peaking values at ca. 510 cm b.s. (Figure 6.3). In contrast, K/Si ratios continuously increase from the unit bottom (0.083) to the top, reaching the maximum value in overlying unit 4 (0.11 at 400 cm b.s.).  $X_{\text{LF}}$  values slightly vary but remain in low ranges (39 (7)  $10^{-8} \text{ m}^3 \text{ kg}^{-1}$ ). This clayey–fine sandy unit is a fine-textured alluvial fan facies (sub-facies Ba).

**Unit 4 (461–371 cm b.s., n = 5)** contains dark yellowish brown (10 YR 4/4) fine to coarse sand with subangular–subrounded fine pebbles. To the top, the unit gradually merges into unit 5 without a sharp boundary. Unit 4 is characterized by varying contents of coarse clasts ( $\text{\O} \geq 2$  mm) on an altogether high level with approximately 15–42 mass%. EC values remain stable at a low level (60 (7)  $\mu\text{S cm}^{-1}$ ).  $\text{LOI}_{550}$  values oscillate around 1.6 mass% and reach the lowest content of 1.5 mass% at 374 cm b.s. K/Si ratios peak at 400 cm b.s. (K/Si = 0.11); in the underlying samples K/Si ratios constantly increase until peaking and then to the top constantly decrease.  $X_{\text{LF}}$  values vary around 45 (7)  $10^{-8} \text{ m}^3 \text{ kg}^{-1}$  without a distinct trend. Unit 4 is interpreted as coarse-textured fan deposits (sub-facies Bb).

**Unit 5 (371–241 cm b.s., n = 9)** is composed of dark yellowish brown (10 YR 4/4) clayey silt with few Fe-Mn mottles. Few fine carbonate nodules occur in the upper part. The boundary to overlying unit 6 is sharp. The charcoal sample from 285 cm b.s. dates to 5587–5320 cal yr BP. Values of  $\text{LOI}_{550}$  slightly vary around 3.48 (0.3) mass% (class 3) and are higher than those in underlying units 1–4 (2.4 (0.5) mass%, n = 20). EC values distinctly increase from units 1–4 (80 (8)  $\mu\text{S cm}^{-1}$ , n = 20) to unit 5 with a median value of 106 (16)  $\mu\text{S cm}^{-1}$ , peaking at the boundary to overlying unit 6 (210  $\mu\text{S cm}^{-1}$  at 246 cm b.s.).  $X_{\text{LF}}$  values remain at an altogether low level around 26 (2)  $10^{-8} \text{ m}^3 \text{ kg}^{-1}$  (class 1). Also, K/Si ratios remain stable around 0.08. This silty unit corresponds to fine-textured fan deposits (sub-facies Ba).

**Unit 6 (241–168 cm b.s., n = 6)** consists of dark brown (10 YR 3/3) fine to medium sand with few subangular–subrounded pebbles. It has a gradual boundary to overlying unit 7. Similar to unit 4, this unit shows relatively high contents of coarse clasts ( $\text{\O} \geq 2$  mm; 18 (6) mass%). K/Si ratios (median = 0.09) are slightly higher than those in underlying unit 5. The values of pH (7.82) and EC (105  $\mu\text{S cm}^{-1}$ ) vary on a relatively low level; while above 200 cm b.s., pH values slightly increase to 8.3 and EC values increase to 158  $\mu\text{S cm}^{-1}$  at the unit top. Values of  $\text{LOI}_{550}$  remain constantly low without distinct variations (2.57 (0.1) mass%). This sandy unit represents coarse-textured fan deposits (sub-facies Bb).

**Unit 7 (168–100 cm b.s., n = 4)** is composed of brown (10 YR 4/3), Fe-mottled clayey silt. It sharply borders overlying unit 8. The mixed charcoal/sediment sample from 117 cm b.s. dates to 3683–3486 cal yr BP. EC values continuously increase from bottom to top and peak at the boundary to overlying unit 8 ( $251 \mu\text{S cm}^{-1}$ , 105 cm b.s.). Sediments are moderately alkaline (pH = 8.31(0)). This silty unit corresponds to fine-textured fan deposits (sub-facies Ba). The slight increase of  $\text{LOI}_{550}$  from 3.1 mass% at the unit base to 3.7 mass% at the unit top may imply an initial soil formation though other soil features are not apparent (Figure 6.3).

**Unit 8 (100–68 cm b.s., n = 3)** is composed of brown (10 YR 3/2) coarse sand with fine subangular to subrounded pebbles. It has a gradual boundary with overlying unit 9. Bulk sediment characteristics correspond to those in coarse-textured units (units 2, 4, and 6), dominated by high contents of coarse clasts, low EC and  $\text{LOI}_{550}$  values, and peaking K/Si ratios. Correspondingly, this unit represents coarse-textured fan deposits (sub-facies Bb).

**Unit 9 (68–0 cm b.s., n = 4)** contains fine sandy silt with color changing from very dark brown (10 YR 2/2) at the bottom to light brownish grey (10 YR 6/2) at the top. The occurrence of roots increases to the surface. The values of pH constantly decrease from 8.3 at 60 cm b.s. to 6.9 at 11 cm b.s. The graph of EC values runs parallel to the graph of pH values, reaching low values around  $90 \mu\text{S cm}^{-1}$  close to the surface (Figure 6.3).  $\text{LOI}_{550}$  peaks with 7.4 mass% at 45 cm b.s. The graph of the K/Si ratio runs inversely to that of  $\text{LOI}_{550}$ , reaching minimum values of 0.08 at 50 cm b.s. This silty unit corresponds to fine-textured fan deposits (sub-facies Ba), modified by soil formation (sub-facies sBa).

## 6.5.2 Other Deliktaş fan sediment profiles

Sediment profile **Del-2** was extracted from the distal part of the Deliktaş alluvial fan (Figure 6.2). This 500-cm-thick profile shows 7 lithostratigraphic units (Figure 6.4 and Figure S6.3). Dark brown clayey to silty sediments dominate the bottom strata with occasional pebbles (units 1–5, below ca. 210 cm b.s.).  $\text{LOI}_{550}$  values in units 1–5 ( $n = 24$ ) average 3.3 (0.6) mass% and peak at 345 cm b.s. with 5.4 mass% (unit 3) and at 222 cm b.s. with 5.1 mass% (unit 5). K/Si ratios slightly vary (0.078 (0.004)) in these units, while Ca/Ti ratios show three times higher values in units 3 and 4 (12.5 (1),  $n = 9$ , 345–262 cm b.s.) than those in other units (4.162 (0.68),  $n = 24$ ). Secondary carbonate concretions and Fe–Mn mottles are abundant in units 3–4. Due to the overall sediment characteristics of units 1–5, these deposits are assigned as floodplain deposits of the Geyikli river (sub-facies Cf). The transition between the floodplain and overlying alluvial fan deposits, corresponding to unit 5, shows the dark brown color of the sediments with high  $\text{LOI}_{550}$  values (4.35 (0.2) mass%, class 3,  $n = 4$ ) and in parallel

relatively low pH (7.93 (0), n = 4) and locally peaking EC value and low K/Si values. Correspondingly, unit 5 is interpreted as a fossil soil developed on the floodplain deposits (sub-facies sCf). Fine pebbly sand layers in units 1, 4, and 5 point to high flood events (sub-facies Csh). In the uppermost layers of Del-2 (units 6–7, above 200 cm b.s.) grain sizes increase, showing dominating sand (unit 6, 208–78 cm b.s., sub-facies Bb) and silt (unit 7, 78–0 cm b.s., sub-facies Ba) components. LOI<sub>550</sub> values in the two units remain low with poor variations (2.5 (0.3) mass%, n = 9). Three radiocarbon datings from units 1–5 indicate that the Geyikli floodplain sediments were deposited from the Middle Holocene (7157–6956 cal ka BP, 450 cm b.s., unit 1) to the beginning of Late Holocene (3478–3378 cal ka BP, 226 cm b.s., unit 5) (Table 6.3). Accordingly, the overlying units 6 and 7, i.e., the Deliktaş fan deposits, were accumulated during the Late Holocene.

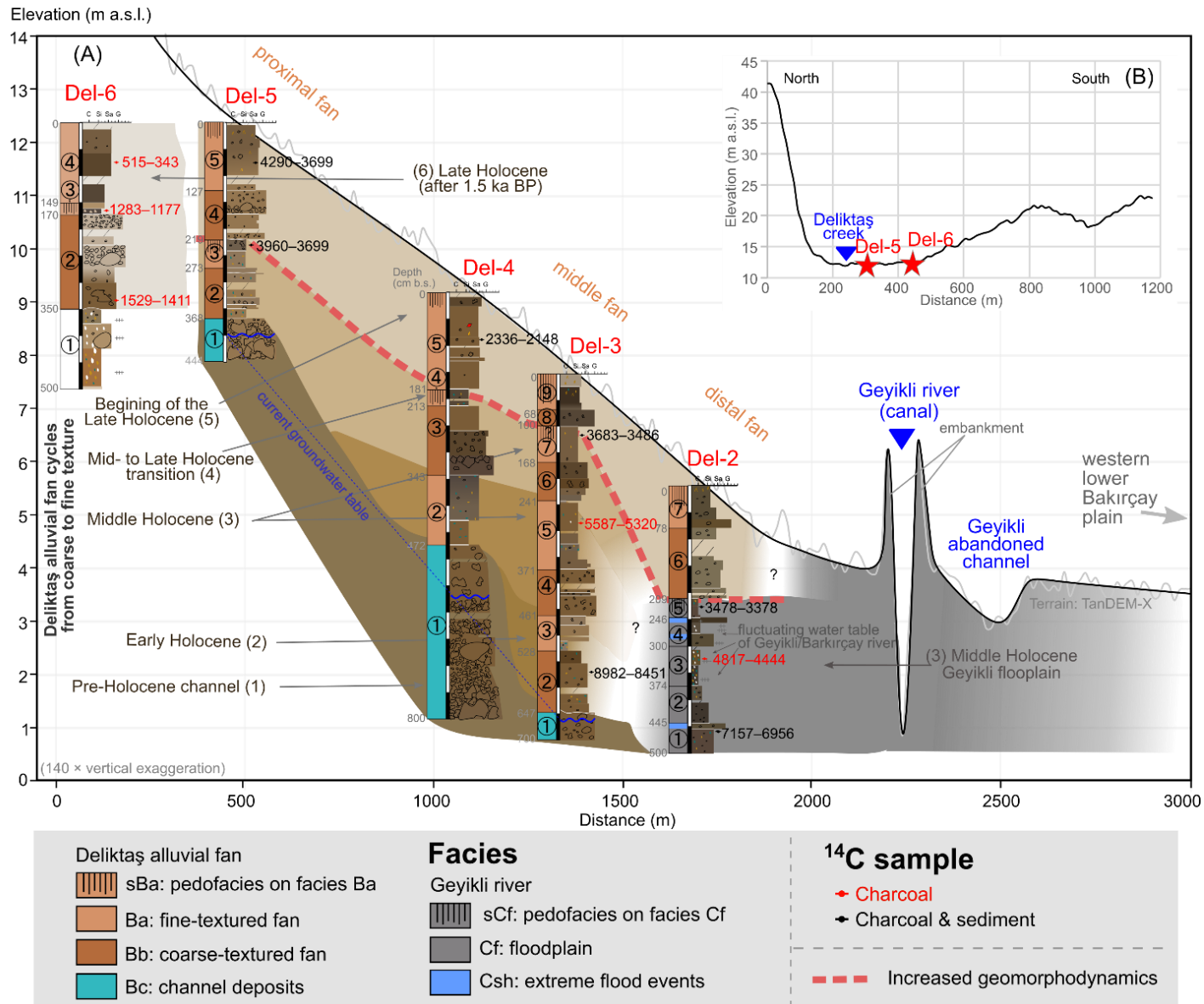
Sediment profile **Del-4** was extracted from the middle part of the alluvial fan (Figure 6.2). This profile is 800 cm thick and divided into 5 lithostratigraphic units (Figure 6.4 and Figure S6.4). The stratigraphy and bulk-chemical characteristics of the sediments are comparable to those described for the key profile Del-3. The sediments with clast-supported fabric at the profile bottom (unit 1, 800–472 cm b.s.) refer to channel deposits (sub-facies Bc). They are overlain by fine-textured alluvial fan sediments (sandy to silty, unit 2, 472–343 cm b.s. and unit 5, 181–0 cm b.s.) corresponding to sub-facies Ba and coarse-textured alluvial fan sediments (pebbly to sandy, unit 3, 343–213 cm b.s.) corresponding to sub-facies Bb. Unit 4 (213–181 cm b.s.) is characterized by dark brown clayey silt with slightly increased values in EC, pH, and LOI<sub>550</sub>, most likely documenting a fossil soil (sub-facies sBa). A non-diagnostic ceramic fragment occurred at 60 cm b.s. The only radiocarbon sample taken from Del-4 (charcoal/sediment mixture from 85 cm b.s.) dates to 2336–2148 cal yr BP (Table 6.3).

Sediment profile **Del-5** is 444 cm thick and was extracted from the proximal fan (Figure 6.2). Del-5 shows five lithostratigraphic units (Figure 6.4 and Figure S6.5). Similar to the key profile Del-3, the basal sediments with a clast-supported fabric point to pebbly channel deposits of sub-facies Bc (unit 1, 444–368 cm b.s.) that are covered by alternating units of coarse-textured alluvial fan sediments of sub-facies Bb (unit 2, 368–273 cm b.s. and unit 4, 219–127 cm b.s.) and fine-textured alluvial fan sediments of sub-facies Ba (unit 3, 273–219 cm b.s. and unit 5, 127–0 cm b.s.). Brown clayey silts at the top of unit 3 (242–219 cm b.s., n = 2) show relatively high LOI<sub>550</sub> values (2.9 mass%) and relatively low pH values (7.88), suggesting a fossil soil. The mixed charcoal/sediment material extracted from this fossil soil dates to 3960–3699 cal yr BP (230 cm b.s.; Table 6.3). However, a radiocarbon age of the charcoal/sediment material from 77 cm b.s. (unit 5) dates to 4290–3699 cal yr BP (Table 6.3), indicating an age inversion.

Sediment profile **Del-6** was extracted from the transitional area of the proximal part of the alluvial fan and the toe of the adjoining hillslope (Figure 6.2). Del-6 has a total thickness of 500 cm and is subdivided into four lithostratigraphic units (Figure 6.4 and Figure S6.6). The basal layers (unit 1, 500–350 cm b.s.) are composed of soft clayey silt to the bottom passing over into weathered bedrock. Along the sediment profile of Del-6 (pH: 8.06 (0.3); EC: 137 (56)  $\mu\text{S cm}^{-1}$ ;  $X_{\text{LF}}$ : 35 (11)  $10^{-8} \text{ m}^3 \text{ kg}^{-1}$ ), samples from the in-situ weathered bedrock ( $n = 10$ ) show the highest pH (8.56 (0.1)) and EC values (208 (26)  $\mu\text{S cm}^{-1}$ ) and the lowest  $X_{\text{LF}}$  values (22 (4)  $10^{-8} \text{ m}^3 \text{ kg}^{-1}$ ). This material is overlain by pebbly sand corresponding to coarse-textured alluvial fan deposits (sub-facies Bb, unit 2, 350–170 cm b.s.), which merges into a fossil soil (sub-facies sBa, unit 3, 170–149 cm b.s.). The structure in unit 3 is crumbly and porous;  $X_{\text{LF}}$  (74 (49)  $10^{-8} \text{ m}^3 \text{ kg}^{-1}$ ,  $n = 2$ ) and  $\text{LOI}_{550}$  values (5.42 (0.1) mass%,  $n = 2$ ) show a sharp increase. The light yellowish-brown color at the top of unit 3 (160–149 cm b.s.) might indicate burning at the soil surface (cf. Terefe et al., 2008). Unit 4 consists of sandy silt corresponding to fine-textured alluvial fan deposits (sub-facies Ba, 149–0 cm b.s.). Along the sediment profile of Del-6, three charcoal samples date the alluvial fan sediments of Del-6 from 1529–1411 cal yr BP (333 cm b.s.) to 515–343 cal yr BP (77 cm b.s.; Table 6.3).

---

**Figure 6.4** (A) The sediment profiles at a longitudinal transect on the Deliktaş alluvial fan (140 × vertical exaggerations). Note the background colors of brown and gray show the correlations of sediment facies among different profiles. (B) The location of the profiles Del-5 and Del-6 at a cross section on the Deliktaş alluvial fan (10 × vertical exaggerations).



## 6.6 Holocene geomorphodynamics

The analyses of sediment profiles from the area of the Deliktaş alluvial fan indicate rapidly changing depositional processes during the Holocene (Table 6.4). Based on the facies classification, seven major geomorphodynamic phases can be deduced (Figure 6.4).

**Table 6.4** Summary of the (pre-)Holocene sediment characteristics (a), depositional processes (b), and landscape and settlement dynamics (c) in the Deliktaş area.

Phase	Sediment characteristics (a)	Depositional process (b)	Landscape and settlement dynamics (c)
(1) Pre-Holocene	<ul style="list-style-type: none"> <li>• high percentage of gravels (<math>\varnothing \geq 2</math> mm) with clast-supported fabric: base of Del-3, 4, 5 (unit 1)</li> </ul>		
(2) Early Holocene	<ul style="list-style-type: none"> <li>• 1<sup>st</sup> cycle of fan sediments: Del-3 (units 2, 3)</li> </ul>		
(3) Middle Holocene	<ul style="list-style-type: none"> <li>• 2<sup>nd</sup> cycle of fan sediments: Del-3 (units 4, 5), Del-4 (unit 2)</li> <li>• 3<sup>rd</sup> cycle of fan sediments: Del-3 (units 6, 7), Del-4 (units 3, 4), Del-5 (units 2, 3)</li> <li>• Geyikli floodplain + extreme flood events + post-depositional process: Del-2 (units 1, 2, 3, 4, 5)</li> </ul>		

Phase	Sediment characteristics (a)	Depositional process (b)	Landscape and settlement dynamics (c)
(4) Mid- to Late Holocene transition	<ul style="list-style-type: none"> <li>soil formation on the Deliktaş alluvial fan and Geyikli floodplain: Del-2 (unit 5), Del-3 (unit 7?), Del-4 (unit 4), Del-5 (unit 3)</li> </ul>		
(5) Beginning of the Late Holocene	<ul style="list-style-type: none"> <li>4th cycle of fan sediments: Del-2 (units 6, 7), Del-3 (units 8, 9), Del-4 (unit 5), Del-5 (units 4, 5)</li> <li>age inversion</li> <li>sediment extension downwards the distal fan</li> <li>soils were buried by alluvial fan progradation</li> </ul>		
(6) Late Holocene (after 1.5 ka BP)	<ul style="list-style-type: none"> <li>5th cycle of fan sediments: Del-6 (units 2, 3, 4)</li> <li>sediments younger than 1.5 ka BP rest directly on weathered bedrock (unit 1, Del-6)</li> <li>sediment hiatus</li> <li>lateral extension towards the southern hillslope</li> </ul>		
(7) Recent 100 years	---		

### **6.6.1 Pre- to Early Holocene (phases 1–2)**

The gravel deposits (sub-facies Bc) form the base of profiles Del-3, Del-4, and Del-5 corresponding to channel sediments accumulated by the Çaylak creek (phase 1; Table 6.4) (cf. Brown, 1997). Locally, channel infills reach up to 3 m thickness (Del-4). The alluvial fan was dominated by channelized flows during this phase (cf. Parker, 1999). At key-profile Del-3, sediments overlying the channel infills date into the Early Holocene (9.0–8.4 cal ka BP, unit 2, 569 cm b.s.; Figure 6.4; Table 6.3), indicating that the channel infills were possibly deposited in the Late Pleistocene. This observation is in line with various reports across the Mediterranean region describing such active channel erosion and subsequent channel infills for the Late Pleistocene (Vita-Finzi, 1969b; Bintliff, 2002).

Alluvial fan deposits with changing textures covered these pre-Holocene channel infills (Figure 6.4). The first cycle of coarse-textured alluvial fan sediments (sub-facies Bb) and fine-textured alluvial fan sediments (sub-facies Ba) occurs at the middle–distal part of the alluvial fan (Del-3, units 2–3) with a radiocarbon age dating to the Early Holocene (phase 2; Table 6.4). The change from sediment sub-facies Bb (coarse texture) to sub-facies Ba (fine texture) represents the conditions of surface runoff changing from high energy to low energy (Blair and McPherson, 2009). This might indicate (a) the shifting location of the Çaylak creek channel on the fan causing alternating depositional environments (cf. Blair and McPherson, 1994, 2009) or (b) alternating intensity of flood events (predominantly triggered by varying climate) (Bull, 1991; Dorn, 1994). The hydro-climatic conditions in the eastern Mediterranean region during the Holocene suggest temporal oscillations between wet and dry periods (Eastwood et al., 2007; Finné et al., 2019; Ocakoğlu et al., 2022), directly affecting run-off dynamics (Dorn, 1994) and hereby processes of erosion and deposition (Dusar et al., 2011). The influence of tectonic activity cannot be proven for the Deliktaş catchment where no major Pleistocene faults are known; however, the catchment is located at a horst structure in a tectonically active area, thus surrounded by fault lines (Karacik et al., 2007).

### **6.6.2 Middle Holocene (phase 3)**

Another cycle of coarse- and fine-textured alluvial fan deposits is observed at the key profile Del-3 (units 4–5) and Del-4 (unit 2), both located at the middle fan (Figure 6.4). The radiocarbon datings from the upper part of the cycle (Del-3, unit 5, 285 cm b.s.) indicate that the sediments were deposited at least until 5.3 cal ka BP, thus during the Middle Holocene. Later, also during the Middle Holocene, the fine-textured fan deposits at the

top of this cycle were covered by an analogous cycle of fan sediments, which extends from the proximal fan (Del-5, units 2–3) to the middle fan (Del-3, units 6–7; Del-4, units 3–4) (Figure 6.4). The two cycles together form the third phase (Table 6.4). These findings indicate (a) a continuous growth of the spatial extent of the Deliktaş alluvial fan since the Early Holocene due to the topography of the channel base, allowing the space for fan growth (Figure 6.4) or (b) re-mobilization processes from the proximal toward the distal area of the fan (cf. Van Dijk et al., 2012). Fan growth remained consistent until the beginning of the Late Holocene in the first assumption as indicated by the constant aggradation rate at Del-3 between ca. 9 to 3.5 cal ka BP ( $89 \text{ cm ka}^{-1}$ ; Figure 6.5). Alternatively, repeated re-deposition processes in a fan environment with shifting channels under a climate characterized by strong seasonality with torrential run-off have to be considered, particularly in its proximal area where the incision and backfilling processes are the most prominent during the experiments by Van Dijk et al. (2012).

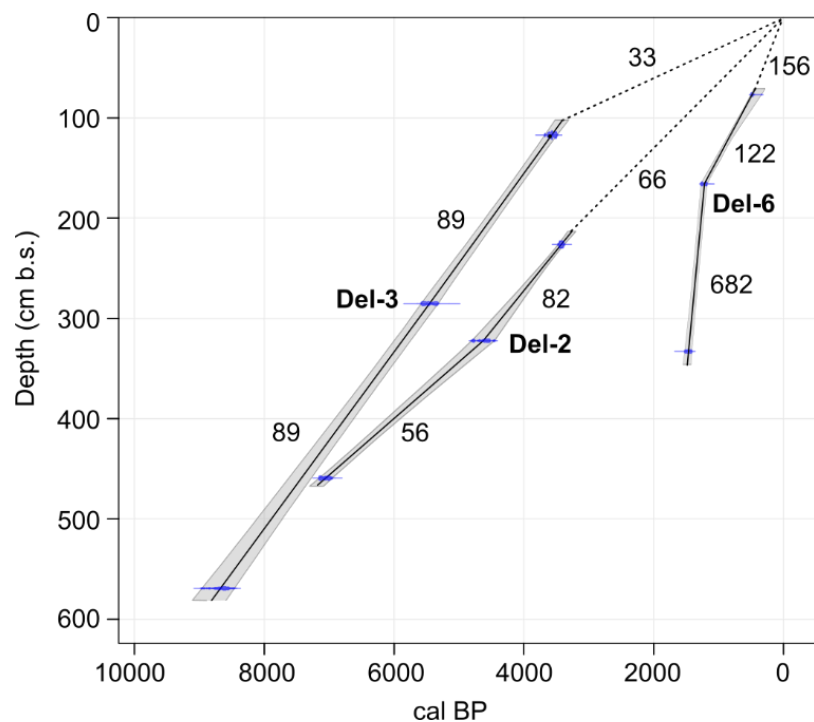


**Figure 6.5** The simplified age-depth modeling of profiles Del-2, Del-3, and Del-6, with the values showing the aggradation rate in  $\text{cm ka}^{-1}$  of each section.

Contemporarily (phase 3), the floodplain of the Geyikli river aggraded and prograded to the foreland of the Deliktaş fan, i.e., the footslopes of the Karadağ mountain (Del-2; Table 6.4). This floodplain accumulation (sub-facies Cf) lasted from ca. 7 to 3.4 cal ka BP (ages from Del-2, unit 1, 459 cm b.s., and unit 5, 226 cm b.s.; Table 6.3), which was occasionally interrupted by stronger Geyikli flood events (sub-facies Csh; Figure 6.4) and post-

sedimentary influenced by carbonate-rich groundwater tables indicated by Fe-Mn mottles and increased Ca/Ti values in units 3 and 4 (Figure 6.4 and Figure S6.3) (cf. Goldberg and Macphail, 2006). The interfingering of Deliktaş fan and Geyikli floodplain deposits cannot be proven for this period.

### **6.6.3 Mid- to Late Holocene transition (phase 4)**

At the top of the second cycle during the third phase, the fine-textured alluvial fan deposits are influenced by pedogenic processes (sub-facies sBa; Del-4, unit 4; Del-5, unit 3) indicating stable geomorphodynamic conditions without striking erosion and deposition processes (phase 4; Table 6.4). Pedofacies sBa in Del-5 dates to 3960–3699 cal yr BP (unit 3, 230 cm b.s.), whereas in Del-3 it was slightly younger with an age of 3683–3486 cal yr BP (unit 7, 117 cm b.s.; Table 6.3). On the Geyikli floodplain, a layer of paleosol (sub-facies sCf) at Del-2 dates again to a slightly younger age of 3478–3378 cal yr BP (unit 5, 226 cm b.s.; Table 6.3). These fan–floodplain soil processes indicate locally (at least at the coring locations) reduced landscape dynamics at the transition from the Middle to Late Holocene (at least during ca. 4–3.4 cal ka BP), a long-lasting period that allowed the development of 30–40 cm thick solum (Figure 6.4).

Mid-Holocene low geomorphodynamics were also observed on a regional scale, e.g., in the nearby Tekkedere catchment around 5–4 cal ka BP (Yang et al., 2023a) and the western lower Bakırçay plain (Pergamon micro-region) around 4.3–4 ka BP (Becker et al., 2020a). Simultaneously, low accumulation rates are reported during ca. 5.8–3.7 ka BP at Lake Gölhisar, SW Türkiye (Eastwood et al., 2007) and during ca. 4.3–4 ka BP in Pasinler Basin, eastern Türkiye (Collins et al., 2005). Although the phases of low erosion/deposition rate in these studies occurred earlier than that in the Deliktaş catchment, they all potentially correspond to the periods of supra-regionally (eastern Mediterranean) low climatic erosion sensitivity with a reduction in Mid-Holocene precipitation (Finné et al., 2011; Roberts et al., 2011a). The contemporary limited human activities might also have facilitated lower geomorphodynamics (Dusar et al., 2011), as it is also the case in the Deliktaş catchment (Table 6.4).

### **6.6.4 Beginning of Late Holocene (phase 5)**

The Mid-Holocene pedofacies on the Deliktaş alluvial fan and Geyikli floodplain were covered—and by this fossilized—by a Late Holocene cycle of coarse- and fine-textured alluvial fan deposits (Del-2, units 6–7; Del-3, units 8–9; Del-5, units 4–5; Figure 6.4). Thus, the fan experienced pronounced progradation, growing downslope faster than upslope

(phase 5; Table 6.4). Old sediments stored along the transportation pathways were reworked as evidenced by the age inversion in Del-5, unit 5 (4290–3699 cal yr BP, 77 cm b.s.), a phenomenon widely discussed for the sediment cascade model in alluvial–colluvial archives (Lang and Hönscheidt, 1999; Fryirs et al., 2007; Fryirs, 2013). Subsuming, for the Deliktaş area, the fifth phase is interpreted as a phase of increased geomorphodynamics coming along with increased erosion and deposition processes (Table 6.4). Radiocarbon age of 2336–2148 cal yr BP in the middle of this phase (Del-4, unit 5, 85 cm b.s.; Table 6.3) points to the increase of geomorphodynamics prior to 2.3 cal ka BP. Considering that radiocarbon ages from buried topsoils could represent the maximum age of burial time (Scharpenseel and Schiffmann, 1977; Nykamp et al., 2020), the fifth phase might have predominately continued between ca. 4–3.4 and 2.3 cal ka BP (Table 6.3) during the beginning of the Late Holocene.

Since this initial Late Holocene phase, the Geyikli floodplain sediments cannot be detected anymore at the sampling locations, prevented by the accumulation of Deliktaş fan and its coinciding spatial growth (Figure 6.4; Table 6.4). The autogenic adjustment of the river channel and floodplain (Croudace and Rothwell, 2015), being reported in the micro-region (Schneider et al., 2015) and western Türkiye (Özpolat et al., 2020), however, cannot be proven in this area.

The intensification of geomorphodynamics, thus, the augmentation of erosion processes in the Deliktaş catchment might be triggered by both human interference and climate change (phase 5; Table 6.4), as frequently observed in wide areas of the eastern Mediterranean during ca. 5–3 ka BP (Dusar et al., 2011; Kuzucuoğlu et al., 2011; Roberts et al., 2019a; 2019b).

Evidence for settlement activities in the Deliktaş catchment is given by the archaeological sites of Zindan Tepe and Hatipler Kalesi (Zimmermann et al., 2015) (Figure 6.2), which have been used latest since the Bronze to the Iron ages (Table S6.1) (Ludwig et al., 2022). This, together with the ceramic remain found in Del-4, unit 5 (Figure S6.4), suggests human activities that likely affected the soil erosion. This is analogous to multiple studies in the Pergamon micro-region where the Middle to Late Holocene landscape shifted from natural to cultural, including processes of woodland clearing, pasture, and agriculture (Shumilovskikh et al., 2016; Schneider et al., 2017; Yang et al., 2023a). Many findings all over the Mediterranean region also emphasize the interrelation between settlement activities and land degradation during the Bronze Age (e.g., Vita-Finzi, 1969b; Dusar et al., 2011; Jouffroy-Bapicot et al., 2021, and references therein).

Beyond, rapid climate changes, including the 4.2 and 3.2 ka BP events (Roberts et al., 2011a; Bini et al., 2019; Manning et al., 2020; Hazell et al., 2022), under altogether semi-arid conditions (Wanner et al., 2008; Finné et al., 2019) might have amplified torrential run-off (Bintliff, 2002; Anderson et al., 2007) and landscape degradation in the eastern Mediterranean (Dusar et al., 2011). This could have intensified the catchment erosive potential and consequently increased alluvial fan deposition (Butzer, 2005). Such a scarce vegetation cover is documented for the areas around the Deliktaş catchment since ca. 3.5 ka BP (Shumilovskikh et al., 2016; 2022).

In the Mediterranean area, accelerated slope erosion is described at several locations, e.g., Arslantepe (eastern Türkiye) (Dreibrodt et al., 2014), albeit few were observed during the time of increased geomorphodynamics in the Deliktaş area (Dusar et al., 2011). This may result from research material bias (Verstraeten et al., 2017; Ocakoğlu et al., 2022) and response time variations among alluvial, fluvial, and lacustrine sediments (Wanner et al., 2008; Becker et al., 2020a; Nykamp et al., 2021). Beside the contribution of climate change and human interference, various features in alluvial development and the increase in geomorphodynamics could also be associated with complex natural characteristics (Butzer, 1980; Szabó et al., 2010), e.g., initial landform and bedrock/soil type (Butzer, 2005; Szabó et al., 2010; Fediuk et al., 2019), threshold difference in geomorphological locations (or the sediment sources and sinks) (Nemec and Kazancı, 1999; Bakker et al., 2013), and variation in landscape sensitivity to accumulation and erosion (Becker et al., 2020a).

### **6.6.5 Late Holocene (phases 6–7)**

Since ca. 1.5 ka BP, sediments were deposited directly on the weathered bedrock at the fan's proximal zone (Del-6, units 2–4; Figure 6.4). This sediment hiatus corresponds to a concomitant higher-energetic process evidenced by the highest aggradation rate among the phases (Figure 6.5), suggesting a new phase of increased geomorphodynamics (phase 6; Table 6.4). The (sub)rounded shape of pebbles in Del-6, unit 2 (Figure 6.4) confirms transport processes by running water and excludes its origin as debris from mass movements at the slopes (cf. Miall, 2006). This further denotes the lateral upslope extension of the alluvial fan (Table 6.4). These young sediments exposed in Del-6 were roughly deposited contemporaneously to the valley bottom sediments in the nearby Tekkedere catchment (Yang et al., 2023a), probably corresponding to the “Younger Fill” (Vita-Finzi, 1969b) in the Mediterranean valleys (Roberts, 2014; Roberts et al., 2019b). The time of erosion should take place after the beginning of the Late Holocene (phase 5:

ca. 4/3.4–2.3 ka BP; Table 6.4) and before the onset of deposition at Del-6 (ca. 1.5 ka BP; Table 6.3), thus, during the profound transformation from the Hellenistic to Roman Imperial period (300 BCE to 300 CE) in the Pergamon micro-region.

In the rural catchment of Deliktaş and its surroundings, the increased number of archaeological sites (Table S6.1; (Ludwig et al., 2022)) corresponds to this micro-regional development. This increased spatial distribution of human settlements indicates the exploitation of formerly untouched lands (Figure 6.2), likely for arboricultural, pastoral, and agricultural practices (Shumilovskikh et al., 2016; 2022). This presumably caused fundamental changes in the ecosystem and thereby increased the erosive susceptibility of the landscape, leading to intensified gullying in the Deliktaş catchment. During this period, intensified geomorphodynamics are also observed at various locations in the micro-region (Becker et al., 2020a), e.g., in the rural catchments of the Geyikli river (Schneider et al., 2013; 2014), the Tekkedere creek (Yang et al., 2023a), and in ancient harbor cities and their immediate surroundings (Seeliger et al., 2013; Shumilovskikh et al., 2016; Fediuk et al., 2019; Seeliger et al., 2019).

In the Deliktaş area, only one cycle of alluvial sediments was observed during the Late Holocene (Figure 6.4) and is in chronological order with the boost of archaeological sites (Ludwig et al., 2022) (phase 6; Table 6.4). In contrast, in the nearby Tekkedere catchment, several alluvial cycles were observed for the same period (Yang et al., 2023a); the difference may be related to a more continuous settlement of the Tekkedere catchment at multiple locations since the Bronze Age (Ludwig, 2020a; Michalski, 2021), beyond the diversity in land use or landform.

Since the 20th century, the construction of the irrigation system and reservoir remarkably changed the hydrological and geomorphological conditions in the Deliktaş area (phase 7; Table 6.4). The Geyikli river was straightened to a canal (Doğramacı canal) with embankments (Schneider, 2014). Both the Deliktaş fan and the adjoining Bakırçay plain owe well-developed irrigation systems and abandoned (distributary) channels (Figure 6.2).

## 6.7 Conclusions

To improve the understanding of the geomorphological history of alluviation, pedogenesis, and erosion, and their driving factors in rural areas of the ancient city of Pergamon, we integrate geomorphological observation in the Deliktaş catchment and the receiving Geyikli river, analyses of alluvial fan and floodplain sediments, and radiocarbon datings. The highly changing sediment texture in the five profiles depicts that the landscape

experienced at least seven phases of profoundly different geomorphodynamics. Deliktaş channel sediments deposited in the Late Pleistocene were covered by sediments of an aggrading alluvial fan during the Early–Middle Holocene. Middle Holocene fossil soils on the Deliktaş fan and Geyikli floodplain indicate landscape stability. An accelerated fan growth and hereby a major increase in geomorphodynamics (phase 5) during ca. 4–2 ka BP coincides with the onset of local settlement activities on hitherto untouched lands under the supra-regional aridization with rapid climate changes, possibly including the 4.2 and 3.2 ka BP drought events. Consequences of soil erosion processes on a local scale, i.e., first/second-order catchments, are soil degradation and accelerated growth of fan deposits at their confluence to the foreland, and—on a regional scale—floodplain aggradation such as that of Geyikli and Bakırçay rivers (Schneider et al., 2015; Becker et al., 2020a; 2022b).

Pronounced sediment hiatus and lateral extension of fan sediments might indicate increased geomorphodynamics before 1.5 ka. The contemporarily increased number of archaeological sites in the Deliktaş area suggests that land use expanded largely to more untouched hillslopes to meet the demand of a growing population in the city of Pergamon and its micro-region, especially during the Roman Imperial period (Laabs and Knitter, 2021). However, uncertain sedimentological and especially chronological results hinder a clear relation between the phases of increased geomorphodynamics in the last 2.5 ka and the major phase of human activities, i.e., the transformation of the Pergamon micro-region between the Hellenism and the Roman Imperial Period. On the contrary, our results indicate a more pronounced increase in geomorphodynamic activity since the beginning of the Late Holocene. This phenomenon is also observed in the Tekkedere catchment (Yang et al., 2023a) in the vicinity of the Deliktaş catchment, but not generally in all parts of the micro-region (Becker et al., 2020a), such as the harbor of Elaia which silted up in the first millennium CE (Seeliger et al., 2013; 2019). Thus, intra-micro-regional variabilities, such as relief, bedrock, and human activities (Yang et al., 2021), are important aspects to understand the geomorphodynamic pattern in a micro-region and wider regions such as the eastern Mediterranean.

## **7. Linking processes with records: modeling the Mid- to Late Holocene soil erosion and deposition risk**

Working package 4

**Climate vs. human impacts on Mid- to Late Holocene geomorphodynamics on the western lower Bakırçay catchment (western Türkiye): an evaluation based on USPED modeling**

**Unpublished report**

**Keywords:** soil erosion and deposition risk; geomorphic modeling; site-based land cover change; AWI-ESM-based monthly rainfall; last 6 millennia; Pergamon micro-region

**Abstract:** The Mediterranean region has been subjected to long-term and severe land degradation, but a comprehensive understanding of its environmental history remains elusive. This study explores the long-term influence of climate regimes and human population on geomorphodynamics in the Pergamon micro-region from the Middle to Late Holocene. To understand the dynamics of soil erosion and deposition risk in recent times and over the last six thousand years, this study employed the Unit Stream Power Erosion Deposition (USPED) model. Particularly, the latest AWI-ESM simulated monthly rainfall data which covers the study period, and the raw count and location pattern of archaeological sites were taken as input to receive the rainfall–runoff erosivity and the land cover–management factors. The modeling results and contributing factors in the Pergamon micro-region display a spatially highly heterogeneous character and vary throughout time. During the Mid- to Late Holocene, the geomorphodynamics most likely experienced five main phases with accelerated processes at ca. 5–3.7 ka BP and 2.5–1.5 ka BP. Among the driving factors, hydro-climatic changes and human activities exhibit contrasting as well as amplifying effects on landscape development over time. Although the results suggest that rainfall factor weakly correlates with soil erosion risk and the importance of rapid climate change events (e.g., 4.2 ka drought event) is not evident in the modeled geomorphodynamics, the Mid- to Late Holocene aridization and climatic fluctuations in the eastern Mediterranean played a role. In contrast, land use intensity highly affected soil erosion processes. Particularly, the evident human-shaped landscape during the Hellenistic–Roman transformation on various spatial scales reveals that the soil erosion risk during this phase was highly likely controlled by human impacts. The soil erosion and deposition modeling and its comparisons to local, micro-regional, and supra-regional studies allow us to access the interfingering and mutually reinforcing effects of climate and settlement activities during the Holocene. This approach, along with future improvements, will contribute to a better understanding of ancient human-environment interactions.

## 7.1 Introduction

The Pergamon micro-region (Figure 7.1) is located in the eastern Mediterranean. The former case studies analyzing alluvial sediments of the Tekkedere and Deliktaş catchments in the western part of the micro-region indicate two major Holocene phases of increased sediment fluxes (Yang et al., 2023a; 2023b) (chapters 5 and 6). The first acceleration is indicated by the burial of a previously stable landscape around 4 ka BP, broadly at least ca. 5–3.4 cal ka BP. These intensified sediment dynamics are primarily

associated with the regional aridization during the Mid- to Late Holocene. This period experienced rapid climate change events, including the 4.2 and even 3.2 ka events, characterized by high intensity and variability of annual precipitation (Fletcher and Zielhofer, 2013; Clarke et al., 2016; Hazell et al., 2022). However, the influence of local human activities during this time cannot be discounted. This geomorphic transition typically occurred during the 3<sup>rd</sup> millennium BP in the Mediterranean region (Walsh et al., 2019).

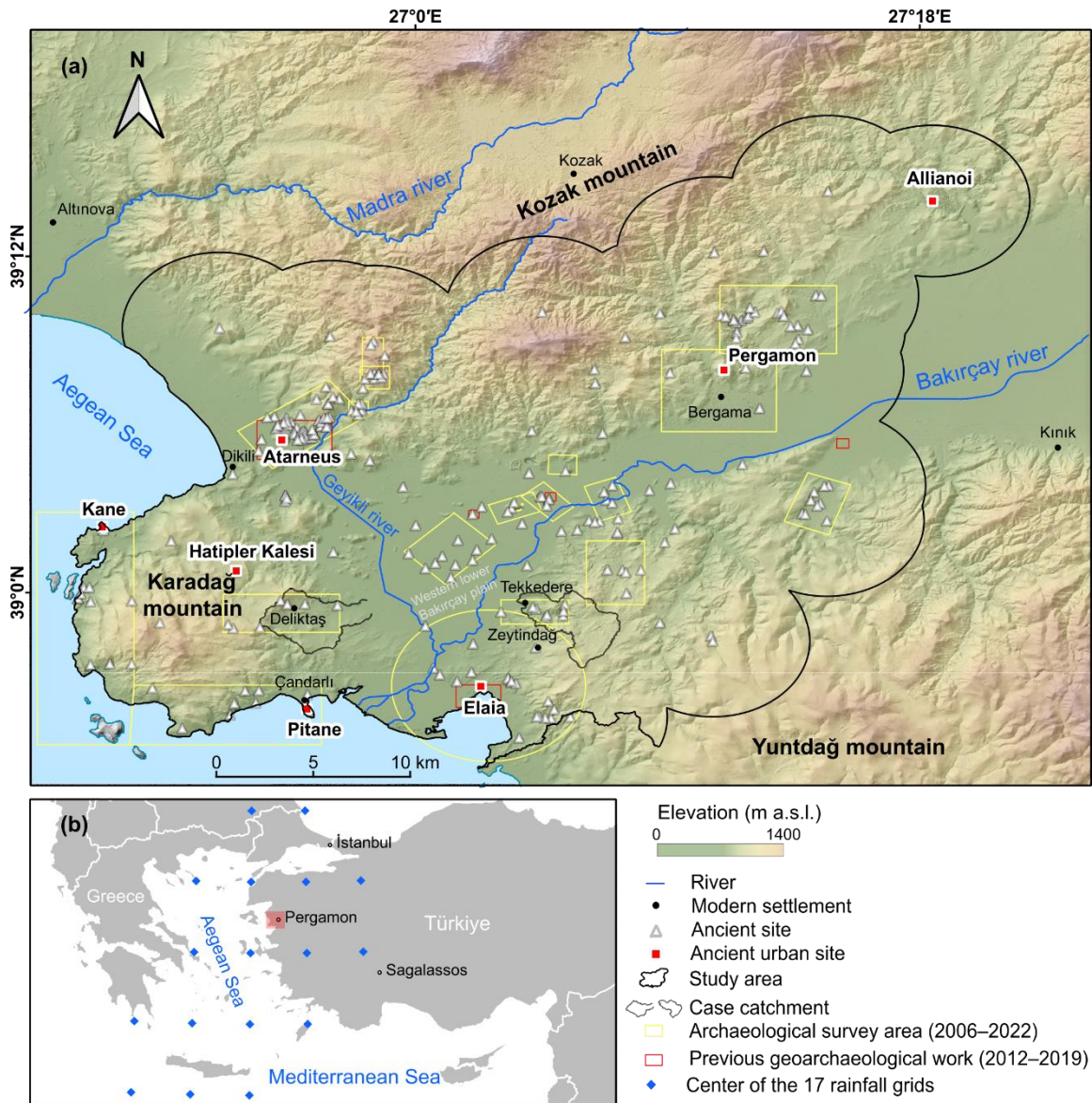


**Figure 7.1** (a) Topographical map (Data source: TanDEM-X, spatial resolution 12.5 m (Rizzoli et al., 2017; Wessel et al., 2018)) with the location of the intensive archaeological survey areas and sites, and geoarchaeological work in the Pergamon micro-region (updated to 2022, the data were provided by Bernhard Ludwig). Note: the circle around the ancient harbor city of Elaiia is the boundary of its archaeological survey area. (b) The location of this study is in the eastern Mediterranean region with the coverage of the 17 rainfall grids (Shi et al., 2022a; 2022b).

The Hellenistic–Roman transformation, spanning from approximately 300 BC to 300 AD, witnessed population growth throughout the Pergamon micro-region (Pirson, 2020), potentially exerting significant human pressure on the environment (cf. Walsh et al., 2019). However, the reconstructed sediment dynamics indicate less distinct geomorphodynamic activities over the last 2500 years compared to the earlier phase around 4 ka BP (Yang et al., 2023a; 2023b) (chapters 5 and 6). Conversely, a meta-data analysis of <sup>14</sup>C radiocarbon datings suggests a remarkable increase in sedimentation rate from the Hellenistic to Roman Imperial periods (Becker et al., 2020a). While this meta-data analysis identifies phases of increased geomorphological activities that were not apparent in the analysis of single sediment sequences (Becker et al., 2020a), limitations arise from the consideration of various temporal scales and wide ranges of geomorphological processes across different locations (Faust and Wolf, 2017; Walsh et al., 2019).

Modeling past soil erosion and deposition risk is a frequently applied method for paleoenvironmental reconstructions in the Mediterranean region (García-Ruiz et al., 2013). The hindcast soil erosion modeling conducted for the vicinity of the ancient city of Sagalassos (Figure 7.1b) has demonstrated a linear relationship between soil erosion and the land cover and land management factor, with only a weak correlation observed for the rainfall factor (Van Loo et al., 2016). However, this study exclusively focused on the last four millennia, leaving the importance of the Mid- to Late Holocene transition unknown. Rather, Van Loo et al. (2016) assume that hillslope erosion prior to the Late Holocene in the enviroing of the ancient Sagalassos was very limited because of the dense forest cover.

Modeling the Mid- to Late Holocene soil erosion risk and deposition risk scenarios in the Pergamon micro-region by simulating the main periods of the dominating impacts by humans or climate on past landscape dynamics will provide a better understanding of spatially and temporally varying landscape sensitivity in terms of the major controlling factors. Specifically, the objectives are to:

- 1) identify the trends of soil erosion risk and deposition risk history during the last 6000 years;
- 2) determine the periods of major increased geomorphodynamic activities, characterized by accelerated sedimentation rates;
- 3) investigate the spatiotemporally varying relationship of soil erosion and deposition risk;
- 4) determine the approximation of the time when human invention surpasses climatic influence on triggering soil erosion.

Various modeling approaches have been employed to predict the spatial patterns of soil erosion (e.g., sheet, rill, and gully erosion) (García-Ruiz et al., 2013), including empirical or statistical models, rule-based approaches, as well as physical models (Mitasova et al., 2013). These models have primarily focused on applications, such as agriculture, soil conservation, sediment pollution control, sustainable military land management, and forestry, particularly in the context of the post-wildfire impacts on various temporal and spatial scales (Mitasova et al., 2013; Benavidez et al., 2018). Among these models, the empirical models require fewer input data and are straightforward to apply, making them the most commonly used models (Alewell et al., 2019). They are frequently based on the Universal Soil Loss Equation (USLE) (Wischmeier and Smith, 1978), such as the Modified Universal Soil Loss Equation (MUSLE) (Williams, 1975), Revised Universal Soil Loss Equation (RUSLE) (Renard et al., 1997), Revised Universal Soil Loss Equation-3D (RUSLE-3D) (Mitasova and Mitas, 1999b), and Unit Stream Power Erosion Deposition (USPED) models (Moore and Burch, 1986). While USLE, MUSLE, RUSLE, and RUSLE-3D focus on the assessment of the soil erosion risk, the USPED model enables the visualization of both soil erosion and deposition risk. Annual rates of soil erosion and deposition are assessed by employing five major factors - topographic condition (DEM), rainfall fluctuation, land cover change, soil texture, and management practices (Aiello et al., 2015).

Our primary objective is less to quantitatively predict the values of soil erosion and deposition rates for the Pergamon micro-region, rather than to assess the long-term trends of the geomorphodynamics as far as triggered by climatic or anthropogenic factors.

## **7.2 Study area**

The study area focuses on the western part of the Pergamon micro-region as for this area intensive archaeological surveys were conducted (Figure 7.1a), including the western lower Bakırçay plain, the southern part of the Kozak mountain, the northern part of the Yuntdağ mountain, and the Karadağ mountain, covering a total approximate area of 1318 km<sup>2</sup> (Figure 7.1a). The natural background of this specific area has been broadly introduced by Yang et al. (2021) (chapter 4).

## **7.3 Methods and materials**

The Unit Stream Power Erosion Deposition (USPED) model was applied to the study area, both for the recent times and conducting hind-cast modeling for selected Mid- to Late

Holocene time slices. The ancient human settlement pattern, i.e., the raw count and spatial distribution of archaeological sites, provide insights into land use sensitivity, considering the duration of the human occupation (cf. Yu et al., 2016) and served as input data to estimate settlement activities. Simulated monthly precipitation data from the AWI-ESM model are available, spanning the last 6000 years (Shi et al., 2022a; 2022b). Due to data limitations, changes in elevation, soil texture, and support practices during the Mid-to Late Holocene are assumed to remain constant. The results of the USPED model are validated using an updated meta-data analysis that includes all sediment and radiocarbon dating archives in the western lower Bakırçay plain. The detailed methods and materials used for the soil erosion and deposition modeling can be found in chapter 3.6.

## **7.4 Results**

### **7.4.1 Present-day situation of soil erosion and deposition**

The USPED modeling for present-day soil erosion and deposition risk incorporates five major contributing input factors. The R factor, reflecting the influence of precipitation on soil erosion and deposition risk, exhibits the highest value of approximately  $190 \text{ MJ mm ha}^{-1} \text{ h}^{-1} \text{ year}^{-1}$  at the Bergama rain gauge station. It gradually decreases to the west to around  $175 \text{ MJ mm ha}^{-1} \text{ h}^{-1} \text{ year}^{-1}$  in Dikili (Figure 7.2a). Overall, the R factor in the western lower Bakırçay area shows minor differences.

The C factor reflects the influence of land use and land coverage on soil erosion and deposition risk. Regionally, the Bakırçay plain area displays the lowest C factor values (Figure 7.2b). The remote Kozak mountain, covered by dense forests, also shows low C factor values (ca. 0.1–0.2). Transitional areas from the mountains to the Bakırçay plain, as well as the mining areas and reservoirs, show generally low vegetation cover and exhibit high C factor values (ca. 0.3–0.5). The catchments of Tekkedere and Deliktaş, located in transitional areas, show low to high C factor values with mean values at ca. 0.2, ranging between 0.01 and 0.5.

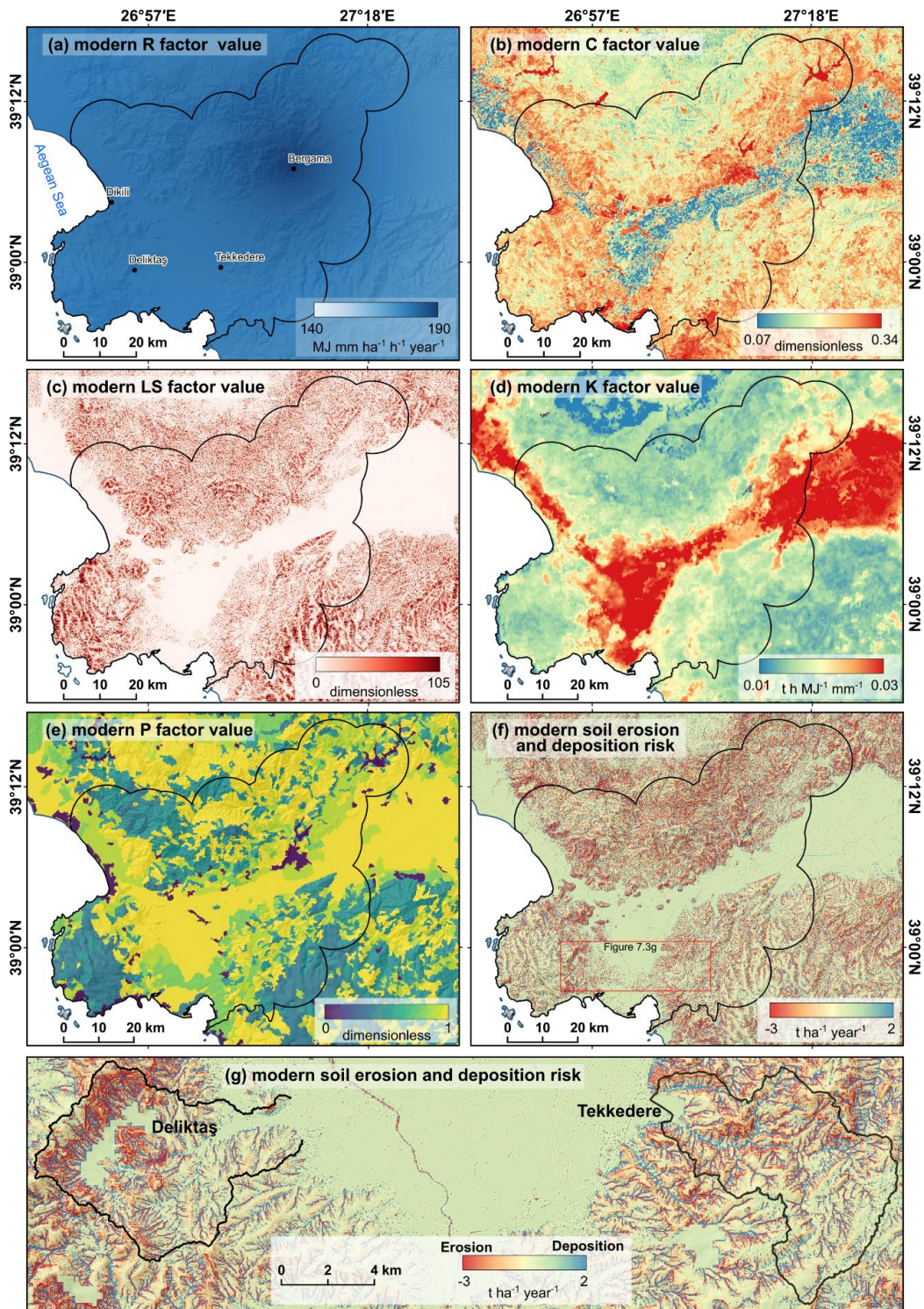


**Figure 7.2** The spatial distribution of the input data and results of the USPED model in the western lower Bakırçay catchment during recent times: (a) rainfall–runoff erosivity factor (R factor) value; (b) soil erodibility factor (K factor) value; (c) cover and management factor (C factor) value; (d) support practice factor (P factor) value; (e) topographic factor (LS factor) value; (f) soil erosion and deposition risk (for prevailing sheet erosion) in the whole area; (g) soil erosion and deposition risk in the Tekkedere and Deliktaş catchments. Note: to clearly show the patterns of the distribution, the max and min values of each factor were not necessarily shown on the map, i.e., C factor value (range: 0 ~ 0.55; map: 2% ~ 98%), LS factor value (range: 0 ~ 63139; map: 5% ~ 95%), K factor value (range: 0.006 ~ 0.038 t h MJ<sup>-1</sup> mm<sup>-1</sup>; map: 2% ~ 98%), and soil erosion and deposition risk (range: -2488 ~ 7891 t ha<sup>-1</sup> year<sup>-1</sup>; map: 10% ~ 90%).

The effect of topography on soil erosion and deposition risk is summarized in the LS factor value. LS factor values in the study area are highest in the Karadağ mountain and generally exceed those of the Kozak and Yuntdağ mountains (Figure 7.2c). Mountainous areas facing the Bakırçay plain show lower LS values compared to those in the inner lands. The Deliktaş catchment, particularly the upper part, demonstrates remarkably higher LS factor values (median:  $23 \pm 341$ ) compared to the Tekkedere catchment (median:  $7 \pm 151$ ).

The K factor values summarize the influence of soil characteristics such as grain size composition, stone coverage, or organic carbon content on soil erodibility and, thus, on soil erosion and deposition risk. Correspondingly, the K factor values in flat plain areas (ca.  $0.3 \text{ t h MJ}^{-1} \text{ mm}^{-1}$ ) due to the high silt fraction (Wischmeier and Smith, 1978; Aiello et al., 2015) are higher than those in the mountainous areas (ca.  $0.01\text{--}0.15 \text{ t h MJ}^{-1} \text{ mm}^{-1}$ ) (Figure 7.2d).

To adapt to soil erosion, nutrient deprivation, seasonal water shortage, and flooding with soil wetness management and melioration measures are implemented; their effects on soil erosion and deposition risk are summarized in the P factor. The Bakırçay plain, widespread under agricultural use, shows the highest P factor value of 1. The value gradually decreases in the transitional areas from the plain to the mountains which are predominantly used for olive groves or specialized crops (Table S7.1). Mountainous areas with forests or woodlands exhibit P factor values around 0.4. Built-up lands and water bodies are considered without support practice (Figure 7.2e).

The USPED modeling results for the soil erosion and deposition risk during recent times in the western lower Bakırçay catchment indicate that most areas remain relatively stable, without apparent soil erosion or deposition risk by water. This stability is particularly evident in the vast Bakırçay plain and the intramountain basins (Figure 7.2f). Soil erosion risk primarily occurs on slopes and reaches the highest values at the transition from the slope to the valley bottom. Areas of high soil erosion risk occur in the southern Kozak and western Karadağ mountains, often accompanied by areas of high soil deposition risk in nearby valley bottoms. The detailed results of the Tekkedere and Deliktaş catchments show distinct different spatial patterns of soil erosion and deposition risk (Figure 7.2g). In the Deliktaş catchment, the western uplands present a high soil erosion risk ( $-5 \sim -10 \text{ t ha}^{-1} \text{ year}^{-1}$ ), which has been validated through field observations (prevailing gullies, bare rocks, and degraded vegetation) (Yang et al., 2023b) (chapter 6, Figure 6.2). Regarding the Tekkedere catchment, the areas with high soil erosion risk have largely decreased and mainly exist on the left side of the valley, which is covered by olive groves. Aided by

support practices, e.g., agricultural terracing, this area with less steep slopes displays reduced soil erosion risk compared to the Deliktaş catchment (Figure 7.2g).

#### **7.4.2 Soil erosion and deposition risk since 6 ka BP**

The USPED modeling results of soil erosion and deposition risk (Figure 7.3a) and the factor values of rainfall–runoff erosivity (Figure 7.3b) and cover–management (Figure 7.3c) during the past 6 millennia show contrasting yet partly comparable distributions of the soil erosion and deposition areas throughout time. The hindcast modeling results indicate a higher percentage of areas trending to be stable with only a small portion at medium soil erosion risk (Figure 7.4), compared to the corresponding modeling for the present-day situation with multiple areas of medium or even high soil erosion risk (Figure 7.2).

The R factor value, calculated from the AWI-ESM rainfall data, varies from around 224 to 265 MJ mm ha<sup>-1</sup> h<sup>-1</sup> yr<sup>-1</sup> during the past six millennia (Figure 7.4a). Spatially, the coastal area displays higher values compared with the hinterland (Figure 7.4b). Temporally, the values slightly decreased from 6000 to 2000 yr BP. Periods with high R factor values (above the third quantile: 250 MJ mm ha<sup>-1</sup> h<sup>-1</sup> yr<sup>-1</sup>) include time intervals of 5800, 5600, 5000–4800, 4500–4300, 4000, 3000, 1100, 400, and 200 yr BP, while periods with low R factor values (below the first quantile: 237 MJ mm ha<sup>-1</sup> h<sup>-1</sup> yr<sup>-1</sup>) encompass time intervals of 4600, 3300, 2800, 2400–2200, 2000, 1500, 900, 600–500, 300, and 100 yr BP.

The temporal and spatial changes of the Holocene C factor values (Figures 7.4c and 7.5b) are estimated from the raw count and spatial distribution of archaeological sites (Figures 1.3 and 1.4). No sites are showing for the Chalcolithic period (Table 2.1). Since the Early Bronze Age, the C factor values have become evident due to continuous occupation in the Pergamon micro-region. The factor values slightly decreased during the Iron Age, primarily because of a decline in the number of rural settlements (Figure 7.3). The C factor value increased again and reached its highest values during the Hellenistic Period. It remained high during the Roman Imperial Period and progressively dropped to the low level observed in periods before the Classical Period. The spatial distribution of the C factor value suggests higher values in the areas adjacent to the Bakırçay plain compared to other areas throughout time (Figure 7.3c). During the Hellenistic and Roman times (ca. 2000 BP), the area from Pergamon to the coast was used with high intensity, higher than the adjoining areas.

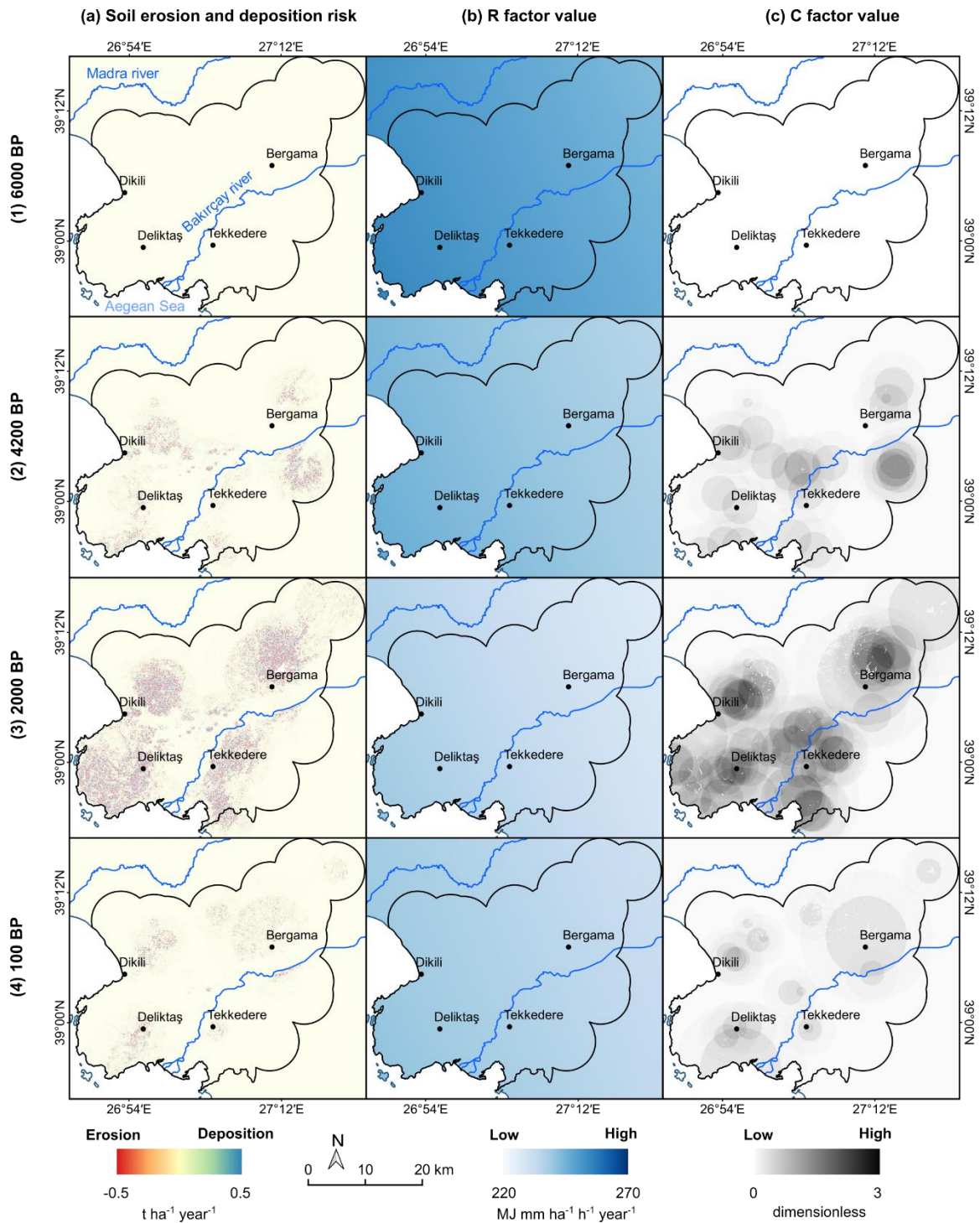


**Figure 7.3** The spatial distribution of soil erosion and deposition risk in the western lower Bakırçay catchment at ca. (1) 6000, (2) 4200, (3) 2000, and (4) 100 yr BP: (a) soil erosion and deposition risk (for prevailing sheet erosion; the actual range at ca. 2000 yr BP is  $-5.5 \sim 5.1 \text{ t ha}^{-1} \text{ year}^{-1}$ ); (b) rainfall–runoff erosivity factor (R factor) value; (c) cover and management factor (C factor) value.

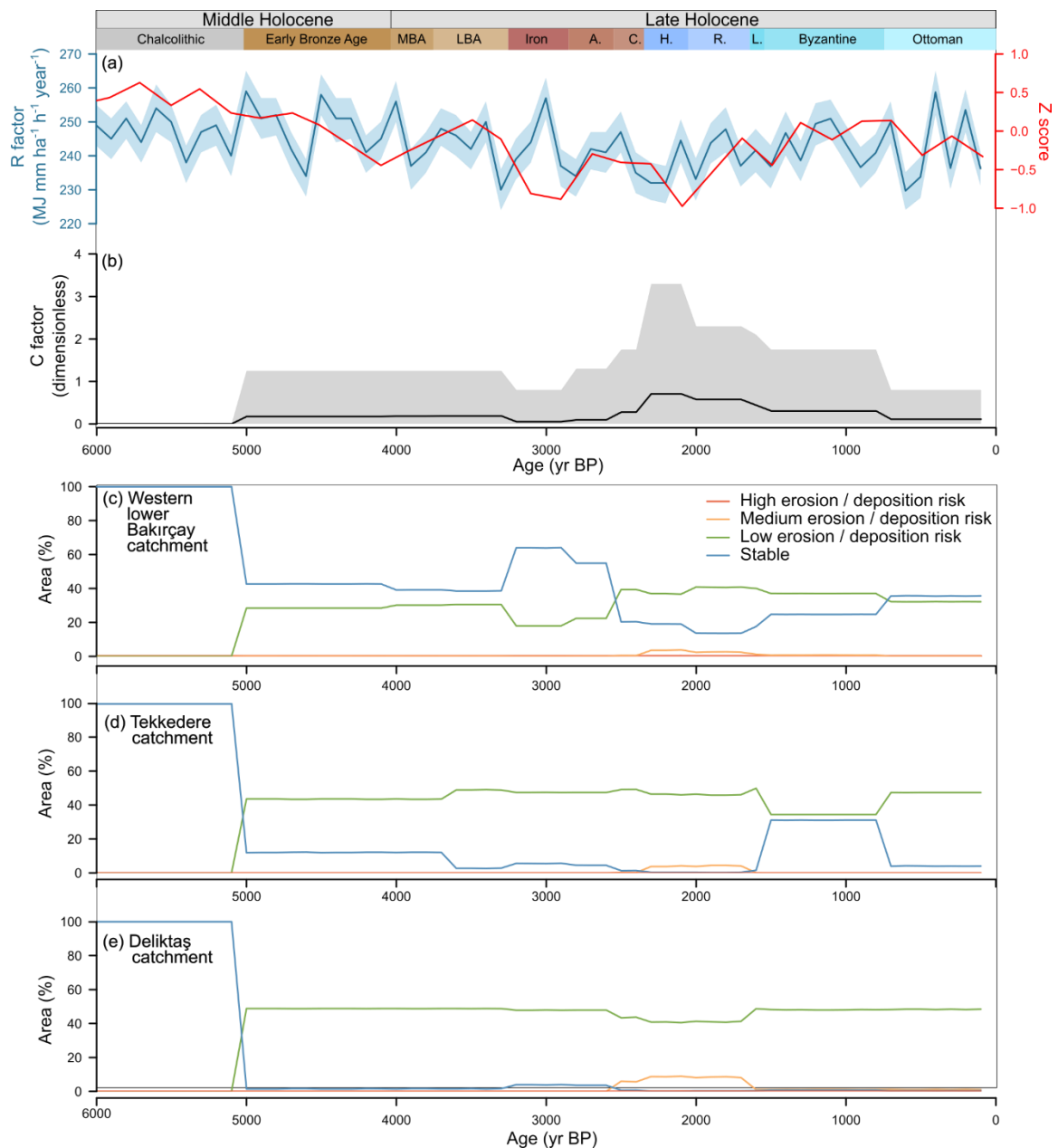


**Figure 7.4** Temporal changes of driving forces of rainfall (figure **a**; R factor: study area average values in the blue line, and max and min values in the light blue shaded band; Z score value of climatic conditions: red line (Finné et al., 2019)) and land cover (figure **b**; C factor: study area average values in black line, and maximum and minimum values in the gray shaded band) for the western lower Bakırçay catchment; the soil erosion and deposition risk in the western lower Bakırçay catchment (figure **c**, the classification of soil erosion and deposition risk see Table 3.4), in the Tekkedere catchment (figure **d**), and the Deliktaş catchment (figure **e**) since the 6000 yr BP.

During the Chalcolithic period, the risk of soil erosion and deposition was very low. The change in soil erosion and deposition risk started at approximately 5.2 ka BP, although the level of soil erosion and deposition risk remained low. Many areas in the western lower Bakırçay catchment stabilized during 3200–2600 yr BP (Iron to Archaic periods). Since then, low soil erosion and deposition rates likely prevailed in the western lower Bakırçay

plain (Figure 7.3a). During the Hellenistic and Roman Imperial periods, medium or even high classes of soil erosion and deposition risk occurred (Figure 7.4c), particularly in the surroundings of Bergama (ancient Pergamon), Dikili (close to the ancient Aterneus), and the vast Yuntdağ and Karadağ mountains (Figure 7.3\_a3). The number of settlement sites ( $n = 79$ ) increased; many sites were situated in erosional landscapes (52% out of 79 sites during the Hellenistic Period) and even in the areas with a high soil erosion risk, compared to the Bronze Age to the Classical Period (Figure 7.5). After 1500 yr BP, soil erosion and deposition risk gradually decreased in the study area (Figure 7.4c).

The soil erosion and deposition risk in the Tekkedere (Figure 7.4d) and Deliktaş (Figure 7.4e) catchments display roughly the same trend as the whole study area (Figure 7.4c). The relatively stable Middle Holocene landscape was likely interrupted during the Early Bronze Age (around 5 ka BP). The relative area of soil stability dropped rapidly to ca. 10% in the Tekkedere catchment and almost 0 in the Deliktaş catchment. In most areas, soil erosional and depositional conditions remained low from the Early Bronze Age. Both catchments might have experienced accelerated soil erosion risk from ca. 2500 to 1600 yr BP (Classical to Roman Imperial periods), based on the increase in areas experiencing medium soil erosion and deposition risk. Between ca. 1600 and 600 yr BP (Late Antiquity to Byzantine periods), the simulated results in the Tekkedere catchment suggest an increase in areas of soil stability, reaching around 40% (Figure 7.4d), indicating a decrease in soil erosion risk.

The rainfall–runoff erosivity factor (R factor) shows a very weak correlation ( $R^2 = 0.05$ ) with the soil erosion risk (Figure 7.6a). In contrast to the R factor, the land cover and management factor (C factor) displays a much higher correlation ( $R^2 = 0.59$ ) with the soil erosion risk in the western lower Bakırçay catchment (Figure 7.6b). Over 75% area of the western lower Bakırçay catchment has experienced soil erosion or deposition during the past 2500 years since the Classical Period.

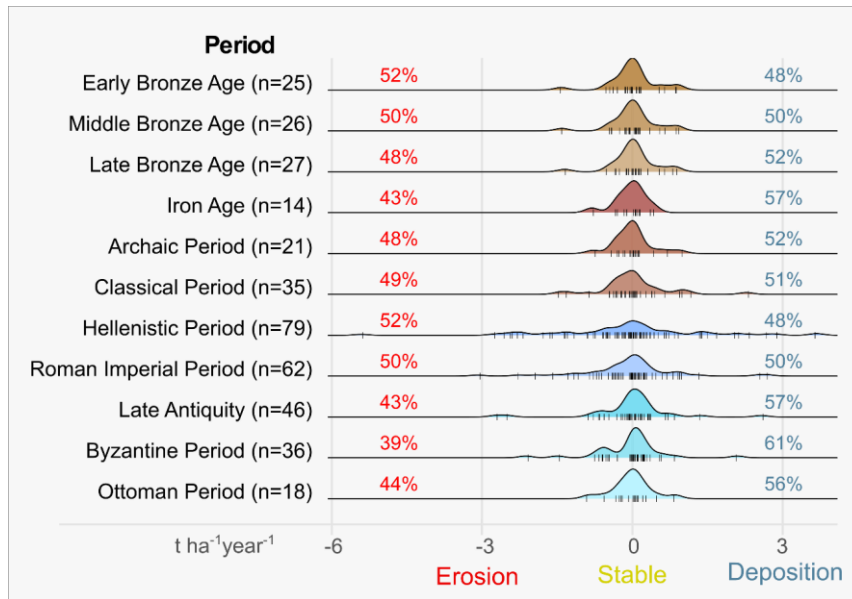


**Figure 7.5** The ridgeline plot of the archaeological sites from the Early Bronze Age to the Ottoman Period on geomorphic locations of soil erosion or deposition risk based on the USPED modeling results in the western lower Bakırçay catchment.

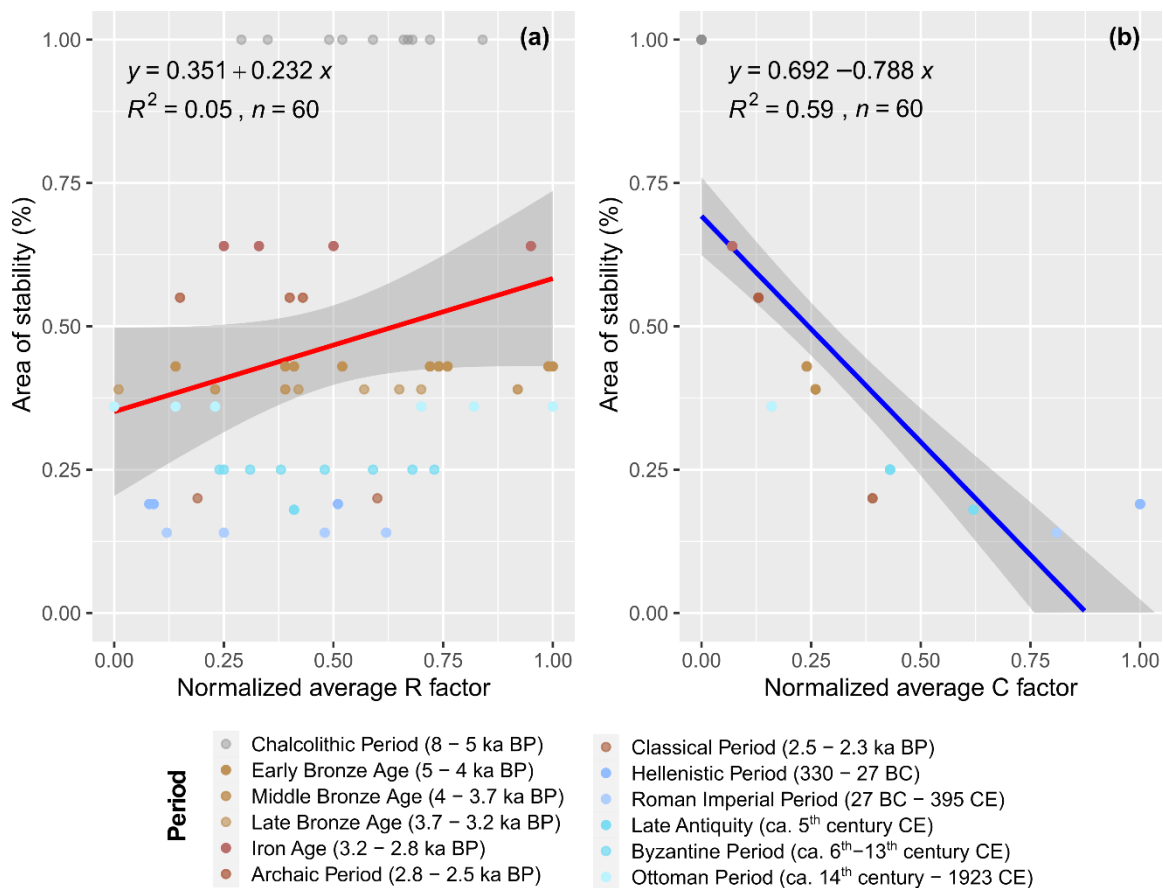


**Figure 7.6** The relationship between the soil erosion risk (represented by the area (%) of relative stability based on the USPED modeling) and the normalized average rainfall (R) factor (a), and the normalized average cover (C) factor (b) during the last 6000 years (before 1950) in the western Pergamon micro-region.

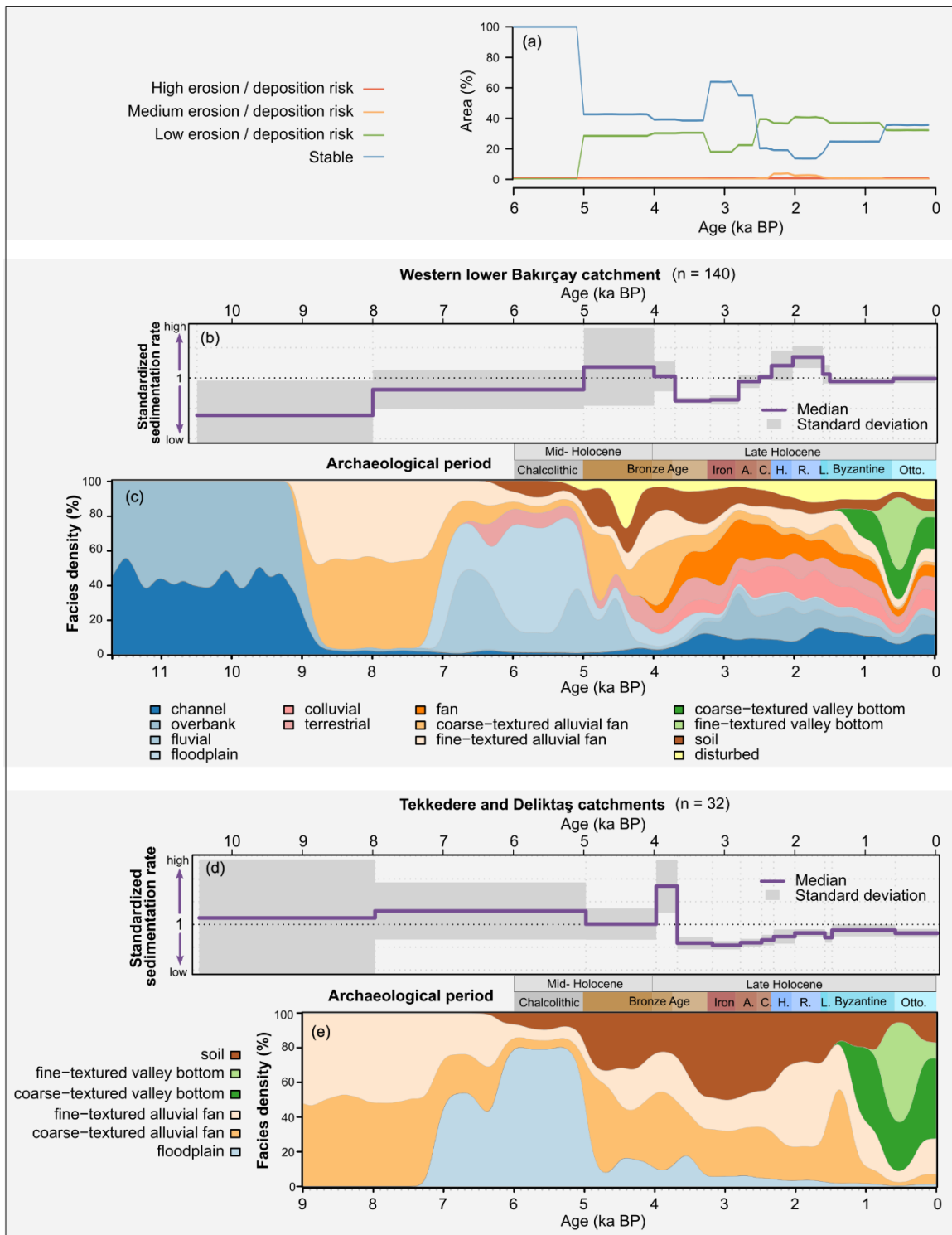
### 7.4.3 Comparison with the updated $^{14}\text{C}$ meta-data analysis

The comparable trend between the modeled sedimentation rate from the updated  $^{14}\text{C}$  meta-data analysis (Figure 7.7b) and the areas under soil erosion and deposition risk resulting from the USPED simulation (Figure 7.7a) in the western lower Bakırçay catchment indicates altogether similar records. Both graphs show low geomorphodynamics before ca. 5 ka BP followed by increased values until ca. 3.5 ka BP. The sedimentation rate became very low from 3.5 to 2.8 ka BP and gradually increased to its highest level during 2–1.6 ka BP. It then dropped abruptly at ca. 1.6 ka BP and afterward remained roughly constant at around 1 (Figure 7.7b).

The USPED modeling results for the Tekkedere and Deliktaş catchments show slightly different graphs (Figure 7.4d and e) compared to the results from the  $^{14}\text{C}$  meta-data analysis (Figure 7.7d). Before ca. 5 ka BP, soil erosion risk was low as indicated by the USPED modeling results, whereas the sedimentation rate was moderate based on the meta-data analysis (Figure 7.7d). After a small decrease between 5 and 4 ka BP, the sedimentation rate reached its highest point for a short period (around 4–3.7 ka BP), which is not displayed in the graphs indicating the soil erosion risk. The sedimentation rate (meta-data analysis) dropped to very low levels during 3.7–2.3 ka BP (Figure 7.7d), which corresponds to the trend of soil erosion risk in the entire western lower Bakırçay catchment (Figure 7.7b). Gradually, the sedimentation rate (meta-data analysis) in the Tekkedere and Deliktaş catchments increased and remained around 0.9 after ca. 2 ka BP. The graphs of sediment facies reveal that the environment became much more diverse after 5 ka BP on both local and micro-regional scales (Figure 7.7c and e).

---

**Figure 7.7** The comparison between soil erosion and deposition risk in the western lower Bakırçay catchment based on USPED modeling during the last 6000 years (**a**) and a meta-data analysis of the updated  $^{14}\text{C}$  datings ( $n = 140$ ) in 38 sediment sequences obtained from the western lower Bakırçay catchment (b–e; the model was modified from Becker et al. (2020a)). Average sedimentation rate in the western lower Bakırçay catchment (**b**) and the catchments of Tekkedere and Deliktaş (**d**) (the data were normalized based on the null model and were averaged over the archaeological periods in Table 2.1; the dashed horizontal lines indicate no difference between the observed data and the null model; grey boxes indicate the variability within the specific archaeological period). Modeled sediment facies density in the whole study area (**c**) and the catchments of Tekkedere and Deliktaş (**e**) (the relative cumulative probability functions of the estimated ages of the sediment layers were associated with different facies; facies terminology was modified from the original publication and is thus not always non-overlapping (Becker et al., 2020a)).



## 7.5 Discussion

The results of soil erosion and deposition risk based on the USPED modeling are compared with field observations, analyses of sediment profiles, and the modeled sedimentation rate from the updated  $^{14}\text{C}$  meta-data analysis, indicating the USPED modeling results are an analogous representation of the real world.

### 7.5.1 Geomorphodynamics during the last 6000 years

The USPED modeling results suggest that the soil erosion and deposition risk in the western lower Bakırçay catchment exhibited a changing and heterogeneous character during the last 6000 years (Figures 7.4 and 7.5). The related geomorphodynamics can be sub-divided into five main phases, with major accelerations occurring during the second (ca. 5–3.7 ka BP) and the fourth phase (ca. 2.5–1.5 ka BP) (Table 7.1). Similar trends in geomorphodynamics are observed in the Bakırçay second and third order catchments (in Hack's stream order (Hack, 1957)) of Tekkedere (Yang et al., 2023a) and Deliktaş (Yang et al., 2023b), as well as on the larger spatial scale of the eastern Mediterranean region (Dusar et al., 2011). However, some evident differences also exist, particularly during the second phase (ca. 5–3.7 ka BP) and the fifth phase (ca. 1.5–0) (Table 7.1).

During the Chalcolithic Period (phase 1), the land surface in the western lower Bakırçay catchment was generally stable, which is consistent with the conditions in contemporary south Türkiye (Wilkinson, 1999) and the Peloponnese region (Fuchs, 2007) in the eastern Mediterranean region (Dusar et al., 2011). The transition from the Chalcolithic Period to the Early Bronze Age (ca. 5.2 ka BP) marked a sudden exposure to soil erosion in the entire area, which persisted until the end of the Middle Bronze Age (ca. 3.7 ka BP) (phase 2). This period of high geomorphodynamics is also evident from the increase in sedimentation rates based on the  $^{14}\text{C}$ -modeling (Figure 7.7b) and the change in dominant sediment facies (Figure 7.7c) in the western lower Bakırçay catchment. However, the distinct soil formation on fans and floodplains in the catchments of Tekkedere and Deliktaş (Figure 7.7e) (Yang et al., 2023a; 2023b) reveals a lower modeled rate of sediment flux prior to reaching its peak for a short time from ca. 4 ka BP to 3.7 ka BP (Figure 7.7d). The process of pedogenesis occurred at different times, with slightly earlier soil formation in the Tekkedere catchment (between ca. 5 and 4 ka) (Yang et al., 2023a) than in the Deliktaş catchment (at least during ca. 4–3.4 cal ka BP) (Yang et al., 2023b). Nonetheless, the transition from a floodplain to an alluvial fan environment in the Tekkedere catchment during ca. 4–3.8 ka roughly corresponds to the period of high geomorphodynamics (Figure

7.7d and Table 7.1). Supra-regionally, similar dynamics during phase 2 were observed in the eastern Mediterranean region (Dusar et al., 2011).

Such varying indications of geomorphic activities between the USPED modeling outcomes and local sediment archives might be primarily related to the age inversions (e.g., Fuchs and Lang, 2009; Yang et al., 2023), which, together with the sediment cascade model (Lang and Hönscheidt, 1999) further complicate the search for causalities (Walsh et al., 2019). Also, the status of initial landscape conditions, such as bedrock and soil (cf. D'Haen et al., 2013a; 2013b), might have contributed to spatial heterogeneity (Yang et al., 2021). In addition, the sediment archives used for the meta-data analyses were sampled from different types of archives (Becker et al., 2020a), including the floodplain deposits of the Bakırçay river (Schneider et al., 2015), the valley bottoms and alluvial fan deposits of the tributaries of the Bakırçay river (Schneider et al., 2013; 2014; Yang et al., 2023a; 2023b), and coastal areas (Seeliger et al., 2019). Those, hence, lead to diverse time lags after the initial land use increase between the upper and lower reaches of the river valleys (Dusar et al., 2012; Verstraeten et al., 2017; Roberts, 2023), the (dis)continuous records and the sensitivity of driving factors to the environmental history (Dotterweich, 2008; Ackermann et al., 2014b), and cause various chronological difference (Dusar et al., 2012).

The relatively low rate of sedimentation that occurred between the end of the Late Bronze Age, Iron Age, and Archaic Period (ca. 3400–2500 yr BP; phase 3) was not distinct in the mountainous catchments of Tekkedere and Deliktaş (Table 7.1). The <sup>14</sup>C-modeled sedimentation rate (Figure 7.7b and d) supports the modeling results of low soil erosion and deposition risk. However, sediment analyses from the Deliktaş catchment suggest relatively high geomorphologic activities between ca. 4–3.4 and ca. 2.3 cal ka BP, hence during the beginning of the Late Holocene (Yang et al., 2023b). Similar trends of high soil erosion are observed in the eastern Mediterranean region (Dusar et al., 2011), for example, in southern Greece during the Thracian period (Iron Age to Classical Greek period) (Lespez, 2003; Fuchs, 2007), and in south Türkiye and NW Syria (Wilkinson, 1999).

**Table 7.1** The comparison of the geomorphodynamics during the Mid- to Late Holocene among the sediment evidence for the two catchments in Tekkedere (Yang et al., 2023a) and Deliktaş (Yang et al., 2023b), the USPED modeling results for this study in the (western) Pergamon micro-region, the updated meta-data analyses of <sup>14</sup>C datings, and the results for the supra-regional scale in the eastern Mediterranean by Dusar et al. (2011), as well as the suggested driving factors. The classes of geomorphodynamics and hypothetical sediment dynamics were grouped into 4 classes: class 0 refers to relatively stable in white shade, and class 4 refers to the highest geomorphodynamic in the highest gray shade.

Phase	Chronology (ka BP)	Archaeological periods in the Pergamon micro-region	Geomorphodynamic class *					Suggested drivers		Eastern Mediterranean (Dusar et al., 2011)		
			Tekkedere and Deliktaş			western lower Bakırçay catchment				Hypothetical sediment dynamics *	Suggested drivers	
			Sediment evidence	USPED model	Updated meta-data analyses of <sup>14</sup> C datings	USPED model	Updated meta-data analyses of <sup>14</sup> C datings	Climate changes	Human settlements		Climate changes	Human settlements
1	6–5	Chalcolithic Period	1?	0	3	0	1	Humid	No	1	Moderate → low	Low → moderate
2	5–3.7	Early and Middle Bronze Age	0 → 4	3	2 → 4	3	3	Drying + 4.2 ka drought event	Onset	3	Low → moderate	Increasing
3	3.7–2.5	Late Bronze Age, Iron Age, and Archaic Period	3	3 → 4	1	2	1	Dry	Low	3 → 4	Moderate → low	Moderate → strong

Phase	Chronology (ka BP)	Archaeological periods in the Pergamon micro-region	Geomorphodynamic class *					Suggested drivers in this study		Eastern Mediterranean (Dusar et al., 2011)		
			Tekkedere and Deliktaş			western lower Bakırçay catchment		Climate changes	Human settlements	Hypothetical sediment dynamics *	Suggested drivers	
			Sediment evidence	USPED model	Updated meta-data analyses of <sup>14</sup> C datings	USPED model	Updated meta-data analyses of <sup>14</sup> C datings				Climate changes	Human settlements
4	2.5–1.5	Classical Period, Hellenistic Period, Roman Imperial Period, and Late Antiquity	3	4	1 → 2	4	4	Dry	Heydays	4 → 0	Moderate	Strong → low
5	1.5–0	Byzantine Period and Ottoman Period	2	2	2	2 → 3	2	Semi-humid	Medium	0 → 2	Moderate	Low → strong

The broadly increased area of medium soil erosion and deposition in the western lower Bakırçay catchment and the Tekkedere and Deliktaş catchments between approximately 2.5 and 1.5 ka BP (phase 4; Table 7.1) suggests that more areas were exposed to severe soil erosion risk during the Classical, Hellenistic, and Roman Imperial periods. These periods in the Pergamon micro-region witnessed a rapid increase in population and the corresponding number of settlements (Pirson, 2020; Ludwig, 2023). The intensive land use for agriculture and pasture, as well as the spread of construction and built-up areas, connects with the accelerated landscape instability and increased soil erosion intensity. Contemporarily, the high modeled sedimentation rate based on the <sup>14</sup>C meta-data analysis (Figure 7.7) supports the assumption. This significant change can be temporally broadly associated with regional soil erosional signals (Dusar et al., 2011), e.g., the severe soil erosion in Greece (Lespez, 2003). Instead of a low sedimentation rate in the surroundings of the Roman Sagalassos (Van Loo et al., 2016), this high geomorphodynamics during phase 4 in the Pergamon micro-region indicates the availability of sediments in the uplands.

During the past 1500 years, most areas in the western lower Bakırçay catchment remained at a low level of soil erosion and deposition risk, with a tendency towards stability (phase 5; Table 7.1). However, the Tekkedere and Deliktaş catchments exhibit different scenarios of geomorphic conditions. The Tekkedere catchment experienced relatively low exposure to soil erosion risk for around one thousand years (ca. 1600–600 yr BP) and changed to a high exposure to soil erosion risk after 600 yr BP (Figure 7.4d). In contrast, the Deliktaş catchment has consistently displayed a high exposure to soil erosion, likely since the Early Bronze Age (Figure 7.4e). This difference between Tekkedere and Deliktaş catchments may be attributed to inter-regional variations in topography and bedrock-soil conditions (Yang et al., 2021). The modeled sedimentation rate in the western lower Bakırçay catchment during 1600–600 yr BP indicates a slight decrease but overall relatively constant values compared to the previous phase (Figure 7.7b). In the Mediterranean region, the contemporary geomorphodynamics corresponded frequently to the high rates of alluvial deposits (Dusar et al., 2011), known as “Younger Fill” (Vita-Finzi, 1969a), for example, near Kinet Höyük in Türkiye after the Hellenistic Period (Beach and Luzzadder-Beach, 2008), in Greece during the Ottoman Period (Walsh et al., 2019), and in Italy during the Late antiquity or medieval period (Goodchild, 2007). Also, the riverine/continental inputs were enhanced in the marine record of the northern Aegean after ca. 1450 AD (Gogou et al., 2016).

## 7.5.2 Factors: climate and human

The relationship between the Mid- to Late Holocene geomorphic processes in the western lower Bakırçay catchment and the relative importance of hydro-climatic change and human intervention as driving factors, suggests not only contrasting but also joint effects throughout time (Figure 7.6).

### Rainfall–runoff erosivity (R factor)

The weak correlation between soil erosion and deposition risk and the rainfall–runoff erosivity (R factor) (Figure 7.7a) in the western lower Bakırçay catchment corresponds to the comparable modeling result in the Gravgaz basin and the environs of Sagalassos, where the R factor is also a weak predictor of sediment delivery rates (Van Loo et al., 2016). Research in south Greece also indicates a weak correlation between climatic fluctuations and sedimentation history during the Early to Middle Holocene (Fuchs, 2007).

During the Chalcolithic Period when human settlements in the western lower Bakırçay catchment were very limited, the landscape remained generally stable independent from fluctuations of the R factor (Figure 7.6a). This stability might be associated with the Mid-Holocene wetter-than-today humid climate trend in the region (Eastwood et al., 2007; Finné et al., 2019) and the corresponding presence of high forest cover as evidenced by palynological records from Elaia (Shumilovskikh et al., 2016). Consequently, soil erosion risk and geomorphodynamics in the mountainous areas were relatively low (Table 7.1), whereas fluvial dynamics for the main river were high (Walsh et al., 2019; Yang et al., 2023a; 2023b).

It is challenging to determine the effects of Mid- to Late Holocene climatic aridization along with storm events (Finné et al., 2019) on land degradation from the USPED modeling results (Figures 7.5 and 7.7a) despite these climatic factors being widely accepted as the main triggers of soil erosion in the Mediterranean region (García-Ruiz et al., 2013; Walsh et al., 2019). The soil erosion risk during periods of the 4.2 and 3.2 events (Bini et al., 2019; Manning et al., 2020), or even the 5.2 ka event (Ghilardi et al., 2015), were limited (Figure 7.4a and c), and the area of stability even increased during ca. 3.4–2.5 ka BP (Figure 7.4c). This is primarily associated with the relatively stable variations in the area-wide average R factor, particularly around 4.2 or 3.2 ka BP (Figure 7.4a, the blue line). The AWI-ESM-based R factor shows a roughly similar trend to the Z score of the reconstructed hydro-climate data from south Türkiye (Finné et al., 2019) (Spearman's correlation:  $r(59) = .35$ ,  $p = .020$ ), except at ca. 3000 yr BP when the reconstructed Z score climate reached one of driest conditions in the observed periods since 6 ka BP

(Figure 7.4a). The input climate data in this study were used due to the availability of monthly rainfall values during the Mid- to Late Holocene (Shi et al., 2022a; 2022b). However, it should be noted that the spatial resolution and accuracy of the AWI-ESM model might not be optimal simulations on large scales.

The transfer of the Mediterranean drought events to the western lower Bakırçay catchment should be treated with caution as different research in the Mediterranean region might reveal contrasting results. While the interval between 4.3 and 3.8 ka BP is generally regarded as a drought event (cf. Francke et al., 2013; Weiberg et al., 2016), related to the so-called Mid–Late Holocene transition (Maltas et al., 2023) in the Mediterranean Basin, the effects of this event underly a strong regional heterogeneity (Bini et al., 2019; Ön, 2023).

The impacts of rapid climate changes on the landscape system of the western lower Bakırçay catchment are likely minor, especially considering its location at the boundary between pronounced and unclear changes in the paleoenvironment before and after 4.2 ka BP (Di Rita et al., 2022). Additionally, the period is occasionally reported to be wetter, associated with an increasing frequency of large floods in some parts of the Mediterranean (Benito et al., 2015; Wolf and Faust, 2015). Hydro-climatic variations from arid to relatively humid environmental conditions can also cause soil erosion (Walsh et al., 2019).

During the Late Holocene, the R factor also weakly correlates with the soil erosion risk based on the USPED modeling results (Figure 7.6). Moisture availability and the centennial scale, e.g., the Roman Warm Period, Late Antique Little Ice Age (Büntgen et al., 2016), Medieval Climate Anomaly, and Little Ice Age (Morellón et al., 2016) revealing variability in vegetation cover, also contributed to the geomorphic processes (Bakker et al., 2011b; Walsh et al., 2019; Weiberg et al., 2021).

The Roman period, often characterized as a time of higher temperature and humidity during the Mid- to Late Holocene, did not necessarily apply uniformly across the Mediterranean region (Finné et al., 2019). For the western lower Bakırçay catchment, climate data suggest relatively dry conditions around 2000 yr BP (Figure 7.3\_b3). Amplified by late-summer and autumn storms and intensified economic activities, severe soil erosion occurred, potentially leading to irreversible threshold crossings observed by Roman writers (Walsh et al., 2019).

## Land cover and management (C factor)

The strong correlation between the C factor and soil erosion risk is consistent with findings in the environs of Sagalassos, where the C factor has a linear effect on sediment delivery (Van Loo et al., 2016). However, in some areas such as east Asia, the relationship between land use and soil erosion risk may exhibit non-linear correspondence over long-term scales (Dearing, 2008; Dotterweich, 2013).

During the Early Holocene in the Pergamon micro-region, only one site, i.e., the Ballık cave in the Kozak mountain, was currently observed and dated to the Late Epipalaeolithic (13.7–12.2 ka BP) and Neolithic (10.5–8 ka BP) periods (Aksan et al., 2022) (Table 2.1), which is assumed to have a neglectable environmental effect on the surroundings. The USPED modeling results of the soil erosion and deposition risk in the western lower Bakırçay catchment indicate that the exposure to soil erosion risk and correspondingly soil erosion processes started from the Early Bronze Age (5–4 ka BP) when the footslopes along the western lower Bakırçay floodplain were initially extensively uprooted and occupied (Figure 7.4b and c), and it remained the same until the end of the Late Bronze Age (ca. 3.2 ka BP). During phase 2, the farmers in western Türkiye adjusted their agricultural strategies to cope with the aridization conditions during the Mid- to Late Holocene transition (Maltas et al., 2023). These findings underline the observations that the Mid-Holocene Mediterranean geomorphic systems were highly exposed to soil erosion due to human-made deforestation and land exposure (Walsh et al., 2019). Importantly, the influence even from a relatively low demographic level might reach or exceed the threshold of a landscape over a long time, leading to the potential of unsuitable lands (Bintliff, 2002). Thus, human activities are suggested to have an important impact on the landscape opening, particularly in the fragile and uncultivated hilly to mountainous Mediterranean areas during the Mid- to Late Holocene, most probably after ca. 5000 yr BP (Dusar et al., 2011), occasionally as early as the Neolithic (7–4.5 ka BC) in Greece (Fuchs, 2007; Glais et al., 2017; Jouffroy-Bapicot et al., 2021) and Spain (May et al., 2021), or later like in the Tekkedere and Deliktaş catchments after the Middle Bronze Age (Ludwig, 2020a; Michalski, 2021; 2023). It is worth noting that human settlements are not necessary to cause severe soil erosion. For instance, nearly three millennia of cultivation during the Bronze and Iron Ages had relatively little contribution to soil erosion in the northern Levant, which has been occupied by agrarian communities since at least 2800 BC (Casana, 2008).

During the Iron, Archaic, and Classical periods, the relatively low human occupation corresponded into a recovery of stable areas, similar to the findings in the Tekkedere and

Deliktaş catchments (Figure 7.4). However, it has to be considered that the geomorphological dynamic equilibrium of the landscapes after the Bronze Age uprooting and hereby triggered that morphodynamics have reached more stable conditions. In the western lower Bakırçay catchment, the Early–Middle Holocene land use shifted from natural oak forests to cultural cultivation with olive, pistachio, walnut, and grape around 2.8 ka BP (Shumilovskikh et al., 2016). Olive horticulture, which likely started around 3.2 ka BP in western Anatolia (Langgut et al., 2019; Stock et al., 2020a), corresponded to the onset of the regionally so-called Beyşehir Occupation phase (approximately 3500 to 1550 yr BP) (Eastwood et al., 1998; Kaniewski et al., 2007; Bakker et al., 2011a). Notwithstanding the importance of olive cultivation, its effects on soil erosion were relatively low compared to other land use types (vine, eucalypti, wheat, and shrubland) (Kosmas et al., 1997; Geeson et al., 2002), which might underline this period of reduced geomorphodynamics in the western lower Bakırçay catchment.

During the Hellenistic and Roman Imperial periods, geomorphodynamics increased synchronously with the emergence of complex socioeconomic systems on different spatial scales in the eastern Mediterranean region, including the catchment, micro-regional, and supra-regional scales (Table 7.1). In the catchments of Tekkedere and Deliktaş, soil erosion increased (Figure 7.4), as also evident by the sediment analyses (Yang et al., 2023a; 2023b). Particularly, the Deliktaş catchment also experienced a settlement boom during this time (Ludwig et al., 2022).

On the micro-regional scale, the western lower Bakırçay catchment was part of the center of the Pergamene Kingdom until the later Roman period (Pirson, 2020); during this period also geomorphodynamics were intense. Compared to the Bronze Age to the Classical Period (cf. Knitter, 2013), the extent distribution of areas under soil erosion and deposition risk during the Hellenistic and Roman Imperial periods indicate the accelerated human activities on the landscape (Figure 7.5). This indicates that not only the lowlands that were normally subjected to initial impact (e.g., in Morocco (Cheddadi et al., 2019)) but also relatively untouched areas were exploited for agriculture and olive cultivation to sustain the growing food demand during the heydays of the Hellenistic–Roman Imperial periods (Shumilovskikh et al., 2016). The Bakırçay plain, which was probably not suitable for human occupation due to the high flooding risk (Knitter et al., 2013; Schneider et al., 2015), was used during this time (Figure 1.3). The desiccation of the alluvial plain due to drier conditions and correspondingly declining near-surface groundwater table (cf. Bakker et al., 2011; Figure 7.3\_b3) might likely provide spaces for small settlements. Thus, phase 4 could be the potential time when a politically driven increase in human impacts largely exceeded climatic stress.

On a supra-regional scale, the Beyşehir Occupation in western Anatolia also reached its prime during this time. It was characterized by large-scale human disturbance, including woodland clearance, fire activity, agriculture, pasture, viticulture, and grazing, which caused landscape changes (Casana, 2008; Bakker et al., 2011a; Duser et al., 2011; Mercuri et al., 2019; Weiberg et al., 2019a; Stock et al., 2020a). Similar human-shaped landscapes have been reported during the Hellenistic to Roman periods in Greece (Glais et al., 2017; Jouffroy-Bapicot et al., 2021) and Spain (Silva-Sánchez et al., 2014; May et al., 2021).

During the Roman Imperial Period, agricultural terracing systems were developed to improve landscape resilience by increasing infiltration and reducing runoff (Arnáez et al., 2015; Walsh et al., 2019). Many hillslopes in the Mediterranean region were supported and maintained with terracing systems. These efforts resulted in less distinct soil erosion during the heydays of the Roman Period, but more evident soil erosion afterward (Casana, 2008; Walsh et al., 2019). The development of the terracing system might be the same in the Pergamon micro-region (Schneider et al., 2013). However, even though, the consequence of reducing landscape degradation was not distinct in the western lower Bakırçay catchment.

After the intensive use of the landscape, geomorphodynamics slightly decreased after the Roman period also on various spatial scales (phase 5; Table 7.1). This decline might be related to climatic and socio-economic changes (Xoplaki et al., 2016), as well as to the depletion of sediments left on the uplands (cf. Bakker et al., 2011; Duser et al., 2012; Verstraeten et al., 2017). Moreover, more sites were built on soil depositional environments since the Late Antiquity (Figure 7.5). In the coastal area, soil erosion processes resulted in a large sediment supply and the siltation of the harbor city of Elaia, triggering the decline of the city in the late Roman time and its subsequent abandonment (Pint et al., 2015; Seeliger et al., 2019).

### **7.5.3 Further research: soil erosion model improvements**

The USPED model used in this study provides a long-term perspective on geomorphodynamics and their relationship with climate and human activities on a micro-regional scale. However, there are several avenues for improving the modeling results and enhancing the potential of soil erosion modeling through the integration of various input datasets, including climate, land cover, topography, soil conditions, and management practices.

The input rainfall data from the AWI-ESM model show low spatial resolution and the 100-year simulation run for the rainfall factor might overlook rainfall extremes and potentially impact the model's performance (Van Loo et al., 2016). Hence, to improve the calculation of the rainfall–runoff erosivity (R) factor, it is crucial to obtain a high spatiotemporal resolution and local scale dataset of hindcast modeled hydro-climatic data which is required to cover the hydro-climatic fluctuations (cf. Van Loo et al., 2016). This would require the use of natural archives with precise and accurate datings (Zanchetta et al., 2011), which demands basic validation and comparison with regional reconstructions. The recently released climate data – LegacyClimate 1.0, which provides pollen-based reconstructions (Herzschuh et al., 2023), could be valuable for this purpose. However, transforming the diverse data with varying temporal lengths and resolutions into monthly precipitation data poses a challenge. The palynological studies in the Pergamon micro-region provide a rather coarse view of the vegetation cover and land use change (Shumilovskikh et al., 2016; 2022) instead of past precipitation estimation.

Enhancements to the land cover (C) factor can be achieved through various methods. Detailed pollen-based analyses (cf. Berger et al., 2019; Fyfe et al., 2019; Woodbridge et al., 2019) or modeling (cf. Arıkan et al., 2016; Knitter et al., 2019) can directly reconstruct past land use and land cover, providing more accurate estimations. The applied approach of estimating land cover from the raw count of archaeological sites requires further improvements. A more detailed classification of settlement size, ranking, or hierarchy (Ludwig, 2023), as well as considering the influence of specific urban centers like Pergamon (Knitter et al., 2013), can enhance accuracy on more localized scales. Differentiating between small farms and large villas and using the area of individual archaeological sites instead of single points can also contribute to more precise modeling. Future research could also explore predictive modeling (Verhagen, 2018) to estimate changing settlement sizes and long-term population patterns, considering the issue of uneven sampling (Palmisano et al., 2017). Furthermore, Monte Carlo approaches and 'aoristic' methods could improve the duration uncertainty of the occupation periods due to the consilience issue of interdisciplinary research among archaeologists (Palmisano et al., 2017; Walsh et al., 2019), historians, and paleoenvironmental scientists (Izdebski et al., 2016a).

Addressing the issue of constant values for topographic changes (LS factor) and soil dynamics (K factor) during the Holocene could involve the use of a diffusion equation (Mitasova et al., 2013) or iteration methods that account for elevation changes associated with soil erosion and accumulation (Peeters et al., 2006). To assess potential changes in ancient soil patterns, future studies could consider incorporating underlying parent

materials or geology (Goodchild, 2007). Detailed detection of past management practices (P factor) requires archaeological surveys and text analyses (Price and Nixon, 2005; Dotterweich, 2013), along with accurate dating of ancient agricultural terraces (cf. Acabado, 2015).

Calibrating the model using published sediment archives can help reduce uncertainties and improve model predictions. Additionally, evaluating the USPED model and its factors requires detailed and accurate chronological control (Fuchs et al., 2004; Strunk et al., 2020) of sediment archives (Dusar et al., 2012) and ancient vegetation changes at multiple sites (Van Loo et al., 2016).

## 7.6 Conclusions

The application of the advanced USPED model for the soil erosion and deposition risk in the western lower Bakırçay catchment underlines the high potential of geomorphic modeling in estimating the effects of various driving factors on the landscape dynamics from the Middle to Late Holocene. By utilizing past monthly rainfall and archaeological site data, and comparing the results with modern USPED outcomes, local sediment archives, and field observations, this study has provided valuable insights into the environmental history of the region during the Mid- to Late Holocene.

The findings reveal five different geomorphic phases during the Mid- to Late Holocene, with notable increases in geomorphodynamics during two specific intervals: approximately 5–3.7 ka BP (phase 2) and 2.5–1.5 ka BP (phase 4). The study indicates that land cover changes caused by human activities exhibit a stronger correlation with soil erosion risk compared to climate variations. In contrast, the rapid climate change events, such as the 4.2/3.2 events, may have less contribution to soil erosion risk, although the impacts of climatic drying and fluctuations cannot be disregarded.

The transformation of the Pergamon micro-region during the Hellenistic-Roman period driven by the complex society likely played a significant role in inducing substantial landscape dynamics on multiple scales and emerged as the primary driver of environmental change. Slight variations in geomorphodynamics among different methods employed by scholars highlight the challenges posed by input data, dating imprecision, and the diversity of natural conditions and sampling locations. To further enhance the application of the USPED model and develop a quantitative understanding of the soil erosion and deposition risk and the ancient human-environment interactions, additional

efforts should focus on advancing the quality of input data and refining the calibration and validation of the model.

Considering the highly tectonic active nature of the geographical region where the Pergamon micro-region is located, at least nine big earthquakes during the last two millennia (Paradisopoulou et al., 2010; Schneider, 2014; Yang et al., 2021), future research should explore the impacts of tectonics (cf. Emmanouilidis et al., 2019), in addition to climate and human activities. Taking the mutual influence among these factors into account would greatly enhance the model's accuracy. For example, different soil types in different topographical locations, under varying climates (including temperature and precipitation), may have diverse impacts on land use and settlement strategies (Goodchild, 2007; Gogou et al., 2016; Izdebski et al., 2016b; Bonnier and Finné, 2020), and socio-economic dynamics (Sadori et al., 2016; Woodbridge et al., 2019).

## 8. Overall conclusions

This doctoral thesis provides insights into the Mid- to Late Holocene geomorphodynamics and their relationships with climate fluctuations and human activities in the western lower Bakırçay catchment as a central area of the Pergamon micro-region. Through the application of multiple methods and analyses on various spatiotemporal scales, this research contributes to the reconstruction of geomorphodynamics, which is essential for assessing the sustainability of complex Mediterranean landscapes exhibiting significant variations across different locations and time intervals. The fragile land surface in these (semi-)arid areas is highly vulnerable to a combination of driving factors that result in severe soil erosion and land degradation. Furthermore, the relationship between drivers and geomorphological processes may vary depending on the characteristics of the study area and the employed research methods. Key debates in this field have centered on the dominance and timing of climate and/or human-induced environments during the Holocene (e.g., Bintliff, 2002; Dusař et al., 2011). In the Pergamon micro-region, abundant archaeological remains have attracted scholars' interest in reconstructing human–environment interactions, particularly in rural areas where the settlement patterns provide insights into the extent and intensity of human impacts on the local landscape (Schneider et al., 2015; Seeliger et al., 2019) and references therein). By integrating multidisciplinary approaches, the study reveals diverse perspectives on geomorphodynamics during recent times, the Hellenistic-Roman transformation, and important climate events on local to micro-regional scales.

### Summary and synthesis

The first paper (Yang et al., 2021, chapter 4) presents a basic geomorphological map of the Pergamon micro-region, covering a vast area of the Bakırçay and Madra river catchments and the adjacent Aegean coasts. The analyses demonstrate a complex morphotectonic landscape influenced by various factors such as tectonics, lithology, sea-level change, and human impacts. The heterogeneous yet relatively stable landscapes during the Holocene have been conducive to various uses, including agriculture, water resources, construction materials, wood, and settlements throughout the Holocene. Notably, the presence of distinct human impacts during the Hellenistic–Roman periods is evident. Particularly, the low-angle colluvial and alluvial deposits from the Yuntdağ, Karadağ, and Kozak mountains and their transition to the Bakırçay plain favor the

development of the rural settlements, which are the accessible materials from the local sediment sinks to study the ancient human–environment interactions in rural areas.

The first study efficiently guides the following local studies (chapters 5 and 6) on the two representative areas in the Pergamon micro-region both from the values of archaeology and geomorphology. The catchments have been occupied at least since the (Middle) Bronze Age (Michalski, 2021; Ludwig et al., 2022) and cover the Yuntdağ and Karadağ mountains which have not been studied. Alluvial fan and valley bottom sediments of a rural catchment close to the village of Tekkedere from the Yuntdağ mountain denote four principal sedimentation phases – the Mid-Holocene Bakırçay floodplain aggradation (phase 1), the soil formation on the floodplain (phase 2), the burial by the extended alluvial fan (phase 3), and the repeated cycles of coarse- and fine-textured fan sediments with age inversions and young valley infills (phase 4) (Yang et al., 2023a, chapter 5). The increased geomorphodynamic activity at phase 3 (ca. 4000 yr BP) is related to a supra-regional aridization and rapid climate change events (e.g., 4.2 ka drought event), superimposed by the onset of local human activities since the Middle Bronze Age (ca. 3.7 ka BP). The strong erosion and redeposition of sediments based on the young valley deposits and age inversions in the last phase might coincide with the increasing human pressure from both the rural settlements and the urban transformation of large settlements (e.g., Pergamon and Elaia) from Hellenistic to the Roman Imperial periods (Pirson, 2020). Uncertainty persists regarding the precise duration of the human-influenced landscape in the Tekkedere catchment.

The additional case study in the Deliktaş catchment (Yang et al., 2023b, chapter 6) explores a different ancient settlement pattern and modern erosional feature from the Tekkedere catchment. This study is the first geoarchaeological study that covers the entire Holocene in the Pergamon micro-region. Seven phases of the Deliktaş alluvial fan development are identified, different from those in the Tekkedere fan. However, both catchments show similarities in the development of floodplain soils and the subsequent accelerated geomorphodynamic activities (the burial of the soils), likely associated with the local onset of human occupation and the regional Mid-Holocene aridization with rapid climate changes. The assumption of increased geomorphodynamics during the last 2.5 ka BP due to the high human pressure represented by the sudden increase of archaeological sites during the Hellenistic–Roman transformation in the Deliktaş catchment is less evident. Both, regional climatic systems and rural–urban settlement patterns are highlighted by the contribution of locally diverse geomorphodynamics in the Pergamon micro-region.

These local studies, together with the application of the Unit Stream Power Erosion Deposition (USPED) model in the last study (chapter 7), contribute to understanding the long-term effects of climate and human population on soil erosion and deposition risk over the past 6,000 years. The hind-cast modeling of soil erosion risk applying the statistical model USPED reveals five main phases during the Mid- to Late Holocene, with notable increases in geomorphodynamics at the second (ca. 5–3.7 ka BP) and fourth phases (ca. 2.5–1.5 ka BP). This is supported by the evidence in the rural catchments of Tekkedere and Deliktaş, as well as the supra-region of the eastern Mediterranean. In addition, the contrasting and cooperative effects of hydro-climatic changes and human activities on landscape stability are highlighted. The impacts of rainfall fluctuations on the soil erosion risk are suggested to be less significant compared to settlement patterns from the USPED model results. Opposite to the sediment analyses from the sub-catchments, the distinct increase in soil erosion risk from the USPED simulation during the Hellenistic–Roman transformation indicates the fourth phase is the most potential time when the impacts of humans exceeded the climate. The research offers an initial step towards integrating soil erosion risk modeling and conducting multi-scale spatial comparisons, revealing the complexity of the landscape system in the Pergamon micro-region.

## **Conclusions**

This dissertation emphasizes the significance of understanding geomorphodynamics and provides insights into the ongoing debate on the cause-and-effect relationships in Mediterranean landscapes. This research extends at least 6000 years into the past, unraveling a diverse and dynamic landscape in the vicinity of the historically significant city of Pergamon. While landscape evolution scenarios during the Mid- to Late Holocene may vary across different locations, five major phases of geomorphodynamics with two geomorphological accelerations are discernible through sedimentary evidence on local scales and model simulations on a regional scale, aligning with broader research on the Mediterranean landscape. The interplay between increased geomorphodynamics and driving factors indicates the remarkable human pressure since at least the Bronze Age, with a potential dominant contribution during the Hellenistic–Roman transformation. In addition, the duration and intensity of the geomorphodynamics are highly related to the research methods, materials, locations, landforms, and scales that are applied in the different studies. The radiocarbon dating results should be treated with caution. The interaction and cause–effect relationship between geomorphodynamics and the drivers are highly complex and they might change when different datasets are used for the association.

## **Future research**

This doctoral research primarily focuses on the Mid- to Late Holocene geomorphodynamics which mainly covers the last 6000 years. The validation of the modern geomorphological mapping was conducted only in selected locations, with many areas in the Northern Highlands left unexplored. The temporal uncertainty of different geomorphodynamic phases in the Tekkedere and Deliktaş catchments arises from the lack of suitable dating materials for high-resolution chronologies. Increasing availability of climate data on regional and global scales in the future may allow for establishing more detailed relationships between climate and geomorphodynamics in the micro-region.

Further improvements in estimating past soil erosion risk could focus on refining the input factors of the USPED model and exploring other widely used models (Mitasova et al., 2013). The incorporation of agent-based models (Günther et al., 2021) and carrying capacity limitations (Laabs and Knitter, 2021) is essential for investigating socio-ecological dynamics and human impacts on geomorphodynamics. Geomorphodynamics, as a crucial component of the ecological-social-cultural sphere (Becker et al., under review), represents an important topic for future research in developing the environmental history of this important ancient city of Pergamon and its surroundings within the Mediterranean context.

## 9. References

- Abrahams, A.D., 1968. Distinguishing between the concepts of steady state and dynamic equilibrium in geomorphology. *Earth Science Journal* 2, 1–7.
- Ackermann, O., Greenbaum, N., Ayalon, A., Bar-Matthews, M., Boaretto, E., Bruins, H.J., Cabanes, D., Horwitz, L.K., Neumann, F.H., Porat, N., Weiss, E., Maeir, A.M., 2014a. Using palaeo-environmental proxies to reconstruct natural and anthropogenic controls on sedimentation rates, Tell es-Safi/Gath, eastern Mediterranean. *Anthropocene* 8, 70–82.
- Ackermann, O., Greenbaum, N., Bruins, H., Porat, N., Bar-Matthews, M., Almogi-Labin, A., Schilman, B., Ayalon, A., Horwitz, L.K., Weiss, E., Maeir, A.M., 2014b. Palaeoenvironment and anthropogenic activity in the southeastern Mediterranean since the mid-Holocene: The case of Tell es-Safi/Gath, Israel. *Quaternary International* 328–329, 226–243.
- Ahnert, F., 1970. Functional relationships between denudation, relief, and uplift in large, mid-latitude drainage basins. *American Journal of Science* 268, 243–263.
- Aiello, A., Adamo, M., Canora, F., 2015. Remote sensing and GIS to assess soil erosion with RUSLE3D and USPED at river basin scale in southern Italy. *Catena* 131, 174–185.
- Akman, Y., Ketenoğlu, O., 1986. The climate and vegetation of Turkey. *Proceedings of the Royal Society of Edinburgh* 89B, 123–134.
- Aksan, Z.M., Ludwig, B., Pirson, F., Ateş, G., Doğan, T., 2022. Ballık Cave, in: Pirson, F. (Ed.), *Pergamon – Die Arbeiten in der Kampagne 2020*, pp. 40–47.
- Aksu, A.E., Konuk, T., Uluğ, A., Duman, M., Piper, D.J.W., 1990. Quaternary tectonic and sedimentary history of eastern Aegean Sea shelf area. *Jeofizik* 4, 3–35.
- Aksu, A.E., Piper, D.J.W., Konuk, T., 1987. Late Quaternary tectonic and sedimentary history of outer Izmir and Candarli bays, western Turkey. *Marine Geology* 76, 89–104.
- Alewell, C., Borrelli, P., Meusburger, K., Panagos, P., 2019. Using the USLE: Chances, challenges and limitations of soil erosion modelling. *International Soil and Water Conservation Research* 7, 203–225.
- Allen, K.J., Reide, F., Gouramanis, C., Keenan, B., Stoffel, M., Hu, A., Ionita, M., 2022. Coupled insights from the palaeoenvironmental, historical and archaeological archives to support social-ecological resilience and the sustainable development goals. *Environmental Research Letters* 17, 1–17.
- Altunkaynak, Ş., Yılmaz, Y., 1998. The Mount Kozak magmatic complex, Western Anatolia. *Journal of Volcanology and Geothermal Research* 85, 211–231.
- Amorosi, A., Centineo, M.C., Colalongo, M.L., Fiorini, F., 2005. Millennial-scale depositional cycles from the Holocene of the Po Plain, Italy. *Marine Geology* 222–223, 7–18.

- Anderson, D.G., Maasch, K.A., Sandweiss, D.H., Mayewski, P.A., 2007. Chapter 1 - Climate and culture change: exploring Holocene transitions, in: Anderson, D.G., Maasch, K.A., Sandweiss, D.H. (Eds.), *Climate Change and Cultural Dynamics*. Academic Press, San Diego, California, United States, pp. 1–23.
- Anthony, E.J., Marriner, N., Morhange, C., 2014. Human influence and the changing geomorphology of Mediterranean deltas and coasts over the last 6000 years: From progradation to destruction phase? *Earth-Science Reviews* 139, 336–361.
- Arnáez, J., Lana-Renault, N., Lasanta, T., Ruiz-Flaño, P., Castroviejo, J., 2015. Effects of farming terraces on hydrological and geomorphological processes. A review. *Catena* 128, 122–134.
- Aucelli, P., Cinque, A., Mattei, G., Pappone, G., Stefanile, M., 2018. Coastal landscape evolution of Naples (Southern Italy) since the Roman period from archaeological and geomorphological data at Palazzo degli Spiriti site. *Quaternary International* 483, 23–38.
- Auerswald, K., Fiener, P., Martin, W., Elhaus, D., 2014. Use and misuse of the K factor equation in soil erosion modeling: An alternative equation for determining USLE nomograph soil erodibility values. *Catena* 118, 220–225.
- Avni, Y., Porat, N., Plakht, J., Avni, G., 2006. Geomorphic changes leading to natural desertification versus anthropogenic land conservation in an arid environment, the Negev Highlands, Israel. *Geomorphology* 82, 177–200.
- Baartman, J., Masselink, R., Keesstra, S., Temme, A., 2013. Linking landscape morphological complexity and sediment connectivity. *Earth Surface Processes and Landforms* 38, 1457–1471.
- Bagarello, V., Di Stefano, C., Ferro, V., Giuseppe, G., Iovino, M., 2009. A Pedotransfer Function for Estimating the Soil Erodibility Factor in Sicily. *Journal of Agricultural Engineering* 40, 7–13.
- Bagha, N., Arian, M., Ghorashi, M., Pourkermani, M., El Hamdouni, R., Solgi, A., 2014. Evaluation of relative tectonic activity in the Tehran basin, central Alborz, northern Iran. *Geomorphology* 213, 66–87.
- Bakker, J., Kaniewski, D., Verstraeten, G., De Laet, V., Waelkens, M., 2011a. Numerically derived evidence for late-Holocene climate change and its impact on human presence in the southwest Taurus Mountains, Turkey. *The Holocene* 22, 425–438.
- Bakker, J., Paulissen, E., Kaniewski, D., De Laet, V., Verstraeten, G., Waelkens, M., 2011b. Man, vegetation and climate during the Holocene in the territory of Sagalassos, Western Taurus Mountains, SW Turkey. *Vegetation History and Archaeobotany* 21, 249–266.
- Bakker, J., Paulissen, E., Kaniewski, D., Poblome, J., De Laet, V., Verstraeten, G., Waelkens, M., 2013. Climate, people, fire and vegetation: new insights into vegetation dynamics in the Eastern Mediterranean since the 1st century AD. *Climate of the Past* 9, 57–87.
- Barsch, D., Liedtke, H., 1985. *Geomorphological mapping in the Federal Republic of Germany*. Im Selbstverlag des Institutes für Physische Geographie der Freien Universität Berlin, Berlin, Germany.

- Bartz, M., Rixhon, G., Kehl, M., El Ouahabi, M., Klasen, N., Brill, D., Weniger, G.-C., Mikdad, A., Brückner, H., 2017. Unravelling fluvial deposition and pedogenesis in ephemeral stream deposits in the vicinity of the prehistoric rock shelter of Ifri n'Ammar (NE Morocco) during the last 100 ka. *Catena* 152, 115–134.
- Bassukas, D., Emmanouilidis, A., Avramidis, P., 2021. Late Holocene Hydro-Climate Variability in the Eastern Mediterranean: A Spatial Multi-Proxy Approach. *Water* 13, 1–11.
- Beach, T.P., Luzzadder-Beach, S., 2008. Geoarchaeology and aggradation around Kinet Höyük, an archaeological mound in the Eastern Mediterranean, Turkey. *Geomorphology* 101, 416–428.
- Becker, F., Knitter, D., Nykamp, M., Schütt, B., 2020a. Meta-Analysis of Geomorphodynamics in the Western Lower Bakırçay Plain (Aegean Region, Turkey). *Land* 9, 1–29.
- Becker, F., Knitter, D., Walser, A.V., Ludwig, B., Tozan, M., Schütt, B., Pirson, F., under review. The Pergamon micro-region from a socio-ecological perspective—instancing geomorphodynamics. *The Holocene*.
- Becker, F., Knitter, D., Yang, X., Schütt, B., 2020b. Geländearbeiten der Physischen Geographie 2019, in: Pirson, F. (Ed.), Pergamon – Das neue Forschungsprogramm und die Arbeiten in der Kampagne 2019. *Archäologischer Anzeiger*, pp. 223–227.
- Becker, F., Yang, X., Doğan, M., Nykamp, M., Schütt, B., 2022a. Arbeiten der Physischen Geographie, in: Pirson, F. (Ed.), Pergamon – Die Arbeiten in der Kampagne 2021. *Archäologischer Anzeiger*, pp. 62–69.
- Becker, F., Yang, X., Nykamp, M., Doğan, M., Schütt, B., 2022b. Sedimentologische Arbeiten der Physischen Geographie, in: Pirson, F. (Ed.), Pergamon – Die Arbeiten in der Kampagne 2020. *Archäologischer Anzeiger*, pp. 50–59.
- Bellin, N., Vanacker, V., De Baets, S., 2013. Anthropogenic and climatic impact on Holocene sediment dynamics in SE Spain: A review. *Quaternary International* 308–309, 112–129.
- Benavidez, R., Jackson, B., Maxwell, D., Norton, K., 2018. A review of the (Revised) Universal Soil Loss Equation ((R)USLE): with a view to increasing its global applicability and improving soil loss estimates. *Hydrology and Earth System Sciences* 22, 6059–6086.
- Benito, G., Macklin, M.G., Zielhofer, C., Jones, A.F., Machado, M.J., 2015. Holocene flooding and climate change in the Mediterranean. *Catena* 130, 13–33.
- Berger, J.-F., Delhon, C., Magnin, F., Bonté, S., Peyric, D., Thiébault, S., Guilbert, R., Beeching, A., 2016. A fluvial record of the mid-Holocene rapid climatic changes in the middle Rhone valley (Espeluche-Lalo, France) and of their impact on Late Mesolithic and Early Neolithic societies. *Quaternary Science Reviews* 136, 66–84.
- Berger, J.-F., Shennan, S., Woodbridge, J., Palmisano, A., Mazier, F., Nuninger, L., Guillon, S., Doyen, E., Begeot, C., Andrieu-Ponel, V., Azuara, J., Bevan, A., Fyfe, R., Roberts, C.N., 2019. Holocene land cover and population dynamics in Southern France. *The Holocene* 29, 776–798.

- Berlet, O., 1911. Die Pergamenische Landschaft. Verlag von Georg Reimer, Berlin, Germany.
- Bernard, B.B., Bernard, H., Brooks, J.M., 1995. Determination of total carbon, total organic carbon and inorganic carbon in sediments. TDI-Brooks International/B&B Laboratories Inc. College Station, Texas, 1–5.
- Bes, P., Keweloh-Kaletta, A., 2022. The Intensive Survey at Çandarlı (Ancient Pitane), in: Pirson, F. (Ed.), Pergamon – Die Arbeiten in der Kampagne 2020. Archäologischer Anzeiger, pp. 287–294.
- Beven, K.J., Kirkby, M.J., 1979. A physically based, variable contributing area model of basin hydrology. *Hydrological Sciences Bulletin* 24, 43–69.
- Bini, M., Zanchetta, G., Perşoiu, A., Cartier, R., Català, A., Cacho, I., Dean, J.R., Di Rita, F., Drysdale, R.N., Finnè, M., Isola, I., Jalali, B., Lirer, F., Magri, D., Masi, A., Marks, L., Mercuri, A.M., Peyron, O., Sadori, L., Sicre, M.-A., Welc, F., Zielhofer, C., Brisset, E., 2019. The 4.2 ka BP Event in the Mediterranean region: an overview. *Climate of the Past* 15, 555–577.
- Bintliff, J., 2002. Time, process and catastrophism in the study of Mediterranean alluvial history: A review. *World Archaeology* 33, 417–435.
- Blaauw, M., 2010. Methods and code for ‘classical’ age-modelling of radiocarbon sequences. *Quaternary Geochronology* 5, 512–518.
- Black, R., Adger, W.N., Arnell, N.W., Dercon, S., Geddes, A., Thomas, D., 2011. The effect of environmental change on human migration. *Global Environmental Change* 21, S3–S11.
- Blair, T.C., McPherson, J.G., 1994. Alluvial fans and their natural distinction from rivers based on morphology, hydraulic processes, sedimentary processes, and facies assemblages. *Journal of Sedimentary Research* 64, 450–489.
- Blair, T.C., McPherson, J.G., 1999. Grain-size and textural classification of coarse sedimentary particles. *Journal of Sedimentary Research* 69, 6–19.
- Blair, T.C., McPherson, J.G., 2009. Processes and Forms of Alluvial Fans, in: Parsons, A.J., Abrahams, A.D. (Eds.), *Geomorphology of Desert Environments*, 2nd ed. Springer, Dordrecht, the Netherlands, pp. 413–467.
- Blong, R., Fryirs, K., Wood, R., King, F., Schneider, L., Dotte-Sarout, E., Fallon, S., Gillespie, R., Chen, Q., Esmay, R., 2023. Inherited age of floating charcoal fragments in a sand-bed stream, Macdonald River, NSW, Australia: Implications for radiocarbon dating of sediments. *The Holocene* 33, 1154–1159.
- Blundell, A., Dearing, J.A., Boyle, J.F., Hannam, J.A., 2009. Controlling factors for the spatial variability of soil magnetic susceptibility across England and Wales. *Earth-Science Reviews* 95, 158–188.
- Bonnier, A., Finnè, M., 2020. Climate variability and landscape dynamics in the Late Hellenistic and Roman north-eastern Peloponnese. *Antiquity* 94, 1482–1500.
- Borrelli, P., 2011. Risk Assessment of Human-induced Accelerated Soil Erosion Processes in the Intermountain Watersheds of Central Italy. A Case Study of the

Upper Turano Watershed (Latium-Abruzzi), Department of Earth Sciences. Freie Universität Berlin, Berlin, Germany, pp. 1–278.

- Borrelli, P., Domdey, C., Hoelzmann, P., Knitter, D., Panagos, P., Schütt, B., 2014. Geoarchaeological and historical implications of late Holocene landscape development in the Carseolani Mountains, central Apennines, Italy. *Geomorphology* 216, 26–39.
- Borrelli, P., Märker, M., Schütt, B., 2015. Modelling Post-Tree-Harvesting Soil Erosion and Sediment Deposition Potential in the Turano River Basin (Italian Central Apennine). *Land Degradation & Development* 26, 356–366.
- Borsi, S., Ferrara, G., Innocenti, F., Mazzuoli, R., 1972. Geochronology and petrology of recent volcanics in the eastern Aegean Sea (West Anatolia and Lesvos Island). *Bulletin Volcanologique* 36, 473–496.
- Bowman, D., 2019. *Principles of Alluvial Fan Morphology*. Springer, Dordrecht, the Netherlands.
- Boyer, P., Roberts, N., Baird, D., 2006. Holocene environment and settlement on the Çarşamba alluvial fan, south - central Turkey: Integrating geoarchaeology and archaeological field survey. *Geoarchaeology* 21, 675–698.
- Bozkurt, E., 2003. Origin of NE-trending basins in western Turkey. *Geodinamica Acta* 16, 61–81.
- Bozyiğit, C., Eriş, K.K., Sicre, M.-A., Çağatay, M.N., Uçarkuş, G., Klein, V., Gasperini, L., 2022. Middle-late Holocene climate and hydrologic changes in the Gulf of Saros (NE Aegean Sea). *Marine Geology* 443, 1–13.
- Brisset, E., Miramont, C., Guiter, F., Anthony, E.J., Tachikawa, K., Poulenard, J., Arnaud, F., Delhon, C., Meunier, J.-D., Bard, E., Suméra, F., 2013. Non-reversible geosystem destabilisation at 4200 cal. BP: Sedimentological, geochemical and botanical markers of soil erosion recorded in a Mediterranean alpine lake. *The Holocene* 23, 1863–1874.
- Brock, F., Higham, T., Ditchfield, P., Ramsey, C.B., 2010. Current Pretreatment Methods for AMS Radiocarbon Dating at the Oxford Radiocarbon Accelerator Unit (ORAU). *Radiocarbon* 52, 103–112.
- Bronk Ramsey, C., 2008. Radiocarbon Dating: Revolutions in Understanding. *Archaeometry* 50, 249–275.
- Brown, A.G., 1997. *Alluvial Geoarchaeology: Floodplain Archaeology and Environmental Change*. Cambridge University Press, Cambridge, United Kingdom.
- Brown, A.G., Walsh, K., 2017. Societal stability and environmental change: Examining the archaeology-soil erosion paradox. *Geoarchaeology* 32, 23–35.
- Brückner, H., Kelterbaum, D., Marunchak, O., Porotov, A., Vött, A., 2010. The Holocene sea level story since 7500 BP – Lessons from the Eastern Mediterranean, the Black and the Azov Seas. *Quaternary International* 225, 160–179.
- Brückner, H., Müllenhoff, M., Gehrels, R., Herda, A., Knipping, M., Vött, A., 2006. From Archipelago to Floodplain – Geographical and Ecological Changes in Miletus and

- its Environs During the Last Six Millennia (Western Anatolia, Turkey). *Zeitschrift Für Geomorphologie* 142, 63–83.
- Brunsdon, D., Thornes, J.B., 1979. Landscape Sensitivity and Change. *Transactions of the Institute of British Geographers* 4, 463–484.
- Buggle, B., Glaser, B., Hambach, U., Gerasimenko, N., Marković, S., 2011. An evaluation of geochemical weathering indices in loess–paleosol studies. *Quaternary International* 240, 12–21.
- Bulkan, Ö., Yalçın, M.N., Wilkes, H., 2018. Geochemistry of Marmara Lake sediments - Implications for Holocene environmental changes in Western Turkey. *Quaternary International* 486, 199–214.
- Bull, W.B., 1977. The alluvial-fan environment. *Progress in Physical Geography: Earth and Environment* 1, 222–270.
- Bull, W.B., 1991. *Geomorphic responses to climatic change*. The Blackburn Press, United States.
- Bull, W.B., 2007. *Tectonic Geomorphology of Mountains: A New Approach to Paleoseismology*. Wiley-Blackwell, Oxford, United Kingdom.
- Büntgen, U., Myglan, V.S., Ljungqvist, F.C., McCormick, M., Di Cosmo, N., Sigl, M., Jungclaus, J., Wagner, S., Krusic, P.J., Esper, J., Kaplan, J.O., de Vaan, M.A.C., Luterbacher, J., Wacker, L., Tegel, W., Kirilyanov, A.V., 2016. Cooling and societal change during the Late Antique Little Ice Age from 536 to around 660 AD. *Nature Geoscience* 9, 231–236.
- Butzer, K.W., 1980. Holocene alluvial sequences: Problems of dating and correlation, in: Cullingford, R.A., Davidson, D.A., Lewin, J. (Eds.), *Timescales in Geomorphology*. John Wiley & Sons, Chichester, United Kingdom, pp. 131–142.
- Butzer, K.W., 2005. Environmental history in the Mediterranean world: cross-disciplinary investigation of cause-and-effect for degradation and soil erosion. *Journal of Archaeological Science* 32, 1773–1800.
- Butzer, K.W., 2012. Collapse, environment, and society. *Proceedings of the National Academy of Sciences* 109, 3632–3639.
- Butzer, K.W., Abbott, J.T., Frederick, C.D., Lehman, P.H., Cordova, C.E., Oswald, J.F., 2008. Soil-geomorphology and “wet” cycles in the Holocene record of North-Central Mexico. *Geomorphology* 101, 237–277.
- Cartelle, V., García-Moreiras, I., Martínez-Carreño, N., Muñoz Sobrino, C., García-Gil, S., 2022. The role of antecedent morphology and changing sediment sources in the postglacial palaeogeographical evolution of an incised valley: The sedimentary record of the Ría de Arousa (NW Iberia). *Global and Planetary Change* 208, 1–21.
- Casana, J., 2008. Mediterranean valleys revisited: Linking soil erosion, land use and climate variability in the Northern Levant. *Geomorphology* 101, 429–442.
- Çelik, G., Karacakaya, R., Mete, Z., Genç, H., Bal, F., 2019. Disasters according to the red Crescent archive documents. Turkish Red Crescent and Istanbul Medeniyet University co-operation, Ankara, Türkiye.

- Charlton, R., 2007. *Fundamentals of Fluvial Geomorphology*. Routledge, Oxford, United Kingdom.
- Cheddadi, R., Palmisano, A., López-Sáez, J.A., Nourelbait, M., Zielhofer, C., Tabel, J., Rhoujjati, A., Khater, C., Woodbridge, J., Lucarini, G., Broodbank, C., Fletcher, W.J., Roberts, C.N., 2019. Human demography changes in Morocco and environmental imprint during the Holocene. *The Holocene* 29, 816–829.
- Chen, H., Wang, X., Lu, H., Van Balen, R., 2021. Anthropogenic impacts on Holocene fluvial dynamics in the Chinese Loess Plateau, an evaluation based on landscape evolution modeling. *Geomorphology* 392, 1–16.
- Chiverrell, R.C., Harvey, A.M., Foster, G.C., 2007. Hillslope gullying in the Solway Firth — Morecambe Bay region, Great Britain: Responses to human impact and/or climatic deterioration? *Geomorphology* 84, 317–343.
- Clarke, J., Brooks, N., Banning, E.B., Bar-Matthews, M., Campbell, S., Clare, L., Cremaschi, M., di Lernia, S., Drake, N., Gallinaro, M., Manning, S., Nicoll, K., Philip, G., Rosen, S., Schoop, U.-D., Tafuri, M.A., Weninger, B., Zerboni, A., 2016. Climatic changes and social transformations in the Near East and North Africa during the 'long' 4th millennium BC: A comparative study of environmental and archaeological evidence. *Quaternary Science Reviews* 136, 96–121.
- Clarke, L.E., 2015. Experimental alluvial fans: Advances in understanding of fan dynamics and processes. *Geomorphology* 244, 135–145.
- Cole, B., Smith, G., Balzter, H., 2018. Acceleration and fragmentation of CORINE land cover changes in the United Kingdom from 2006–2012 detected by Copernicus IMAGE2012 satellite data. *International Journal of Applied Earth Observation and Geoinformation* 73, 107–122.
- Collins, P.E.F., Rust, D.J., Salih Bayraktutan, M., Turner, S.D., 2005. Fluvial stratigraphy and palaeoenvironments in the Pasinler Basin, eastern Turkey. *Quaternary International* 140–141, 121–134.
- Connor, S.E., Vanni re, B., Colombaroli, D., Anderson, R.S., Carri n, J.S., Ejarque, A., Gil Romera, G., Gonz lez-Samp riz, P., Hofer, D., Morales-Molino, C., Revelles, J., Schneider, H., van der Knaap, W.O., van Leeuwen, J.F.N., Woodbridge, J., 2019. Humans take control of fire-driven diversity changes in Mediterranean Iberia's vegetation during the mid–late Holocene. *The Holocene* 29, 886–901.
- Conrad, O., Bechtel, B., Bock, M., Dietrich, H., Fischer, E., Gerlitz, L., Wehberg, J., Wichmann, V., B hner, J., 2015. System for Automated Geoscientific Analyses (SAGA) v. 2.1.4. *Geoscientific Model Development* 8, 1991–2007.
- Constante, A., Pe a, J.L., Mu oz, A., Picazo, J., 2010. Climate and anthropogenic factors affecting alluvial fan development during the late Holocene in the central Ebro Valley, northeast Spain. *The Holocene* 21, 275–286.
- Conze, A., 1912. *Altert mer von Pergamon (Band I, Text 1): Stadt und Landschaft*. Verlag von Georg Reimer, Berlin, Germany.
- Coulthard, T.J., Macklin, M.G., Kirkby, M.J., 2002. A cellular model of Holocene upland river basin and alluvial fan evolution. *Earth Surface Processes and Landforms* 27, 269–288.

- Crema, E.R., Bevan, A., 2021. Inference from Large Sets of Radiocarbon Dates: Software and Methods. *Radiocarbon* 63, 23–39.
- Cremaschi, M., Mercuri, A.M., Torri, P., Florenzano, A., Pizzi, C., Marchesini, M., Zerboni, A., 2016. Climate change versus land management in the Po Plain (Northern Italy) during the Bronze Age: New insights from the VP/VG sequence of the Terramara Santa Rosa di Poviglio. *Quaternary Science Reviews* 136, 153–172.
- Croudace, I.W., Rothwell, R.G., 2015. *Micro-XRF Studies of Sediment Cores: Applications of a non-destructive Tool for the Environmental Sciences*. Springer Dordrecht, the Netherlands.
- Danacıoğlu, S., Tağıl, Ş., 2017. Evaluation of the erosion risk by using the RUSLE model in Bakırçay basin (in Turkish). *Balıkesir Üniversitesi Sosyal Bilimler Enstitüsü Dergisi* 20, 1–18.
- Danacıoğlu, S., Tağıl, Ş., 2019. Watershed management based on ecological risk characterization in Bakırçay watershed. *Fresenius Environmental Bulletin* 28, 62–76.
- Das, S., 2018. Geomorphic characteristics of a bedrock river inferred from drainage quantification, longitudinal profile, knickzone identification and concavity analysis: a DEM-based study. *Arabian Journal of Geosciences* 11, 1–13.
- Dean, W.E., 1974. Determination of carbonate and organic matter in calcareous sediments and sedimentary rocks by loss on ignition; comparison with other methods. *Journal of Sedimentary Research* 44, 242–248.
- Dearing, J.A., 1994. *Environmental Magnetic Susceptibility: Using the Bartington MS2 System*. Chi Publishing, Kenilworth, United Kingdom.
- Dearing, J.A., 2008. Landscape change and resilience theory: a palaeoenvironmental assessment from Yunnan, SW China. *The Holocene* 18, 117–127.
- Dearing, J.A., Dann, R., Hay, K., Lees, J., Loveland, P., Maher, B.A., O'grady, K., 1996. Frequency-dependent susceptibility measurements of environmental materials. *Geophysical Journal International* 124, 228–240.
- Degroot, D., Anchukaitis, K.J., Tierney, J.E., Riede, F., Manica, A., Moesswilde, E., Gauthier, N., 2022. The history of climate and society: a review of the influence of climate change on the human past. *Environmental Research Letters* 17, 1–35.
- Demirci, A., Karaburun, A., 2012. Estimation of soil erosion using RUSLE in a GIS framework: a case study in the Buyukcekmece Lake watershed, northwest Turkey. *Environmental Earth Sciences* 66, 903–913.
- Di Rita, F., Magri, D., 2009. Holocene drought, deforestation and evergreen vegetation development in the central Mediterranean: a 5500 year record from Lago Alimini Piccolo, Apulia, southeast Italy. *The Holocene* 19, 295–306.
- Di Rita, F., Michelangeli, F., Celant, A., Magri, D., 2022. Sign-switching ecological changes in the Mediterranean Basin at 4.2 ka BP. *Global and Planetary Change* 208, 1–8.
- Dikau, R., Eibisch, K., Eichel, J., Meßenzehl, K., Schlummer-Held, M., 2019.

- Geomorphologische Systeme und Prozesse, in: Dikau, R., Eibisch, K., Eichel, J., Meßenzehl, K., Schlummer-Held, M. (Eds.), *Geomorphologie*. Springer Spektrum, Berlin, Heidelberg, Germany, pp. 33–60.
- Dill, H.G., Dohrmann, R., Kaufhold, S., Çiçek, G., 2015. Mineralogical, chemical and micromorphological studies of the argillic alteration zone of the epithermal gold deposit Ovacik, Western Turkey: Tools for applied and genetic economic geology. *Journal of Geochemical Exploration* 148, 105–127.
- Dinelli, E., Tateo, F., Summa, V., 2007. Geochemical and mineralogical proxies for grain size in mudstones and siltstones from the Pleistocene and Holocene of the Po River alluvial plain, Italy. *Geological Society of America* 420, 25–36.
- Doğan, T., İlkmen, E., Kulak, F., 2021. A new national 1 MV AMS laboratory at TÜBİTAK MRC in Turkey. *Nuclear Instruments and Methods in Physics Research Section B: Beam Interactions with Materials and Atoms* 509, 48–54.
- Dorn, R.I., 1994. The Role of Climatic Change in Alluvial Fan Development, in: Abrahams, A.D., Parsons, A.J. (Eds.), *Geomorphology of Desert Environments*. Chapman & Hall, London, United Kingdom, pp. 593–615.
- Dotterweich, M., 2008. The history of soil erosion and fluvial deposits in small catchments of central Europe: Deciphering the long-term interaction between humans and the environment — A review. *Geomorphology* 101, 192–208.
- Dotterweich, M., 2013. The history of human-induced soil erosion: Geomorphic legacies, early descriptions and research, and the development of soil conservation—A global synopsis. *Geomorphology* 201, 1–34.
- Dreibrodt, S., Lubos, C., Lomax, J., Sipos, G., Schroedter, T., Nelle, O., 2014. Holocene landscape dynamics at the tell Arslantepe, Malatya, Turkey – Soil erosion, buried soils and settlement layers, slope and river activity in a middle Euphrates catchment. *The Holocene* 24, 1351–1368.
- Dusar, B., 2011. Late Holocene sediment dynamics in a Mediterranean mountain environment. *Katholieke Universiteit Leuven*, pp. 1–259.
- Dusar, B., Verstraeten, G., D'Haen, K., Bakker, J., Kaptijn, E., Waelkens, M., 2012. Sensitivity of the Eastern Mediterranean geomorphic system towards environmental change during the Late Holocene: a chronological perspective. *Journal of Quaternary Science* 27, 371–382.
- Dusar, B., Verstraeten, G., Notebaert, B., Bakker, J., 2011. Holocene environmental change and its impact on sediment dynamics in the Eastern Mediterranean. *Earth-Science Reviews* 108, 137–157.
- Eastwood, W.J., Leng, M.J., Roberts, N., Davis, B., 2007. Holocene climate change in the eastern Mediterranean region: a comparison of stable isotope and pollen data from Lake Gölhisar, southwest Turkey. *Journal of Quaternary Science* 22, 327–341.
- Eastwood, W.J., Roberts, N., Lamb, H.F., 1998. Palaeoecological and archaeological evidence for human occupation in southwest Turkey: the Beyşehir Occupation Phase. *Anatolian Studies* 48, 69–86.
- Efe, R., 1996. The ecological conditions of the natural vegetation in Yuntdağ and its

environs. *Türk Coğrafya Dergisi* 31, 77–114.

- Emre, Ö., Doğan, A., 2010. 1:250,000 Scale Active Fault Map Series of Turkey, Ayvalık (NJ 35-2) Quadrangle. Serial number: 2. General Directorate of Mineral Research and Exploration, Ankara, Türkiye.
- Emre, Ö., Doğan, A., Özalp, S., 2011a. 1:250.000 Scale Active Fault Map Series of Turkey, Balıkesir (NJ 35-3) Quadrangle. Serial number: 4. General Directorate of Mineral Research and Exploration, Ankara, Türkiye.
- Emre, Ö., Özalp, S., 2011. 1:250,000 Scale Active Fault Map Series of Turkey, Urla (NJ 35-6) Quadrangle. Serial number: 5. General Directorate of Mineral Research and Exploration, Ankara, Türkiye.
- Emre, Ö., Özalp, S., Dogan, A., Özaksoy, V., Yildirim, C., Göktas, F., 2005. İzmir yakın Çevresinin diri fayları ve deprem potansiyelleri (Active faults and earthquake potential in the İzmir region). General Directorate of Mineral Research and Exploration, Ankara, Türkiye, pp. 1–80.
- Emre, Ö., Özalp, S., Duman, T.Y., 2011b. 1:250,000 Scale Active Fault Map Series of Turkey, İzmir (NJ 35-7) Quadrangle. Serial number: 6. General Directorate of Mineral Research and Exploration, Ankara, Türkiye.
- Erlat, E., 2007. Climatic conditions in Altınova and the Madra River Delta, in: Lambrianides, K., Spencer, N. (Eds.), *The Madra River Delta: Regional Studies on the Aegean Coast of Turkey 1: Environment, Society and Community from Prehistory to the Present*. The British Institute at Ankara, London, United Kingdom, pp. 51–59.
- Faust, D., Wolf, D., 2017. Interpreting drivers of change in fluvial archives of the Western Mediterranean - A critical view. *Earth-Science Reviews* 174, 53–83.
- Faust, D., Zielhofer, C., Escudero, R.B., Olmo, F.D.d., 2004. High-resolution fluvial record of late Holocene geomorphic change in northern Tunisia: climatic or human impact? *Quaternary Science Reviews* 23, 1757–1775.
- Fediuk, A., Wilken, D., Wunderlich, T., Rabbel, W., Seeliger, M., Laufer, E., Pirson, F., 2019. Marine seismic investigation of the ancient Kane harbour bay, Turkey. *Quaternary International* 511, 43–50.
- Feuser, S., Mania, U., Pirson, F., 2020. Stadtentwicklung und städtische Physiognomie im Kontext von Mikroregion oder Kulturlandschaft? Das Beispiel Elaia, in: Mohr, E.-M., Rheidt, K., Arslan, N. (Eds.), *Urbanism and Architecture in Ancient Aiolis. (Proceedings of the International Conference from 7th–9th April 2017 in Çanakkale)*. Asia-Minor-Studien 95. (Bonn 2020), Dr. Rudolf Habelt GMBH, Bonn, pp. 203–216.
- Finné, M., Holmgren, K., Sundqvist, H.S., Weiberg, E., Lindblom, M., 2011. Climate in the eastern Mediterranean, and adjacent regions, during the past 6000 years – A review. *Journal of Archaeological Science* 38, 3153–3173.
- Finné, M., Woodbridge, J., Labuhn, I., Roberts, C.N., 2019. Holocene hydro-climatic variability in the Mediterranean: A synthetic multi-proxy reconstruction. *The Holocene* 29, 847–863.
- Fletcher, W.J., Zielhofer, C., 2013. Fragility of Western Mediterranean landscapes during Holocene Rapid Climate Changes. *Catena* 103, 16–29.

- Flohr, P., Fleitmann, D., Matthews, R., Matthews, W., Black, S., 2016. Evidence of resilience to past climate change in Southwest Asia: Early farming communities and the 9.2 and 8.2 ka events. *Quaternary Science Reviews* 136, 23–39.
- Florenzano, A., Mercuri, A.M., Rinaldi, R., Rattighieri, E., Fornaciari, R., Messori, R., Arru, L., 2017. The Representativeness of *Olea* Pollen from Olive Groves and the Late Holocene Landscape Reconstruction in Central Mediterranean. *Frontiers in Earth Science* 5, 1–11.
- Fowler, A.J., Gillespie, R., Hedges, R.E.M., 1986. Radiocarbon Dating of Sediments. *Radiocarbon* 28, 441–450.
- Francke, A., Dosseto, A., Panagiotopoulos, K., Leicher, N., Lacey, J.H., Kyrikou, S., Wagner, B., Zanchetta, G., Kouli, K., Leng, M.J., 2019. Sediment residence time reveals Holocene shift from climatic to vegetation control on catchment erosion in the Balkans. *Global and Planetary Change* 177, 186–200.
- Fryirs, K., 2013. (Dis)Connectivity in catchment sediment cascades: a fresh look at the sediment delivery problem. *Earth Surface Processes and Landforms* 38, 30–46.
- Fryirs, K.A., Brierley, G.J., Preston, N.J., Kasai, M., 2007. Buffers, barriers and blankets: The (dis)connectivity of catchment-scale sediment cascades. *Catena* 70, 49–67.
- Fuchs, M., 2007. An assessment of human versus climatic impacts on Holocene soil erosion in NE Peloponnese, Greece. *Quaternary Research* 67, 349–356.
- Fuchs, M., Lang, A., 2009. Luminescence dating of hillslope deposits—A review. *Geomorphology* 109, 17–26.
- Fuchs, M., Lang, A., Wagner, G.A., 2004. The history of Holocene soil erosion in the Phlious Basin, NE Peloponnese, Greece, based on optical dating. *The Holocene* 14, 334–345.
- Fyfe, R.M., Woodbridge, J., Palmisano, A., Bevan, A., Shennan, S., Burjachs, F., Legarra Herrero, B., García Puchol, O., Carrión, J.-S., Revelles, J., Roberts, C.N., 2019. Prehistoric palaeodemographics and regional land cover change in eastern Iberia. *The Holocene* 29, 799–815.
- García-Ruiz, J.M., Nadal-Romero, E., Lana-Renault, N., Beguería, S., 2013. Erosion in Mediterranean landscapes: Changes and future challenges. *Geomorphology* 198, 20–36.
- Geeson, N.A., Brandt, C.J., Thornes, J.B., 2002. *Mediterranean Desertification: A Mosaic of Processes and Responses* John Wiley & Sons, London, United Kingdom.
- Gehrke, H.-J., 2014. A Brief History of Pergamon, in: Scholl, A., Pirson, F. (Eds.), *Pergamon – Anadolu'da Hellenistik Bir Başkent / A Hellenistic Capital in Anatolia*. Yapi Kredi Yayinlari, Istanbul, Türkiye, pp. 122–141.
- Ghilardi, M., Cordier, S., Carozza, J.-M., Psomiadis, D., Guilaine, J., Zomeni, Z., Demory, F., Delanghe-Sabatier, D., Vella, M.-A., Bony, G., Morhange, C., 2015. The Holocene fluvial history of the Tremithos river (south central Cyprus) and its linkage to archaeological records. *Environmental Archaeology* 20, 184–201.
- Giraudi, C., 2018. The climate-triggered western shift of the confluence between the Dora

- Baltea and Po rivers (north-western Italy) during the late Holocene. *The Holocene* 29, 432–444.
- Girma, R., Gebre, E., 2020. Spatial modeling of erosion hotspots using GIS-RUSLE interface in Omo-Gibe river basin, Southern Ethiopia: implication for soil and water conservation planning. *Environmental Systems Research* 9, 1–14.
- Gladfelter, B.G., 1977. Geoarchaeology: The Geomorphologist and Archaeology. *American Antiquity* 42, 519–538.
- Glais, A., Lespez, L., Vanni re, B., L pez-S ez, J.A., 2017. Human-shaped landscape history in NE Greece. A palaeoenvironmental perspective. *Journal of Archaeological Science: Reports* 15, 405–422.
- Gogou, A., Triantaphyllou, M., Xoplaki, E., Izdebski, A., Parinos, C., Dimiza, M., Bouloubassi, I., Luterbacher, J., Kouli, K., Martrat, B., Toreti, A., Fleitmann, D., Rousakis, G., Kaberi, H., Athanasiou, M., Lykousis, V., 2016. Climate variability and socio-environmental changes in the northern Aegean (NE Mediterranean) during the last 1500 years. *Quaternary Science Reviews* 136, 209–228.
- Goldberg, P., Macphail, R.I., 2006. *Practical and Theoretical Geoarchaeology*. Blackwell Publishing, Malden, United States.
- Goldberg, P., Mandel, R.D., Holliday, V.T., Sternberg, R.S., 2017. Encyclopedia of Geoarchaeology, in: Gilbert, A.S. (Ed.), *Encyclopedia of Earth Sciences Series*. Springer Reference, Dordrecht, the Netherlands, pp. 1–1046.
- Goldewijk, K.K., Beusen, A., Janssen, P., 2010. Long-term dynamic modeling of global population and built-up area in a spatially explicit way: HYDE 3.1. *The Holocene* 20, 565–573.
- Goodchild, H., 2007. Modelling Roman agricultural production in the middle Tiber valley, central Italy, institute of Archaeology and Antiquity, School of Historical Studies. The University of Birmingham, Birmingham, United Kingdom, pp. 1–453.
- Goodchild, H., 2013. Agriculture and the Environment of Republican Italy, in: Evans, J.D. (Ed.). Blackwell Publishing Ltd, pp. 198–213.
- Goudie, A., 2004. Encyclopedia of Geomorphology, in: Goudie, A. (Ed.), *Encyclopedia of Geomorphology*. Routledge, London, United Kingdom, pp. 272–276.
- GRASS Development Team, 2020. Geographic Resources Analysis Support System (GRASS) Software, Version 7.8, Open Source Geospatial Foundation.
- Grove, A.T., Rackham, O., 2003. *The Nature of Mediterranean Europe: An Ecological History*. Yale University Press, New Haven, United States.
- Guisan, A., Weiss, S.B., Weiss, A.D., 1999. GLM versus CCA spatial modeling of plant species distribution. *Plant Ecology* 143, 107–122.
- G lersoy, A.E., 2008. Bakir ay havzası'nda dođal ortam kořullari ile arazi kullanimi arasındaki iliřkiler. Dokuz Eyl l  niversitesi, İzmir, T rkiye, pp. 1–494.
- G nther, G., Clemen, T., Duttmann, R., Sch tt, B., Knitter, D., 2021. Of Animal Husbandry and Food Production—A First Step towards a Modular Agent-Based Modelling

Platform for Socio-Ecological Dynamics. *Land* 10, 1–25.

- Gutiérrez, F., Gutiérrez, M., 2016. Granite Landforms, in: Gutiérrez, F., Gutiérrez, M. (Eds.), *Landforms of the Earth*. Springer, Cham, Switzerland, pp. 103–109.
- Hack, J., 1957. *Studies of longitudinal stream profiles in Virginia and Maryland*. U.S. Geological Survey Professional Paper 294-B, 1–59.
- Hancock, C.L., McKay, N.P., Erb, M.P., Kaufman, D.S., Routson, C.R., Ivanovic, R.F., Gregoire, L.J., Valdes, P., 2023. Global Synthesis of Regional Holocene Hydroclimate Variability Using Proxy and Model Data. *Paleoceanography and Paleoclimatology* 38, 1–19.
- Harmon, R.S., Doe, W.W., 2001. *Landscape Erosion and Evolution Modeling*. Springer New York, United States.
- Harris, I., Jones, P.D., Osborn, T.J., Lister, D.H., 2014. Updated high-resolution grids of monthly climatic observations – the CRU TS3.10 Dataset. *International Journal of Climatology* 34, 623–642.
- Hazell, C.J., Pound, M.J., Hocking, E.P., 2022. High-resolution Bronze Age palaeoenvironmental change in the Eastern Mediterranean: exploring the links between climate and societies. *Palynology* 46, 1–20.
- Heiri, O., Lotter, A.F., Lemcke, G., 2001. Loss on ignition as a method for estimating organic and carbonate content in sediments: reproducibility and comparability of results. *Journal of Paleolimnology* 25, 101–110.
- Hengl, T., Mendes de Jesus, J., Heuvelink, G.B., Ruiperez Gonzalez, M., Kilibarda, M., Blagotic, A., Shangguan, W., Wright, M.N., Geng, X., Bauer-Marschallinger, B., Guevara, M.A., Vargas, R., MacMillan, R.A., Batjes, N.H., Leenaars, J.G., Ribeiro, E., Wheeler, I., Mantel, S., Kempen, B., 2017. SoilGrids250m: Global gridded soil information based on machine learning. *PLoS One* 12, 1–40.
- Hengl, T., Reuter, H.I., 2009. Geomorphometry – Concepts, Software, Applications, in: Hartemink, A.E., McBratney, A.B. (Eds.), *Developments in Soil Science*. Elsevier, Amsterdam, the Netherlands, pp. 1–796.
- Herzschuh, U., Böhmer, T., Li, C., Chevalier, M., Hébert, R., Dallmeyer, A., Cao, X., Bigelow, N.H., Nazarova, L., Novenko, E.Y., Park, J., Peyron, O., Rudaya, N.A., Schlütz, F., Shumilovskikh, L.S., Tarasov, P.E., Wang, Y., Wen, R., Xu, Q., Zheng, Z., 2023. LegacyClimate 1.0: a dataset of pollen-based climate reconstructions from 2594 Northern Hemisphere sites covering the last 30 kyr and beyond. *Earth System Science Data* 15, 2235–2258.
- Hofierka, J., Mitášová, H., Neteler, M., 2009. Geomorphometry in GRASS GIS, *Geomorphometry: Concepts, Software, Applications*. Developments in Soil Science. Elsevier, pp. 387–410.
- Hökerek, S., Özçelik, O., 2015. Organic Facies Characteristics of the Miocene Soma Formation (Lower Lignite Succession-KM2), Soma Coal Basin, Western Turkey. *Energy Procedia* 76, 27–32.
- Horejs, B., 2010a. Bronzezeitliche Besiedlungsmuster im Kaikostal. Interpretationen erster Surveyergebnisse im Umland von Pergamon (Türkei) (in German), in: Horejs,

- B., Kienlin, T.L. (Eds.), *Siedlung und Handwerk - Studien zu sozialen Kontexten in der Bronzezeit*. Dr. Rudolf Habelt, Bonn, Germany, pp. 47–67.
- Horejs, B., 2010b. Yeni Yeldeğirmen-tepe, in: Pirson, F. (Ed.), *Pergamon-Bericht über die Arbeiten in der Kampagne 2009*. *Archäologischer Anzeiger*, pp. 164–168.
- Horejs, B., 2011a. Bergama and the Bakırçay Valley in Prehistory, in: Önen, E., Mutluer, M., Çetin, N. (Eds.), *International Bergama Symposium, Bergama, Türkiye*, pp. 48–65.
- Horejs, B., 2011b. Prähistorische Surveys am Yeni Yeldeğirmen-tepe und im Umland von Pergamon, in: Pirson, F. (Ed.), *Pergamon - Bericht über die Arbeiten in der Kampagne 2010*. *Archäologischer Anzeiger*, pp. 146–150.
- Horejs, B., 2014. Pergamon and the Kaikos Valley in Prehistoric Times, in: Scholl, A., Pirson, F. (Eds.), *Pergamon – Anadolu’da Hellenistik Bir Başkent / A Hellenistic Capital in Anatolia*. Yapi Kredi Yayinlari, Istanbul, Türkiye, pp. 106–119.
- Huggett, R.J., 2017. *Fundamentals of Geomorphology*, fourth edition ed. Routledge, Milton Park, Abingdon, Oxon ; New York, NY.
- Hughes, R., Weiberg, E., Bonnier, A., Finné, M., Kaplan, J., 2018. Quantifying Land Use in Past Societies from Cultural Practice and Archaeological Data. *Land* 7, 1–21.
- İnci, U., 2002. Depositional evolution of Miocene coal successions in the Soma coalfield, western Turkey. *International Journal of Coal Geology* 51, 1–29.
- Izdebski, A., Holmgren, K., Weiberg, E., Stocker, S.R., Büntgen, U., Florenzano, A., Gogou, A., Leroy, S.A.G., Luterbacher, J., Martrat, B., Masi, A., Mercuri, A.M., Montagna, P., Sadori, L., Schneider, A., Sicre, M.-A., Triantaphyllou, M., Xoplaki, E., 2016a. Realising consilience: How better communication between archaeologists, historians and natural scientists can transform the study of past climate change in the Mediterranean. *Quaternary Science Reviews* 136, 5–22.
- Izdebski, A., Pickett, J., Roberts, N., Waliszewski, T., 2016b. The environmental, archaeological and historical evidence for regional climatic changes and their societal impacts in the Eastern Mediterranean in Late Antiquity. *Quaternary Science Reviews* 136, 189–208.
- Jahn, R., Blume, H.-P., Asio, V.B., Spaargaren, O., Schad, P., 2006. *Guidelines for soil description*, 4th ed. FAO, Rome, Italy.
- Jalut, G., Dedoubat, J.J., Fontugne, M., Otto, T., 2009. Holocene circum-Mediterranean vegetation changes: Climate forcing and human impact. *Quaternary International* 200, 4–18.
- Jasiewicz, J., Stepinski, T.F., 2013. Geomorphons — a pattern recognition approach to classification and mapping of landforms. *Geomorphology* 182, 147–156.
- Jouffroy-Bapicot, I., Pedrotta, T., Debret, M., Field, S., Sulpizio, R., Zanchetta, G., Sabatier, P., Roberts, N., Tinner, W., Walsh, K., Vannièrè, B., 2021. Olive groves around the lake. A ten-thousand-year history of a Cretan landscape (Greece) reveals the dominant role of humans in making this Mediterranean ecosystem. *Quaternary Science Reviews* 267, 1–24.

- Kaniewski, D., Paulissen, E., De Laet, V., Dossche, K., Waelkens, M., 2007. A high-resolution Late Holocene landscape ecological history inferred from an intramontane basin in the Western Taurus Mountains, Turkey. *Quaternary Science Reviews* 26, 2201–2218.
- Kapur, S., Akça, E., Günal, H., 2017. *The Soils of Turkey*. Springer, Cham, Switzerland.
- Karacik, Z., Yilmaz, Y., Pearce, J., 2007. The Dikili-Çandarlı Volcanics, Western Turkey: Magmatic Interactions as Recorded by Petrographic and Geochemical Features. *Turkish Journal of Earth Sciences* 16, 493–522.
- Karaoğlu, Ö., 2014. Tectonic controls on the Yamanlar volcano and Yuntdağı volcanic region, western Turkey: Implications for an incremental deformation. *Journal of Volcanology and Geothermal Research* 274, 16–33.
- Karayiğit, A.İ., Littke, R., Querol, X., Jones, T., Oskay, R.G., Christanis, K., 2017. The Miocene coal seams in the Soma Basin (W. Turkey): Insights from coal petrography, mineralogy and geochemistry. *International Journal of Coal Geology* 173, 110–128.
- Kassambara, A., 2023. ggpubr: 'ggplot2' Based Publication Ready Plots. R package version 0.6.0, <<https://CRAN.R-project.org/package=ggpubr>>.
- Kaya, O., Ünay, E.n., Göktaş, F.k., Saraç, G., 2007. Early Miocene stratigraphy of central west Anatolia, Turkey: implications for the tectonic evolution of the eastern Aegean area. *Geological Journal* 42, 85–109.
- Kayan, İ., 1988. Late Holocene sea-level changes on the western Anatolian coast. *Palaeogeography, Palaeoclimatology, Palaeoecology* 68, 205–218.
- Kayan, İ., 1997. Bronze Age Regression and Change of Sedimentation on The Aegean Coastal Plains of Anatolia (Turkey), in: Dalfes, H.N., Kukla, G., Weiss, H. (Eds.), *Third Millennium BC Climate Change and Old World Collapse*. Springer, Berlin, Heidelberg, Germany, pp. 431–450.
- Kayan, İ., 1999. Holocene stratigraphy and geomorphological evolution of the Aegean coastal plains of Anatolia. *Quaternary Science Reviews* 18, 541–548.
- Kayan, İ., 2019. Landscape Development and Changing Environment of Troia (North-western Anatolia), in: Kuzucuoğlu, C., Çiner, A., Kazancı, N. (Eds.), *Landscapes and Landforms of Turkey*. Springer, Cham, Switzerland, pp. 277–291.
- Kayan, İ., Vardar, S., 2007a. Geomorphological formation and development of the delta plain of the Madra River, in: Lambrianides, K., Spencer, N. (Eds.), *The Madra River Delta: Regional Studies on the Aegean Coast of Turkey 1: Environment, Society and Community from Prehistory to the Present*. The British Institute at Ankara, London, United Kingdom, pp. 23–30.
- Kayan, İ., Vardar, S., 2007b. The physical geography of the Madra River Delta, in: Lambrianides, K., Spencer, N. (Eds.), *The Madra River Delta: Regional Studies on the Aegean Coast of Turkey 1: Environment, Society and Community from Prehistory to the Present*. The British Institute at Ankara, London, United Kingdom, pp. 9–23.
- Kennett, D.J., Masson, M., Lope, C.P., Serafin, S., George, R.J., Spencer, T.C., Hoggarth, J.A., Culleton, B.J., Harper, T.K., Pruffer, K.M., Milbrath, S., Russell, B.W., Gonzalez,

- E.U., McCool, W.C., Aquino, V.V., Paris, E.H., Curtis, J.H., Marwan, N., Zhang, M., Asmerom, Y., Polyak, V.J., Carolin, S.A., James, D.H., Mason, A.J., Henderson, G.M., Brenner, M., Baldini, J.U.L., Breitenbach, S.F.M., Hodell, D.A., 2022. Drought-Induced Civil Conflict Among the Ancient Maya. *Nature Communications* 13, 1–10.
- Kidder, T.R., Adelsberger, K.A., Arco, L.J., Schilling, T.M., 2008. Basin-scale reconstruction of the geological context of human settlement: an example from the lower Mississippi Valley, USA. *Quaternary Science Reviews* 27, 1255–1270.
- Kirchhoff, M., Engelmann, L., Zimmermann, L.L., Seeger, M., Marzloff, I., Ait Hssaine, A., Ries, J.B., 2019. Geomorphodynamics in Argan Woodlands, South Morocco. *Water* 11, 1–25.
- Knipping, M., Müllenhoff, M., Brückner, H., 2007. Human induced landscape changes around Bafa Gölü (western Turkey). *Vegetation History and Archaeobotany* 17, 365–380.
- Knitter, D., 2013. *Central Places and the Environment: Investigations of an Interdependent Relationship*, Department of Earth Sciences. Freie Universität Berlin, Berlin, Germany, pp. 59–65.
- Knitter, D., Blum, H., Horejs, B., Nakoinz, O., Schütt, B., Meyer, M., 2013. Integrated centrality analysis: A diachronic comparison of selected Western Anatolian locations. *Quaternary International* 312, 45–56.
- Kobes, v.J., 1999. *Fremdes Getreide. Beobachtungen zum Problem der Getreideversorgung in der kaiserzeitlichen Provinz Asia, Laverna: Beiträge zur Wirtschafts- und Sozialgeschichte der Alten Welt*. St. Katharinen: Scripta Mercaturae-Verl, Marburg, Germany, pp. 81–98.
- Kock, S.T., Schitteck, K., Lücke, A., Maldonado, A., Mächtle, B., 2019. Geomorphodynamics as recorded in a high-Andean cushion peatland of the western Chilean Central Andes (27° S) during the last 1800 cal. yr BP. *Zeitschrift für Geomorphologie, Supplementary Issues* 62, 183–205.
- Kökten, K., 1949. 1949 yılı tarih öncesi araştırmaları hakkında kısa rapor. *Bellekten* 13, 811–831.
- Kondolf, M., Piégay, H., 2011. *Geomorphology and Society*, in: Gregory, K.J., Goudie, A.S. (Eds.), *The SAGE Handbook of Geomorphology*. SAGE Publications, London, United Kingdom, pp. 105–118.
- Kosmas, C., Danalatos, N., Cammeraat, L.H., Chabart, M., Diamantopoulos, J., Farand, R., Gutierrez, L., Jacob, A., Marques, H., Martinez-Fernandez, J., Mizara, A., Moustakas, N., Nicolau, J.M., Oliveros, C., Pinna, G., Puddu, R., Puigdefabregas, J., Roxo, M., Simao, A., Stamou, G., Tomasi, N., Usai, D., Vacca, A., 1997. The effect of land use on runoff and soil erosion rates under Mediterranean conditions. *Catena* 29, 45–59.
- Kovda, I., Lynn, W., Williams, D., Chichagova, O., 2001. Radiocarbon Age of Vertisols and Its Interpretation Using Data on Gilgai Complex in the North Caucasus. *Radiocarbon* 43, 603–610.
- Kraft, J.C., Bückner, H., Kayan, İ., Engelmann, H., 2007. The geographies of Ancient Ephesus and the Artemision in Anatolia. *Geoarchaeology* 22, 121–149.

- Kraft, J.C., Kayan, İ., Erol, O., 1980. Geomorphic Reconstructions in the Environs of Ancient Troy. *Science* 209, 776–782.
- Kraft, J.C., Rapp, G., Brückner, H., Kayan, İ., 2011. Results of the struggle at ancient Ephesus: natural processes 1, human intervention 0. *Geological Society, London, Special Publications* 352, 27–36.
- Kraft, J.C., Rapp, G., Kayan, İ., Luce, J.V., 2003. Harbor areas at ancient Troy: Sedimentology and geomorphology complement Homer's Iliad. *Geology* 31, 163–166.
- Kuzucuoğlu, C., 1995. River response to Quaternary tectonics with examples from northwestern Anatolia, Turkey, in: Lewin, J., Macklin, M.G., Woodward, J.C. (Eds.), *Mediterranean Quaternary river environments*. Balkema, Rotterdam, the Netherlands, pp. 45–53.
- Kuzucuoğlu, C., Celâl Şengör, A.M., Çiner, A., 2019a. The Tectonic Control on the Geomorphological Landscapes of Turkey, in: Kuzucuoğlu, C., Çiner, A., Kazancı, N. (Eds.), *Landscapes and Landforms of Turkey*. Springer, Cham, Switzerland, pp. 17–40.
- Kuzucuoğlu, C., Çiner, A., Kazancı, N., 2019b. The Geomorphological Regions of Turkey, in: Kuzucuoğlu, C., Çiner, A., Kazancı, N. (Eds.), *Landscapes and Landforms of Turkey*. Springer, Cham, Switzerland, pp. 41–178.
- Kuzucuoğlu, C., Dörfler, W., Kunesch, S., Goupille, F., 2011. Mid- to late-Holocene climate change in central Turkey: The Tecer Lake record. *The Holocene* 21, 173–188.
- Laabs, J., Knitter, D., 2021. How Much Is Enough? First Steps to a Social Ecology of the Pergamon Microregion. *Land* 10, 1–19.
- Lague, D., 2014. The stream power river incision model: evidence, theory and beyond. *Earth Surface Processes and Landforms* 39, 38–61.
- Lambrianides, K., Spencer, N., 2007. *The Madra River Delta: Regional Studies on the Aegean Coast of Turkey 1: Environment, Society and Community from Prehistory to the Present*. The British Institute at Ankara, London, United Kingdom.
- Lane, S.N., 2014. Good practice in authoring manuscripts on geomorphology. *Earth Surface Processes and Landforms* 39, 126–132.
- Lang, A., Hönscheidt, S., 1999. Age and source of colluvial sediments at Vaihingen–Enz, Germany. *Catena* 38, 89–107.
- Langgut, D., Cheddadi, R., Carrión, J.S., Cavanagh, M., Colombaroli, D., Eastwood, W.J., Greenberg, R., Litt, T., Mercuri, A.M., Miebach, A., Roberts, C.N., Woldring, H., Woodbridge, J., 2019. The origin and spread of olive cultivation in the Mediterranean Basin: The fossil pollen evidence. *The Holocene* 29, 902–922.
- Laufer, E., 2015. Der neue Survey auf der Kane-Halbinsel (Kane Regional Harbour Survey), in: Pirson, F. (Ed.), *Pergamon – Bericht über die Arbeiten der Kampagne 2014*. Archäologischer Anzeiger, Deutsches Archäologisches Institut/German Archaeological Institute, Berlin, Germany, pp. 139–150.

- Lawrence, D., Palmisano, A., de Gruchy, M.W., 2021. Collapse and continuity: A multi-proxy reconstruction of settlement organization and population trajectories in the Northern Fertile Crescent during the 4.2kya Rapid Climate Change event. *PLoS One* 16, 1–20.
- Leigh, D.S., Gragson, T.L., Lefebvre, B., 2019. Rapid alluvial sedimentation aided expansion of Moissac during the High Middle Ages along the Tarn River in southern France. *Geomorphology* 331, 49–58.
- Lespez, L., 2003. Geomorphic responses to long-term land use changes in Eastern Macedonia (Greece). *CATENA* 51, 181–208.
- Lionello, P., 2012. *The Climate of the Mediterranean Region: From the Past to the Future*, 1st ed. Elsevier London, United Kingdom.
- Lolling, H., 1879. Atarneus. *Mitteilungen des Deutschen Archäologischen Instituts Athenische Abteilung* 4, 1–10.
- Lü, J., Mo, D., Zhuang, Y., Jiang, J., Liao, Y., Lu, P., Ren, X., Feng, J., 2019. Holocene geomorphic evolution and settlement distribution patterns in the mid-lower Fen River basins, China. *Quaternary International* 521, 16–24.
- Ludwig, B., 2019. Das Umland von Pergamon. *Die Arbeiten des Umland-Surveys 2018*, in: Pirson, F. (Ed.), *Pergamon – Bericht über die Arbeiten in der Kampagne 2018*. *Archäologischer Anzeiger*, pp. 113–116.
- Ludwig, B., 2020a. Das Umland von Pergamon. *Die Arbeiten des Umland-Surveys 2019*, in: Pirson, F. (Ed.), *Pergamon – Das neue Forschungsprogramm und die Arbeiten in der Kampagne 2019*. *Archäologischer Anzeiger*, pp. 205–216.
- Ludwig, B., 2020b. Reconstructing the Ancient Route Network in Pergamon's Surroundings. *Land* 9, 1–39.
- Ludwig, B., 2023. *Beyond the city of Pergamon. A landscape archaeological study of the Pergamon Micro-Region from the Hellenistic to the Roman Imperial Period*, Department of Earth Sciences. Freie Universität Berlin, Berlin, Germany, pp. 1–269.
- Ludwig, B., Pirson, F., Aksan, Z.M., Ateş, G., Rabbel, W., Erkul, E., Kaplanvural, İ., 2022. Das Umland von Pergamon. *Die Arbeiten des Umland-Surveys 2021*, in: Pirson, F. (Ed.), *Pergamon – Die Arbeiten in der Kampagne 2021*. *Archäologischer Anzeiger*, pp. 48–62.
- Lynch, J., 1990. Provisional elemental values for eight new geochemical lake sediment and stream sediment reference materials LKSD - 1, LKSD - 2, LKSD - 3, LKSD - 4, STSD - 1, STSD - 2, STSD - 3, and STSD - 4\*. *Geostandards Newsletter* 14, 153–167.
- Macklin, M., Lewin, J., Woodward, J., 1995. Quaternary fluvial systems in the Mediterranean basin, in: Lewin, J., Macklin, M., Woodward, J. (Eds.), *Mediterranean Quaternary river environments*. Balkema, Rotterdam, the Netherlands, pp. 1–25.
- Macphail, R.I., Goldberg, P., 2017. *Applied Soils and Micromorphology in Archaeology*. Cambridge University Press, Cambridge, United Kingdom.
- Maher, B.A., Thompson, R., 1991. Mineral magnetic record of the Chinese loess and

paleosols. *Geology* 19, 3–6.

Mahmood, S.A., Gloaguen, R., 2012. Appraisal of active tectonics in Hindu Kush: Insights from DEM derived geomorphic indices and drainage analysis. *Geoscience Frontiers* 3, 407–428.

Maltas, T., Şahoğlu, V., Erkanal, H., 2023. Agricultural adaptations to mid-late Holocene climate change in western Türkiye. *Scientific Reports* 13, 1–12.

Manning, S.W., Lorentzen, B., Welton, L., Batiuk, S., Harrison, T.P., 2020. Beyond megadrought and collapse in the Northern Levant: The chronology of Tell Tayinat and two historical inflection episodes, around 4.2ka BP, and following 3.2ka BP. *PLoS One* 15, 1–38.

Marriner, N., Morhange, C., 2007. Geoscience of ancient Mediterranean harbours. *Earth-Science Reviews* 80, 137–194.

Mattivi, P., Franci, F., Lambertini, A., Bitelli, G., 2019. TWI computation: a comparison of different open source GISs. *Open Geospatial Data, Software and Standards* 4, 1–12.

May, S.M., Norpoth, M., Pint, A., Shumilovskikh, L., Raith, K., Brill, D., Rixhon, G., Moret, P., Jiménez - Vialás, H., Grau - Mira, I., García - Jiménez, I., Marzoli, D., León - Martín, C., Reicherter, K., Brückner, H., 2021. Mid - to late Holocene environmental changes and human - environment interactions in the surroundings of La Silla del Papa, SW Spain. *Geoarchaeology* 36, 573–600.

Mayewski, P.A., Rohling, E.E., Curt Stager, J., Karlén, W., Maasch, K.A., David Meeker, L., Meyerson, E.A., Gasse, F., van Kreveland, S., Holmgren, K., Lee-Thorp, J., Rosqvist, G., Rack, F., Staubwasser, M., Schneider, R.R., Steig, E.J., 2004. Holocene climate variability. *Quaternary Research* 62, 243–255.

Mazzini, I., Gliozzi, E., Galaty, M., Bejko, L., Sadori, L., Soulié-Märsche, I., Koçi, R., Van Welden, A., Bushati, S., 2016. Holocene evolution of Lake Shkodra: Multidisciplinary evidence for diachronic landscape change in northern Albania. *Quaternary Science Reviews* 136, 85–95.

McHugh, C.M.G., Seeber, L., Cormier, M.-H., Dutton, J., Cagatay, N., Polonia, A., Ryan, W.B.F., Gorur, N., 2006. Submarine earthquake geology along the North Anatolia Fault in the Marmara Sea, Turkey: A model for transform basin sedimentation. *Earth and Planetary Science Letters* 248, 661–684.

McLeman, R.A., 2011. Settlement abandonment in the context of global environmental change. *Global Environmental Change* 21, S108–S120.

Mecking, R., Meinecke, M., Erkul, E., Driehaus, B., Bolten, A., Pirson, F., Rabbel, W., 2020. The Yiğma Tepe of Pergamon: stratigraphic construction of a monumental tumulus from seismic refraction measurements. *Archaeological Prospection* 27, 73–105.

Mercuri, A.M., Florenzano, A., Burjachs, F., Giardini, M., Kouli, K., Masi, A., Picornell-Gelabert, L., Revelles, J., Sadori, L., Servera-Vives, G., Torri, P., Fyfe, R., 2019. From influence to impact: The multifunctional land use in Mediterranean prehistory emerging from palynology of archaeological sites (8.0-2.8 ka BP). *The Holocene* 29,

830–846.

- Miall, A.D., 2006. *The geology of fluvial deposits: sedimentary facies, basin analysis, and petroleum geology*, 4th ed. Springer, Berlin, Germany.
- Miall, A.D., 2014. *Fluvial depositional systems*. Springer International Publishing, Cham, Switzerland.
- Michalski, P., 2021. A Rural Settlement in the Surroundings of Pergamon - Survey Analysis of the Kuyulu Kaya in the Lower Western Kaikos Valley. Humboldt-Universität zu Berlin, Berlin, Germany, pp. 1–292.
- Mills, H.H., 1979. Downstream rounding of pebbles—a quantitative review. *Journal of Sedimentary Research* 49, 295–302.
- Mitas, L., Mitasova, H., 1998. Distributed soil erosion simulation for effective erosion prevention. *Water Resources Research* 34, 505–516.
- Mitasova, H., Barton, M., Ullah, I., Hofierka, J., Harmon, R.S., 2013. GIS-Based Soil Erosion Modeling, in: Shroder, J., Bishop, M.P. (Eds.), *Treatise on Geomorphology*. Academic Press, San Diego, California, United States, pp. 228–258.
- Mitasova, H., Hofierka, J., Zlocha, M., Iverson, L.R., 1996. Modelling topographic potential for erosion and deposition using GIS. *International journal of geographical information systems* 10, 629–641.
- Mitasova, H., Mitas, L., 1999a. Erosion/deposition modeling with USPED using GIS. Last accessed on May 2023: <http://fatra.cnr.ncsu.edu/~hmitaso/gmslab/denix/uspded.html>.
- Mitasova, H., Mitas, L., 1999b. Modeling soil detachment with RUSLE 3D using GIS. Last accessed on May 2023: <http://fatra.cnr.ncsu.edu/~hmitaso/gmslab/erosion/usle.html>.
- Moore, I.D., Burch, G.J., 1986. Physical basis of the length-slope factor in the universal soil loss equation. *Soil Science Society of America* 50, 1294–1298.
- Moore, I.D., Grayson, R.B., Ladson, A.R., 1991. Digital Terrain Modeling: A Review of Hydrological, Geomorphological, and Biological Applications. *Hydrological Processes* 5, 3–30.
- Morellón, M., Anselmetti, F.S., Ariztegui, D., Brushulli, B., Sinopoli, G., Wagner, B., Sadori, L., Gilli, A., Pambuku, A., 2016. Human–climate interactions in the central Mediterranean region during the last millennia: The laminated record of Lake Butrint (Albania). *Quaternary Science Reviews* 136, 134–152.
- Moscariello, A., 2018. Alluvial fans and fluvial fans at the margins of continental sedimentary basins: geomorphic and sedimentological distinction for geo-energy exploration and development. Geological Society, London, Special Publications 440, 215–243.
- MTA, 2002. *Geological Map of Turkey, 1:500,000 (İzmir)*. General Directorate of Mineral Research and Exploration, Ankara, Türkiye.
- Müller, S., Tarasov, P.E., Hoelzmann, P., Bezrukova, E.V., Kossler, A., Krivonogov, S.K.,

2014. Stable vegetation and environmental conditions during the Last Glacial Maximum: New results from Lake Kotokel (Lake Baikal region, southern Siberia, Russia). *Quaternary International* 348, 14–24.
- Mustafaoğlu, G., Dağ, H.U., 2012. Cultural heritage works of the Gebze-İzmir Motorway Project in the west of Turkey. *European Association of Archaeologists*, 25–30.
- Nalbant, S.S., Hubert, A., King, G.C.P., 1998. Stress coupling between earthquakes in northwest Turkey and the north Aegean Sea. *Journal of Geophysical Research: Solid Earth* 103, 24469–24486.
- Naveh, Z., 1982. Mediterranean landscape evolution and degradation as multivariate biofunctions: Theoretical and practical implications. *Landscape Planning* 9, 125–146.
- Nemec, W., Kazancı, N., 1999. Quaternary colluvium in west - central Anatolia: sedimentary facies and palaeoclimatic significance. *Sedimentology* 46, 139–170.
- Niwa, Y., Sugai, T., Saegusa, Y., Ogami, T., Sasao, E., 2011. Use of electrical conductivity to analyze depositional environments: Example of a Holocene delta sequence on the Nobi Plain, central Japan. *Quaternary International* 230, 78–86.
- Notebaert, B., Verstraeten, G., Vandenberghe, D., Marinova, E., Poesen, J., Govers, G., 2011. Changing hillslope and fluvial Holocene sediment dynamics in a Belgian loess catchment. *Journal of Quaternary Science* 26, 44–58.
- Nykamp, M., Becker, F., Braun, R., Pöllath, N., Knitter, D., Peters, J., Schütt, B., 2021. Sediment cascades and the entangled relationship between human impact and natural dynamics at the pre - pottery Neolithic site of Göbekli Tepe, Anatolia. *Earth Surface Processes and Landforms* 46, 430–442.
- Nykamp, M., Knitter, D., Schütt, B., 2020. Late Holocene geomorphodynamics in the vicinity of Göbekli Tepe, SE Turkey. *Catena* 195, 1–14.
- Ocakoğlu, F., Çilingiroğlu, Ç., Erkara, İ.P., Ünan, S., Dinçer, B., Akkiraz, M.S., 2019. Human-climate interactions since the neolithic period in Central Anatolia: Novel multi-proxy data from the Kureyşler area, Kütahya, Turkey. *Quaternary Science Reviews* 213, 1–17.
- Ocakoğlu, F., Kuzucuoğlu, C., Akbulut, A., Çilingiroğlu, Ç., 2022. Lake level changes and paleo-precipitation estimations based on colluvial stratigraphy of Holocene sediments in West Anatolia (Simav Graben). *Palaeogeography, Palaeoclimatology, Palaeoecology* 597, 1–21.
- Okay, A., 2008. Geology of Turkey: A Synopsis. *Anschitt* 21, 19–42.
- Ölgen, K., 2004. Determining lineaments and geomorphic features using Landsat 5-TM data on lower Bakırçay plain, Western Turkey. *Aegean Geographical Journal* 13, 47–57.
- Ön, Z.B., 2023. A Bayesian change point analysis re-examines the 4.2 ka BP event in southeast Europe and southwest Asia. *Quaternary Science Reviews*, 1–26.
- Oskay, R.G., Bechtel, A., Karayiğit, A.İ., 2019. Mineralogy, petrography and organic geochemistry of Miocene coal seams in the Kınık coalfield (Soma Basin-Western

- Turkey): Insights into depositional environment and palaeovegetation. *International Journal of Coal Geology* 210, 1–22.
- Ozdemir, H., Bird, D., 2008. Evaluation of morphometric parameters of drainage networks derived from topographic maps and DEM in point of floods. *Environmental Geology* 56, 1405–1415.
- Özpolat, E., Yıldırım, C., Görüm, T., 2020. The Quaternary landforms of the Büyük Menderes Graben System: the southern Menderes Massif, western Anatolia, Turkey. *Journal of Maps* 16, 405–419.
- Özpolat, E., Yıldırım, C., Görüm, T., Gosse, J.C., Şahiner, E., Şarıkaya, M.A., Owen, L.A., 2022. Three-dimensional control of alluvial fans by rock uplift in an extensional regime: Aydin Range, Aegean extensional province. *Scientific Reports* 12, 1–14.
- Özürlan, G., Candansayar, M.E., Şahin, M.H., 2006. Deep resistivity structure of the Dikili-Bergama region, west Anatolia, revealed by two-dimensional inversion of vertical electrical sounding data. *Geophysical Prospecting* 54, 187–197.
- Palmisano, A., Bevan, A., Shennan, S., 2017. Comparing archaeological proxies for long-term population patterns: An example from central Italy. *Journal of Archaeological Science* 87, 59–72.
- Palmisano, A., Lawrence, D., de Gruchy, M.W., Bevan, A., Shennan, S., 2021. Holocene regional population dynamics and climatic trends in the Near East: A first comparison using archaeo-demographic proxies. *Quaternary Science Reviews* 252, 1–27.
- Palmisano, A., Woodbridge, J., Roberts, C.N., Bevan, A., Fyfe, R., Shennan, S., Cheddadi, R., Greenberg, R., Kaniewski, D., Langgut, D., Leroy, S.A.G., Litt, T., Miebach, A., 2019. Holocene landscape dynamics and long-term population trends in the Levant. *The Holocene* 29, 708–727.
- Panin, P.G., Filippova, K.G., Bukhonov, A.V., Karpukhina, N.V., Kalinin, P.I., Ruchkin, M.V., 2021. High-resolution analysis of the Likhvin loess-paleosol sequence (the central part of the East European Plain, Russia). *Catena* 205, 1–15.
- Paradisopoulou, P.M., Papadimitriou, E.E., Karakostas, V.G., Taymaz, T., Kiliyas, A., Yolsal, S., 2010. Seismic Hazard Evaluation in Western Turkey as Revealed by Stress Transfer and Time-dependent Probability Calculations. *Pure and Applied Geophysics* 167, 1013–1048.
- Pavúk, P., Horejs, B., 2018. Ceramics, Surveys, and Connectivity in Western Anatolia: The Middle and Late Bronze Age Bakırçay/Kaikos Valley Restudied. *Ägypten Levante* 28, 457–485.
- Peel, M.C., Finlayson, B.L., McMahon, T.A., 2007. Updated world map of the Köppen-Geiger climate classification. *Hydrology and Earth System Sciences* 11, 1633–1644.
- Peeters, I., Rommens, T., Verstraeten, G., Govers, G., Van Rompaey, A., Poesen, J., Van Oost, K., 2006. Reconstructing ancient topography through erosion modelling. *Geomorphology* 78, 250–264.
- Pérez-Lambán, F., Peña-Monné, J.L., Badía-Villas, D., Picazo Millán, J.V., Sampietro-Vattuone, M.M., Alcolea Gracia, M., Aranbarri, J., González-Sampériz, P., Fanlo

- Loras, J., 2018. Holocene environmental variability in the Central Ebro Basin (NE Spain) from geoarchaeological and pedological records. *Catena* 163, 147–164.
- Philippson, A., 1912. Geographisch-geologische Übersicht der Landschaft, in: Conze, A. (Ed.), *Altertümer von Pergamon: Stadt und Landschaft*. Verlag von Georg Reimer, Berlin, Germany, pp. 43–58.
- Piccarreta, M., Caldara, M., Capolongo, D., Boenzi, F., 2011. Holocene geomorphic activity related to climatic change and human impact in Basilicata, Southern Italy. *Geomorphology* 128, 137–147.
- Pint, A., Seeliger, M., Frenzel, P., Feuser, S., Erkul, E., Berndt, C., Klein, C., Pirson, F., Brückner, H., 2015. The environs of Elaia's ancient open harbour – a reconstruction based on microfaunal evidence. *Journal of Archaeological Science* 54, 340–355.
- Pirson, F., 2008. Das Territorium der hellenistischen Residenzstadt Pergamon: Herrschaftlicher Anspruch als raumbezogene Strategie, in: Jöchner, C. (Ed.), *Räume der Stadt: Von der Antike bis heute*. Reimer, Berlin, Germany, pp. 27–50.
- Pirson, F., 2010. Pergamon – Bericht über die Arbeiten in der Kampagne 2009. *Archäologischer Anzeiger*, 139–236.
- Pirson, F., 2014. Elaia, der (maritime) Satellit Pergamons, in: Ladstätter, S., Pirson, F., Schmidts, T. (Eds.), *Harbors and Harbor Cities in the Eastern Mediterranean from Antiquity to the Byzantine Period: Recent Discoveries and Current Approaches*. Byzas Istanbul, Türkiye, pp. 339–356.
- Pirson, F., 2015. Stadt und Umland von Pergamon. Stand der Forschung und Perspektiven, in: Yalçın, Ü., Bienert, H.D. (Eds.), *Anatolien — Brücke der Kulturen*. Bochum, Bonn, Germany, pp. 289–310.
- Pirson, F., 2017. Die Siedlungsgeschichte Pergamons. Überblick und kritische Revision. Mit einem Appendix von Anneke Keweloh-Kaletta. *Istanbul Mitteilungen* 67, 43–130.
- Pirson, F., 2019. Pergamon – Bericht über die Arbeiten in der Kampagne 2018. *Archäologischer Anzeiger*, 1–157.
- Pirson, F., 2020. Pergamon – Das neue Forschungsprogramm und die Arbeiten in der Kampagne 2019. *Archäologischer Anzeiger* 2, 1–245.
- Pirson, F., 2022. Pergamon – Die Arbeiten in der Kampagne 2020. *Archäologischer Anzeiger* 2, 231–323.
- Pirson, F., Ateş, G., Bartz, M., Brückner, H., Feuser, S., Mania, U., Meier, L., Seeliger, M., 2015. Elaia: Eine aiolische Polis im Dienste der hellenistischen Residenzstadt Pergamon?, in: Matthaei, A., Zimmermann, M. (Eds.), *Urbane Strukturen und bürgerliche Identität im Hellenismus*. Verlag Antike, Heidelberg, Germany, pp. 22–55.
- Pirson, F., Horejs, B., Laufer, E., Schwall, C., Schwarz, A.J., 2016. Pergamon – Bericht über die Arbeiten in der Kampagne 2015. *Archäologischer Anzeiger* 2, 135–223.
- Pirson, F., Scholl, A., 2014. Pergamon – Anadolu'da Hellenistik Bir Başkent / A Hellenistic Capital in Anatolia. *Yapi Kredi Yayinlari*, Istanbul, Türkiye.

- Pirson, F., Zimmermann, M., 2014. The Hinterland of Pergamon. Economic Resources, Rural Settlements and Political Manifestation, in: Scholl, A., Pirson, F. (Eds.), Pergamon – Anadolu'da Hellenistik Bir Başkent / A Hellenistic Capital in Anatolia. Yapi Kredi Yayinlari, Istanbul, Türkiye, pp. 144–161.
- Pope, K.O., van Andel, T.H., 1984. Late quaternary alluviation and soil formation in the southern Argolid: its history, causes and archaeological implications. *Journal of Archaeological Science* 11, 281–306.
- Prasannakumar, V., Vijith, H., Abinod, S., Geetha, N., 2012. Estimation of soil erosion risk within a small mountainous sub-watershed in Kerala, India, using Revised Universal Soil Loss Equation (RUSLE) and geo-information technology. *Geoscience Frontiers* 3, 209–215.
- Price, S., Nixon, L., 2005. Ancient Greek Agricultural Terraces: Evidence from Texts and Archaeological Survey. *American Journal of Archaeology* 109, 665–694.
- QGIS Development Team, 2020. QGIS Geographic Information System, Open Source Geospatial Foundation Project.
- QGIS Development Team, 2023. QGIS Geographic Information System, Open Source Geospatial Foundation Project.
- R Core Team, 2021. R: A language and environment for statistical computing. R Foundation for Statistical Computing, Vienna, Austria.
- R Core Team, 2022. R: A language and environment for statistical computing. R Foundation for Statistical Computing, Vienna, Austria.
- Radt, W., 2016. Pergamon: Geschichte und Bauten einer antiken Metropole. Primus in Wissenschaftliche Buchgesellschaft, Darmstadt, Germany.
- Reimer, P.J., Austin, W.E.N., Bard, E., Bayliss, A., Blackwell, P.G., Bronk Ramsey, C., Butzin, M., Cheng, H., Edwards, R.L., Friedrich, M., Grootes, P.M., Guilderson, T.P., Hajdas, I., Heaton, T.J., Hogg, A.G., Hughen, K.A., Kromer, B., Manning, S.W., Muscheler, R., Palmer, J.G., Pearson, C., van der Plicht, J., Reimer, R.W., Richards, D.A., Scott, E.M., Southon, J.R., Turney, C.S.M., Wacker, L., Adolphi, F., Büntgen, U., Capano, M., Fahrni, S.M., Fogtmann-Schulz, A., Friedrich, R., Köhler, P., Kudsk, S., Miyake, F., Olsen, J., Reinig, F., Sakamoto, M., Sookdeo, A., Talamo, S., 2020. The IntCal20 Northern Hemisphere Radiocarbon Age Calibration Curve (0–55 cal kBP). *Radiocarbon* 62, 725–757.
- Remondo, J., Soto, J., González-Díez, A., Díaz de Terán, J.R., Cendrero, A., 2005. Human impact on geomorphic processes and hazards in mountain areas in northern Spain. *Geomorphology* 66, 69–84.
- Renard, K.G., Foster, G.R., Weesies, G.A., McCool, D.K., Coordinators, 1997. Predicting soil erosion by water: a guide to conservation planning with the Revised Universal Soil Loss Equation (RUSLE). United States Government Printing, Washington DC, United States.
- Rhoads, B.L., 2020. River Dynamics: Geomorphology to Support Management. Cambridge University Press, Cambridge, United Kingdom.
- Rizzoli, P., Martone, M., Gonzalez, C., Wecklich, C., Borla Tridon, D., Bräutigam, B.,

- Bachmann, M., Schulze, D., Fritz, T., Huber, M., Wessel, B., Krieger, G., Zink, M., Moreira, A., 2017. Generation and performance assessment of the global TanDEM-X digital elevation model. *ISPRS Journal of Photogrammetry and Remote Sensing* 132, 119–139.
- Roberts, C.N., Woodbridge, J., Palmisano, A., Bevan, A., Fyfe, R., Shennan, S., 2019a. Mediterranean landscape change during the Holocene: Synthesis, comparison and regional trends in population, land cover and climate. *The Holocene* 29, 923–937.
- Roberts, N., 2014. *The Holocene: an environmental history*, 3rd ed. Wiley Blackwell, New York, United States.
- Roberts, N., 2019. How humans changed the face of Earth. *Science* 365, 865–866.
- Roberts, N., 2023. Holocene Climate Changes and Human Consequences, *Handbook of Archaeological Sciences*, pp. 321–337.
- Roberts, N., Allcock, S.L., Barnett, H., Mather, A., Eastwood, W.J., Jones, M., Primmer, N., Yiğitbaşıoğlu, H., Vannièrè, B., 2019b. Cause-and-effect in Mediterranean erosion: The role of humans and climate upon Holocene sediment flux into a central Anatolian lake catchment. *Geomorphology* 331, 36–48.
- Roberts, N., Brayshaw, D., Kuzucuoğlu, C., Perez, R., Sadori, L., 2011a. The mid-Holocene climatic transition in the Mediterranean: Causes and consequences. *The Holocene* 21, 3–13.
- Roberts, N., Eastwood, W.J., Kuzucuoğlu, C., Fiorentino, G., Caracuta, V., 2011b. Climatic, vegetation and cultural change in the eastern Mediterranean during the mid-Holocene environmental transition. *The Holocene* 21, 147–162.
- Robustelli, G., Lucà, F., Corbi, F., Pelle, T., Dramis, F., Fubelli, G., Scarciglia, F., Muto, F., Cugliari, D., 2009. Alluvial terraces on the Ionian coast of northern Calabria, southern Italy: Implications for tectonic and sea level controls. *Geomorphology* 106, 165–179.
- Rohdenburg, H., 1983. Beiträge zur allgemeinen geomorphologie der tropen und subtropen Geomorphodynamik und vegetation klimazyklische sedimentation panplain/pediplain-pediment-terrassen-treppen. *Geomorphodynamik und vegetation klimazyklische sedimentation panplain/pediplain-pediment-terrassen-treppen. CATENA* 10, 393–438.
- Rohling, E.J., Marino, G., Grant, K.M., Mayewski, P.A., Wenginger, B., 2019. A model for archaeologically relevant Holocene climate impacts in the Aegean-Levantine region (easternmost Mediterranean). *Quaternary Science Reviews* 208, 38–53.
- Russell, B., 2013a. *The Economics of the Roman Stone Trade*. Oxford University Press, Oxford, United Kingdom.
- Russell, B., 2013b. *Gazetteer of Stone Quarries in the Roman World*. Version 1.0. Last accessed on December 2020: [oxrep.classics.ox.ac.uk/databases/stone\\_quarries\\_database/](http://oxrep.classics.ox.ac.uk/databases/stone_quarries_database/). Oxford Roman Economy Project, p. 6.
- Sadori, L., Giraudi, C., Masi, A., Magny, M., Ortu, E., Zanchetta, G., Izdebski, A., 2016. Climate, environment and society in southern Italy during the last 2000 years. *A*

- review of the environmental, historical and archaeological evidence. *Quaternary Science Reviews* 136, 173–188.
- Sanğu, E., Gürer, Ö.F., Gürer, A., 2020. Fault kinematic and Plio-Quaternary paleostress evolution of the Bakırçay Basin, Western Turkey. *International Geology Review* 62, 1245–1261.
- Santisteban, J.I., Mediavilla, R., López-Pamo, E., Dabrio, C.J., Zapata, M.B.R., García, M.J.G., Castaño, S., Martínez-Alfaro, P.E., 2004. Loss on ignition: a qualitative or quantitative method for organic matter and carbonate mineral content in sediments? *Journal of Paleolimnology* 32, 287–299.
- Sauer, T., Ries, J.B., 2008. Vegetation cover and geomorphodynamics on abandoned fields in the Central Ebro Basin (Spain). *Geomorphology* 102, 267–277.
- Scharpenseel, H., Schiffmann, H., 1977. Soil radiocarbon analysis and soil dating. *Geophysical Surveys* 3, 143–156.
- Schlunegger, F., Hinderer, M., 2003. Pleistocene/Holocene climate change, re-establishment of fluvial drainage network and increase in relief in the Swiss Alps. *Terra Nova* 15, 88–95.
- Schneider, S., 2014. *Geoarchaeological Case Studies in the Bakırçay Valley – Paleogeography and Human-environmental Interactions in the Chora of Pergamon in Western Turkey*, Department of Earth Sciences. Freie Universität Berlin, Berlin, Germany, pp. 1–146.
- Schneider, S., Matthaei, A., Bebermeier, W., Schütt, B., 2014. Late Holocene human–environmental interactions in the Eastern Mediterranean: Settlement history and paleogeography of an ancient Aegean hill-top settlement. *Quaternary International* 324, 84–98.
- Schneider, S., Matthaei, A., Schlöffel, M., Meyer, C., Kronwald, M., Pint, A., Schütt, B., 2015. A geoarchaeological case study in the chora of Pergamon, western Turkey, to reconstruct the late Holocene landscape development and settlement history. *Quaternary International* 367, 62–76.
- Schneider, S., Nykamp, M., Matthaei, A., Bebermeier, W., Schütt, B., 2013. Alluvial geoarchaeology of a small drainage basin in western Anatolia: Late Holocene landscape development and the question of the mouth of the Paleo-Bakırçay. *Quaternary International* 312, 84–95.
- Schneider, S., Schlöffel, M., Schwall, C., Horejs, B., Schütt, B., 2017. First stratigraphic evidence and absolute dating of a Bronze Age settlement in the Bakırçay valley in western Turkey. *Journal of Archaeological Science: Reports* 12, 316–322.
- Schumm, S.A., 1973. Geomorphic thresholds and complex response of drainage systems, in: Morisawa, M. (Ed.), *Fluvial Geomorphology*. Publications of Geomorphology, State University of New York, Binghamton, United States, pp. 299–310.
- Schumm, S.A., 1977. *The Fluvial System*. Wiley, New York, United States.
- Seeliger, M., Bartz, M., Erkul, E., Feuser, S., Kelterbaum, D., Klein, C., Pirson, F., Vött, A., Brückner, H., 2013. Taken from the sea, reclaimed by the sea: The fate of the closed harbour of Elaia, the maritime satellite city of Pergamum (Turkey).

Quaternary International 312, 70–83.

- Seeliger, M., Brill, D., Feuser, S., Bartz, M., Erkul, E., Kelterbaum, D., Vött, A., Klein, C., Pirson, F., Brückner, H., 2014. The purpose and age of underwater walls in the Bay of Elaia of western Turkey: a multidisciplinary approach. *Geoarchaeology* 29, 138–155.
- Seeliger, M., Pint, A., Feuser, S., Riedesel, S., Marriner, N., Frenzel, P., Pirson, F., Bolten, A., Brückner, H., 2019. Elaia, Pergamon's maritime satellite: the rise and fall of an ancient harbour city shaped by shoreline migration. *Journal of Quaternary Science* 34, 228–244.
- Seeliger, M., Pint, A., Frenzel, P., Feuser, S., Pirson, F., Riedesel, S., Brückner, H., 2017. Foraminifera as markers of Holocene sea-level fluctuations and water depths of ancient harbours — A case study from the Bay of Elaia (W Turkey). *Palaeogeography, Palaeoclimatology, Palaeoecology* 482, 17–29.
- Seeliger, M., Pint, A., Frenzel, P., Weisenseel, P., Erkul, E., Wilken, D., Wunderlich, T., Başaran, S., Bücherl, H., Herbrecht, M., Rabbel, W., Schmidts, T., Szemkus, N., Brückner, H., 2018. Using a Multi-Proxy Approach to Detect and Date a Buried part of the Hellenistic City Wall of Ainos (NW Turkey). *Geosciences* 8, 1–17.
- Sherriff, S.C., 2014. Environmental Magnetism: Sediment Source Tracing, in: Cook, S.J., Clarke, L.E., Nield, J.M. (Eds.), *Geomorphological Techniques* (Online Edition). British Society for Geomorphology, London, United Kingdom, pp. 1–14.
- Shi, X., Werner, M., Krug, C., Brierley, C.M., Zhao, A., Igbinsola, E., Braconnot, P., Brady, E., Cao, J., D'Agostino, R., Jungclaus, J., Liu, X., Otto-Bliesner, B., Sidorenko, D., Tomas, R., Volodin, E.M., Yang, H., Zhang, Q., Zheng, W., Lohmann, G., 2022a. Calendar effects on surface air temperature and precipitation based on model-ensemble equilibrium and transient simulations from PMIP4 and PACMEDY. *Climate of the Past* 18, 1047–1070.
- Shi, X., Werner, M., Wang, Q., Yang, H., Lohmann, G., 2022b. Simulated Mid-Holocene and Last Interglacial Climate Using Two Generations of AWI-ESM. *Journal of Climate* 35, 4211–4231.
- Shumilovskikh, L., Seeliger, M., Brückner, H., 2022. Vegetation Changes and Human Impact during the Last 3500 Years in Western Anatolia – a Pilot Study from the Crater Lake Kara Göl, in: Pirson, F. (Ed.), *Pergamon – Die Arbeiten in der Kampagne 2020*. *Archäologischer Anzeiger*, pp. 72–81.
- Shumilovskikh, L.S., Seeliger, M., Feuser, S., Novenko, E., Schlütz, F., Pint, A., Pirson, F., Brückner, H., 2016. The harbour of Elaia: A palynological archive for human environmental interactions during the last 7500 years. *Quaternary Science Reviews* 149, 167–187.
- Silva-Sánchez, N., Martínez Cortizas, A., López-Merino, L., 2014. Linking forest cover, soil erosion and mire hydrology to late-Holocene human activity and climate in NW Spain. *The Holocene* 24, 714–725.
- Soil Science Division Staff, 2017. *Soil Survey Manual*, 4th ed. United States Department of Agriculture Handbook No. 18, Washington DC, United States.
- Soil Survey Division Staff, 1993. *Kellogg Soil Survey Laboratory Methods Manual*. Soil

Survey Investigations Report No. 42, 5th ed. U.S. Department of Agriculture, Natural Resources Conservation Service, Washington DC, United States.

Soil Survey Staff, 1999. *Soil Taxonomy: A Basic System of Soil Classification for Making and Interpreting Soil Surveys*, 2nd ed. United States Department of Agriculture, Washington DC, United States.

Sommerey, K.M., 2008. Die Chora von Pergamon: Studien zu Grenzen, Siedlungsstruktur und Wirtschaft, in: Pirson, F., Bachmann, M. (Eds.), *Istanbuler Mitteilungen*. Ernst Wasmuth, Tübingen, Germany, pp. 135–170.

Stamatis, D., Emmanouilidis, A., Masi, A., Izdebski, A., Avramidis, P., 2022. Holocene Hydroclimatic Changes in Northern Peloponnese (Greece) Inferred from the Multiproxy Record of Lake Lousoi. *Water* 14, 1–12.

Stock, F., Knipping, M., Pint, A., Ladstätter, S., Delile, H., Heiss, A.G., Laermanns, H., Mitchell, P.D., Ployer, R., Steskal, M., Thanheiser, U., Urz, R., Wennrich, V., Brückner, H., 2016. Human impact on Holocene sediment dynamics in the Eastern Mediterranean - the example of the Roman harbour of Ephesus. *Earth Surface Processes and Landforms* 41, 980–996.

Stock, F., Laermanns, H., Pint, A., Knipping, M., Wulf, S., Hassl, A.R., Heiss, A.G., Ladstätter, S., Opitz, S., Schwaiger, H., Brückner, H., 2020a. Human-environment interaction in the hinterland of Ephesus – As deduced from an in-depth study of Lake Belevi, west Anatolia. *Quaternary Science Reviews* 244, 1–17.

Stock, F., Pint, A., Horejs, B., Ladstätter, S., Brückner, H., 2013. In search of the harbours: New evidence of Late Roman and Byzantine harbours of Ephesus. *Quaternary International* 312, 57–69.

Stock, F., Seyer, M., Symanczyk, A., Uncu, L., Brückner, H., 2020b. On the geoarchaeology of Limyra (SW Anatolia)—new insights into the famous Lycian city and its environs. *Geoarchaeology* 35, 487–502.

Stoddart, S., Woodbridge, J., Palmisano, A., Mercuri, A.M., Mensing, S.A., Colombaroli, D., Sadori, L., Magri, D., Di Rita, F., Giardini, M., Mariotti Lippi, M., Montanari, C., Bellini, C., Florenzano, A., Torri, P., Bevan, A., Shennan, S., Fyfe, R., Roberts, C.N., 2019. Tyrrhenian central Italy: Holocene population and landscape ecology. *The Holocene* 29, 761–775.

Stow, D.A., 2005. *Sedimentary Rocks in the Field: A color guide*. Manson Publishing, London, United Kingdom.

Strunk, A., Olsen, J., Sanei, H., Rudra, A., Larsen, N.K., 2020. Improving the reliability of bulk sediment radiocarbon dating. *Quaternary Science Reviews* 242, 1–13.

Szabó, J., Dávid, L., Lóczy, D., 2010. *Anthropogenic Geomorphology: A Guide to Man-Made Landforms*. University of Debrecen, Debrecen, Hungary.

Tassios, T.P., 2007. Water supply of ancient Greek cities. *Water Supply* 7, 165–172.

Telbisz, T., Kovács, G., Székely, B., Szabó, J., 2013. Topographic swath profile analysis: a generalization and sensitivity evaluation of a digital terrain analysis tool. *Zeitschrift für Geomorphologie* 57, 485–513.

- Torri, D., Poesen, J., Borselli, L., 1997. Predictability and uncertainty of the soil erodibility factor using a global dataset. *Catena* 31, 1–22.
- Tosun, H., Tosun, T., Hariri-Ardebili, M., 2020. Total risk and seismic hazard analysis of large embankment dams: case study of Northwest Anatolia, Turkey. *Life Cycle Reliability and Safety Engineering* 9, 329–338.
- Tozan, M., 2022. Osmanische Dokumente und ihre Bedeutung für die historischarchäologische Erforschung der Mikroregion Pergamon: Perspektiven und erste Beobachtungen, in: Pirson, F. (Ed.), *Pergamon – Die Arbeiten in der Kampagne 2020*. *Archäologischer Anzeiger*, pp. 47–49.
- Türkeş, M., Erlat, E., 2005. Climatological responses of winter precipitation in Turkey to variability of the North Atlantic Oscillation during the period 1930–2001. *Theoretical and Applied Climatology* 81, 45–69.
- Ülgen, U.B., Franz, S.O., Biltekin, D., Çagatay, M.N., Roeser, P.A., Doner, L., Thein, J., 2012. Climatic and environmental evolution of Lake Iznik (NW Turkey) over the last ~4700 years. *Quaternary International* 274, 88–101.
- Vacchi, M., Rovere, A., Chatzipetros, A., Zouros, N., Firpo, M., 2014. An updated database of Holocene relative sea level changes in NE Aegean Sea. *Quaternary International* 328–329, 301–310.
- Van Andel, T.H., Zangger, E., Demitrack, A., 1990. Land use and soil erosion in prehistoric and historical Greece. *Journal of Field Archaeology* 17, 379–396.
- Van Dijk, M., Kleinhans, M.G., Postma, G., Kraal, E., 2012. Contrasting morphodynamics in alluvial fans and fan deltas: effect of the downstream boundary. *Sedimentology* 59, 2125–2145.
- Van Loo, M., Duser, B., Verstraeten, G., Renssen, H., Notebaert, B., D'Haen, K., Bakker, J., 2016. Human induced soil erosion and the implications on crop yield in a small mountainous Mediterranean catchment (SW-Turkey). *Catena* 149, 491–504.
- Verhagen, P., 2018. Predictive modeling, in: Varela, S.L.L. (Ed.), *The Encyclopedia of Archaeological Sciences*. John Wiley & Sons, Inc, pp. 1–3.
- Verstraeten, G., 2014. Quantification of human–environment interactions in the past. *Anthropocene* 8, 1–5.
- Verstraeten, G., Broothaerts, N., Van Loo, M., Notebaert, B., D'Haen, K., Duser, B., De Brue, H., 2017. Variability in fluvial geomorphic response to anthropogenic disturbance. *Geomorphology* 294, 20–39.
- Vita-Finzi, C., 1969a. Late Quaternary Continental Deposits of Central and Western Turkey. *Man* 4, 605–692.
- Vita-Finzi, C., 1969b. *The Mediterranean Valleys: Geological Changes in Historical Times*. Cambridge University Press, Cambridge, United Kingdom.
- Vita-Finzi, C., 1995. Solar history and paleohydrology during the last two millennia. *Geophysical Research Letters* 22, 699–702.
- Von Diest, W., 1889. Von Pergamon über den Dindymos zum Pontus. Justus Perthes,

Gotha, Germany.

- Vött, A., Brückner, H., Handl, M., Schriever, A., 2006. Holocene palaeogeographies of the Astakos coastal plain (Akarnania, NW Greece). *Palaeogeography, Palaeoclimatology, Palaeoecology* 239, 126–146.
- Walker, M., Head, M.J., Lowe, J., Berkelhammer, M., Björck, S., Cheng, H., Cwynar, L.C., Fisher, D., Gkinis, V., Long, A., Newnham, R., Rasmussen, S.O., Weiss, H., 2019. Subdividing the Holocene Series/Epoch: formalization of stages/ages and subseries/subepochs, and designation of GSSPs and auxiliary stratotypes. *Journal of Quaternary Science* 34, 173–186.
- Walker, R.T., Fattahi, M., 2011. A framework of Holocene and Late Pleistocene environmental change in eastern Iran inferred from the dating of periods of alluvial fan abandonment, river terracing, and lake deposition. *Quaternary Science Reviews* 30, 1256–1271.
- Walsh, K., 2013. *The Archaeology of Mediterranean Landscapes: Human-Environment Interaction from the Neolithic to the Roman Period*. Cambridge University Press, Cambridge, United Kingdom.
- Walsh, K., Berger, J.-F., Roberts, C.N., Vanniére, B., Ghilardi, M., Brown, A.G., Woodbridge, J., Lespez, L., Estrany, J., Glais, A., Palmisano, A., Finné, M., Verstraeten, G., 2019. Holocene demographic fluctuations, climate and erosion in the Mediterranean: A meta data-analysis. *The Holocene* 29, 864–885.
- Walstra, J., Heyvaert, V., Verkinderen, P., 2009. Remote sensing for the study of fluvial landscapes in Lower Khuzestan, SW Iran, in: Paron, P. (Ed.), *Geomorphological Mapping: Methods and Applications*. Elsevier, Leicester, United Kingdom, pp. 551–575.
- Wang, J., Zhen, J., Hu, W., Chen, S., Lizaga, I., Zeraatpisheh, M., Yang, X., 2023. Remote sensing of soil degradation: Progress and perspective. *International Soil and Water Conservation Research* 11, 429–454.
- Wang, Y., Amundson, R., Trumbore, S., 1996. Radiocarbon Dating of Soil Organic Matter. *Quaternary Research* 45, 282–288.
- Wanner, H., Beer, J., Bütikofer, J., Crowley, T.J., Cubasch, U., Flückiger, J., Goosse, H., Grosjean, M., Joos, F., Kaplan, J.O., Küttel, M., Müller, S.A., Prentice, I.C., Solomina, O., Stocker, T.F., Tarasov, P., Wagner, M., Widmann, M., 2008. Mid- to Late Holocene climate change: an overview. *Quaternary Science Reviews* 27, 1791–1828.
- Warren, S.D., Mitasova, H., Hohmann, M.G., Landsberger, S., Iskander, F.Y., Ruzycski, T.S., Senseman, G.M., 2005. Validation of a 3-D enhancement of the Universal Soil Loss Equation for prediction of soil erosion and sediment deposition. *Catena* 64, 281–296.
- Wei, T., Simko, V., 2021. R package 'corrplot': Visualization of a Correlation Matrix (Version 0.92). Last accessed on May 2023: <https://github.com/taiyun/corrplot>.
- Weiberg, E., Bevan, A., Kouli, K., Katsianis, M., Woodbridge, J., Bonnier, A., Engel, M., Finné, M., Fyfe, R., Maniatis, Y., Palmisano, A., Panajiotidis, S., Roberts, C.N., Shennan, S., 2019a. Long-term trends of land use and demography in Greece: A

comparative study. *The Holocene* 29, 742–760.

- Weiberg, E., Bonnier, A., Finné, M., 2021. Land use, climate change and 'boom-bust' sequences in agricultural landscapes: Interdisciplinary perspectives from the Peloponnese (Greece). *Journal of Anthropological Archaeology* 63, 1–12.
- Weiberg, E., Finné, M., 2022. Human-environment dynamics in the ancient Mediterranean. Keywords of a research field. *Opuscula. Annual of the Swedish Institutes at Athens and Rome* 15, 221–252.
- Weiberg, E., Hughes, R.E., Finné, M., Bonnier, A., Kaplan, J.O., 2019b. Mediterranean land use systems from prehistory to antiquity: a case study from Peloponnese (Greece). *Journal of Land Use Science* 14, 1–20.
- Weiss, A., 2001. Topographic position and landforms analysis. ESRI user conference (Poster Presentation), San Diego, California, United States.
- Weiss, H., 2016. Global megadrought, societal collapse and resilience at 4.2–3.9 ka BP across the Mediterranean and west Asia. *PAGES MAGAZINE* 24, 62–63.
- Weninger, B., Alram-Stern, E., Bauer, E., Clare, L., Danzeglocke, U., Jöris, O., Kubatzki, C., Rollefson, G., Todorova, H., van Andel, T., 2006. Climate forcing due to the 8200 cal yr BP event observed at Early Neolithic sites in the eastern Mediterranean. *Quaternary Research* 66, 401–420.
- Wessel, B., Huber, M., Wohlfart, C., Marschalk, U., Kosmann, D., Roth, A., 2018. Accuracy assessment of the global TanDEM-X Digital Elevation Model with GPS data. *ISPRS Journal of Photogrammetry and Remote Sensing* 139, 171–182.
- Wilkinson, T.J., 1999. Holocene Valley fills of Southern Turkey and Northwestern Syria: Recent geoarchaeological contributions. *Quaternary Science Reviews* 18, 555–571.
- Wilkinson, T.J., 2005. Soil erosion and valley fills in the Yemen highlands and southern Turkey: Integrating settlement, geoarchaeology, and climate change. *Geoarchaeology* 20, 169–192.
- Williams, J.R., 1975. Sediment routing for agricultural watersheds. *JAWRA Journal of the American Water Resources Association* 11, 965–974.
- Williamson, C.G., 2016. Mountain, Myth, and Territory: Teuthrania as Focal Point in the Landscape of Pergamon, in: McInerney, J., Sluiter, I. (Eds.), *Valuing Landscape in Classical Antiquity: Natural Environment and Cultural Imagination*. Brill, Leiden, the Netherlands, pp. 70–99.
- Wischmeier, W.H., Johnson, C.B., Ross, B.V., 1971. A soil erodibility nomograph for farmland and construction sites. *Journal of Soil and Water Conservation* 26, 189–193.
- Wischmeier, W.H., Smith, D.D., 1978. Predicting Rainfall Erosion Losses. A Guide to Conservation Planning. *The USDA Agricultural Handbook*, No. 537, 1–58.
- Wolf, D., Faust, D., 2015. Western Mediterranean environmental changes: Evidences from fluvial archives. *Quaternary Science Reviews* 122, 30–50.
- Woodbridge, J., Roberts, C.N., Palmisano, A., Bevan, A., Shennan, S., Fyfe, R., Eastwood, W.J., Izdebski, A., Çakırlar, C., Woldring, H., Broothaerts, N., Kaniewski,

- D., Finné, M., Labuhn, I., 2019. Pollen-inferred regional vegetation patterns and demographic change in Southern Anatolia through the Holocene. *The Holocene* 29, 728–741.
- Woodward, J., 2009. *The Physical Geography of the Mediterranean*, 1st ed. Oxford University Press, New York, United States.
- Wulf, U., 1994. Der Stadtplan von Pergamon: zu Entwicklung und Stadtstruktur von der Neugründung unter Philetairos bis in spätantike Zeit. *Istanbuler Mitteilungen* 44, 135–175.
- Xoplaki, E., Fleitmann, D., Luterbacher, J., Wagner, S., Haldon, J.F., Zorita, E., Telelis, I., Toreti, A., Izdebski, A., 2016. The Medieval Climate Anomaly and Byzantium: A review of the evidence on climatic fluctuations, economic performance and societal change. *Quaternary Science Reviews* 136, 229–252.
- Yang, X., Becker, F., Knitter, D., Schütt, B., 2021. An Overview of the Geomorphological Characteristics of the Pergamon Micro-Region (Bakırçay and Madra River Catchments, Aegean Region, West Turkey). *Land* 10, 1–27.
- Yang, X., Becker, F., Nykamp, M., Ludwig, B., Doğan, M., Doğan, T., Knitter, D., Schütt, B., 2023a. Mid- to Late Holocene geomorphodynamics in a long-term settled mountain catchment in the Pergamon micro-region, western Turkey. *Quaternary Research* 114, 69–92.
- Yang, X., Becker, F., Nykamp, M., Ludwig, B., Doğan, M., Schütt, B., 2023b. Holocene geomorphodynamics of a rural catchment in the Pergamon micro-region (eastern Mediterranean). *The Holocene* 33, 1407–1427.
- Yang, X., Becker, F., Nykamp, M., Schütt, B., 2022. Dataset of sediment analyses (pH, electrical conductivity, magnetic susceptibility, loss on ignition, and X-ray fluorescence) from the Tekkedere catchment in the Pergamon Micro-Region, western Turkey, in: Yang, X. (Ed.). *Pangaea*.
- Yang, X., Becker, F., Nykamp, M., Schütt, B., 2023c. Dataset of sediment analyses (pH, electrical conductivity, magnetic susceptibility, loss on ignition, and X-ray fluorescence) from the Deliktaş catchment in the Pergamon micro-region, western Türkiye, in: Yang, X. (Ed.). *Pangaea*.
- Yilmaz, H., Oyman, T., Arehart, G.B., Colakoglu, A.R., Billor, Z., 2007. Low-sulfidation type Au–Ag mineralization at Bergama, Izmir, Turkey. *Ore Geology Reviews* 32, 81–124.
- Yilmaz, H., Oyman, T., Sönmez, F.N., Arehart, G.B., Billor, Z., 2010. Intermediate sulfidation epithermal gold-base metal deposits in Tertiary subaerial volcanic rocks, Sahinli/Tespil Dere (Lapseki/Western Turkey). *Ore Geology Reviews* 37, 236–258.
- Yilmaz, Y., Genç, Ş.C., Gürer, F., Bozcu, M., Yilmaz, K., Karacik, Z., Altunkaynak, Ş., Elmas, A., 2000. When did the western Anatolian grabens begin to develop?, in: Bozkurt, E., Winchester, J.A., Piper, J.D.A. (Eds.), *Tectonics and Magmatism in Turkey and the Surrounding Area*. Geological Society of London, London, United Kingdom, pp. 353–384.
- Yu, Y., Wu, H., Finke, P.A., Guo, Z., 2016. Spatial and temporal changes of prehistoric human land use in the Wei River valley, northern China. *The Holocene* 26, 1788–

1801.

- Zanchetta, G., Sulpizio, R., Roberts, N., Cioni, R., Eastwood, W.J., Siani, G., Caron, B., Paterne, M., Santacroce, R., 2011. Tephrostratigraphy, chronology and climatic events of the Mediterranean basin during the Holocene: An overview. *The Holocene* 21, 33–52.
- Zangger, E., 1992. Neolithic to present soil erosion in Greece, in: Bell, M., Boardman, J. (Eds.), *Past and Present Soil Erosion: Archaeological and Geographical Perspectives*.
- Zhang, H., Cheng, H., Sinha, A., Spötl, C., Cai, Y., Liu, B., Kathayat, G., Li, H., Tian, Y., Li, Y., Zhao, J., Sha, L., Lu, J., Meng, B., Niu, X., Dong, X., Liang, Z., Zong, B., Ning, Y., Lan, J., Edwards, R.L., 2021. Collapse of the Liangzhu and other Neolithic cultures in the lower Yangtze region in response to climate change. *Science Advances* 7, 1–9.
- Zimmermann, M., 2011. *Pergamon. Geschichte, Kultur, Archäologie*. C.H. Beck, München, Germany.
- Zimmermann, M., Matthaei, A., Ateş, G., 2015. Die Chora von Pergamon: Forschungen im Kaikostal und in der antiken Stadt Atarneus, in: Matthaei, A., Zimmermann, M. (Eds.), *Urbane Strukturen und bürgerliche Identität im Hellenismus*. Verlag Antike, Heidelberg, Germany, pp. 193–236.



# Supplementary materials

## To chapter 1

**Table S1.1** The summary of names of mountains and Bakırçay river used by different scholars.

Karadağ mountain	Kozak mountain	Yuntdağ mountain	Bakırçay river	Reference
Kara D. Aiga - oros	Kosak	Jürt - Dagħ	Kaikos	(Von Diest, 1889)
Kara Dağ Kane Oros (ancient name)	Kosak Pindasos (ancient name)	Jünd Dağ Aspordenon (ancient name)	Kaikos	(Berlet, 1911)
--	Madaras - Dağ Pindasos (ancient name)	Jünd - Dağ Aspordenon (ancient name)	Kaikos	(Conze, 1912)
--	Kozak Mountains	--	--	(Kuzucuoğlu, 1995)
--	Mount Kozak Kozak Horst	Yuntdağ mountain Maruflar Horst	--	(Yılmaz et al., 2000)
--	--	Yuntdağ Volcanic complex	--	(İnci, 2002)
Karadağ	Madra Dağ	Zeytindağ Highland	--	(Ölgen, 2004)
Dikili-Çandarlı high Dikili-Çandarlı Volcanics	--	--	--	(Karacik et al., 2007)
--	Madra Mountain	--	--	(Lambrianides and Spencer, 2007)
Kara Dağ	Kosak Madradağ Gürondağ	Yünd Dağ	Kaikos Bakır Çay	(Sommerer, 2008)
Kane Peninsula	Kozak Horst	Zeytindağ Horst Yuntdağ Mountain Complex	--	(Seeliger et al., 2013)
Karadağ massif	Kozak Horst	Maruflar Horst	--	(Schneider et al., 2014)

Karadağ mountain	Kozak mountain	Yuntdağ mountain	Bakırçay river	Reference
Karadağ Mountains Kane Peninsula	Kozak Mountains	Yuntdağ Mountains	--	(Seeliger et al., 2014)
Kane Peninsula Karadağ	Kozak Horst Kozak Mountain Complex	Zeytindağ Horst Yuntdağ Mountain Complex	--	(Seeliger et al., 2019)
Kara Dağı	Kozak Madra Dağı	Yund Dağı	Bakırçay	(Ludwig, 2020b)
--	Kozak mountain	Yuntdağ mountains Maruflar horst	Bakırçay	(Becker et al., 2020a)
--	Pindasos	Aspordenon	--	(Laabs and Knitter, 2021)
--	Madra Dağı	Yunt Mountains	--	(Sanğu et al., 2020)
Kara Dağı Mountains	Kozak Mountains	Yunt Dağı Mountains	Bakırçay River	(Yang et al., 2021; Yang et al., 2023a)
Karadağ mountain	Kozak mountain	Yuntdağ mountain	Bakırçay river	(Yang et al., 2023b)

## To chapter 2

**Table S2.1** The summary of the geomorphodynamics and dominating drivers in the Mediterranean region.

Study area	Study period	Geomorphodynamics	Dominating drivers	Reference
S Greece	Late Quaternary	Landscape stability: Early Holocene to ca. 4.5 ka BP; many upheavals of the later Bronze Age, the Dark Ages, the early historical period, and the late Roman period. Increased debris flows and widespread aggradation: ca. 4.5 ka BP (land clearance in the Early Bronze Age); 2.3 - 2 ka BP; 1 ka BP (expanded maquis clearance).	Human activity (land clearing, or lack conservation) after 4.5 ka BP	(Pope and van Andel, 1984)
Greece	Holocene	Increased soil erosion: at the Neolithic/Early Bronze Age transition	human cause of prehistoric deforestation	(Zangger, 1992)
S Greece	Holocene	Increased colluviation: 9 ka BP (onset of the Neolithic; the start of farming activities); 4 ka BP (Middle and Late Bronze Age); 2.1–1.5 ka BP (the Roman period); since 0.4 ka BP. Reduced colluviation: 6.5–4 ka BP (Chalcolithic to the Early Bronze Age); 3–2.7 ka BP (Early Iron Age). Landscape stability: no.	Human activity	(Fuchs et al., 2004)
S Greece	Holocene	High sedimentation rates: 9 ka BP (Early Neolithic).	Trigger: human activity; Amplification: high precipitation.	(Fuchs, 2007)
S Greece	Holocene	High water level: 10.9–7.7 ka BP (wet climate). Increased sediment deposition: ca. 8.2 ka BP (climate shift)	Climate	(Stamatis et al., 2022)

Study area	Study period	Geomorphodynamics	Dominating drivers	Reference
N Italy	Holocene	Rapid landward migration of a barrier-estuary-lagoon system: Early–Middle Holocene. Extensive delta progradation: since 6 ka BP.	Sea level change	(Amorosi et al., 2005)
S Italy	Holocene	Increased fluvial activity: 7.2–6.8; 4.8–4.5; 4.3–4.1; 3.4–3.1; 2.3–1.8; 1.7–1.3; 1–0.8, and 0.3–0.12 ka BP.	Primary driver: climate; Intensification: human impact.	(Piccarreta et al., 2011)
N Spain	Late Quaternary	Increases landslide: ca. 5.5 ka (Neolithic revolution); 0.2 ka BP (Industrial revolution).	Human activity	(Remondo et al., 2005)
N Tunisia	Late Holocene	Increased fluvial dynamics: ca. 4.7, 3.0, 1.7, 1.0, 0.7, and 0.4 ka cal BP. Alluvial soils: Antiquity, ca. 1.3, 0.8, and 0.5 ka cal BP.	Climate	(Faust et al., 2004)
SW Türkiye	Holocene	General colluvial stable: since 4 ka BP. Major colluviation / upper valley alluviation: ca. 2.5 ka BP. Major lower valley alluviation: since 1 ka BP.	Human activity	(Dusar et al., 2012)
Israel	Mid- to Late Holocene	High sedimentation rate: ca. 2.8 ka BP	Human activity	(Ackermann et al., 2014a)
Mediterranean	Holocene	Extremely rapid silting up: since Neolithic (new agricultural practices) Deltaic development: since 3 ka BP Rapid delta growth: Roman period Progradation dynamic: Little Ice Age (strong rural population growth)	Human activity	(Anthony et al., 2014)
C Türkiye	Late Quaternary	Fluvial activity: Late Glacial times ( $15.4 \pm 2.5$ , $12.8 \pm 3.1$ ka BP) and frequently after Roman times. Slope and soil erosion: Early ( $10.6 \pm 1.4$ , $8.2 \pm 0.7$ ka BP); Middle Holocene ( $6.7 \pm 0.9$ , $5.4 \pm 0.7$ – $4.7 \pm 0.7$ ka BP), and Late Holocene ( $2.8$ – $2.3$ , $2.1$ – $1.6$ ka BP, and since 1 ka BP).	Human activity	(Dreibrodt et al., 2014)

Study area	Study period	Geomorphodynamics	Dominating drivers	Reference
W Mediterranean	Late Quaternary	Supra-regional floodplain sedimentation: 8–7, 5–3.8, 2.2–1.5, ca. 1, and 0.4 ka BP. Supra-regional soil formation: 13.3–12.7, 7–5.1, 2.8–2.3, 1.4–1.2, and 0.8–0.5 ka BP.	Climatic aridification events and phases of climate change	(Wolf and Faust, 2015)
W Türkiye	Late Holocene	High sedimentation rate: since 2.8 ka BP, particularly since the Hellenistic period Decline: 1.5 - 1 ka BP (the influence of Ephesus declined)	Human activity (deforestation, ploughing agriculture, and goat grazing)	(Stock et al., 2016)
W Türkiye	Holocene	Higher fluvial activity: ca. 10.3–8.3 ka BP	Humid climate and active tectonics	(Bulkan et al., 2018)
NE Spain	Holocene	Sedimentation: 8.4/8.1–7.2 ka BP; 7–6.8 ka BP (drier condition, Neolithic societies); 6.7–4.2 ka BP; 1–0.3 ka BP (Middle Ages). Stable period: 7.2–7 ka BP (a wetter climate); 6.8–6.6 ka BP.	Wetter climate: Early Holocene; Human: Late Holocene	(Pérez-Lambán et al., 2018)
N Greece	Late Quaternary	Catchment-wide erosion processes: Late Glacial and the Early Holocene (wetter climates). Hillslope stabilization: Middle Holocene (vegetation cover: dense woodland). Soil degradation: Late Holocene (human land use).	Climate: Early Holocene Vegetation: Middle Holocene Human: Late Holocene	(Francke et al., 2019)
E Mediterranean	Holocene	12–6/5 ka BP: moderate dynamics and related with the enhanced precipitation; (2) 6/5–1.5 ka BP: stepwise increasing dynamics and human impact became more widespread; (3) 1.5–0 ka BP: dramatically decreased dynamics after the Roman Period probably related to climate drying and population decreasing, and progressively increase afterward.	Climate: main driver (Early Holocene); Human impact: widespread at some point (likely since the Bronze Age).	(Dusar et al., 2011)



## To chapter 4 (working package 1)

**Table S4.1** The definition and classification rules of landform units for the geomorphological map (modified from Walstra et al. (2009)).

Landform unit* <sup>1</sup>	Definition	Classification rules based on different sources* <sup>2</sup>
<b>Upland</b>		
Ridge	The chain of hills; generally higher than the surrounding slopes from certain distance	Merged by the geomorphons classes <i>summit</i> and <i>ridge</i> (Dg).
Slope with debris cover	The slope areas covered by vegetation and debris	Merged by the geomorphons classes <i>shoulder</i> , <i>spur</i> and <i>slope</i> (Dg); slope with bare rock (see below) was excluded.
Slope with bare rock	Bare solid bedrock exposed on the mountainous surface; vegetation, soil and sediment covers are sparse or lacking	Bright color in the satellite imagery; no obvious vegetation cover (GE).
Valley without fluvial deposits	Intramountainous valleys without infill fluvial deposits	First, geomorphons classes <i>hollow</i> , <i>footslope</i> , <i>valley</i> and <i>depression</i> in the mountains were merged into valley; then, valley without fluvial deposits was extracted by subtracting the fluvial infill valley (Dg).
Valley with fluvial deposits	Intramountainous valleys filled with fluvial deposits	F; valley cross profiles show a saucer shape (De); often used as an arable land (GE).

Landform unit* <sup>1</sup>	Definition	Classification rules based on different sources* <sup>2</sup>
<b>Lowland</b>		
Colluvial zone	Connecting area between the elevated mountain and the plain; generally covered by loose, unconsolidated colluvial sediments and alluvial fans (Goudie, 2004)	Elevation decreases from the elevated area to plain (Ds); L2 and L3.
Alluvial plain	Largely flat terrain adjacent to main river	Generally flat (Ds); often used as irrigated arable land (GE).
Littoral plain	The flat–gently inclined area adjacent to the Aegean Sea and covered by intercalated terrestrial, littoral and marine deposits	Generally flat (De); often used as an irrigated land or other agricultural areas (GE); L3.
Delta	The area formed at the river mouth to the sea and filled within fluvio–littoral sediments	Delta-shaped (GE); L3 and L4.
Alluvial fan	Fan-shaped body, deposited by avulsive channels which emerge from a mountainous catchment to an adjoining valley (Blair and McPherson, 2009)	Fan shape, elevation decreases from fan apex to toe (De, Dh, Ds, GE); L2.
Perennial stream	Natural watercourse	L1.
Intermittent stream	Natural watercourse; always ceases to flow in dry periods	L1.
Paleochannel	Abandoned river channel	Curved structure on the plain and separated from the main river (Dh); usually holds water (GE).
Assumed paleochannel	Older abandoned river channel or oxbow	Curved structure (Dh) with 1–2 m elevation difference to the adjacent plain (De); water is not visible at least during dry seasons, and color in the satellite imageries shows different tone (darker) to the adjacent area (GE); F.

Landform unit* <sup>1</sup>	Definition	Classification rules based on different sources* <sup>2</sup>
<b>Anthropogenic</b>		
Reservoir	Water body closed by dam within the intramountainous valley	CLC; dark (blue) and broadened water surface (GE); sometimes bright-colored sediments when low water stands (GE).
Mining area	Surface mine or quarry, including those currently in use and abandoned ones	CLC; bright-colored bare surface with artificial terrain (GE).
Agricultural terrace area	Area with artificial terraces	Continuous or discontinuous lines with intervals between 1 and 20 m (sometimes up to 50 m), always developed along contour lines (GE); F.
Irrigation/drainage canal	Artificial watercourse for irrigation or drainage of the cultivated land	Dark, straight line on the plain (GE); F.

\*1 Other features, e.g., small water bodies, settlements and roads, were merged into their nearest classification.

\*2 GE: Google Earth (last accessed 8 June 2020); D: TanDEM-X (e: elevation; h: hillshade; s: slope; g: geomorphons); CLC: Corine Land Cover 2018 (Cole et al., 2018); F: field observation; L: literature (1: (Emre and Doğan, 2010; Emre et al., 2011a; Emre and Özalp, 2011; Emre et al., 2011b); 2: (Schneider et al., 2013; Schneider et al., 2014; Schneider et al., 2015; Schneider et al., 2017); 3:(Lambrianides and Spencer, 2007); 4: (Seeliger et al., 2019)). The order shows the priority of different sources.

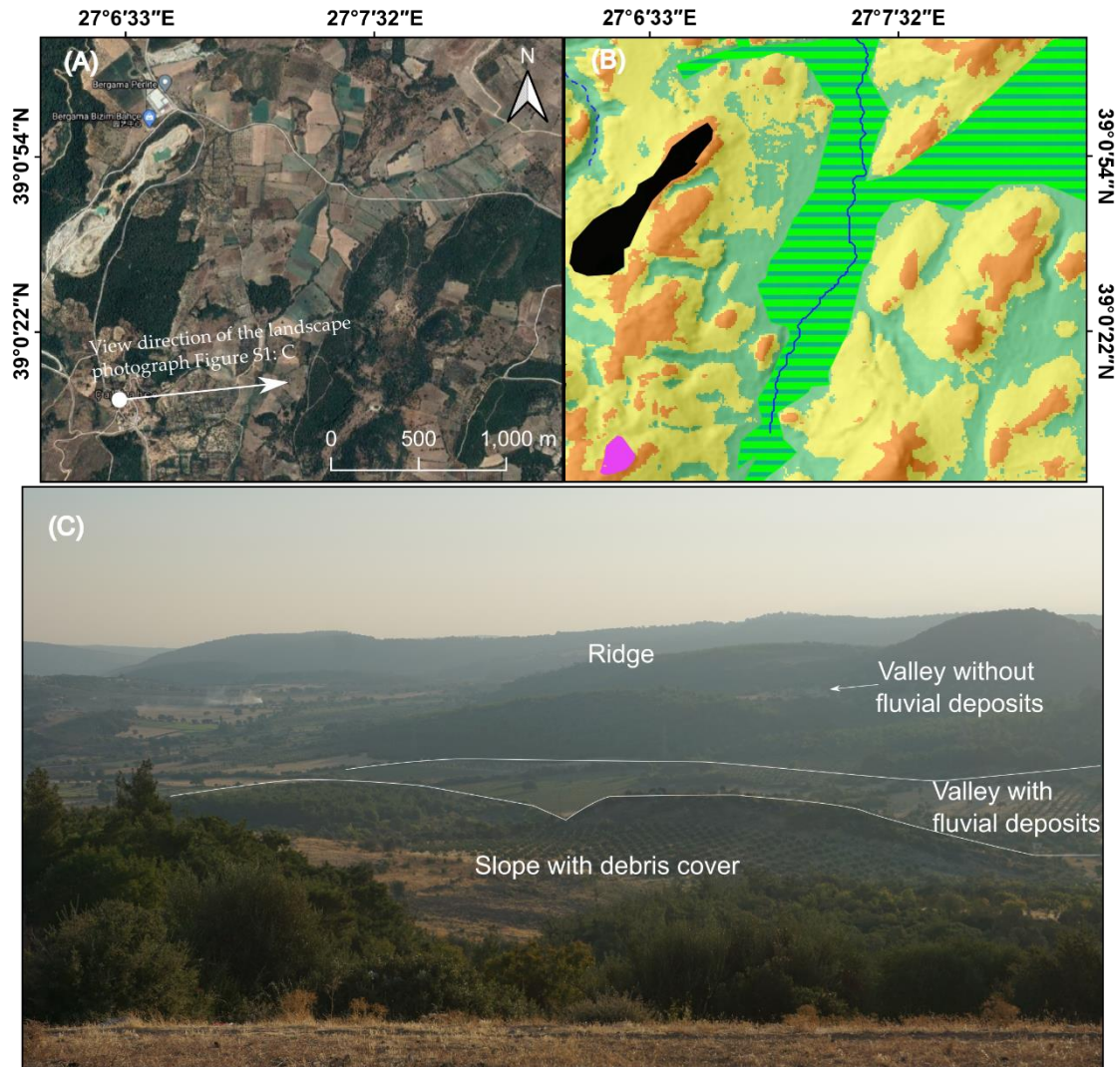


**Figure S4.1** Çalıbahçe basin, indicating how we use the satellite images and geomorphons to generate the geomorphological map (ridge, valley without fluvial deposits, valley with fluvial deposits and slope with debris cover) and the validation in the field. (A) Data: Google Earth satellite images (WorldView-2, last accessed 8 June 2020). (B) Geomorphological map (legend refers to Figure 4, same below). (C) Landscape photograph.

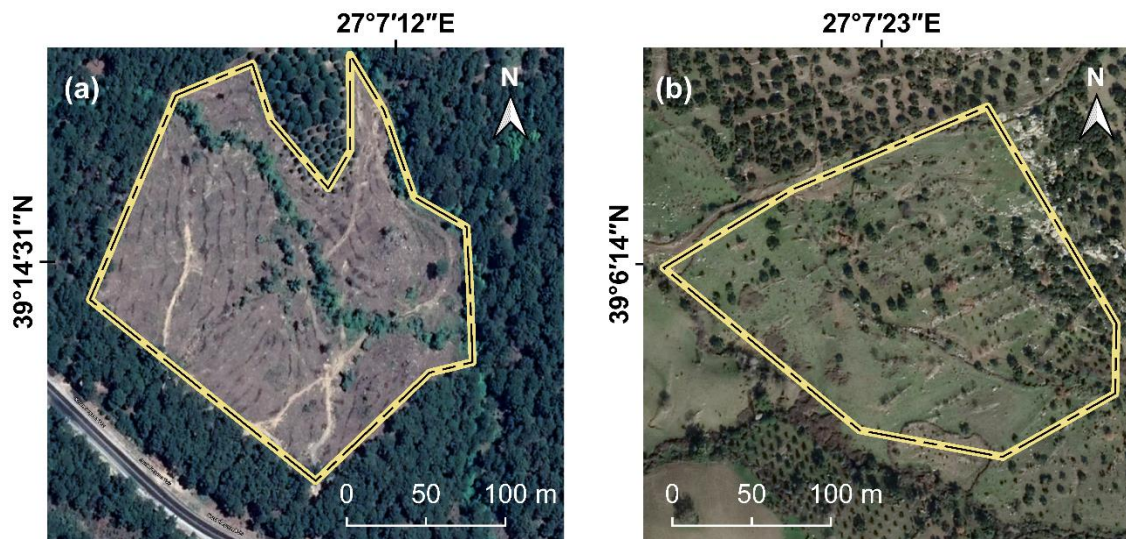


**Figure S4.2.** Terrace examples: continuous (a) and discontinuous (b). Data: Google Earth satellite images (WorldView-2, last accessed 8 June 2020).

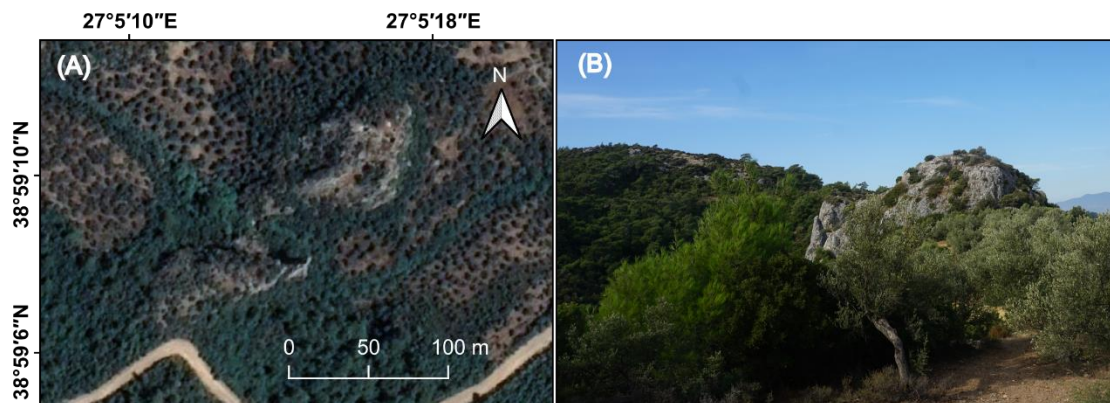


**Figure S4.3** Slope with bare rock in Tekkedere valley. (A) Data: Google Earth satellite images (WorldView-2, last accessed 8 June 2020). (B) Landscape photograph.

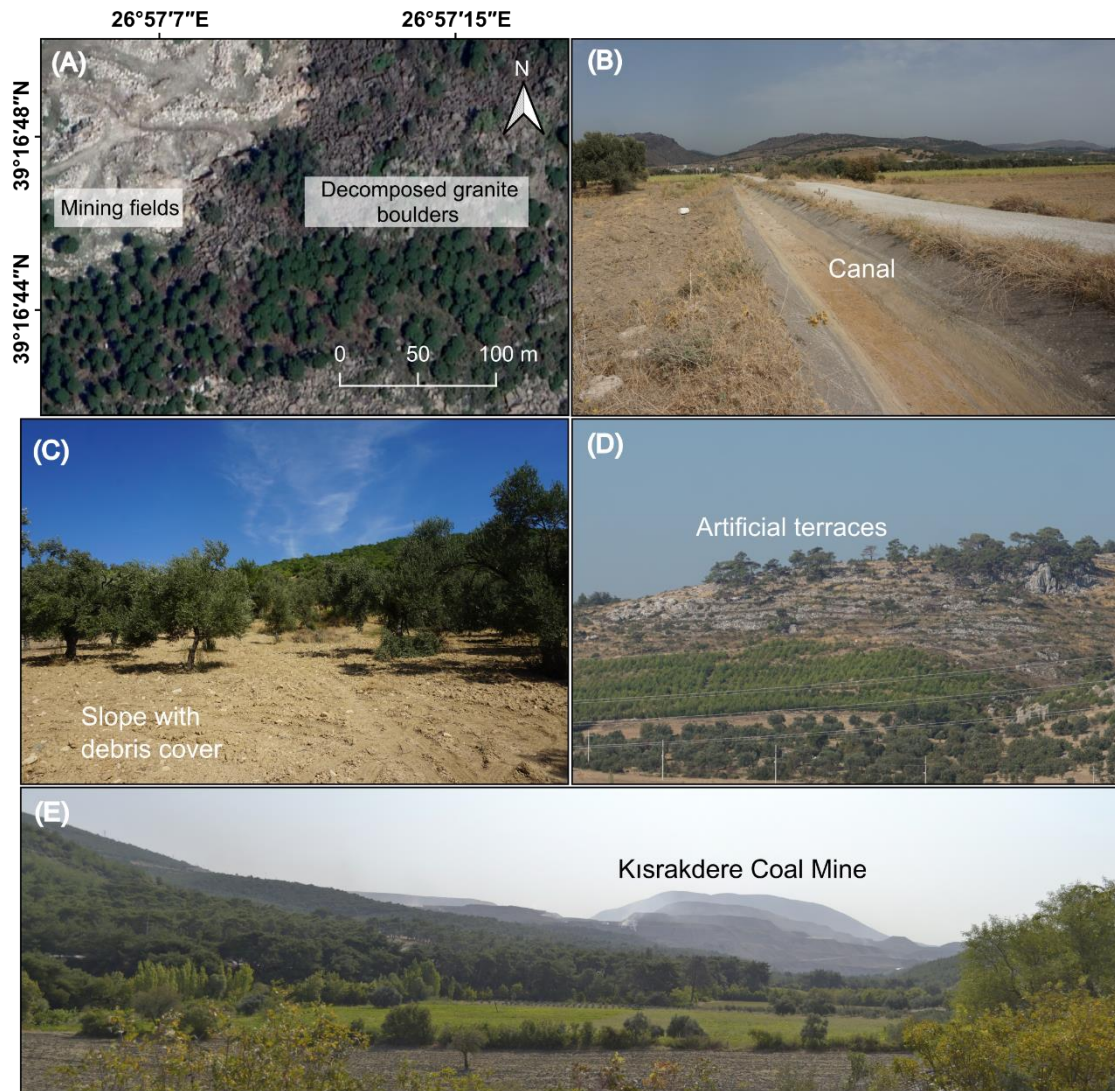


**Figure S4.4** (A) An example of mining fields and decomposed granite boulders at the northwestern slopes of the Kozak interior plain (subunit 2.1). Data: Google Earth satellite images (WorldView-2, last accessed 8 June 2020). Photographs of a canal on the Bergama Fan (B), slope with debris cover in the Tekkedere valley (C), artificial terraces in Çalibahçe basin (D), Kısradere Coal Mine (E).

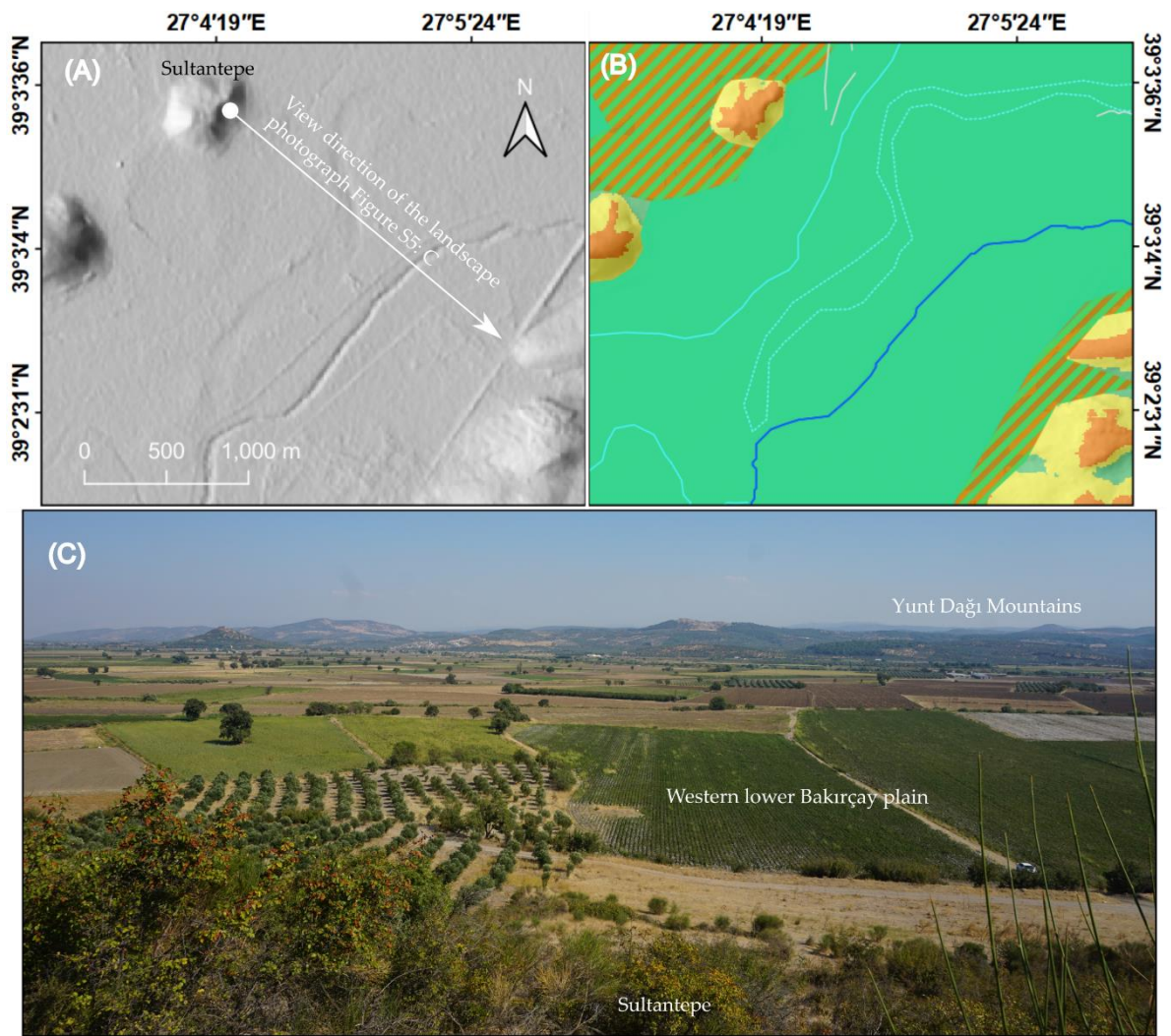


**Figure S4.5** The western lower Bakırçay plain from the Sultantepe to the Yunt Dağı Mountains. (A) The hillshade of TanDEM-X data, indicating the features of alluvial plain and paleochannels which are highlighted in Figure S4.5: B. (B) Geomorphological map. (C) Landscape photograph.

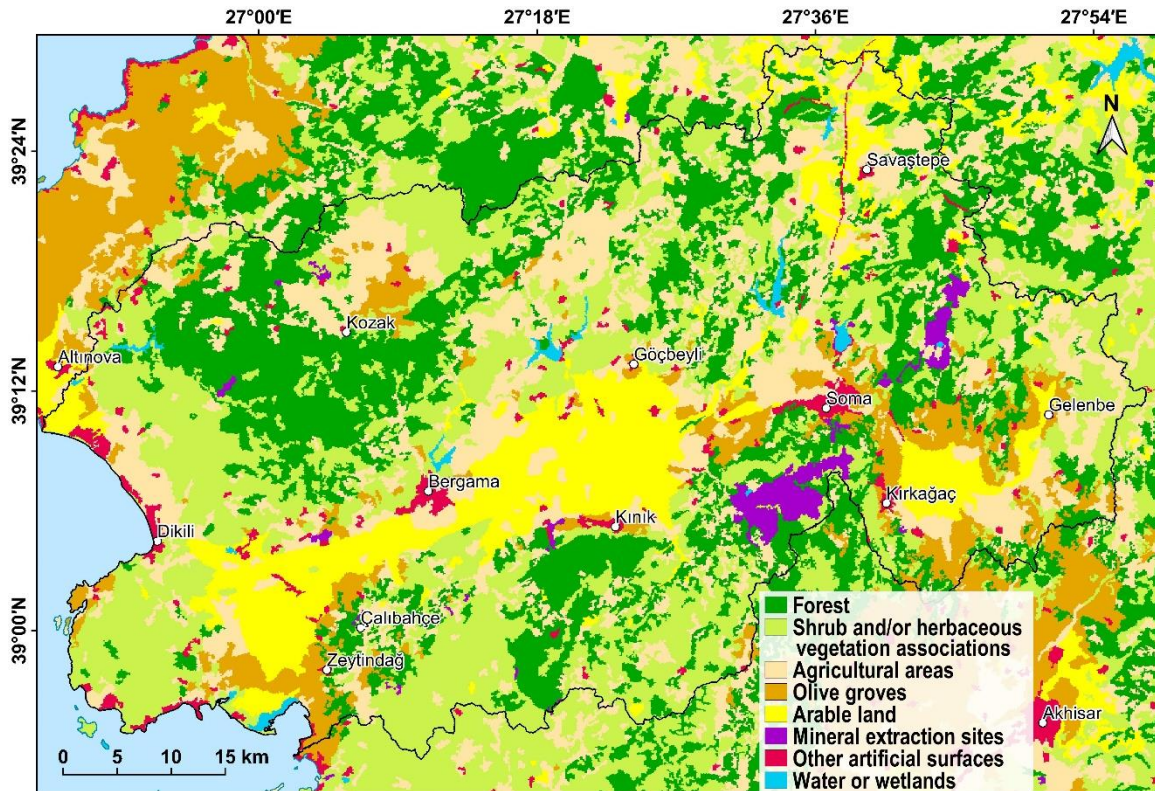


**Figure S4.6** The land cover map of the Bakırçay and Madra River catchments and the adjacent coastal areas. Data: Corine Land Cover (CLC) 2018 (Version 2020\_20u1) (Cole et al., 2018).

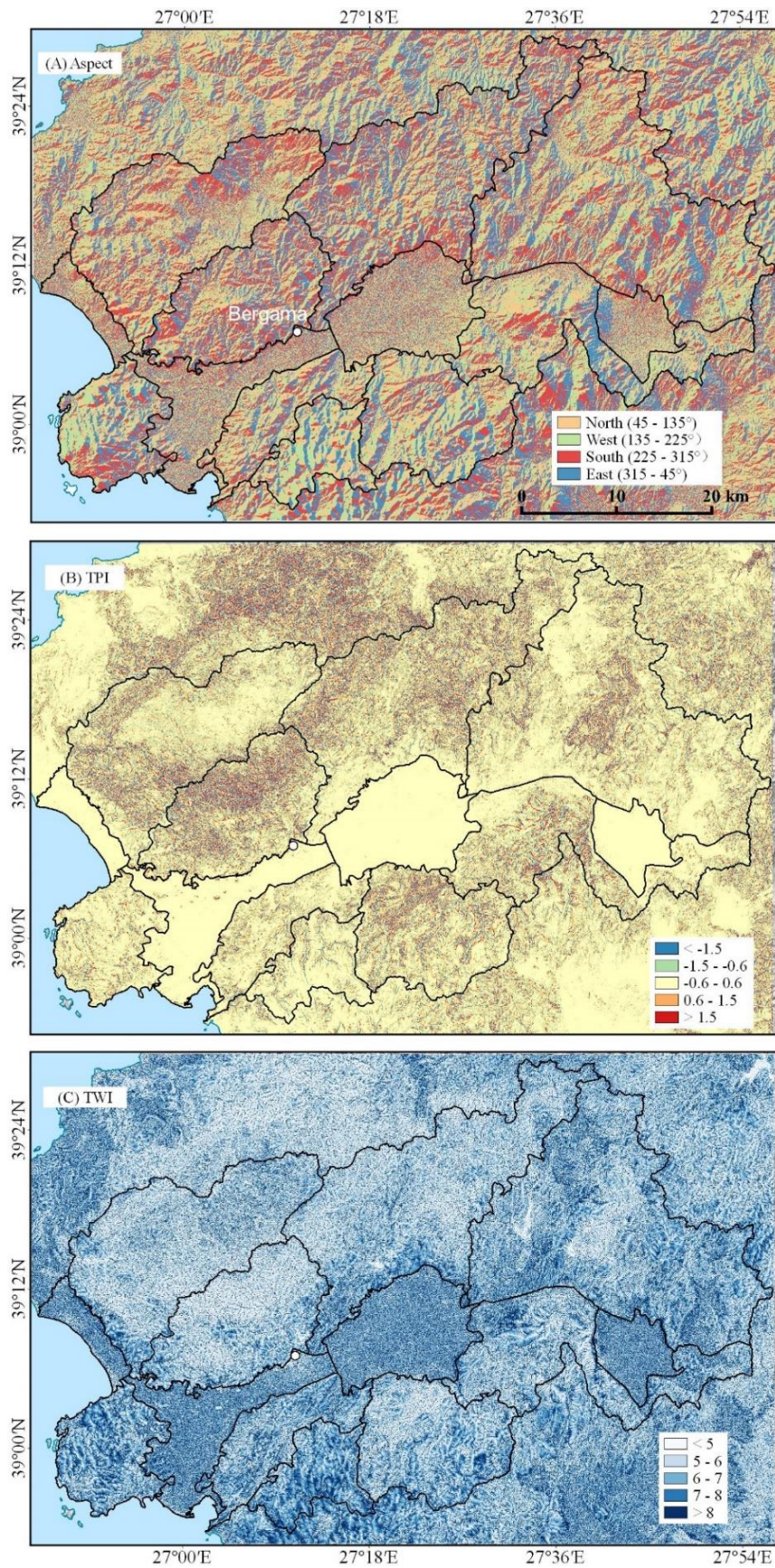


**Figure S4.7** Additional geomorphometric parameter maps derived from TanDEM-X data. (A) Aspect. (B) Topographic Position Index (TPI). (C) Topographic Wetness Index (TWI).



## To chapter 5 (working package 2)

The sediment profiles in the supplementary material were taken from the Tekkedere valley infill (Tek-1 and Tek-3) and the Tekkedere alluvial fan (Tek-4, Tek-4-2, and Tek-5-2) (Figure S5.1). The detailed description of the sediment profiles and the analyzed measurements are shown in the text and the corresponding illustrations. Raw data of the measurements and the calculation results of the proxies according to different units can be found in Yang et al. (2022).

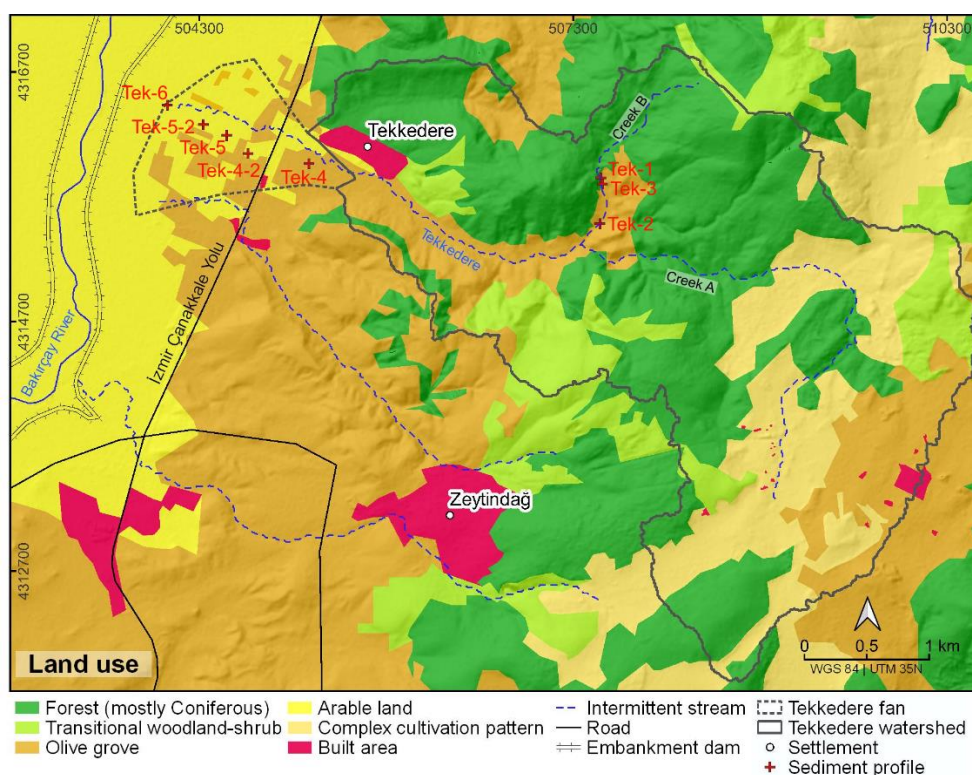


**Figure S5.1** The location of the sediment profiles and the land use (data based on Corine Land Cover data (Cole et al., 2018)) in the surroundings of the Tekkedere catchment.

### Tekkedere valley infill: Sediment profile Tek-1

Sediment profile **Tek-1** is located close to the headwater area of Tekkedere creek B (Figure S5.1). The profile has a total thickness of 176 cm and shows 6 macroscopically distinguishable units of silty/sandy and pebbly layers (Figure S5.2). Roots are present in most units. The sediments are mostly strongly calcareous and they are slightly alkaline (pH: 7.7 (0), n = 14) throughout the profile. Electrical conductivity values (EC: 172 (6)  $\mu\text{S}/\text{cm}$ , class 1, n = 14) are very low and show a slightly increasing trend with decreasing depth. Magnetic susceptibility values ( $X_{\text{LF}}$ : 11 (2)  $10^{-8} \text{ m}^3/\text{kg}$ , class 1, n = 14) are very low

and a slight peak ( $16 \cdot 10^{-8} \text{ m}^3/\text{kg}$ ) occurs in the middle part of the profile (ca. 120–100 cm below surface [bs]).  $\text{LOI}_{550}$  values (3.5 (0.4) mass%, class 3,  $n = 14$ ) show a small increase at 120–100 cm bs and continue to increase in the upper part of the profile.

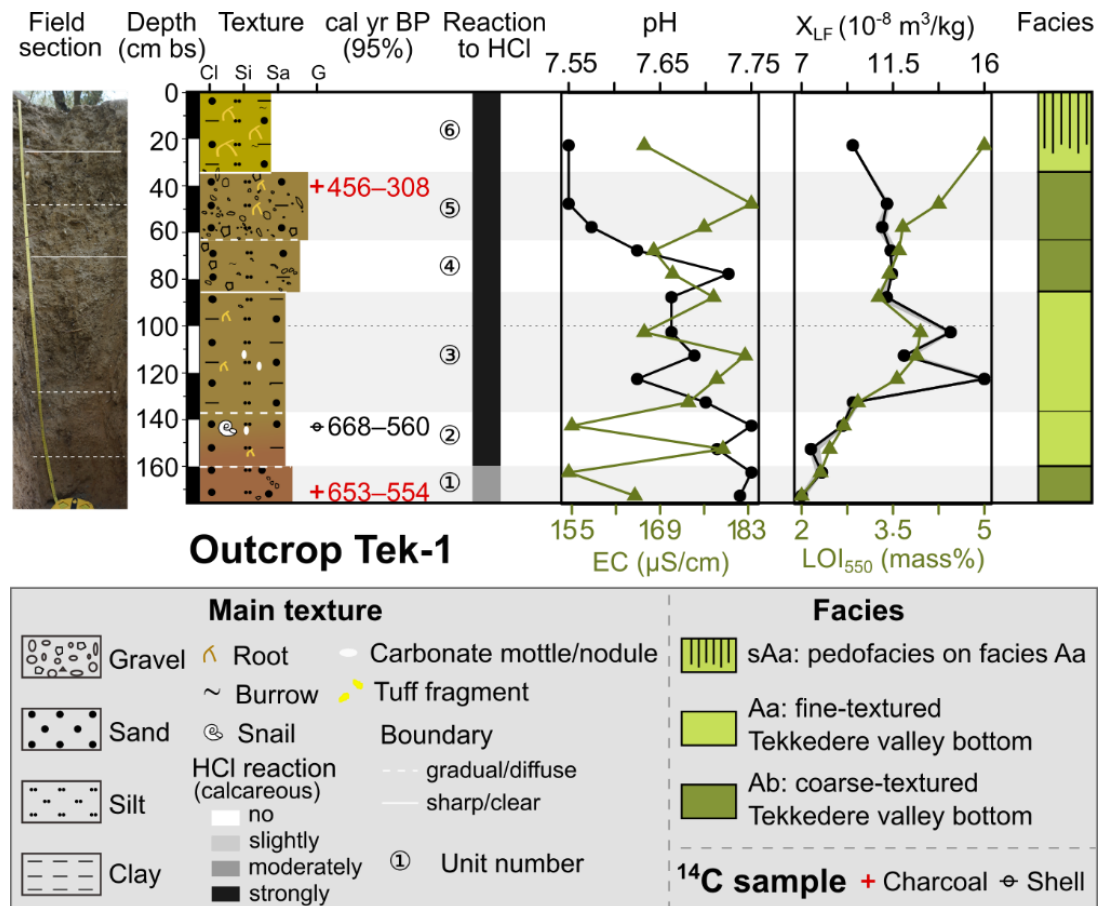


**Figure S5.2** The lithostratigraphy, radiocarbon dates, and sediment analyses of outcrop Tek-1. The color of the sediment texture column represents the color observed in the field. The shaded band represents the different units and the dashed line refers to the depth in every meter.

**Unit 1 (176–160 cm bs)** consists of reddish brown, moderate compacted silty sand and contains a lens (length is 20–30 cm) of subangular, highly spherical pebbles ( $\varnothing < 1.5\text{--}3$  cm; abundance 50%).  $X_{LF}$  ( $7$  (1)  $10^{-8} \text{ m}^3/\text{kg}$ , class 1,  $n = 2$ ) and  $\text{LOI}_{550}$  (2.4 (0.1) mass%, class 2,  $n = 2$ ) values are low. A charcoal sample at 172 cm bs dates to 653–554 cal yr BP. The boundary to the overlying unit 2 is gradual.

**Unit 2 (160–136 cm bs)** consists of reddish to light brown, moderate compacted silty sand with slightly subangular fine pebbles ( $\varnothing < 1$  cm). Very few fine roots occur in this unit. Carbonate precipitations and a shell (radiocarbon dating: 668–560 cal yr BP at 144 cm bs) occur in the upper part of the unit.  $X_{LF}$  ( $8$  (1)  $10^{-8} \text{ m}^3/\text{kg}$ , class 1,  $n = 2$ ) and  $\text{LOI}_{550}$  (2.8

(0.1) mass%, class 2, n = 2) values are low and slightly increased compared to unit 1. The boundary between units 2 and 3 is diffuse.

**Unit 3 (136–85 cm bs)** consists of brown, slightly moist, strongly compacted slightly pebbly silty sand. The unit has very few coarse roots ( $\varnothing < 8$  mm) and burrows. Carbonate precipitations occur around 110 cm bs. This unit shows peaks in  $X_{LF}$  (12 (2)  $10^{-8}$  m<sup>3</sup>/kg, class 1, n = 5) and  $LOI_{550}$  (3.5 (0.3) mass%, class 3, n = 5). The boundary to unit 4 is clear.

**Unit 4 (85–63 cm bs)** consists of brown, slightly moist, strongly compacted, and poorly sorted pebbly sand. The coarse material consists of few subangular medium pebbles ( $\varnothing < 2$  cm) and very few angular very coarse pebbles ( $\varnothing < 5$  cm). The pebbles include strong weathered Molasse-conglomerate. Few fine roots occur throughout the unit.  $X_{LF}$  (11 (0)  $10^{-8}$  m<sup>3</sup>/kg, class 1, n = 2) values slightly decrease compared to unit 3 and remain low to the top of the profile. The boundary between units 4 and 5 is diffuse.

**Unit 5 (63–34 cm bs)** consists of brown, slightly moist, moderately compacted, and poorly sorted sandy pebbles. The coarse material includes common subangular fine pebbles ( $\varnothing < 1$  cm) and very few angular very coarse pebbles ( $\varnothing < 6$  cm). Strongly weathered Molasse-conglomerate are included. Few fine to medium roots and very few burrows occur. A charcoal sample at 40 cm bs dates to 456–308 cal yr BP. The boundary to the overlying unit is clear.

**Unit 6 (34–0 cm bs)** represents the Ap soil horizon. It consists of light brown, slightly moist, moderately compacted, and poorly sorted sandy silt with few angular to subangular medium pebbles ( $\varnothing < 2$  cm). The unit is strongly rooted ( $\varnothing < 3$  cm) and presents very few burrows.  $LOI_{550}$  values increase from 3.4 mass% (class 2) at the bottom of unit 4 to 4.7 mass% (class 3) at the top of the profile.

### **Tekkedere valley infill: Sediment profile Tek-3**

Profile **Tek-3** is located adjacent to Tek-1 (Figure S5.1) and the 220-cm-thick profile shows 8 macroscopically distinguishable units (Figure S5.3). Unit 1 at the base consists of silty sand and is nearly free of gravel. The sediments above (units 2–7) are characterized by fine to medium pebbles. Animal burrows and fine roots occur commonly. The sediments slightly change from moderately to slightly alkaline (pH: 8.1 to 7.6, n = 19) from the base to the top of the profile. Electrical conductivity (EC) values fluctuate around 143 (11)  $\mu$ S/cm (class 1, n = 19). Magnetic susceptibility values are generally very low ( $X_{LF}$ : 9 (3)  $10^{-8}$  m<sup>3</sup>/kg, class 1, n = 19) and slightly increase at 145–120 cm bs.  $LOI_{550}$  values also alternate in the low class (3.2 (0.2) mass%, class 2, n = 19).

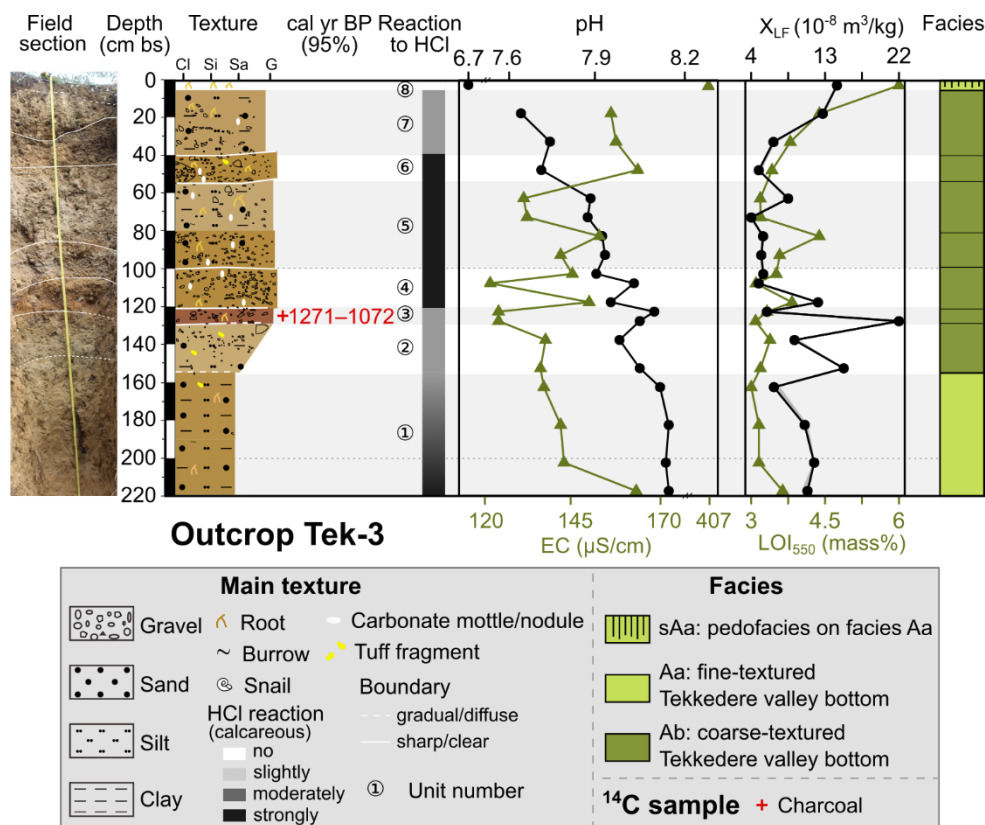


**Figure S5.3** The lithostratigraphy, radiocarbon date, and sediment analyses of outcrop Tek-3.

**Unit 1 (220–155 cm bs)** consists of light brown, strongly compacted, and slightly moist sandy silt with few tuff pieces in the upper part. The sediments are strongly to moderately calcareous with decreasing depth. A small lens of strongly weathered and reddish blackish ("rusty") fine pebbles occurs in the lower part. The unit has few fine roots and burrows. Two coarse roots (size ca. 2.5 cm) occur at 155–145 cm and 210–180 cm bs. Electrical conductivity values average 143 (3)  $\mu\text{S}/\text{cm}$  (class 1,  $n = 4$ ) and change from 165  $\mu\text{S}/\text{cm}$  at the bottom to 136  $\mu\text{S}/\text{cm}$  at the top. Both  $X_{LF}$  (11 (1)  $10^{-8}$  m<sup>3</sup>/kg, class 1,  $n = 4$ ) and  $\text{LOI}_{550}$  (3.0 (0.1) mass%, class 2,  $n = 4$ ) values remain constantly low. The boundary to the overlying unit 2 is diffuse.

**Unit 2 (155–130 cm bs)** consists of light brown, strongly compacted, slightly moist, and inversely graded sediments with few fine roots. Sediment texture changes from sandy silt to silty sandy pebbles with decreasing depth. The medium pebbles ( $\varnothing < 2$  cm) are mainly subangular and few rounded pebbles and tuff pieces ( $\varnothing < 5$  cm) occur. The sediments are moderately calcareous but lack secondary carbonate precipitations. The EC (137 (1)  $\mu\text{S}/\text{cm}$ , class 1,  $n = 2$ ),  $X_{LF}$  (12 (3)  $10^{-8}$  m<sup>3</sup>/kg, class 1,  $n = 2$ ) and  $\text{LOI}_{550}$  (3.1 (0.1) mass%,

class 2, n = 2) values are in the same range in comparison with the underlying unit. The boundary from unit 2 to unit 3 is clear.

**Unit 3 (130–120 cm bs)** consists of reddish brown, slightly moist sandy medium pebbles ( $\varnothing < 2$  cm). The sediments are moderately calcareous, lack secondary carbonate precipitations, and contain few fine roots. Compared to unit 2, the EC values drop to 124 (0)  $\mu\text{S}/\text{cm}$  (class 1, n = 2). The  $X_{\text{LF}}$  value ( $22 \cdot 10^{-8} \text{ m}^3/\text{kg}$ , class 1) is the highest in this profile. The  $\text{LOI}_{550}$  shows no change compared to unit 2. A charcoal sample at 125 cm bs dates to 1271–1072 cal yr BP. The boundary between unit 3 and unit 4 is clear.

**Unit 4 (120–100 cm bs)** consists of light brown, moderately sorted, sub-angular to rounded, slightly organized, spherical to platy medium pebbles ( $\varnothing < 2$  cm) with few angular very coarse pebbles ( $\varnothing < 5$  cm). The sediment matrix consists of silty sand and is strongly calcareous with secondary carbonate precipitations. Few fine roots ( $\varnothing < 1$  mm) and an olive core occur in this unit. EC (146 (5)  $\mu\text{S}/\text{cm}$ , class 1, n = 3),  $X_{\text{LF}}$  ( $6 (1) \cdot 10^{-8} \text{ m}^3/\text{kg}$ , class 1, n = 3) and  $\text{LOI}_{550}$  (3.3 (0.3) mass%, class 2, n = 3) remain generally low. The boundary from unit 4 to unit 5 is clear to slightly irregular.

**Unit 5 (100–55 cm bs)** consists of grayish to light brown, compacted, fine pebbly ( $\varnothing < 1$  cm) silty sand at the bottom to spherical medium pebbly ( $\varnothing < 2$  cm) sandy silt at the top. The sediments are strongly calcareous with few secondary carbonate precipitations. Few fine roots ( $\varnothing < 1$  mm) occur at the bottom and common coarse roots ( $\varnothing < 2$  cm) at the top. Burrows are generally fine ( $\varnothing < 1$  cm). The sediments in units 1–5 are moderately alkaline and generally decrease with decreasing depth. EC (138 (6)  $\mu\text{S}/\text{cm}$ , class 1, n = 4) and  $\text{LOI}_{550}$  (3.2 (0.2) mass%, class 2, n = 4) show similar trends with a small peak at ca. 80 cm bs. The values of  $X_{\text{LF}}$  ( $6 (1) \cdot 10^{-8} \text{ m}^3/\text{kg}$ ) remain very low (class 1, n = 4). The boundary to the overlying unit 6 is sharp and irregular.

**Unit 6 (55–40 cm bs)** consists of light brown, slightly to moderately compacted, silty sandy, coarse pebbles ( $\varnothing < 3$  cm). The clasts are spherical, sub-angular to rounded, and contain angular tuff pieces ( $\varnothing < 7$  cm). A lens of olive cores occurs in the strongly calcareous sediment matrix. Medium roots ( $\varnothing < 5$  mm) and fine burrows ( $\varnothing < 1$  cm) occur abundantly. The EC value increases to 166  $\mu\text{S}/\text{cm}$  (class 1, n = 1). The boundary to unit 7 is sharp.

**Unit 7 (40–5 cm bs)** consists of light brown, moderately compacted, fine pebbly ( $\varnothing < 1$  cm) silty sand. The unit contains moderately calcareous sediment and commonly fine roots and burrows. A single olive core occurs at ca. 25 cm bs. Sediments in units 6–7 are slightly alkaline (pH: 7.7 (0.1), n = 3). The EC values are in a comparable range to unit 6.  $X_{\text{LF}}$  and  $\text{LOI}_{550}$  increase from unit 6 to unit 7. The boundary to the overlying unit is sharp.

**Unit 8 (5–0 cm bs)** represents the Ah soil horizon. It consists of dark brown, slightly to moderately compacted, and slightly moist, slightly sandy silt. The unit shows non-calcareous sediments and contains abundant fine roots and macro plant remains. The pH rapidly decreases to 6.7 (sediments are neutral,  $n = 1$ ). Electrical conductivity increases to 408  $\mu\text{S}/\text{cm}$  (class 3,  $n = 1$ ).  $X_{\text{LF}}$  ( $15 \cdot 10^{-8} \text{ m}^3/\text{kg}$ , class 1,  $n = 1$ ) and  $\text{LOI}_{550}$  (6 mass%, class 4,  $n = 1$ ) continue to increase, too.

### Tekkedere fan apex: Sediment profile Tek-4

Sediment profile **Tek-4** is located at the Tekkedere fan apex (Figure S5.1) and has a total thickness of 200 cm. Two macroscopically distinguishable units are characterized by normally graded deposits (Figure S5.4).

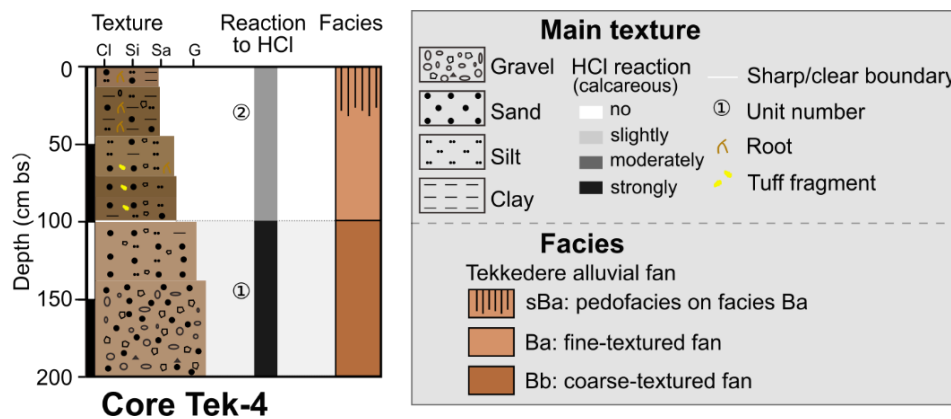


**Figure S5.4** The lithostratigraphy of core Tek-4.

**Unit 1 (200–100 cm bs)** consists of light brown (7.5YR 6/4), heavily compacted, poorly sorted matrix-supported sediments. The unit gradually changes from medium pebbles at the base to fine pebbly sand at the top. The sediment matrix is strongly calcareous silty sand. The boundary between unit 1 and unit 2 is sharp.

**Unit 2 (100–0 cm bs)** shows normally graded sediments with distinct changes in color and compaction. The sediments at the base are (dark yellowish) brown (10YR 4/4, 10YR 4/3) silty sand with few angular fine to coarse pebbles ( $\varnothing < 3 \text{ cm}$ ). The coarse white clasts likely consist of tuff fragments. The middle part is yellowish brown (10YR 5/4) silty sand with few angular fine and medium pebbles ( $\varnothing < 2 \text{ cm}$ ). The sediments at the top are brown (10YR 4/3), sandy silt with very few angular fine pebbles ( $\varnothing < 1 \text{ cm}$ ). The moderately calcareous sediments contain abundant vegetation remains and few fine roots. The top of this unit represents the modern soil horizon.

### **Tekkedere mid-fan: Sediment profile Tek-4-2**

Profile Tek-4-2 is located in the middle part of the Tekkedere alluvial fan (Figure S5.1), has a total thickness of 700 cm, and shows 7 units (Figure S5.5). This profile is generally characterized by alternating units of fine (silty) and coarse (sandy to fine pebbly) deposits. The sediments are slightly calcareous below 463 cm bs and moderately calcareous above. The average pH value is 7.9 (0.1, moderately alkaline, n = 32) and the sediments gradually change from moderately alkaline at the bottom to slightly alkaline at the top. Electricity conductivity (EC: 273 (28)  $\mu\text{S}/\text{cm}$ , class 2, n = 32) is generally low and the  $\text{LOI}_{550}$  alternates between low (2.2–3.5 mass%, class 2) and medium values (3.7–4.8 mass%, class 3) in the coarse and fine units.

**Unit 1 (700–600 cm bs)** consists of strong brown (7.5YR 4/6), moderately compacted sandy silt. This unit contains common fine manganese mottles and nodules, and few fine secondary precipitated carbonate concretions. The values (n = 4) of pH (8 (0), moderately alkaline), EC (290 (5)  $\mu\text{S}/\text{cm}$ , class 2), and  $\text{LOI}_{550}$  (4 (0.1) mass%, class 3) in this unit remain roughly constant. The boundary to the overlying unit is diffuse.

**Unit 2 (600–463 cm bs)** consists of brown (7.5YR 4/3) moderately compacted sandy silt with very few subangular fine pebbles occurring at 600–560 cm bs. Common blackish fine manganese mottles and nodules and few fine secondary precipitated carbonates occur. The values (n = 7) of EC (from 224 to 367  $\mu\text{S}/\text{cm}$ , class 2) and  $\text{LOI}_{550}$  (from 3.6 to 4.1 mass%, class 3) similarly increase with decreasing depth. A sample with a mixture of charcoal and sediment in the upper part of this unit (469 cm bs) dates to 4971–4653 cal yr BP. The boundary from unit 2 to unit 3 is sharp.

**Unit 3 (463–404 cm bs)** consists of strong brown (7.5YR 4/6), loose to moderately compacted silty sand with subangular, fine to coarse pebbles ( $\varnothing < 3$  cm). Some of the clasts are weathered. Fine manganese mottles and nodules occur at 445–422 cm bs. EC (227 (50)  $\mu\text{S}/\text{cm}$ , class 2, n = 3) and  $\text{LOI}_{550}$  (2.8 (0.1) mass%, class 2, n = 3) values are lower than in unit 2. Unit 3 has a sharp boundary with unit 4.

**Unit 4 (404–253 cm bs)** consists of strong brown (7.5YR 4/6), loose silty sand with common subangular, fine to medium pebbles ( $\varnothing < 2$  cm). Two fine pieces of shell occur at 258–255 cm and 360–357 cm bs. The average electrical conductivity values slightly increase to 267 (25)  $\mu\text{S}/\text{cm}$  (class 2, n = 7) and  $\text{LOI}_{550}$  values remain low (2.9 (0.2) mass%, class 2, n = 7). The boundary to the overlying unit is sharp.

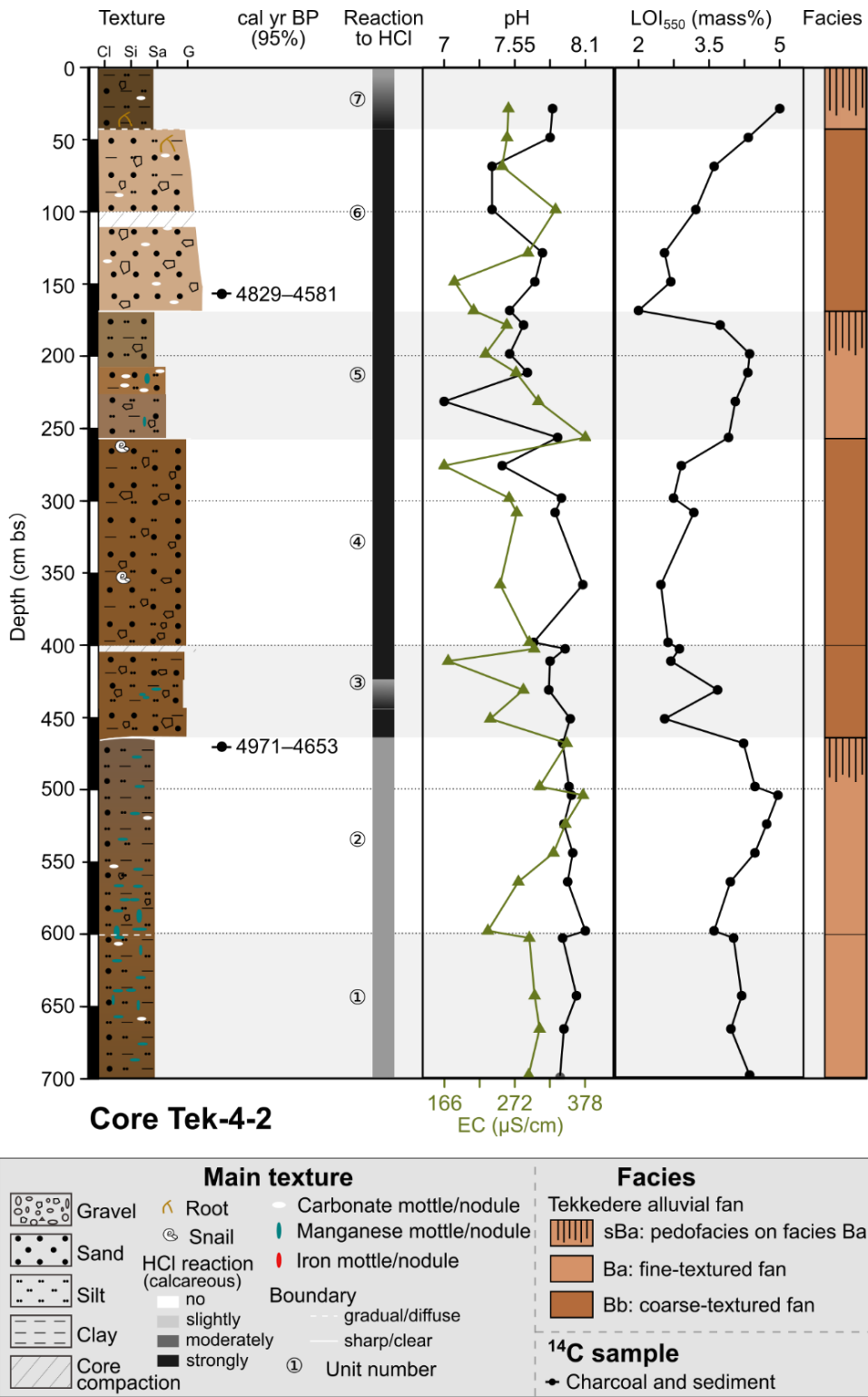


**Figure S5.5** The lithostratigraphy, radiocarbon dates, and sediment analyses of core Tek-4-2.

**Unit 5 (234–174 cm)** consists of brown (7.5YR 5/4), loose to moderately compacted sandy silt at the top, and yellowish brown (10YR 5/4) silty sand at the bottom. Carbonate mottles occur commonly in the middle part and few fine manganese mottles occur in the middle to lower part. From the bottom to the top, the pH values (pH: 7.6 (0.1), slightly

alkaline,  $n = 4$ ) slightly decrease and EC values decrease from 300  $\mu\text{S}/\text{cm}$  (class 2) to 220  $\mu\text{S}/\text{cm}$  (class 1).  $\text{LOI}_{550}$  values increase (4.1 (0.1) mass%, class 3,  $n = 4$ ) compared to unit 4. The boundary from unit 5 to unit 6 is sharp.

**Unit 6 (174–45 cm bs)** consists of pink (7.5YR 7/4), loose normal graded sediments. The texture changes from sandy (sub)angular coarse pebbles ( $\varnothing < 3$  cm) at the base to silty sand with few fine pebbles ( $\varnothing < 1$  cm) at the top. The sediments contain common carbonate nodules and few fresh fine roots at ca. 54 cm bs. The pH (7.6 (0.2), slightly alkaline,  $n = 6$ ) and EC (249 (41)  $\mu\text{S}/\text{cm}$ , class 2,  $n = 6$ ) values show minor fluctuations.  $\text{LOI}_{550}$  values drop to 2.2 mass% (class 2) at the bottom and gradually increase to 4.2 mass% (class 3) to its top. A sample with a mixture of charcoal and sediments at 161 cm bs dates to 4829–4581 cal yr BP. Unit 6 has a gradual boundary with the overlying unit 7.

**Unit 7 (45–0 cm bs)** represents the present-day plow horizon. The dark yellowish brown (10YR 3/4) loose sediments are characterized by slightly gravelly silts and contain few carbonate nodules and fresh fine roots. The sediment sample is moderately alkaline (pH: 7.9) and has an EC value of 255  $\mu\text{S}/\text{cm}$  (class 2) and a  $\text{LOI}_{550}$  value of 4.8 mass% (class 3).

#### **Tekkedere mid-fan: Sediment profile Tek-5-2**

Profile **Tek-5-2** is located in the middle-lower part of the alluvial fan (Figure S5.1), has a total thickness of 400 cm, and shows 6 units (Figure S5.6). The sediments are mainly composed of sandy silt with common manganese mottles and show abundant secondary precipitated carbonate concentrations in the lower part. The boundaries between all units are gradual. The sediments are moderately to strongly calcareous and moderately to strongly alkaline (pH: 8.6 (0.2),  $n = 17$ ). EC values (608 (58)  $\mu\text{S}/\text{cm}$ ) are high (class 4,  $n = 17$ ) and vary between 242 and 803  $\mu\text{S}/\text{cm}$ . Generally,  $\text{LOI}_{550}$  values (4.3 (0.7) mass%, class 3,  $n = 17$ ) display a decreasing trend from the bottom to the top. Geochemical ratios of Ca/Ti (17.07 (4.3)) and Zr/Rb (1.39 (0.2)) present a parallel pattern with values roughly increasing from the bottom to the top.

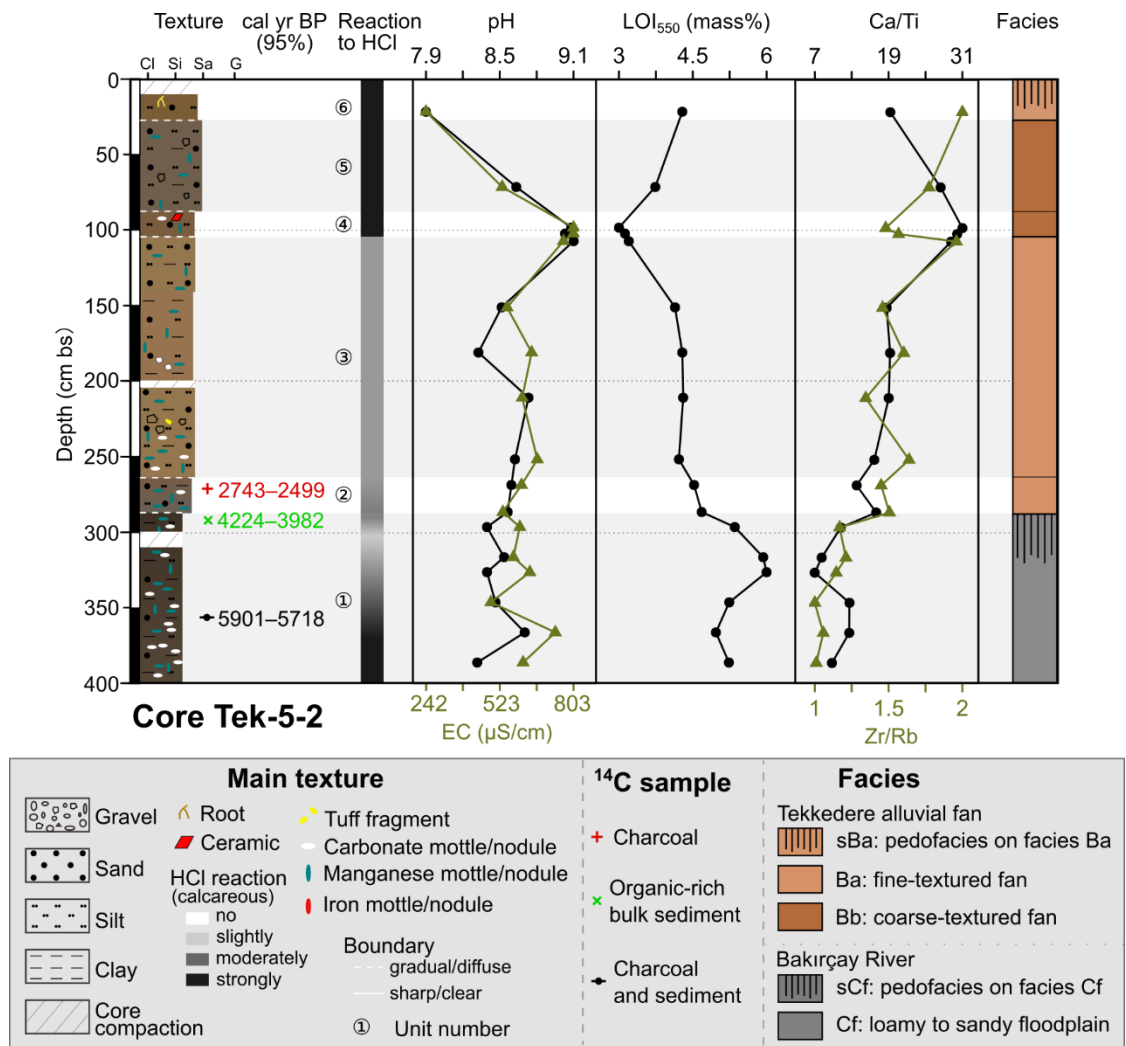


**Figure S5.6** The lithostratigraphy, radiocarbon dates, and sediment analyses of core Tek-5-2.

**Unit 1 (400–284 cm bs)** consists of very dark brown (10YR 2/2) clayey silt. The sediments change from strongly calcareous at the base to moderately calcareous at the top. Secondary precipitated carbonate nodules and manganese mottles occur commonly throughout the unit. The pH (8.5 (0.1), strongly alkaline,  $n = 7$ ) and EC values (599 (38)  $\mu\text{S}/\text{cm}$ , class 4,  $n = 7$ ) show minor fluctuations. LOI<sub>550</sub> values (5.2 (0.3) mass%, class 4,  $n = 7$ ) are high and peak (6 mass%, class 4) at ca. 330 cm bs. The Ca/Ti ratio shows a minor drop at the same depth (ca. 330 cm bs) and increases towards the top. The Zr/Rb ratio gradually increases with decreasing depth. A sample with a mixture of charcoal and sediments at 354 cm bs dates to 5901–5718 cal yr BP and a bulk sample containing organic matter from 285–286 cm bs dates to 4224–3982 cal yr BP.

**Unit 2 (284–265 cm bs)** consists of moderately calcareous sandy silt. The color gradually changes from dark gray (7.5YR 4/1) at the bottom to brown (7.5YR 4/3) at the top. The

amount of blackish manganese mottles decreases. The LOI<sub>550</sub> value decreases to 4.5 (0) mass% (class 3, n = 1). A charcoal sample from 273 cm bs dates to 2743–2499 cal yr BP.

**Unit 3 (265–104 cm bs)** consists of yellowish brown (10YR 5/4), very soft, and moderately calcareous sandy silt. Few fine to medium pebbles (including rounded tuff) occur at 235–225 cm bs and few coarse, weathered carbonate fragments at 186–178 cm bs. The sediments from 200 to 140 cm bs contain more reddish clay. Manganese mottles and fine nodules commonly occur in this unit, particularly at 265–247 cm bs where secondary precipitated carbonate concentrations occur, too. The values (n = 5) of pH (8.7 (0.1), strongly alkaline) and EC values (644 (36)  $\mu$ S/cm, class 4) are in the same range as the underlying two units. The LOI<sub>550</sub> values (4.2 (0.1) mass%, class 3, n = 5) continue to decrease to the top of unit 3 and the ratios of Ca/Ti (19.08 (0.3)) and Zr/Rb (1.50 (0.1)) generally increase with decreasing depth.

**Unit 4 (104–85 cm bs)** consists of dark yellowish brown (10YR 4/4) slightly sandy silt. The sediments are strongly calcareous and contain few carbonate nodules and manganese mottles. A broken brick fragment occurs at 82 cm bs. The pH (9.1 (0), very strongly alkaline, n = 2) and EC (803 (0)  $\mu$ S/cm, class 5, n = 2) values markedly increase compared to the units below and above, whereas LOI<sub>550</sub> (3 (0.1) mass%, class 2, n = 2) markedly drops to its lowest values. The Zr/Rb ratio slightly decreases to 1.44 (0) and the Ca/Ti ratio slightly increases to 30.47 (0.4).

**Unit 5 (85–30 cm bs)** consists of dark grayish brown (10YR 4/2) fine pebbly sandy silt. The sediments are strongly calcareous and contain few manganese mottles.

**Unit 6 (30–0 cm bs)** is the present-day plow horizon. The brown (10YR 4/3) loose sediments consist of strongly calcareous, slightly sandy silt with few fine roots. From unit 5 to unit 6, the sediments change from strongly alkaline (pH: 8.7) to moderately alkaline (pH: 7.9), EC values (from 532 to 242  $\mu$ S/cm) and Ca/Ti ratio (from 27.4 to 19.3) decrease, whereas LOI<sub>550</sub> (from 3.7 to 4.2 mass%) and Zr/Rb ratio (from 1.64 to 1.82) increase.



## To chapter 6 (working package 3)

**Table S6.1** The archaeological sites and the preliminary chronology within and in the vicinity of the Deliktaş catchment (Ludwig et al., 2022).

Site	x	y	Location	Bronze Age	Iron Age	Archaic	Classical Period	Hellenistic	Roman Imperial Period	Late Antiquity	Byzantine	Ottoman
Zindan Tepe	494305	4316022	Deliktaş	yes	yes	-	yes	dominated	few	-	-	-
Dedekırağı Tepe	493050	4316260	Deliktaş	-	-	-	yes	yes	yes	-	-	-
Kale Tepe	493398	4316007	Deliktaş	-	-	-	yes	yes	yes	-	-	-
Bozalan	496037	4315869	Deliktaş	-	-	-	-	-	yes	yes	few	-
Haciosman Tepe	491991	4314487	Deliktaş	-	-	-	yes	yes	yes	-	Late B.	yes
Kocagöl Tepe	490609	4314430	vicinity	-	-	-	yes	yes	-	-	-	-
*	490344	4314682	vicinity	-	-	-	-	yes	yes	-	-	-
Hatıpler Kalesi	490768	4318213	vicinity	yes	yes	yes	yes	Early H.	-	-	yes	-
Emirali Tepe	495768	4319451	vicinity	-	-	-	yes	yes	Early R.	-	-	-

\* represents an unnamed site.

**Table S6.2** The classification of the sediment proxies (modified from Yang et al. (2023a)).

class	≥2mm (mass%)	pH		EC ( $\mu\text{S cm}^{-1}$ )	$X_{\text{LF}}$ ( $10^{-8} \text{ m}^3 \text{ kg}^{-1}$ )	LOI <sub>550</sub> (mass-%)
class 1 (very low)	0–20	6.5–7.3	neutral	84–227	4–32	0.7–2.1
class 2 (low)	20–40	7.3–7.8	slightly alkaline	227–371	32–60	2.1–3.5
class 3 (medium)	40–60	7.8–8.4	moderately alkaline	371–515	60–87	3.5–4.9
class 4 (high)	60–80	8.4–9	strongly alkaline	515–659	87–115	4.9–6.2
class 5 (very high)	80–100	≥ 9	very strongly alkaline	659–803	115–143	6.2–7.6

### The relationship between TOC and LOI<sub>550</sub>, TIC and LOI<sub>900</sub>

Samples from two sediment cores (AD29 and AD30, both 8 m thick) in the western lower Bakırçay plain (Figure S6.1) were additionally analyzed with a LECO TruSpec CHN analyzer and a Shimadzu TOC-L CPH system to precisely quantify total carbon (TC) and total organic carbon (TOC) contents, respectively, in the sedimentary laboratory of Freie Universität Berlin. The total inorganic carbon (TIC) contents are calculated as the difference between TC and TOC (Bernard et al., 1995; Müller et al., 2014). The quality control is assessed using chemicals and certified reference materials (EDTA, Leco 502–308, Leco 502–062, and CaCO<sub>3</sub>) for TC measurements and (WEPAL-QUASIMEME ISE sample 955 and ISE sample 986) for TOC measurements. Linear regression analysis with Pearson product-moment correlation is used to compare the relationships between LOI<sub>550</sub> and TOC and between LOI<sub>900</sub> and TIC the in the R software (version 4.1) (R Core Team, 2022).

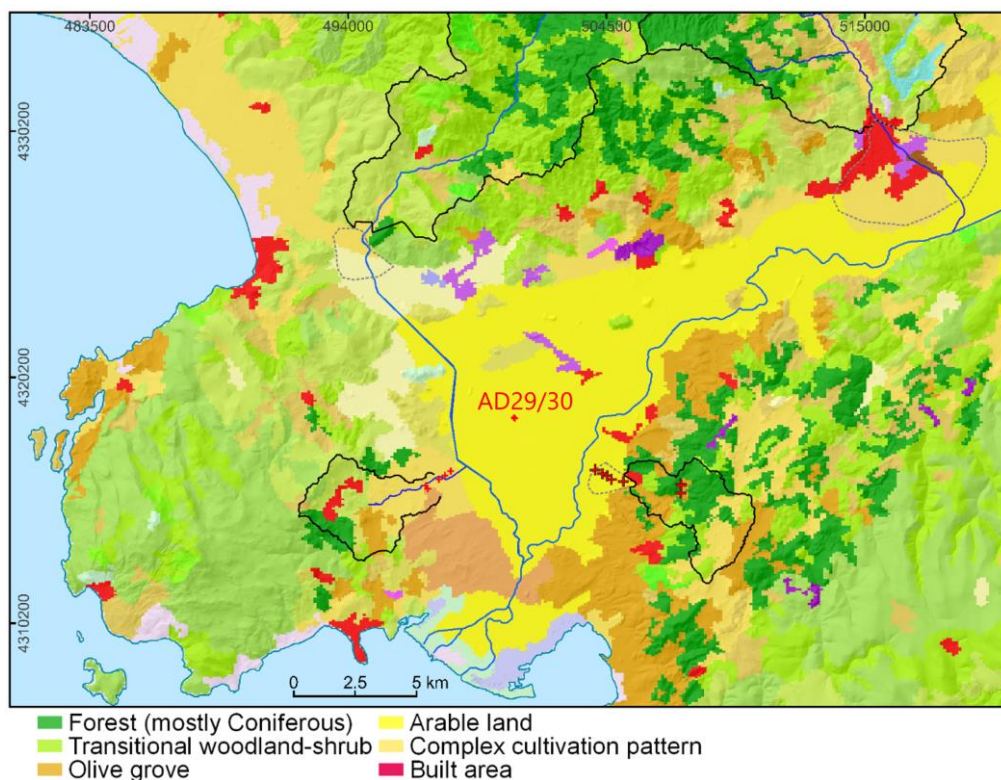


**Figure S6.1** The land use of the study area (data based on Corine Land Cover data (Cole et al., 2018)) with the location of sediment profiles AD29/30 in the western lower Bakırçay plain.

The coefficients of determination between LOI<sub>550</sub> and TOC ( $R^2 = 0.71$ ,  $\alpha < 0.05$ ,  $n = 86$ ) and between LOI<sub>900</sub> and TIC ( $R^2 = 0.79$ ,  $\alpha < 0.05$ ,  $n = 84$ ) show strong positive relationships (Figure S6.2). We did not calibrate the values of LOI<sub>550</sub> to get the organic carbon content by applying the equation between LOI<sub>550</sub> and TOC, though the organic

matter contents are likely overestimated by LOI<sub>550</sub> determinations (intercept = 2.08, Figure S6.2A) because of the dehydration of clay minerals or metal oxides (Heiri et al., 2001).

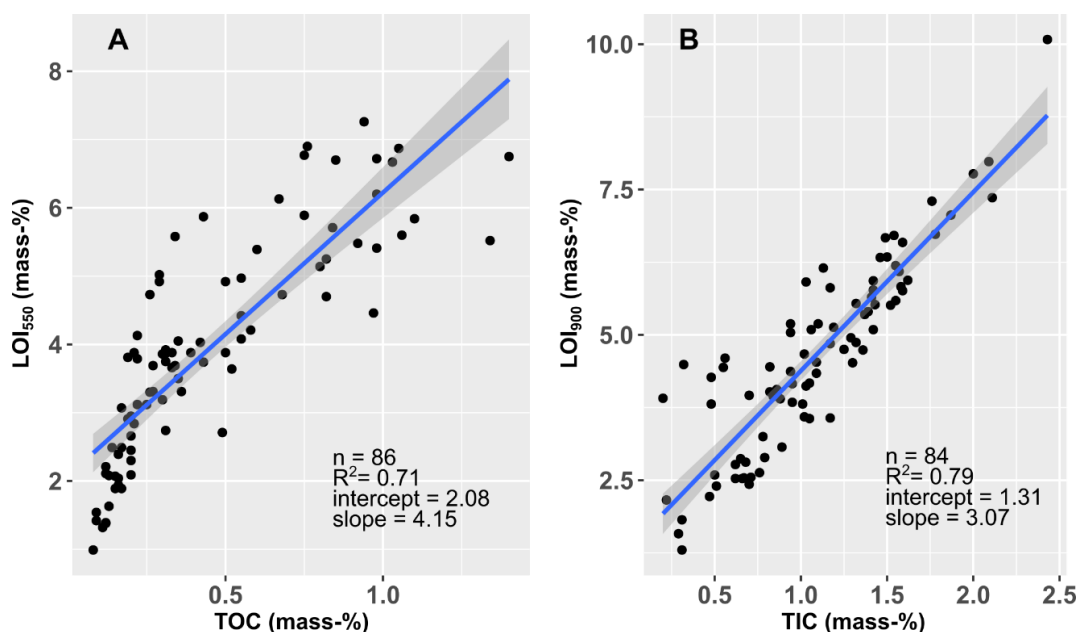


**Figure S6.2** Pearson product-moment correlation and linear regression analysis of LOI<sub>550</sub> and TOC (A) and LOI<sub>900</sub> and TIC (B) from sediment profiles AD29 and AD30. The shaded areas mark the 95% confidence intervals of the linear regression lines.

## Detailed description of sediment profiles

### Profile Del-2

Basal **unit 1 (500–445 cm b.s.)** consists of two layers (Figure S6.3). Dark brown (7.5 YR 3/2) sediments at 500–452 cm b.s. are soft, fine sandy silt with few pebbles and Fe-Mn mottles. An unknown fragment occurs at the bottom, which might be a ceramic. The upper layer contains brown (10 YR 4/3) fine pebbly coarse sand with 20 mass% coarse components. It sharply transits to the overlying sediments. The mixed charcoal/sediment sample from 459 cm b.s. dates to 7157–6956 cal yr BP. Five sediment samples indicate a slight increase in EC (median 95 (10)  $\mu\text{S cm}^{-1}$ , class 1) and LOI<sub>550</sub> (2.24 mass%, class 2), and a rapid decrease of  $X_{LF}$  (from 65 to 17  $10^{-8} \text{ m}^3 \text{ kg}^{-1}$ , class 2) with decreasing depth. This unit refers to the silty floodplain deposits from the Geyikli River (facies Cf). The sandy layer at the top represents an event of sheet flood (facies Csh).

**Unit 2 (445–374 cm b.s.)** is characterized by dark grayish brown (10 YR 4/2) clayey fine silt with few Mn-Fe mottles (Figure S6.3). Units 1 and 2 remain constant pH (ca. 7.93, moderately alkaline). EC and LOI<sub>550</sub> of 6 samples in unit 2 continue to increase towards

the unit top. Units 1 and 2 together show a normally graded texture with distinct gradual changing trends. This unit is also silty floodplains (facies Cf).

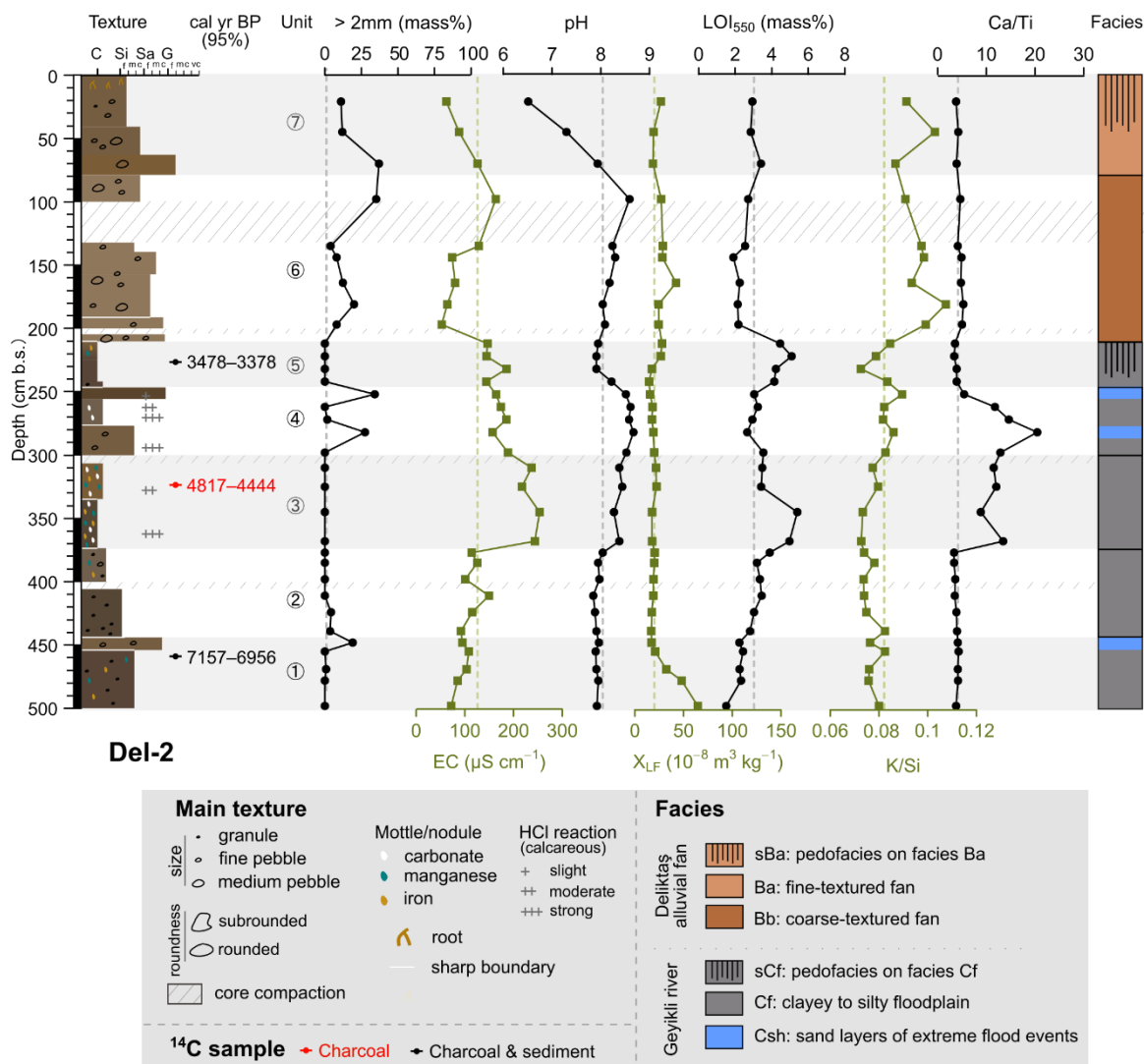


**Figure S6.3** The lithostratigraphy, radiocarbon datings, sediment bulk characters, and sediment facies of profile Del-2. 1) colors of the sediment texture column represent the color observed in the field; 2) shaded bands separate different units; 3) the vertical dashed lines of each sedimentary analysis represent the median values of the whole profile.

**Unit 3 (374–300 cm b.s.)** contains dark grayish brown (10 YR 4/4), soft, strongly calcareous, silty clay (Figure S6.3). This unit is characterized by common secondary carbonates and distinct Fe-Mn mottles. The charcoal from 322 cm b.s. dates to 4817–4444 cal yr BP (Table 6.3). The measurements ( $n = 4$ ) show remarkable enrichments in pH (8.38, moderately alkaline), EC (from 115 (13)  $\mu\text{S cm}^{-1}$  (class 1) in unit 2 to 241 (9)  $\mu\text{S cm}^{-1}$  (class 2) in unit 3), LOI<sub>550</sub> (from 3.27 (0.2) mass% (class 2) in unit 2 to 4.22 (0.8)

mass% (class 3) in unit 3), and Ca/Ti ratio (ca. 11.8). This unit represents clayey floodplains (facies Cf).

**Unit 4 (300–246 cm b.s.)** consists of three layers. Sediments at 300–276 cm b.s. are dark grayish brown (10YR 4/2), strongly calcareous, fine sandy silts. Comparable to unit 3, the middle layer (276–256 cm b.s.) also contains soft, silty clay with common secondary carbonates. The upper thin layer shows dark brown (10YR 3/3), slightly calcareous, silty coarse sand. The content of >2mm fraction displays two peaks at the two coarser layers. Five sediment samples show a gradual decrease in EC from unit 3 to unit 4. The record of pH remains constant as in unit 3.  $X_{LF}$  keeps the lowest values from units 2 to 4.  $LOI_{550}$  slightly decreases to 3.04 (0.2) mass% (class 2). Ca/Ti reaches the highest value at the unit bottom and gradually decreases to the background value at the top. This unit is intercalated with two layers as sheet floods (facies Csh) to the floodplain layer (facies Cf).

**Unit 5 (246–209 cm b.s.)** is characterized by dark brown (7.5 YR 3/2), very soft clay with few Fe-Mn mottles at the top (Figure S6.3). The mixed charcoal/sediment sample from 226 cm b.s. dates to 3478–3378 cal yr BP. The 4 samples in unit 5 measured continuously decreasing EC and pH.  $X_{LF}$  displays a slight increase at the unit top.  $LOI_{550}$  reaches the highest values of 4.34 (0.2) mass% (class 3), and the K/Si shows a low value in the middle part. This clayey unit with high  $LOI_{550}$  represents a soil horizon developed on the floodplain (facies sCf).

**Unit 6 (209–78 cm b.s.)** contains brown (10 YR 5/3) silty fine sand with few subrounded to rounded fine–medium pebbles (Figure S6.3). To the bottom, medium-coarse sand prevails. This unit shows a gradual boundary to overlying unit 7. The proxies of 6 samples show distinct differences in comparison with the underlying units 1–5. The >2mm components increase to 10 (4) mass%. EC values drop rapidly to the lowest (77 (19)  $\mu\text{S cm}^{-1}$ , class 1) and slightly increase to the unit top. The pH displays a similar rising trend and has a median value of 8.21 (0.1) (moderately alkaline).  $X_{LF}$  shows slightly increased values of 28 (2)  $10^{-8} \text{ m}^3 \text{ kg}^{-1}$  (class 1). Comparable to EC and pH,  $LOI_{550}$  decreases to 2.21 (0.2) mass% (class 1). By contrast, the K/Si ratio largely increases from ca. 0.08 in units 1–5 to 0.1 in unit 6. These differences in sediment texture and analyses indicate a coarse-texture (sandy) alluvial fan facies (facies Bb).

**Unit 7 (78–0 cm b.s.)** mainly contains brown (10 YR 4/3) silts mixed with fine sands at the top and fine–medium pebbles towards the bottom (Figure S6.3). Pebbles include tuff or rhyolite. Common fine–medium roots exist above 13 cm b.s. The analyses of 3 samples present decreasing values in >2mm, EC, and pH. Particularly, sediments become neutral at the surface (pH = 6.51). The rest proxies remain constant as in unit 6. This silty unit

refers to fine-textured alluvial fan facies (facies Ba). The upper part is the modern ploughing layer (facies sBa).

#### **Profile Del-4**

**Unit 1 (800–472 cm b.s.)** is characterized by clast-supported, poorly sorted subangular to subrounded, medium-coarse pebbles (Gm) with occasionally distributed fine cobbles (up to 10 cm in size) (Figure S6.4). Below 575 cm b.s., the sediments are under the groundwater table. Above the water table, the sediments are dark yellowish brown (10 YR 4/4) coarse to fine sand with pebbles, showing a normal graded texture. The 12 samples show the highest percentage of the >2mm components (ca. 60 mass%). The sediments are moderately alkaline (pH = 7.84) and very low in EC (83 (15)  $\mu\text{S cm}^{-1}$ ), and LOI<sub>550</sub> (1.97 (0.4) mass%). X<sub>LF</sub> values in this unit are the highest (58 (5)  $10^{-8} \text{ m}^3 \text{ kg}^{-1}$ , class 2). This basal unit is the incised channel.

**Unit 2 (472–343 cm b.s.)** contains dark greyish brown (10 YR 4/2) sandy silt with few fine pebbles and common Fe-Mn mottles (Figure S6.4). The 7 samples indicate a slightly alkaline (pH = 7.51) unit with rising EC (96 (6)  $\mu\text{S cm}^{-1}$ ) and LOI<sub>550</sub> (3.51 (0.4) mass%, class 3). X<sub>LF</sub> values remain very low. This unit represents fine-textured alluvial fan facies.

**Unit 3 (343–213 cm b.s.)** contains dark yellowish brown (10 YR 4/4) fine sands at the top and is overlain by dark brown (10 YR 3/3) sand with subangular to subrounded, fine-medium pebbles (Figure S6.4). Particularly, the sediments at 320–304 cm are clast-supported subangular-angular coarse pebbles. The 7 samples in this unit show a distinct enrichment in coarse component content. EC and LOI<sub>550</sub> values gradually increase with decreasing depth. This unit is a coarse-textured alluvial fan facies.

**Unit 4 (213–181 cm b.s.)** is characterized by very dark grayish brown (10 YR 3/2) clayey silt with few granules and Fe-Mn mottles (Figure S6.4). Slightly elevated values in EC, pH, and LOI<sub>550</sub> further show a soil formation layer.

**Unit 5 (181–0 cm b.s.)** contains dark yellow brown (10 YR 4/4) silty fine sand with few subangular fine pebbles and roots (Figure S6.4). The slight increase in coarse component content at the top might be related to the ploughing activity. A ceramic-like fragment occurs at 60 cm b.s. The sediments become neutral and pH decreases from units 4 to 5. EC slightly decreases with decreasing depth. X<sub>LF</sub> values remain constant at units 2–5. LOI<sub>550</sub> shows no difference at the unit. This unit represents the fine-textured alluvial fan deposits.

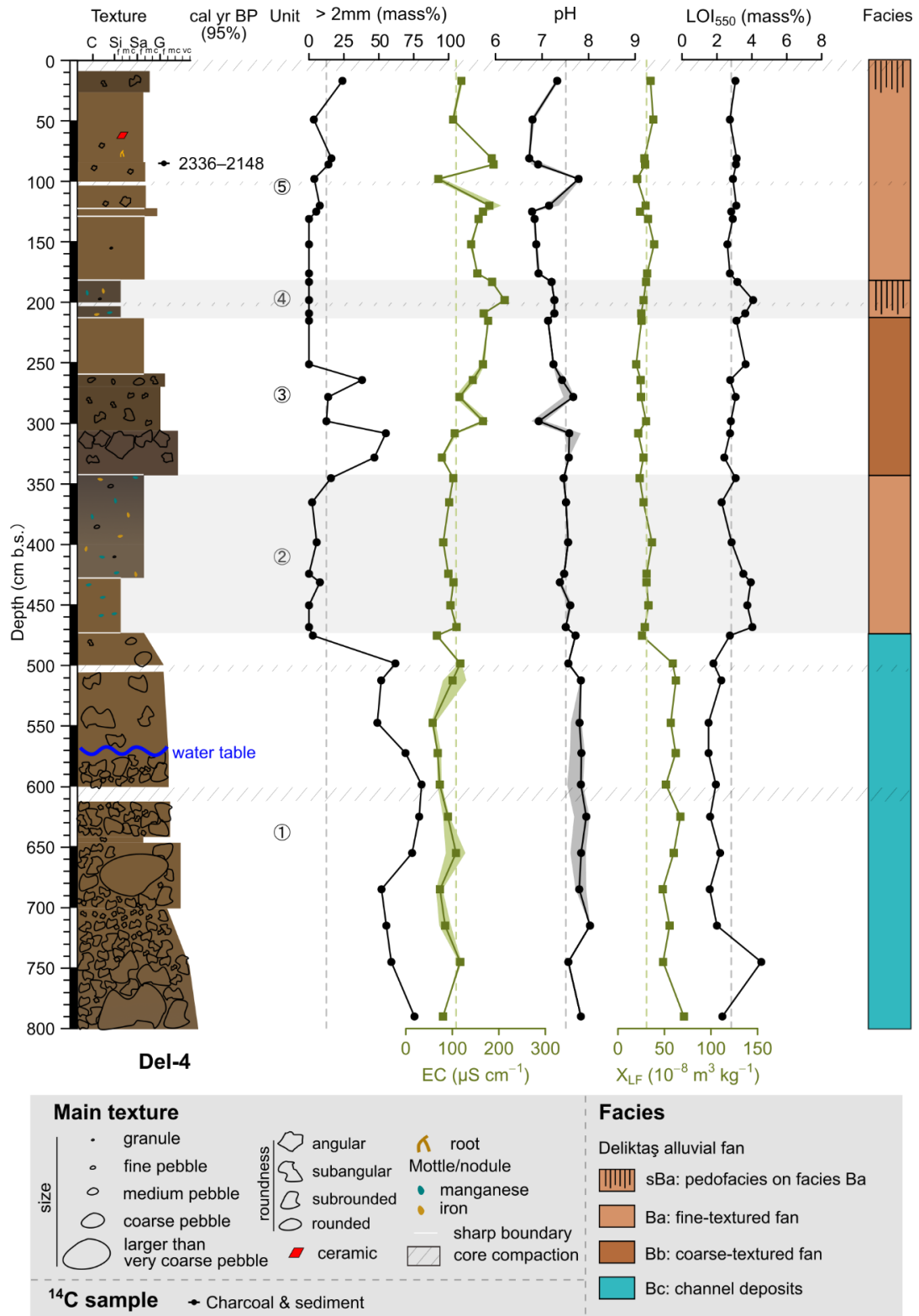


**Figure S6.4** The lithostratigraphy, radiocarbon datings, sediment bulk characters, and sediment facies of profile Del-4.

## Profile Del-5

**Unit 1 (444–368 cm b.s.)** contains clast-supported, subangular-subrounded, medium-coarse pebbles with few fine cobbles (Figure S6.5). Ground water table occurs at ca. 400 cm b.s. Sediment samples (n = 2) indicate this unit is moderately alkaline and low in LOI<sub>550</sub> (2.96 mass%). Similar to the bottom of Del-3 and Del-4, this unit is the channel deposit.

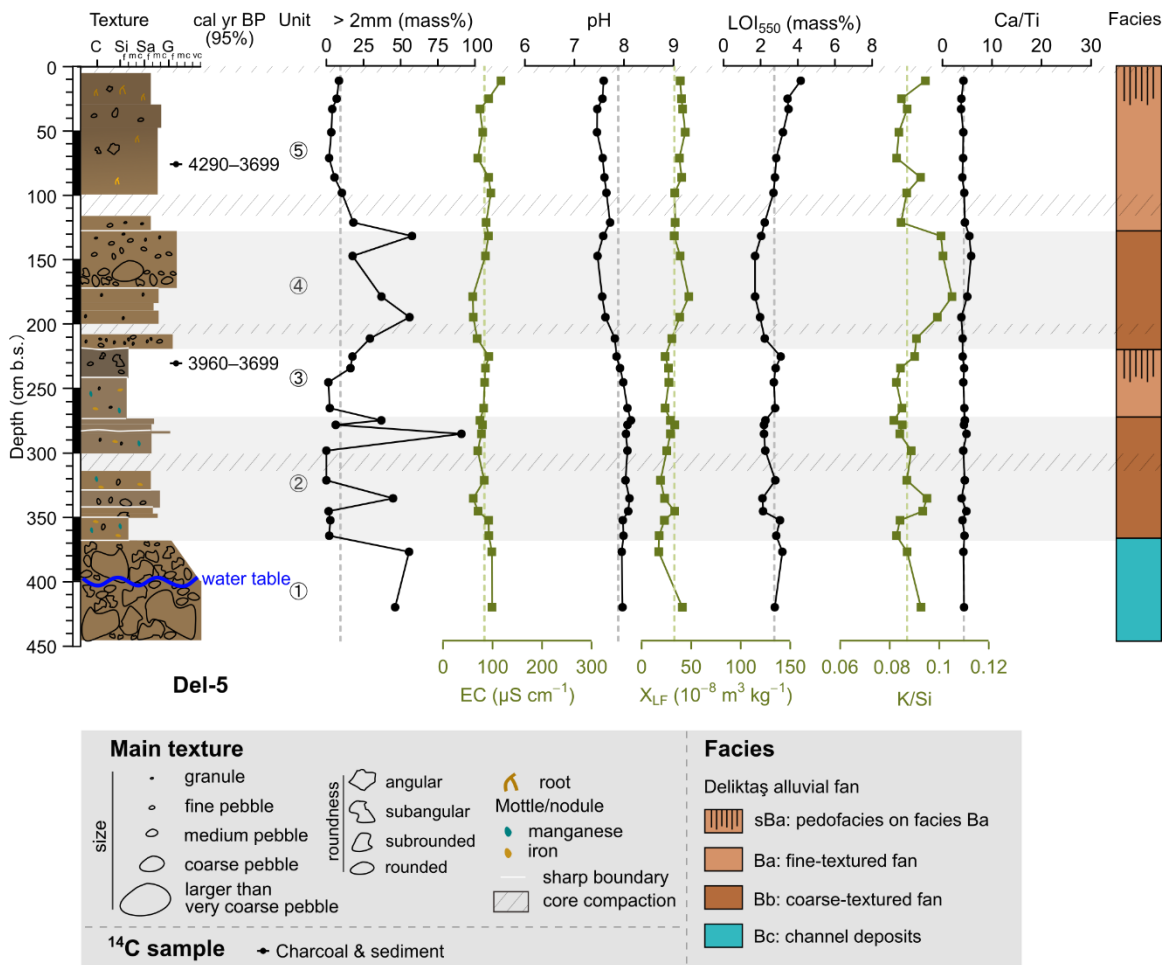


**Figure S6.5** The lithostratigraphy, radiocarbon datings, sediment bulk characters, and sediment facies of profile Del-5.

**Unit 2 (368–273 cm b.s.)** is characterized by brown (10 YR 5/3) fine pebbly fine-medium sands and a bottom layer of sandy silt (Figure S6.5). Few Fe-Mn mottles occur at this unit. The analyses of 9 samples display various peaks in the >2mm component, up to 88 mass%. EC, X<sub>LF</sub>, and LOI<sub>550</sub> slightly decrease. K/Si shows gradually decreasing values from the unit bottom to top. This unit is the coarse-textured fan facies and its lower part might be intercalated with finer sediments.

**Unit 3 (273–219 cm b.s.)** consists of dark greyish brown (10 YR 4/2) and brown (10 YR 5/3) clayey silt with few subangular pebbles and Fe-Mn mottles (Figure S6.5). This unit has a sharp and inclined boundary to unit 4. The mixed charcoal/sediment sample from 230 cm b.s. dates to 3960–3699 cal yr BP (Table 6.3). Four samples show a slight increase in LOI<sub>550</sub> and a decrease in pH and K/Si. Fine-textured fan sediments deposited in this unit and its upper part imply a soil horizon.

**Unit 4 (219–127 cm b.s.)** contains thin layers of fine-coarse sand and subrounded-rounded fine-medium pebbles (Figure S6.5). The pebbly sediments are clast supported (tuff and quartzite) at 171–156 cm b.s. Samples (n = 5) measured elevated values in the coarse component and K/Si ratio. EC, pH, and LOI<sub>550</sub> show distinct decreased values; sediments are slightly alkaline and LOI<sub>550</sub> only averages 1.97 (0.3) mass% (class 1). This unit represents the alluvial fan sediments with a coarse texture. The deposition of rounded pebbles might be influenced by the water.

**Unit 5 (127–0 cm b.s.)** is characterized by brown (10 YR 4/3) and yellowish brown (10 YR 5/4) fine sandy silt with few pebbles and roots (Figure S6.5). The mixed charcoal/sediment sample from 77 cm b.s. dates to 4290–3699 cal yr BP, showing the age inversion (Table 6.3). The measurements of 8 samples show slightly alkaline sediments with a slightly increasing in EC and X<sub>LF</sub>, particularly in the upper part. LOI<sub>550</sub> values display a distinct increase from units 4 to 5 and reach the value of 4.2 mass% at the top. K/Si decreases again and is comparable to unit 3. Thus, this unit is fine-textured alluvial fan deposits with a ploughing layer at the top.

### **Profile Del-6**

**Unit 1 (500–350 cm b.s.)** is characterized by the soft layers of weathered bedrock (Figure S6.6). At the top, the light olive brown (2.5 Y 5/3), Fe-mottled, clayey silts contain few carbonatic rocks. Sediments start to become strongly calcareous downwards. Light yellowish brown (10 YR 6/4) fine sand with few angular fine pebbles deposited in the middle, occasionally occurring a subrounded, fine cobble (quartzite?). At 495–424 cm b.s., sediments are clayey silt with strong brown colour (7.5 YR 5/6) due to the common Fe-Mn mottles on white carbonate lime powdery and fresh carbonate rocks. The last few centimetres are very pale brown (10 YR 8/2) and strongly weathered granite. This unit shows a sharp and wavy contact with unit 2. Ten samples show enrichment of coarse components in the middle. Sediments are strongly alkaline (pH = 8.56) and keep the highest values of EC (208 (26)  $\mu\text{S cm}^{-1}$ , class 1) and the lowest values of X<sub>LF</sub> (22 (4)  $10^{-8}$   $\text{m}^3 \text{kg}^{-1}$ , class 1). LOI<sub>550</sub> averages 2.98 (0.4) mass% (class 2). The soft materials in these

layers are associated with strongly weathered bedrock, mostly carbonatic rocks (facies Bd).

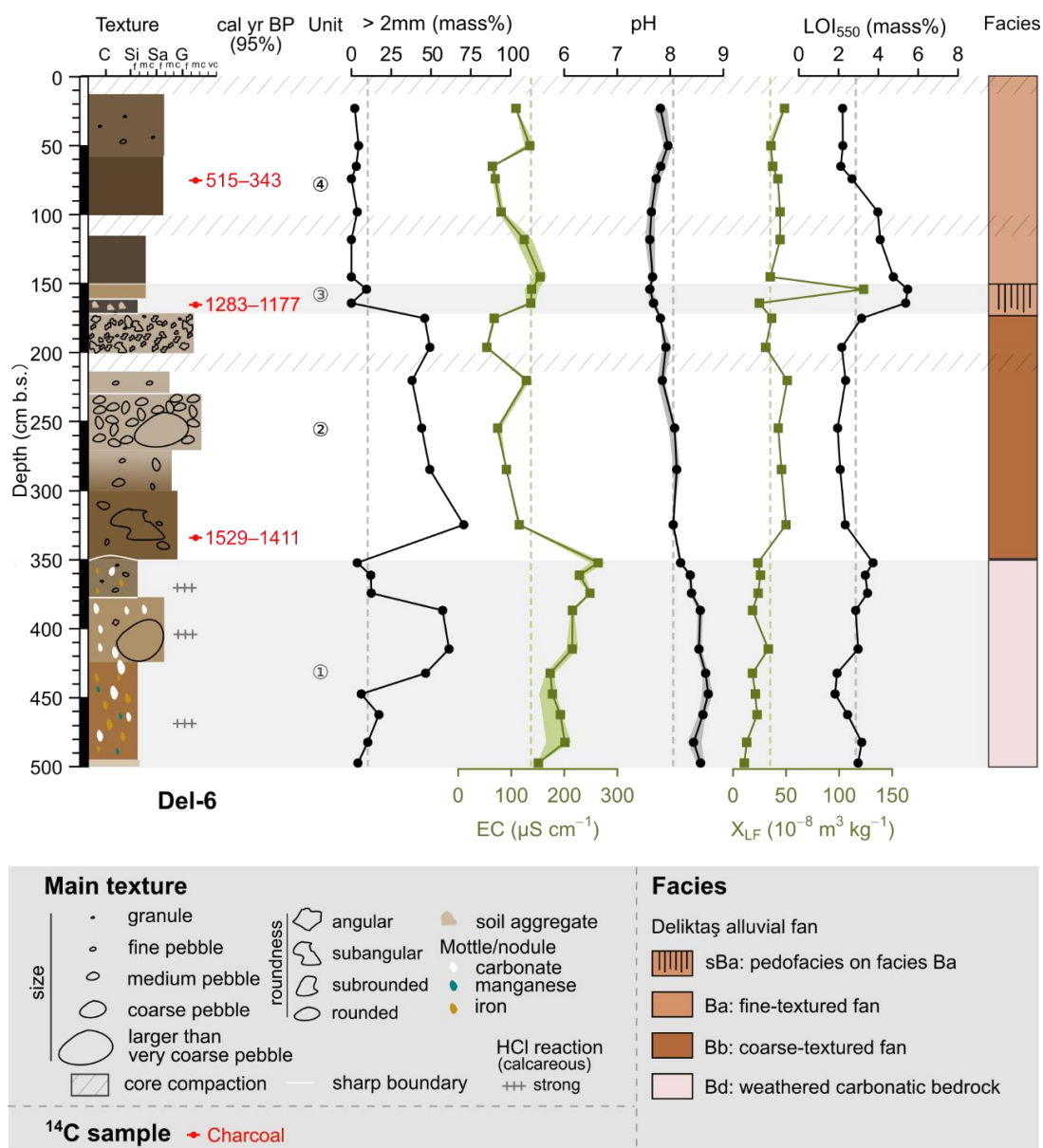


**Figure S6.6** The lithostratigraphy, radiocarbon datings, sediment bulk characters, and sediment facies of profile Del-6.

**Unit 2 (350–170 cm b.s.)** contains layers of clast-supported subangular fine–medium pebbles at the top, poorly sorted (sub)rounded medium–very coarse pebbles at 270–230 cm b.s., and fine–coarse sand with few fine–medium pebbles at the bottom (Figure S6.6). Pebbles prevail in rhyolite, tuff, or granite. The charcoal from 333 cm b.s. dates to 1529–1411 cal yr BP. Samples ( $n = 6$ ) measured a medium content of coarse components (ca. 48 mass%), low EC ( $83 (22) \mu\text{S cm}^{-1}$ , class 1), and  $\text{LOI}_{550}$  (ca. 2.25 mass%, class 2). The pH values gradually decrease to 7.82 at the unit top.  $X_{\text{LF}}$  values ( $45 (6) 10^{-8} \text{ m}^3 \text{ kg}^{-1}$ , class

2) are slightly higher than in unit 1. Similar to unit 4 in Del-5, this unit refers to the alluvial fan sediments with a coarse texture (facies Bb), and the clast-supported, (sub)rounded pebbles might be transported by rivers.

**Unit 3 (170–149 cm b.s.)** contains two thin layers of light yellowish brown (10 YR 6/4) fine sandy silt and very dark grey (7.5 YR 3/1) clayey silt (Figure S6.6). The latter occurs in 1–2-cm size brownish aggregates with pores. The charcoal from 166 cm b.s. dates to 1283–1177 cal yr BP. Sediments ( $n = 2$ ) are slightly alkaline and have high values of LOI<sub>550</sub> (5.42 mass%, class 4) and slightly increased EC (138  $\mu\text{S cm}^{-1}$ , class 1). Particularly, the brown layer has a very high  $X_{\text{LF}}$ , reaching 123  $10^{-8} \text{ m}^3 \text{ kg}^{-1}$  (class 5). This unit represents the paleosol formation (facies sBa). The high  $X_{\text{LF}}$  indicates the upper layer may have been burned.

**Unit 4 (149–0 cm b.s.)** contains brown (10 YR 4/3) and dark brown (10 YR 3/3) fine sand with few pebbles at the top (Figure S6.6). The charcoal from 77 cm b.s. dates to 515–343 cal yr BP. Sediments ( $n = 7$ ) are slightly alkaline and have decreasing values of EC and LOI<sub>550</sub> (to 2.2 mass% at the top) with decreasing depth.  $X_{\text{LF}}$  remains at low values of 42 (5)  $10^{-8} \text{ m}^3 \text{ kg}^{-1}$  (class 2). This unit is the fine-textured alluvial fan deposits (facies Ba).

## To chapter 7 (working package 4)

**Table S7.1** The soil structure and permeability index according to the soil texture class. For soil structure index: 1 means very fine granular, 2 fine granular, 3 medium or coarse granular, and 4 blocky, platy, or massive. For the soil permeability index: 2 means moderate to rapid, 3 moderate, 4 slow to moderate, and 5 slow (Wischmeier et al., 1971; Bagarello et al., 2009).

Soil texture class	Soil structure	Soil permeability
Sandy loam (SaLo), Loamy-sand, Sand	1	2
Silt loam, Loam (Lo), Sandy clay loam (SaClLo)	2	3
Sandy clay, Silt	2	4
Silty clay loam, Clay loam (ClLo),	3	4
Clay	4	4
Silty clay	4	5

**Table S7.2** The three-tier hierarchy of the 44 land cover classes of the CORINE nomenclature (Cole et al., 2018) and their corresponding P values. Refs (references): a (Aiello et al., 2015), b (Prasannakumar et al., 2012), and c means no reference but was assigned by the authors.

Level 1		Level 2		Level 3		P value	Refs		
1	Artificial surfaces	11	Urban fabric	111	Continuous urban fabric	0	c		
				112	Discontinuous urban fabric	0	c		
		12	Industrial, commercial, and transport units	121	Industrial or commercial units	0	c		
				122	Road and rail networks and associated land	0	c		
				123	Port areas	0	c		
				124	Airports	0	c		
		13	Mine, dump, and construction sites	131	Mineral extraction sites	1	c		
				132	Dump sites	0	c		
				133	Construction sites	1	c		
		14	Artificial, non-agricultural vegetated areas	141	Green urban areas	0	c		
				142	Sports and leisure facilities	0	c		
		2	Agricultural areas	21	Arable land	211	Non-irrigated arable land	1	a
						212	Permanently irrigated arable land	1	a
						213	Rice fields	1	a
				22	Permanent crops	221	Vineyards	0.8	a
						222	Fruit trees and berry plantations	0.8	a
223	Olive groves					0.8	a		
23	Pastures			231	Pastures	1	a		
24	Heterogeneous agricultural areas			241	Annual crops associated with permanent crops	0.9	a		
				242	Complex cultivation patterns	0.9	a		
				243	Land principally occupied by agriculture with significant areas of natural vegetation	0.9	a		
				244	Agro-forestry areas	0.9	a		

Level 1		Level 2		Level 3		P value	Refs		
3	Forests & semi-natural areas	31	Forests	311	Broad-leaved forest	0.5	a		
				312	Coniferous forest	0.1	a		
				313	Mixed forest	0.5	a		
		32	Shrub and/or herbaceous vegetation associations	321	Natural grassland	1	b		
				322	Moors and heathland	1	c		
				323	Sclerophyllous vegetation	0.4	a		
				324	Transitional woodland scrub	0.5	a		
		33	Open spaces with little or no vegetation	331	Beaches, dunes, and sand plains	1	a		
				332	Bare rock	1	a		
				333	Sparsely vegetated areas	1	a		
				334	Burnt areas	1	a		
				335	Glaciers and perpetual snow	1	a		
		4	Wetlands	41	Inland wetlands	411	Inland marshes	0.4	a
						412	Peat bogs	0.4	a
				42	Coastal wetlands	421	Salt marshes	0.4	a
422	Salines					0.4	a		
423	Intertidal flats					0.4	a		
5	Water bodies			51	Continental waters	511	Watercourses	0	a
		512	Water bodies			0	a		
		52	Marine waters	521	Coastal lagoons	0	a		
				522	Estuaries	0	a		
				523	Sea and ocean	0	a		



## **Curriculum vitae**

The CV is not included in the online version for data protection reasons.

The CV is not included in the online version for data protection reasons.

The CV is not included in the online version for data protection reasons.



# Eidesstattliche Erklärung

Hiermit versichere ich, Xun Yang, dass ich die Dissertation „Mittel- bis spätholozäne Geomorphodynamik und die Wechselwirkungen mit Klimaveränderungen und menschlichen Siedlungen in der Mikroregion Pergamon, Westtürkei (Mid- to Late Holocene geomorphodynamics and the interactions with climate changes and human settlements in the Pergamon micro-region, western Türkiye)“ selbstständig angefertigt habe und keine anderen als die von mir angegebenen Quellen und Hilfsmittel verwendet habe.

Ich erkläre hiermit, dass die Dissertation bisher nicht in dieser oder anderer Form in einem anderen Prüfungsverfahren vorgelegen hat.

Xun Yang

Berlin, June 2023